

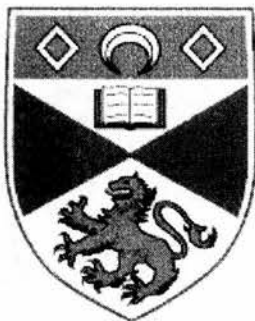
University of St Andrews



Full metadata for this thesis is available in
St Andrews Research Repository
at:

<http://research-repository.st-andrews.ac.uk/>

This thesis is protected by original copyright



New Ruthenium Sensitisers for Nanocrystalline Titanium Dioxide Solar Cells

Hunan Yi

School of Chemistry, University of St Andrews

A thesis presented by Hunan Yi to the University of St Andrews pursuing
for the degree of Doctor of Philosophy

Supervisors: Joe A Crayston and John T. S. Irvine

Date of submission: July 30th, 2002



Declarations

I, Hunan Yi, hereby certify that this thesis, which is approximately 50,000 words in length, has been written by me, that it is a record of work carried out by me and that it has not been submitted in any previous application for a higher degree.

Signed_

Date 12th Nov. 2002

I was admitted as a research student in March 1999 and as a candidate of the degree of Ph.D. in August 2002; the higher study for which this is a record was carried out in the University of St Andrews between year 1999 and 2002.

Signed_

Date 12th Nov. 2002

I hereby certify that the candidate has fulfilled the conditions of the Resolution and Regulations appropriate to the degree of Ph. D. in the University of St Andrews and that the candidate is qualified to submit this thesis in application for that degree.

Signed_

Date 12th November 2002

Declaration

In submitting this thesis to the University of St Andrews, I understand that I am giving permission for it to be made available for its use in accordance with the regulations of the University library for the time being in force, subject to any copyright vested in the work not being affected thereby. I also understand that the title and abstract will be published, and that a copy of the work may also be made and supplied to any *bona fide* library or research worker.

Signed_

Date 12th Nov. 2002

To Mum and Dad.

Contents

Chapter one Introduction

1.1	Fossil Fuels	2
1.2	Renewable Energy	5
1.3	Solar energy	7
1.4	Solar Radiation	11
1.5	Solar energy Storage	14
1.6	Photoelectrochemical cells	16
	1.6.1 Semiconductor	19
	1.6.2 The <i>p-n</i> junction	22
	1.6.3 Optical processes in semiconductors	24
	1.6.4 Photovoltaic Process in a solar cell	26
1.7	Dye-sensitized photoelectrochemical solar cells	31
	1.7.1 History	32
	1.7.2 Semiconductor-solution interface	37
	1.7.3 The Dye-sensitized semiconductor interface	40
	1.7.4 Dye-sensitized photoelectrochemical solar cells	42
	1.7.5. Comparison to solid state cells	47
1.8	Aim of Work	48
1.9	References	50

Chapter two Dye-sensitized nanocrystalline TiO₂ solar cells

2.1	Introduction	55
2.2	Key component of the solar cells	57
	2.2.1 Titanium Oxide	58
	2.2.2 Dye-sensitizer	67
	2.2.3 Anchoring groups	69
	2.2.4 Redox couple	71

2.3	Octahedral complexes	73
2.4	Molecular engineering of dye-sensitizers	78
	2.4.1 General considerations	78
	2.4.2 Tuning of the t_{2g} and π^* levels in polypyridyl complexes	82
2.5	Kinetics of the dye-sensitized solar cells	84
	2.5.1 Operating principles	85
	2.5.2 Charge injection from the dye to the semiconductor TiO_2	88
	2.5.3 Back electron transfer	93
	2.5.4 Regeneration of the oxidized dye	94
	2.5.5 Dark current	95
	2.5.6 Counter electrode performance	97
	2.5.7 Summary of the kinetics	98
2.6	Experimental	99
	2.6.1 Dye-sensitizer synthesis	100
	2.6.2 Hydrolysis of titanium isopropoxide	103
	2.6.3 Cell preparation	105
2.7	Results and discussions	106
	2.7.1 Synthesis	106
	2.7.2. Electronic absorption spectra	109
	2.7.3 Electrochemistry	111
	2.7.4 Surface chemistry	115
	2.7.5 Solar cell performance	117
2.8	Conclusions	119
2.9	References	120

Chapter three Ruthenium Complexes of Polypyridyl Benzimidazole

3.1	Introduction	127
3.2	Ligand modification	129
3.3	Charge separation	131

3.4	Experimental	137
3.4.1	Synthesis of the ligands	139
3.4.2	Synthesis of the complexes	142
3.5	Results and discussions	145
3.5.1	Synthesis	145
3.5.2	¹ H NMR study of the complexes	147
3.5.3	Electronic absorption and luminescence spectra	152
3.5.4	Electrochemistry	157
3.5.5	Surface attachment chemistry	170
3.5.6	Time-resolved photoluminescence Spectroscopy	175
3.5.7	Solar cell performance	177
3.6	Conclusions	181
3.7	Reference	183

Chapter four Derivatives of Tris(2-pyridylmethyl)amine

4.1	Introduction	187
4.2	Experimental	190
4.2.1	Synthesis of the ligands	191
4.2.2	Synthesis of the complexes	202
4.3	Results and discussions	203
4.3.1	Synthesis of the ligands and the complexes	203
4.3.2	Regioselective reduction of the pyridyl diesters	211
4.3.3	Electrochemistry	217
4.3.4	UV-Vis absorption	225
4.3.5	IR spectroscopy	227
4.4	Conclusions	228
4.5	References	229

Chapter five Future work

5.1	Some other metal complexes	233
5.2	Future work	235
5.3	References	240

Acknowledgements

Upon finishing my study and thesis, I would like to express my sincere gratitude to Dr. Joe Crayston and Prof. John Irvine whose assiduous work, enthusiasm and great knowledge which have guided me through all three years of my Ph.D. study in the University of St Andrews. Without their invaluable aid I would not be able to present my work. I would like to especially thank Dr. Crayston for his kindness, generosity and patience with me.

I would also like to thank Prof. Sameul Ifor from physics for the fluorescence and time-resolved fluorescence experiments and thank Dr. Ebinazar Namdas for giving a helping hand for the test. Thanks also due to Dr. Bruce Sinclair from physics for the solar cells performance experiment setting up and tests. Thank for those who have given me precious ideas and aid, all those people have been very kind and great help for me for my work and my study.

Thank for those who have been working in Lab. 414 and have done their best to help me on not only my work but also my life in this rather fascinating different culture. Dr. Dave Richens, Chanaka De Lewis, Joanne Ritchie, Sneh Jain, Ann McConnell deserve mentions by name.

I am indebted to ORS scholarship for financial support throughout my course and Department Travel Fund for supporting conference travel. I am also much obliged for Mary Wang Award for my final year support.

Abstract

The direct conversion of solar energy into electricity is one of the best known solar energy conversion strategies. The common photovoltaic devices function in a purely physical manner, but photoelectrochemical devices store a significant amount of energy as chemical potential under open circuit conditions and release it as electricity when an external circuit is closed. This thesis describes work in this important area.

First of all, in order to understand the fundamental theory of how the sensitizer complex in the solar cell works, the so-called "standard dye" *cis*-[Ru(dcbpy)(SCN)₂] (dcb = 4,4'-bipyridinedicarboxylic acid) was synthesized and its electronic absorbance, electrochemical behavior, surfaces chemistry on TiO₂ electrode and solar cell performance have been tested as a benchmark for the new sensitizers.

Secondly, 2-(2-Pyridyl)benzimidazole (pbimH), its carboxylic acid derivatives of different chain-lengths (N-alkylated pbim(CH)_nCOOH where n = 1-3) and their ruthenium complexes [Ru(bpy)₂(pbim)](PF₆)₂ have been synthesized and characterized. 2D COSY and NOESY NMR spectroscopy were used to aid the assignment of the pbim signals. The effect of chain-length on the cyclic voltammetry (CV) and the pH-dependence of the pbimH complex on the UV-vis spectroscopy were investigated. A symmetrical, surface-confined Ru^{III/II} wave was observed in the CV, while the IR revealed a band at 1620 cm⁻¹ due to the bound carboxylate (COO...Ti) group. The efficiencies of solar cells using these sensitizers have been further investigated using time-resolved fluorescence spectroscopy and the results are discussed in terms of the distance between the sensitizer and the surface and the location of the charge-separated excited state.

And finally, some new *tris*(2-pyridylmethyl)amine (tpma) carboxylic acid derivatives and their ruthenium complexes [Ru(tpma)Cl₂]⁺, [Ru(tpma242)(dmsO)Cl]⁺ and [(μN₂)(Ru(tpma)Cl)₂]²⁺ have been synthesized. Alternative synthetic methods of the target compound have been described and compared. A route involving the selective

borohydride reduction of pyridine diesters was selected after a study of the effect of cations on the reaction. The tpma complexes were characterized the usual methods and by UV spectroscopy and cyclic voltammetry. Electrochemistry showed a low E^0 for both $\text{Ru}^{\text{III/II}}$ processes for $[\text{Ru}(\text{tpma})\text{Cl}_2]^+$ and $[(\mu\text{N}_2)(\text{Ru}(\text{tpma})\text{Cl})_2]^{2+}$. Low energy MLCT bands were observed in the UV-vis spectrum, and preliminary sensitizer studies have been performed.

CHAPTER ONE

INTRODUCTION

The sun's radiant energy is the only completely renewable and absolutely safe source of energy that we know how to use today. Thanks to the experimentation involving over a century of assiduous and dedicated scientific work, we now possess the capability to heat and cool space and water, to generate steam for various technological process including power generation, and to convert solar radiation directly into electricity.

The most important process in which solar radiation plays a vitally important role is photosynthesis, by which the green plants living on land and in the sea convert solar energy, water and carbon dioxide into oxygen and chemical energy to maintain the life and civilisation of human beings and other lifestyles on the earth. Photosynthesis has been occurring on our planet for untold billions of years and it has been the subject of many hours of research work in some of the world's finest laboratories. Whilst higher efficiencies than natural photosynthesis are now possible in artificial systems, a simple blade of grass can still do a more cost-effective job of converting sunlight to chemical energy. This sounds frustrating but nevertheless, we human beings are gradually making progress in the use of solar energy, finding ways of coping with nature to ensure a better quality of life on the earth.

1.1 FOSSIL FUELS

Much of our present material prosperity depends on an abundant supply of coal, gas and oil, which provides energy to operate our machines. They are still the main sources of delivered energy and of primary energy. These fossil fuels are limited in quantity and are essentially irreplaceable. We can't blithely assume that our descendants can continue indefinitely to have all the fuel that they desire even though the world will not suffer a shortage of fuel in this generation.

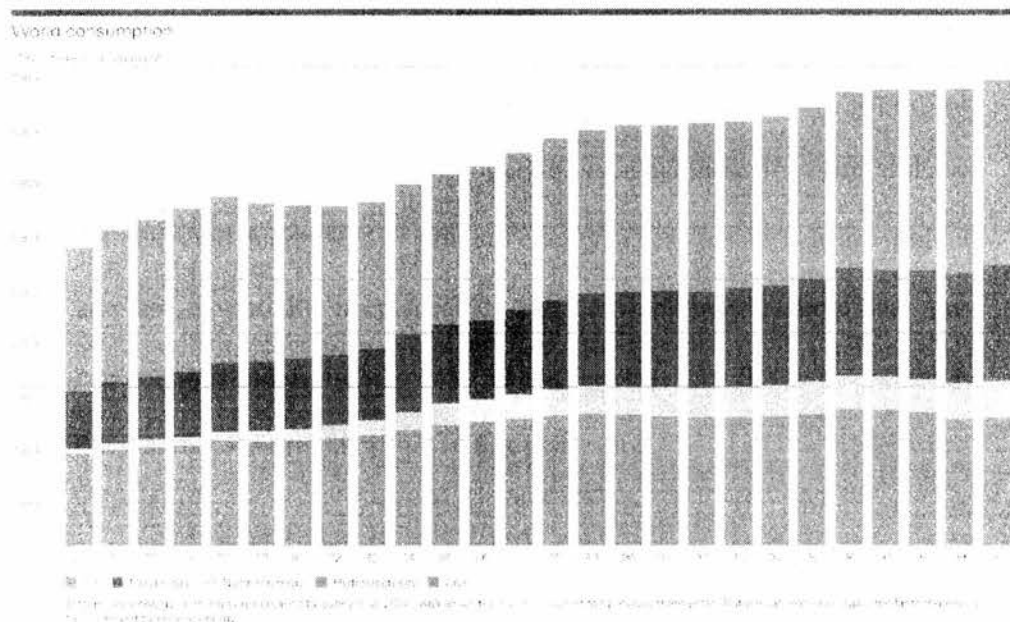


Fig. 1.1. World energy consumption in the millions tons of oil equivalent from year 1975 to 2000. Going down each column is the percentage of oil, natural gas, nuclear energy, hydroelectricity and coal respectively that was consumed.¹ (Total primary energy consumption increased by over 2% in 2002, well above the sub-1% pace of the previous three years. Natural gas was once again the fast-growing fuel, followed by nuclear energy)

Chapter One: Introduction

Coal, more than oil and gas, has been long used for industry and domestic consumption and is still widely used in most developing countries. But in the long run, the integrated whole consumption of coal, due to environmental side-effects and much more urgent constraints than either world resource base or the historic and importance of this fossil fuel industry, is going to be limited in particular regions and most countries.

In recent decades, coal was extensively replaced by oil and gas,² and the two latter fuels accounted for about all growth in primary use. The whole world has become steadily more dependent on energy supplies in general, and oil and natural gas in particular. Oil, which has been the "life-blood" of the transport and the source of most chemical raw materials such as methanol, occupies a central part on the energy scene in almost all of the developed countries nowadays. The uses of natural gas which is regarded as most representative of premium demands are high-temperature industrial direct heat for energy and other processes and much domestic cooking and heating. In this case, it is very inefficient to burn high-grade fuel to produce low-grade heat.

The most serious risk from fossil fuel combustion is probably the emission of CO₂, whose long-term climatic effects are unknown but possibly grave.³ The use of coal liberates significantly more CO₂ per unit of primary energy than oil or natural gas. Climatologists generally agree that, through a complex and poorly understood mechanism, the use of fossil fuels will probably perturb global climate significantly unless present trends are markedly altered. Carbon dioxide, emitted by burning coal and other fossil fuels, absorbs infrared radiation to which the atmosphere would

Chapter One: Introduction

otherwise be transparent. In this way, the heat balance between the earth's surface and different layers of the atmosphere would be strongly affected. It will lead to a greenhouse effect that would lead to global climatic changes and raising the earth's temperature.^{4,5} The latter change could cause melting of the Arctic and Antarctic ice caps, leading to accentuated coastal erosion and finally forcing the abandonment of many coastal cities of sea level. From estimates of the possible effect on atmospheric CO₂ concentration of different rates of fossil fuel consumption, we would view as alarming in risk the trend in long-term and a more prudent course for using fossil fuels is demanded with regard to this risk. Global mean surface temperatures have increased 0.5 ~ 1.0 °F since the late 19th century. The 20th century's 10 warmest years all occurred in the last 15 years of the century. Of these, 1998 was the warmest year on record. Globally, sea level has risen 4 ~ 8 inches over the past century. Worldwide precipitation over land has increased by about one percent. Scientists expect that the average global surface temperature could rise 1 ~ 4.5 °F (0.6 ~ 2.5°C) in the next fifty years, and 2.2 ~ 10 °F (1.4 ~ 5.8° C) in the next century, with significant regional variation.⁶

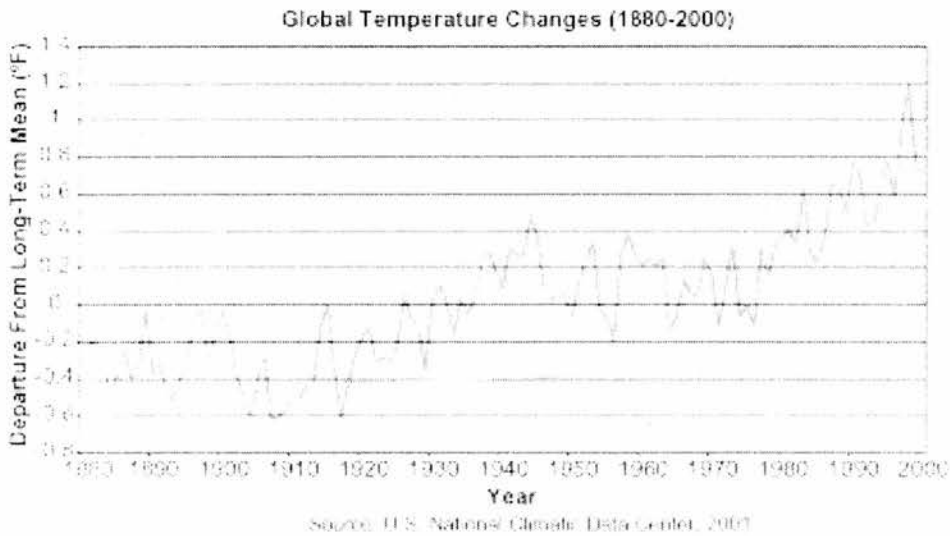


Fig. 1.2. Global temperature changes from the year 1880 to 2000.⁶

1.2 RENEWABLE ENERGY

The world has developed and become more affluent during the last century or more, which has been associated with a large growth in energy consumption, especially of fossil fuels, coal, oil and natural gas. If the world population was to increase as forecast by the United Nations (UN), and if per capita consumption of oil and natural gas stayed the same as today, our mother earth would exhausted its entirely likely remaining oil deposit in some 60 and it's natural gas in 70 years.⁷ The distribution of fossil fuel reserves is far from uniform. Approximately 50% of the world's ultimately recoverable oil reserves are thought likely to be in the nations of the Organisation of Petroleum Exporting Countries (OPEC). Approximately 50% of the world's recoverable gas reserves may be beneath the soil of Russia and formal Soviet Union countries, and another 20% in OPEC countries.⁸

Oil and gas are not only increasingly scarce, they have become a major source of political and economic instability. In recent decades, developed countries have come to be fuelled by a few giant oil fields, and their consumers have become vulnerable to disruptions of supply in remote countries. The rapid rise of the oil price has dramatically affected the world economy, and brought the energy problem to the top of the international economic agenda.

Our fuels were produced millions of years ago and through geological accident preserved for us in the form of oil, gas and coal. They are essentially irreplaceable yet we are using them at a rapid rate, the exhaustion of our fossil fuels is inevitable, if not imminent. And because of the reasons above-mentioned, we are

Chapter One: Introduction

looking for ways for the alternative energy sources, including: bio-fuels, onshore wind power, wave power, hydroelectric, geothermal fuel cells and photovoltaic generation. This is what is meant by renewable energy, which covers a whole range of different technologies, from the very simple to the very advanced. *The term "Renewable Energy Resource" is used for energy flows which are replenished at rates comparable to which they are used.*⁹ In 1997, renewable energy accounted for 13.8 per cent of world energy production,¹⁰ but still, at the moment, renewable forms of energy play a very much minor part in energy production, especially in the developed world. A lot of work will need to be done to change that situation in the near future.

Of all the alternative energy sources, the sun's radiation is our greatest source of continuing power. The energy in all our food and fuels comes originally from the sun through the photosynthesis in plants. Solar energy will always be available as long as there are people on the earth to use it. Theoretically, the sun's rays bring to the earth far more heat than is needed even for our present great energy-consuming civilisation.

Apart from solar power, bio-fuels,¹¹ wind, wave power and hydroelectric power have long been the energy form which have been captured for different uses. Of the renewable energy sources, biomass plays an important role around the world, especially in some developing countries.¹² The role of biomass could almost certainly be augmented by utilising waste which has been produced in past years and disposed of. Biomass can also be processed into liquid fuels. Wind energy conversion into linear motion of a body has been utilized extensively, in particular for transportation across water surface. It has been the driving force of wind mills and ship sailing in the

human history and wind turbines are used primarily to generate electricity. Hydroelectric power today supplies about 2 ~ 3% of electricity generated around the world. Hydroelectric power, as well as biomass, on the other hand, still might be environmentally cost-effective.

1.3 SOLAR ENERGY

Most solar energy applications involve tapping sunlight as heat; however, it would be advantageous if the direct conversion of solar energy to electricity or storage as chemical energy was readily available. Almost all of the latter processes occur with a photochemical reaction as the primary process. The amount of solar energy intercepted by the earth and hence the amount of the energy flowing in the "solar energy cycle" is about 5.4×10^{24} J per year. The total world-wide demand for end-use energy has been estimated to be about 1.1×10^{20} J per year,¹³ which allows us to reach the conclusion that the energy of less than 10 minutes of sunshine on the planet earth is equal to the total yearly human energy consumption. This statement should provide sufficient justification and motivation for anybody to undertake research in the area of solar energy. The heat of the sun energy flowing, however, is of little significance for direct utilisation because it comes to earth in so diffuse a form and at such a low temperature that is not now being converted into useful work except through agriculture. It is very difficult to make practical use of solar energy, but it is not impossible. Moreover, easily storable fossil fuels in the form of coal, oil and gas, suitable for operating our engines efficiently, has been so abundant and cheap that we had little incentive to put the sun to work.

The use of solar energy has taken several different forms, including space heating and domestic uses such as: cooking and water heating; power generation in the form of electricity; solar evaporation and distillation of sea water to give salt and drinking water; solar furnaces for attaining high temperature; photosynthetic and photochemical utilisation of solar energy.

Solar energy emitted by the sun and the earth's surface is a form of electromagnetic radiation that is available over a wide spectral range (300-2100 nm). In order to be used, the radiation must be converted into an energy form suitable for our needs. Four efficient types of solar energy conversion methods are currently available for this purpose.¹⁴

1) Thermal solar energy conversion

This type of solar energy usage involves the use of solar radiation to directly heat water and to get high temperature for industrial uses. Solar house heating appears to be the simplest direct application of solar energy because a relatively slight elevation of temperature is needed. There are other domestic uses of solar energy such as cooking and air conditioning.

2) Thermoelectric solar energy conversion

Solar energy is transformed into heat, which in turn is used to generate electricity using conventional oil heat exchanges and steam turbines. It involves a large investment, especially in solar concentrators, making production of power from

solar energy more expensive than methods currently in use, even though there is no fuel cost of solar power. It seems unlikely that large scale solar power will become economical using this method in the near future, unless the cost of oil and coal becomes much higher than it is today.

3) Photoelectric solar energy conversion

The direct conversion of solar energy into electricity is one of the best known method of solar energy conversion, which involves physical and chemical processes essential to the transduction of electromagnetic radiation to electrical power by means of a photovoltaic device. The device may function as a simple transducer or may store significant amounts of energy as chemical potential under open-circuit conditions and release it as electricity when an external circuit is closed.

4) Chemical solar energy conversion

Photochemistry provides a very important long range hope for the storage and utilization of solar energy. The conversion of solar energy into chemical energy is one of the most widely used form of solar energy such as the photosynthesis, which supplies us with practically all our food, fuel and fibre. The products of photosynthesis represent stored energy. In principle, it should be easy to break up a coloured compound by sunlight in a chemical reaction which absorbs heat, and then allow the reaction to reverse itself and release heat. In practice, most reactions of this type reverse themselves too quickly for efficient storage. A classical example for this type of photochemical reaction is the norbornadiene cycle^{15, 16} shown in Fig. 1.3.

Chapter One: Introduction

Norbornadiene undergoes a $2\pi + 2\pi$ Paterno-Buchi cycloaddition to quadricyclene. The energy of one photon is thereby stored in one molecule of quadricyclene, which is an energetically higher state than the starting material. Thus, by choosing an appropriate catalyst¹⁷ the reaction barrier can be lowered to allow the exothermic back reaction to take place. Via use of this mechanism, the system can store energy at a high volumetric energy density of approximately 1000 J cm^{-3} . This very elegant reaction combines organic photochemistry, catalysis and solar technology. The simplicity of the scheme is striking and it is unfortunate that large scale application has never been realized, perhaps because of it is not competitive with conventional solar heat exchange.

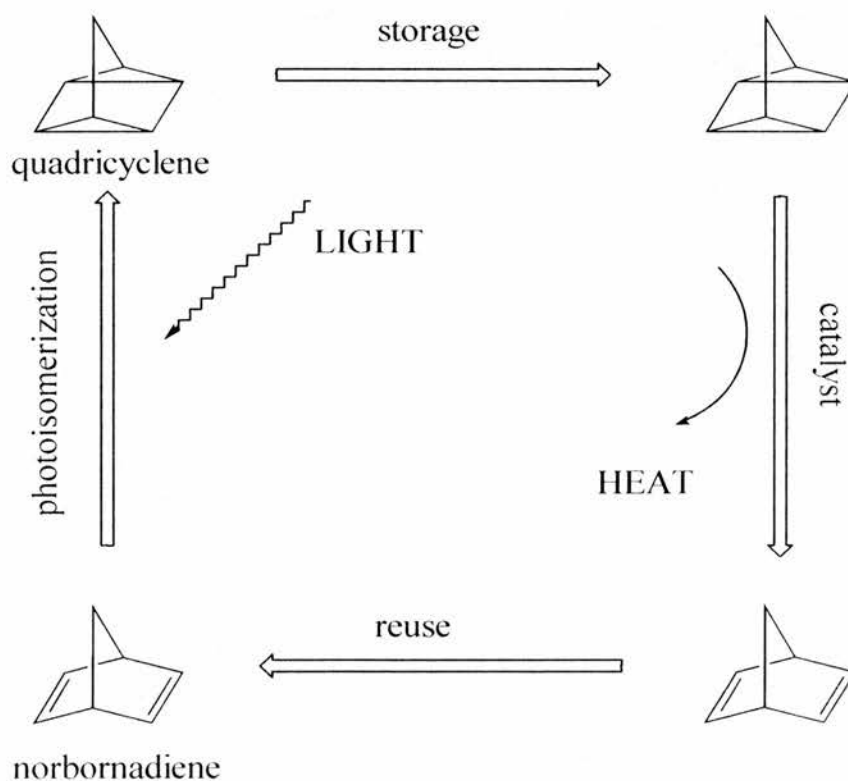


Fig. 1.3. Schematic diagram of the norbornadiene / quadricyclene energy cycle.

1.4 SOLAR RADIATION

The sun is a sphere of intensely hot gaseous matter lying at an average distance of 1.5×10^8 km from the Earth. Its temperature ranges from approximately 6000 K at the surface to $> 10^6$ K in the interior regions.¹⁸ These extremely high temperatures result from a series of nuclear reaction, the end result of which is the fusion of four protons to form an alpha particle (helium nucleus). This process liberates energy which ultimately is radiated into space.

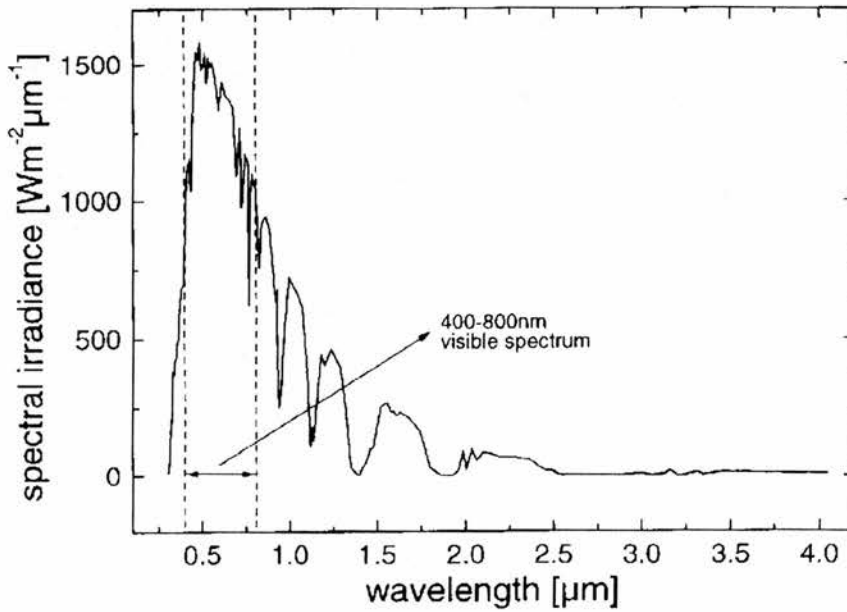


Fig. 1. 4. Spectral distribution of solar radiation.

Air mass 1.5 global spectrum¹⁹

The radiation received at the earth's surface consists of direct and scattered (plus reflected) short-wavelength radiation from sky and clouds, originating as

Chapter One: Introduction

thermal emission or by reflection of thermal radiation from the ground. Radiation is partly absorbed and scattered during the course of its journey through the atmosphere. Water and carbon dioxide absorb the infrared radiation and ozone the ultraviolet radiation. Scattering of radiation is caused by *Rayleigh scattering* by molecules, *Mie scattering* by aerosols and *Cirrus scattering* by clouds.¹⁸ For example, in central Europe on a cloudless summer day with the sun at the zenith, up to 70% of the total solar radiation can be due to diffuse (scattered and reflected) light and only 30% of the light actually hits the surface perpendicular to the sun's path. Furthermore, due to the nature of scattering, the diffuse light component contains a higher fraction of the higher energy ultra violet radiation. Thus, solar cell devices depending on the light arriving at a certain angle will be significantly limited in efficiency so that cells which can collect solar radiation over a large angle and are tuned for optimal performance under diffuse light conditions will be preferred.

Specific solar radiation conditions are defined by the *Air Mass* (AM) value. The spectral distribution and total flux of radiation just outside the earth's atmosphere, similar to the radiation of a black body of 5800 K, has been defined as AM-0. In passing through the atmosphere the radiation becomes attenuated by complex and varying extinction processes mentioned above. At the equator at sea level at noon when the incidence of sunlight is vertical ($\alpha = 90^\circ$, sun in zenith) and the light travels the shortest distance through the atmosphere and the air ("air-mass") to the surface, the spectral solar radiance and flux (1.07 kWm^{-2}) is defined as AM-1. However, if the angle of light incidence is smaller than 90° , the light has to travel through more air-mass than under AM-1 conditions. The relative path-length through the atmosphere by the shortest geometrical path is given by:

$$AM = \frac{1}{\sin \alpha} \quad (1.1)$$

The relationship described in equation 1.1 is only valid for a planar atmosphere. But only introduces an error of less than 1% from the curved atmosphere of the earth, if $\alpha > 20^\circ$. For accurate measurements, the local atmospheric pressure also has to be considered. This problem has led to introduction of the relative air mass AM^* , given by ($p_0 = 1.013 \text{ bar}$):

$$AM^* = \frac{p}{p_0} AM \quad (1.2)$$

The so-called AM-1.5 conditions are achieved when the sun is at an angle of 41.8° above the horizon and results in the spectral distribution shown in Fig. 1.4 and a solar flux of 963 W m^{-2} . This angle of incidence is commonly encountered in western countries and hence AM-1.5 is taken as a standard condition for solar cell testing and referencing. In the last few years, the AM-1.5 spectrum has been standardized by both the International Standards Organization (ISO 9845-1:1992) and by the American Society for Testing and Materials (ASTM E892-87:1992), although the latter standard is more commonly referred to in respect of solar cell testing. For convenience, the flux of the standardized AM-1.5 spectrum has been corrected to 1000 W m^{-2} . However, despite availability of standards, great care must be taken when results reported in the literature are compared. For example, often AM-1.5 conditions are reported, but this may only mean that a radiance of 1000 W m^{-2} has been used, with the proper spectral distribution being neglected.

1.5 SOLAR ENERGY STORAGE

Apart from the captured chemical energy from the sun radiation through photosynthesis, there must be ways to carry over the sun's daytime radiation for use at night or for a period of cloudy weather when the availability is lowest. The task of storage is currently one of the biggest challenges in the field of solar energy conversion technology.

Nature furnishes a photochemical solution to the problem of energy storage with the process of photosynthesis in green plants. Through a complex series of steps, carbon dioxide and water are converted photochemically into oxygen and combustible carbohydrate. The challenge for the photochemist is to devise an artificial cycle which accomplishes the same task, namely, the production of a storable fuel from readily available and inexpensive raw materials.

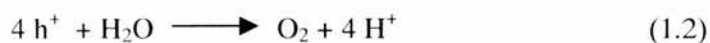
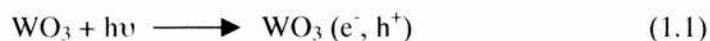
In principle, the energy can also be stored by pumping water to a higher level and letting it flow back through a water turbine which operates an electrical dynamo. In practice, very large water reservoirs would be required to meet extensive demands for night-time electricity. In some locations, it would be possible to combine solar engines or generators with hydroelectric plants operated from reservoirs and dams. When the sun is shining, electricity would be generated directly from solar energy and the amount of water allowed following through the water turbine could be reduced accordingly. At night or on cloudy days the hydroelectric plant would take over, with the help of extra water saved by the operation of the solar engines.

Another obvious way of storing solar energy is through the use of storage batteries. A much more powerful energy storage medium is hydrogen, which has the advantage of being used both as temporary energy storage medium and as a fuel. Hydrogen is a clean fuel that is transportable and storable on a large scale in gaseous or liquid form. It is capable of serving most, if not all, of the fuel functions served by today's fossil fuels. In principle, hydrogen can be produced in almost unlimited amounts from the sole material feedstock, water. During the energy-producing step, hydrogen is burnt with oxygen and reacts to give water without producing pollutants and green house gases upon combustion, and hence it is a renewable energy source.

As water is transparent to light, a sensitizer is required in order to absorb the solar photons and transducer their radiant energy to generate the chemical potential required to split the H₂O molecules. The optional absorption threshold for a single photo-converter has been calculated to be an energy of 1.6 eV,²⁰ implying that all solar photons below 770 nm are absorbed.

In the university of Geneva and Bern,²¹ a tandem device has been developed to achieve the direct cleavage of water into hydrogen and oxygen by visible light. It is based on a series connection of two photo-systems. A thin film of nanocrystalline tungsten trioxide absorbs the blue part of the solar spectrum. The valence band holes (h⁺) created by the band gap excitation of WO₃ serve to oxidize water to oxygen, while the conduction band electrons are fed into the second photo-system. It consists of a dye-sensitized nanocrystalline TiO₂ film. The latter is placed directly behind the WO₃ film capturing the green and red part of the solar spectrum that is transmitted through the top electrode. The photovoltage generated by the second photo-system

enables the generation of hydrogen by the conduction band electrons. The overall reaction corresponds to the splitting of the water by visible light (equations 1.1 – 1.3). The overall AM 1.5 solar light to chemical conversion efficiency achieved with this device is reported to be 4.5%.



1.6 PHOTOELECTROCHEMICAL CELLS

In the past decades, an ever increasing interest has been directed towards photochemical and photoelectrochemical process which are applicable to solar energy conversion.²²⁻²⁴ It is well known that photoelectrochemical cells can be used for solar energy conversion as well as for production of chemical fuels. Photovoltaic cells are based on purely solid state devices and have been used for a long time, for instance, in various optical electronic devices. They consist either of *pn*-junctions or of Schottky type²⁵ junctions, and single crystal devices of both types having high conversion efficiency have been made. Today, the single-crystal silicon solar cell is a mature product. It is based on process of photo-excitation and charge separation in space, the physics of which are well understood.

Photoelectrochemical devices for direct conversion of solar energy to electrical energy can be divided into three main categories: (a) those in which absorption of ultra-band-gap light by a semiconductor electrode or particle results in

Chapter One: Introduction

minority carrier injection into solution thereby driving a desirable Faradaic process at a thermodynamic under-potential; (b) those in which a homogeneous photochemical reaction, nearly always an electron transfer, yields electroactive products which can diffuse to, and react at conventional electrodes and (c) those in which light absorption in a pigmented micelle, membrane or coating yields charge separation in or across an insulating support medium.

The observation of photovoltaic effects can be dated back to more than 150 years ago. In 1839, Becquerel detected a photovoltage when sunlight was allowed to shine on one of two electrodes he had placed in an electrolytic solution.²⁶ In 1954, the first practical conversion of solar radiation into electric energy was achieved by using a *p-n* junction type solar cell with 6 % efficiency in Bell Telephone Laboratories.²⁷ Photovoltaic cells made of semiconductor-grade silicon quickly became the power source of choice for use on satellites with the advent of the space program. The systems were very reliable, and the cost was of little concern. Serious consideration of photovoltaic cells as a terrestrial power source has been realized because of the disruption of oil supplies to the industrialized world in the early 1970s. This work has been focusing research attention on improving performance, lowering costs and increasing reliability. These three issues remain important today, even though extraordinary progress has been made over the years.

Photovoltaics represent a high technology approach to converting sunlight directly into electrical energy. The electricity obtained in this process can be directly used to operate direct current devices, converted to an alternating current or stored for later uses. In its simplest form, conceptually, a photovoltaic device is a solar-powered

Chapter One: Introduction

battery which consumes light and turns it into another potential energy form like electricity. Furthermore, the operation is environmentally benign and if the device is correctly insulated against harm from the environment, there is nothing to wear out. Photovoltaic devices are of many benefits which makes them usable and acceptable to all the habitants on our planet because sunlight is universally available. Their electrical power output can be engineered for virtually application of not only low powered consumer uses such as wristwatches or calculators but also high capacity solar power plants. Moreover, incremental power additions are easily accommodated in photovoltaic systems, unlike more conventional approaches based on the use of fossil or nuclear fuel, which require multi-megawatt plants to be economically feasible. It has been estimated²⁸ that a photovoltaic power plant of an area of 140 km² located in an average part of the US could generate all the electricity demanded by the country, assuming reliable conditions and a system efficiency of 10 %.

To understand the many facets associated with generation of photovoltaic power, one must understand the fundamentals of how the devices work. Although photovoltaic cells come in many forms, the most common structure is based on the use of a semiconductor material into which a large-area diode, or *p-n* junction, has been formed. The fabrication process tends to be based on traditional semiconductor approaches-diffusion, ion implantation, etc. Electrical current is taken from the device through a grid contact structure on the front that allows the sunlight to enter the solar cell, a contact on the back that complete the circuit, and an antireflection coating that minimizes the amount of sunlight reflecting from the device.

1.6.1 Semiconductor

The study of semiconductors focuses a part of the wider subject known as solid-state physics. The concern is with the passage of electric current through solids as opposed to liquids and gases. For about 100 years, solids have been known with resistivities in the range of 10^{-3} to $10^{-4} \Omega \text{ m}$.²⁹ It is within this group that semiconductors exist. However, while some impure or heavily doped semiconductors can have electrical properties quite similar to metals, those in a very pure state may be good insulators, especially if maintained at low temperature.

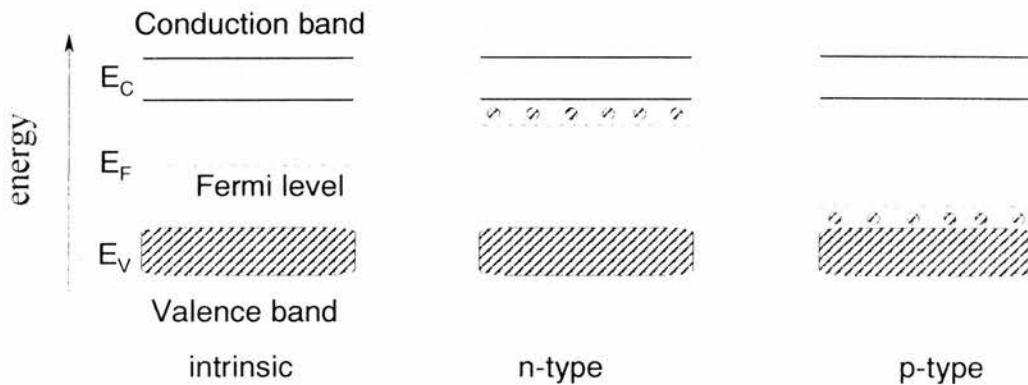


Fig. 1.5. Energy diagram of semiconductors with intrinsic, n-type and p-type properties. E_C = energy of conduction band, E_V = energy of valence band and E_F = energy of Fermi level respectively.

In a semiconductor, the electrons reside within two energetic values or bands, the valence band and the conduction band. Separating these two bands is a band of forbidden state, the energy gap (E_g). According to band theory, a solid body is characterized by a unified electron spectrum in which each electron is delocalised

Chapter One: Introduction

over the entire lattice rather than localized to an individual band. The energy band diagram of that part of the spectrum which determines the electrical and optical characteristics of a semiconductor in the range of interest shown in Fig. 1.5.

To remove electrons from the covalent bonds of an intrinsic semiconductor (to form an electron-hole pair) requires a significant amount of energy. For example, the energy gap between the top of the valence band and the bottom of the conduction band is 0.75 eV for germanium and 1.1 eV for silicon.³⁰ When a controlled amount of impurity is introduced into the lattice structure of an intrinsic semiconductor, it can become an extrinsic semiconductor. Introducing a pentavalent impurity (to produce *n*-type germanium, for example) creates additional electrons to those in the covalent bonding and so creates new donor energy level within the forbidden gap just below the conduction band. The gap between this new level and the bottom of the conduction band is much less than the energy gap in the intrinsic semiconductor. For germanium it is 0.75 eV, when doped with pentavalent antimony, for example, the new level is only 0.05 eV or less below the bottom of the conduction band. Doped germanium is consequently a much superior conductor to pure germanium, with electrons as the majority carriers. Introducing a trivalent impurity (to produce *p*-type silicon for example) creates additional positive holes and so produces new acceptor energy level in the forbidden gap just above the top of the valence band. Electrons from the valence band can readily be thermally excited into those vacancies leaving correspondingly vacant energy levels within the valence band which becomes partly unfilled. The conduction therefore increases greatly, with positive holes as the majority carriers.

Chapter One: Introduction

In contrast, with the valence and the conduction bands overlapping, there is no forbidden state exists in a metal. An insulator is always identified as a material having a band gap $E_g > 3.0$ eV (e.g. diamond 5.4 eV). However, TiO_2 is still considered to be a semiconductor even though it has a band gap energy $E_g = 3.2$ eV. At all temperatures $T > 0$ K, there are always electrons with a kinetic energy larger than E_g , which means that some electrons are excited into the conduction band, leaving positive holes in the valence band. In the simplest case, the equilibrium concentrations of electrons and holes are equal, $n_0 = p_0$. The electrons in the conduction band and the holes in the valence band are responsible for transmission of electron current. Such an ideal semiconductor is called intrinsic. The equilibrium behaviour of electron system of a solid body is described by the electrochemical potential of electrons known as the Fermi level. In this context, the electrochemical potential represents the increase in the system's free energy when an electron is added. The thermal excitation of electrons into higher energetic level is given by the Boltzmann distribution and allows the equilibrium concentration of electrons and holes to be calculated by equation 1.3.

$$n_0 = N_c \exp\left(\frac{F - E_c}{kT}\right) \quad p_0 = N_v \exp\left(\frac{E_v - F}{kT}\right) \quad (1.3)$$

Where N_c and N_v are the effective density of states in the conduction and valence bands, which can be treated as constants; k is the Boltzmann constant (1.38×10^{-23} J K^{-1}) and T is the absolute temperature. The Fermi energy of an intrinsic semiconductor lies half way between the conduction and valence band energy at a temperature of $T = 0$ K. Similarly, at higher temperatures, excited electrons must be taken into account resulting in equation 1.4:

$$E_F = \frac{1}{2} [(E_V + E_C) - kT \ln \frac{N_C}{N_V}] \quad (1.4)$$

1.6.2 The p-n junction

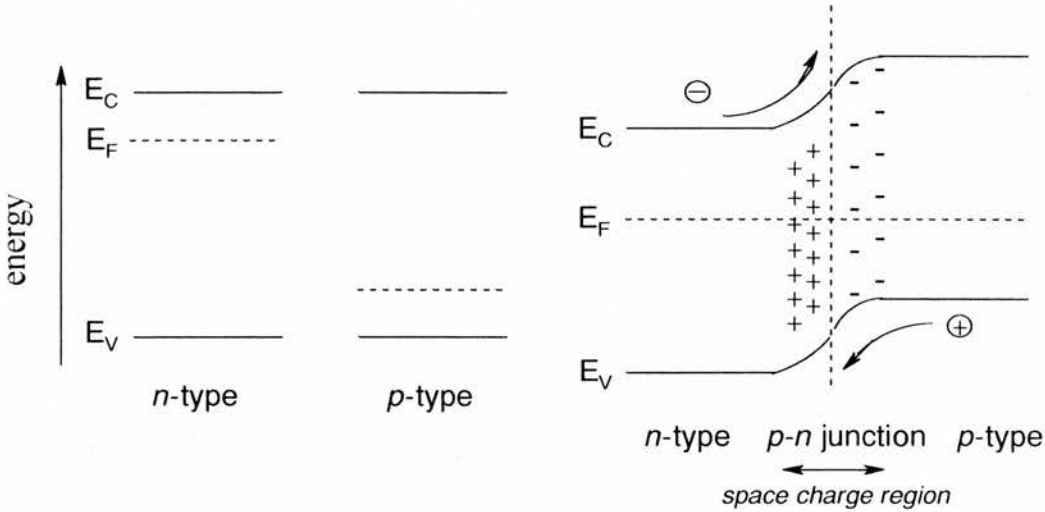


Fig. 1.6 The charge dipole and space charge region produced at p-n junction.

To carry out the conversion of the energy of sunlight into electrical energy and to deliver that electrical energy to an external load by a solar cell, a current has to flow within the semiconductor composed of the positively charged electron holes and negatively charged electrons which the light has generated. In this process, these holes and electrons will recombine unless separated by some means, for example, by an applied external electric field. However, the purpose of the cell would not be achieved since the energy delivered to the external load would come from the electricity source

Chapter One: Introduction

which is applied and thus not from the photons generated by the sunlight. Within the semiconductor, an electric field needs to be generated, which is independent of any external energy source. This electric field will separate the optically generated hole-electron pairs and then be used to transport charge.

To generate an internal electric field in a semiconductor,³¹ the most common method used in solid state solar cells is the creation of a $p-n$ junction. A $p-n$ junction might be visualised either theoretically as one piece of semiconductor with one side p -doped and the other side n -doped, or, practically, as two semiconductor samples, one p -doped and the other n -doped, metallurgically joined to one uniform sample. The $p-n$ junction is the vital component of most semiconductor devices.

As soon as n -type and p -type regions of a semiconductor are joined to form a continuous crystal, the carriers redistribute themselves in such a way as to equalize the Fermi level throughout the semiconductor (see Fig. 1.6). In the neighbourhood of this juncture, electrons from donors transfer to nearby acceptors, and a dipole layer is formed, consisting of positive empty (ionized) fixed-site donors on the n -type side and negative occupied (ionized) fixed-site acceptors on the p -type side. The dipole generates an electrical field which would drive a conduction band electron to the n -type side and valence band hole to the p -type side. The junction proper is defined by that location where the Fermi level is in the middle of the gap. The dipole layer extends on either side of junction and the total extent of this depletion layer is called the *junction thickness*. This motion of electrons and holes, leaving the unbalanced ion charges which produce the electric field, occurs instantaneously on forming the junction. Immediately, the field reaches an equilibrium value which forbids further electron or hole migration across the $p-n$ junction. This is an uphill reaction, and thus

energetically unfavourable. Driven solely by the concentration gradient, an instantaneous diffusion current will arise. The ionized acceptor and donor atoms, which are no longer electrically compensated since they cannot diffuse, remain behind as fixed space charges. Correspondingly, as occurs in a plate capacitor, an electric field is generated at the p-n junction, which is directed so that it drives the diffusion charge carriers in the opposite direction of the diffusion. Hence, diffusion of electrons and holes continue until an equilibrium is established. The resulting internal field exists, even if both sides of the semiconductor are grounded.

1.6.3 Optical processes in semiconductors³²

Electrons and holes can move to a higher energy state when the semiconductor absorbs light. At low frequencies where $h\nu$ is considerably less than the band gap energy, the principle source of absorption comes from the free carriers moving to higher energy. In pure semiconductors this interaction is weak because there are few carriers. Free carrier absorption will continue over a range of energies and, as the photon energy increases, electrons may be excited from impurity states into the conduction band, or holes into the valence band. As the photon energy approaches that of the band gap so excitons can start to be produced. The exciton is a hole-electron pair that behaves in many ways like the proton-electron pair of the hydrogen atom.

Once the photon energy exceeds the band gap energy ($h\nu \geq E_g$) then the principal source of absorption for the photons will be through excitation of hole-electron pairs in the valence and conduction bands. The rate of production of holes or

Chapter One: Introduction

electrons is closely linked to the rate at which light is absorbed by the solid. One can define a characteristic length $1/\alpha$ so that the intensity (I) decay by a fraction α per unit distance of travel of the light through the solid is:

$$\frac{d I}{d x} = - \alpha I \quad (1.5)$$

In general α is dependent on frequency and temperature and sometimes on the intensity itself. If, however, α is independent of the intensity, then $I = I_0 \exp (- \alpha x)$, where I_0 is the intensity just inside the surface of the semiconductor and x is the coordinate. This process creates non-equilibrium carrier in pairs so that $\Delta n = \Delta p$, where Δn and Δp are the excess concentration of electrons and holes, compared to the equilibrium concentrations (n_0 and p_0) and is called the intrinsic or fundamental absorption.

The charged hole-electron pairs that are generated must be separated in order to obtain electricity from a solar semiconductor device. Charge recombination, the natural force opposing any charge separation, occurs when the electron in the conduction band drops back into the valence band and recombines with an electron hole either by radiative, non-radiative or defect level (impurity) recombination. The carrier pair can be separated either by diffusion or by an electric field (migration). In a field free doped semiconductor, the recombination process is pseudo first order because there is a large excess of one type of carriers, assuming that the illumination does not change the majority carrier concentration. Thus, the recombination process can be characterized by a first order minority lifetime τ_{\min} (in the order of 10^{-5} to 10^{-7}

Chapter One: Introduction

s), which is sensitive to crystal purity and doping density. Minority carriers are also characterized by their diffusion coefficient (D), and when considering the problem of carrier collection, it is convenient to define the majority carrier diffusion length³³ as a measure of the distance that a photo-generated minority carrier travels in the field free (quasi-neutral) region before recombination. Once the minority carriers have reached the surface, a region characterized by an abrupt ending of the semiconductor crystal structure and the presence of foreign atoms on or in the surface (2 to 10 nm in thickness), they are free to participate in electron transfer reactions, either with redox species in solution or within the semiconductor lattice. Alternatively they can be collected at a metal back contact, which acts as an electron sink.

$$L_{\min} = (\pi D \tau_{\min})^{1/2} \quad (1.6)$$

1.6.4 Photovoltaic process in a solar cell³⁴

As we mentioned before, the most important application of photovoltaic effect is conversion of solar energy into electrical energy. For this application the dominant parameters are conversion efficiency and the power output. The solar spectrum dictates the range of materials that can be used for the generation of photoelectricity, the smaller the energy gap of the semiconductor, the larger the portion of the solar spectrum which is utilized, but the maximum photovoltage obtainable is corresponding smaller. On the other hand, the larger energy gap can give a higher photovoltage and a lower leakage across the junction.

Chapter One: Introduction

Illumination of a semiconductor containing a *p-n* junction (see equation 1.6) generates a hole-electron pair for an intrinsic semiconductor. However, if the hole-electron generation occurs within the carrier diffusional length of the *p-n* junction, the charge will be separated. The electron will be drawn to the *n*-side, which is the side of the junction with minimum energy for electrons, and the hole to the *p*-side of the junction, which on the other hand exhibits minimum energy for holes.

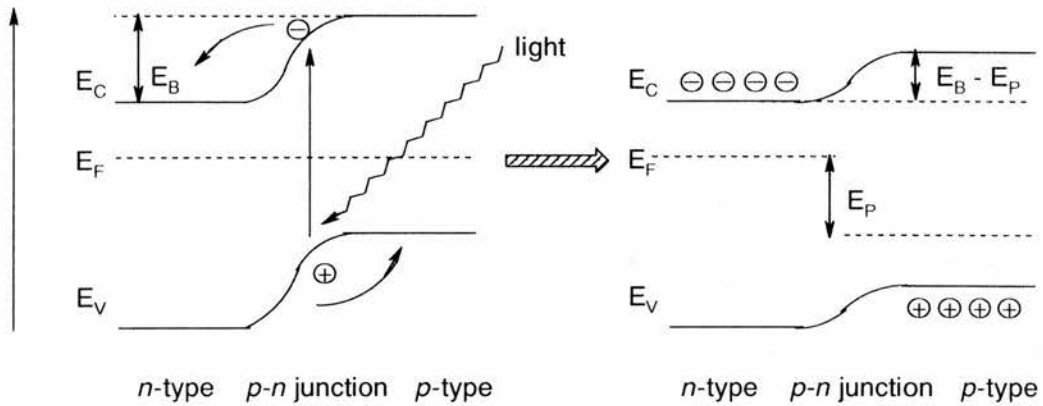


Fig. 1.7. The *p-n* junction under illumination. Left: A photon induced hole-electron pair is separated by the local field of the junction. Right: The origin of the photovoltage E_P . E_B = Energy barrier created by the *p-n* junction, E_P = Energy equivalent of the photovoltage.

As illustrated in the Fig. 1.7, continuous irradiation leads to a reduction of the energy barrier (E_B) created by the *p-n* junction that generates the desired photovoltage E_P . Eventually a steady-state condition will be reached between holes and electrons generated by the light and their recombination. The band gap energy determines the maximum photovoltage that can be generated, which is called the open circuit

Chapter One: Introduction

potential, E_{oc} or V_{oc} . The current versus voltage characteristic of an ideal $p-n$ junction is quantitatively given by Equation 1.7:

$$I = I_s [\exp(\frac{qE_p}{kT}) - 1] \quad (1.7)$$

Where q is the elemental charge, k is the Boltzmann constant, T is the absolute temperature and I_s the saturation current of the junction. The qualitative description of a $p-n$ under illumination is illustrated in Fig. 1. 8.

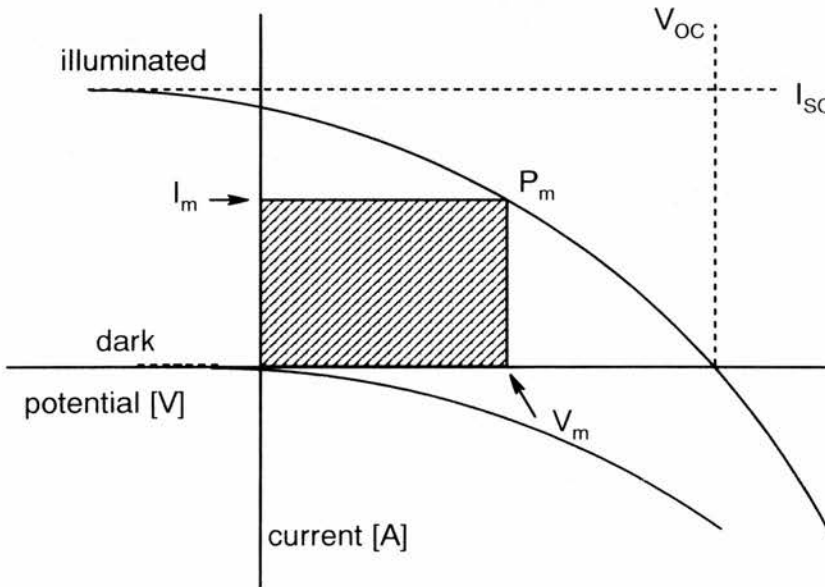


Fig. 1.8. Voltage-current characteristic of a solar cell. V_{oc} and I_{sc} are the open circuit potential and the short current, respectively. V_m and I_m are the voltage and the current at the operating point and P_m is the maximum achievable power output. Shaded area represents the maximum power output achievable.

Chapter One: Introduction

(a) Short circuit current, I_{sc}

Short circuit current is the current obtained when the solar cell is short-circuited, that is there is no potential across the cell. Furthermore, the short circuit current is equal to the absolute number of photons converted to hole-electron pairs.

(b) Open circuit potential, V_{oc}

The open-circuit potential is obtained when no current is drawn from the solar cell. High values are achieved when

- Diffusion length of charge carriers is as high as possible
- Dopant concentration as high as possible
- Crystal volume is as small as possible, *i.e.*, thin wafer

(c) Fill factor

Optimal power output requires a suitable resistor, which corresponds to the ratio V_m / I_m (Fig. 1.8). V_m and I_m are the voltage and current at the optimum operating point where $P_m = V_m I_m$ is the maximum achievable power output. The ratio of peak output $V_m I_m$ to $V_{oc} I_{sc}$ is called the fill factor (FF) of a solar cell and is an important quality criterion.³⁵

$$FF = \frac{V_m I_m}{V_{oc} I_{sc}} \quad (1.8)$$

Chapter One: Introduction

The name fill factor is derived from its graphic representation. It indicates how much area underneath the I-V characteristic curve is filled by the rectangle described by $V_m I_m$ (shaded area in Fig. 1.8) in relation to the rectangle $V_{oc} I_{sc}$. The theoretically maximum obtainable FF is a function of the open circuit potential; the higher is the V_{oc} the higher the FF. Fill factor for optimised solar cells are typically within the range of 0.6 ~ 0.75.

(d) Efficiency

The efficiency of a solar cell (η) is defined as the ratio of the photovoltaically generated electric output and the energy of the incident irradiant solar light.

$$\eta = \frac{V_m I_m}{P_{\text{light}}} = \frac{FF V_{oc} I_{sc}}{P_{\text{light}}} \quad (1.9)$$

P_{light} is the energy of the light shining in the solar cell and is obtained when the light intensities of the whole spectral range are integrated.

(e) IPCE Value (Incident Monochromatic Photon-to-Current Conversion Efficiency)

The incident monochromatic photon-to-current conversion efficiency is defined as the ratio between the number of collected electrons (current) and the number of incident light photons. As the name suggests, the value is commonly only measured for a specific light wavelength. Plots of IPCE versus wavelength illustrate the spectral operation range of a specific solar cell. For high performance solar cells,

the IPCE value can reach unity over a large spectral section. The discrepancy between a low conversion efficiency and a high IPCE value is due to energetic losses; for example, a 3 eV photon absorbed by a 1 eV bandgap semiconductor solar cell will lose 67% of its initial energy at the charge generation step. In order to quote a favourable IPCE, it is often measured close to the λ_{\max} of its absorption spectrum of the cells. The IPCE value can be calculated by the following equation:³⁶

$$\text{IPCE} = \frac{125 \times \text{photocurrent density [A/cm}^2\text{]}}{\text{wavelength [nm]} \times \text{photon flux [mW/cm}^2\text{]}} \quad (1.10)$$

1.7 DYE-SENSITIZED PHOTOELECTROCHEMICAL SOLAR CELLS

In the previous section, the fundamental theory of semiconductor based light-to-electricity conversion has been demonstrated. Two energetically distinctive electronic states (valence and conduction band) allow an electron to directly acquire the energy of an incident light photon and thereby transit into an energetically higher state. Thus charge is separated and a potential created. Therefore within the semiconductor, light absorption and charge separation are directly coupled and both occur. These two processes are separated in a dye sensitized photoelectrochemical cell. The dye, which is also called a sensitizer, absorbs the light and charge separation is achieved when the acquired light energy of the now excited dye is passed to the semiconductor in the form of an electron injected into the conduction band. The oxidized dye is then regenerated by the redox couple.

1.7.1 History

The photovoltaic effect was firstly observed in the 19th century.³⁷ In June 1887, about half a century after Becquerel's discovery of the photovoltaic effect, Dr. Moser from the physical-chemical laboratories at the Vienna University reported the first dye sensitized photoelectric effect:³⁸

Note about strengthening of photoelectric current by optical sensibilization. *I wish to report that I could significantly increase the photoelectric currents discovered by E. Becquerel, by bathing both chlorinate, iodited or bromited silver plates in a dye solution, e.g. erythrosin. For example, between two chlorinated silver plates the eletromotoric force was 0.02, between two similarity treated but bathed plates it was 0.04 Volt.....using iodited plates eltromotoric forces of up to 1/15 Volt can usually be measured. I could achieve 1/4 Volt by bathing the iodited plates in erythosin...*

The importance of these results was rapidly recognised by researchers working in the area of photography, and eventually led to the development of colour photography. However, it took almost a century after Moser's discovery before these effects were investigated in the context of solar energy conversion and photovoltaics. In the 1960's, the first experiments were carried out using single crystal semiconductor electrodes immersed into dye solution. Theoretical and practical studies showed that only molecules directly adsorbed onto the electrode surface caused photovoltaic effects and that a closed packed mono-layer surface coverage was

Chapter One: Introduction

advantageous. This is because thicker layers prevent electron transfer from the excited dye into the semiconductor and eventually block adsorption of light. Disappointingly, using the photovoltaic devices constructed in this way, less than 0.5% conversion efficiency and poor long-term stability is observed, partly caused by the low absorbance that a single mono-layer of dye on a plane surface can exhibit. Actually monolayered dyes in photovoltaic devices were constructed for the application in the water splitting reaction rather than being used for the direct conversion of the solar energy into electricity. A very valuable discussion on this topic is available in the conference proceedings of the Third International conference on Photochemical Conversion of and Storage of Solar Energy (1980) during when the use of $[\text{Ru}(\text{bpy})_2]^{2+}$ and some other potential dye-sensitizers like porphyrins has been discussed.¹⁴ Further discussion of the energy conversion by employing different systems such as solid state solar cell and wet liquid solar cell has been held recently at the First International Semiconductor Photoelectrochemical conference (SP-1) in Glasgow (2001). The use of TiO_2 as the nanocrystalline semiconductor material and the future development of the photoelectrochemical cells have been discussed.

In 1976, a breakthrough in conversion efficiency was reported by Tsubomura and co-workers when powdered high porosity multi-crystalline ZnO was introduced instead of a single crystal semiconductor, thereby significantly increasing the surface area of the electrode.³⁹ Although the dye, rose bengal, was still adsorbed in mono-layer coverage, light absorbance was significantly increased due to the large surface area. The cell had an energy conversion efficiency of 1.5%, which was about one order of magnitude higher than previous achievement. And it is noteworthy that Tsubomura and co-workers have already pointed out that the iodide/triiodide redox

shuttle system was better performing than other systems and was beneficial for obtaining high conversion efficiency. However, systematic mechanistic studies started only in the late 1960s with work on dye-sensitization of ZnO and SnO₂ electrodes carried out by Gerischer,⁴⁰ Terenin,⁴¹ Memming⁴² and Hauffe⁴³ and their co-workers. Only then did the basic framework for quantitative analysis of electron-transfer process involving semiconductors emerge. In 1972, Fujishima and Honda⁴⁴ demonstrated that the excitation of *n*-type TiO₂ above its band gap (3 eV) led to photo-assisted O₂ generation, the counter electrode producing H₂. However, the above-mentioned dyes used for dye-sensitization on semiconductor electrodes were deposited simply by immersing the electrode in the dye solution for a short period and subsequently drying in air. As a result, only low dye coverages and therefore only a small fraction of the light incident on the electrode can be absorbed by photosensitizer molecules that are close enough to transfer electrons.

Much of the work on photochemical systems for solar energy conversion has been focused on the complex [Ru(bpy)₃]²⁺ (where bpy represents 2,2'-bipyridyl). It is thermally and photolytically stable in aqueous solutions and has advantageous spectral properties.⁴⁵⁻⁵⁰ Excitation in its intense visible ($\lambda_{\text{max}} \approx 455$ nm) absorption band produces a relatively long-lived (~ 0.5 μs) triplet charge transfer (MLCT) excited state with high quantum yield (> 0.9), thanks to efficient intersystem crossing induced by the heavy Ru atom. This readily donates or accepts an electron, producing a powerful oxidant [Ru(bpy)₃]³⁺ or reductant [Ru(bpy)₃]⁺. The energy is adequate for the simultaneous oxidation and reduction of H₂O to give O₂ and H₂, if kinetic barriers can be overcome. Spritschink reported⁵¹ that the strong luminescence of surfactant ruthenium bipyridyl complexes could be quenched by immersion of assemblies

containing the complex into water, thus concomitantly, leading to the light-induced cleavage of water to yield oxygen and hydrogen. This recognition has spawned wide variety of innovative studies based upon photo-induced electron transfer reactions to accomplish this end.⁵²

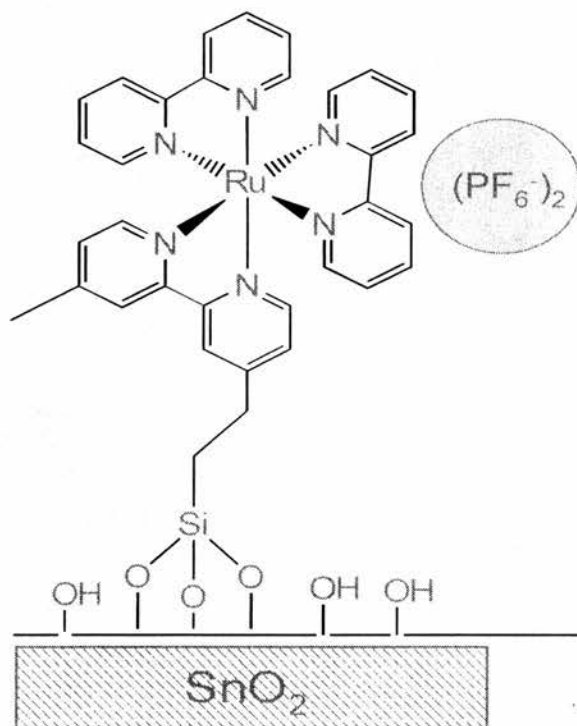


Fig. 1.10. Binding mode of the dye used by Ghösh⁵³

The limitation of the above-mentioned early work was alleviated by increasing the surface concentration of photosensitizer molecules by attaching them to the electrode. Ghösh was the first to use *n*-type SnO₂ as an electrode surface for the attachment of [Ru(bpy)₃]²⁺ derivatives (see Fig. 1.10).⁵³ Since then, different anchoring groups like carboxylate, phosphate and sulphuric functional groups have been employed to ensure uniform (monomolecular) distribution of dyes on the oxide

surface and to promote electronic coupling of donor levels of the dye with the acceptor levels of the semiconductor.

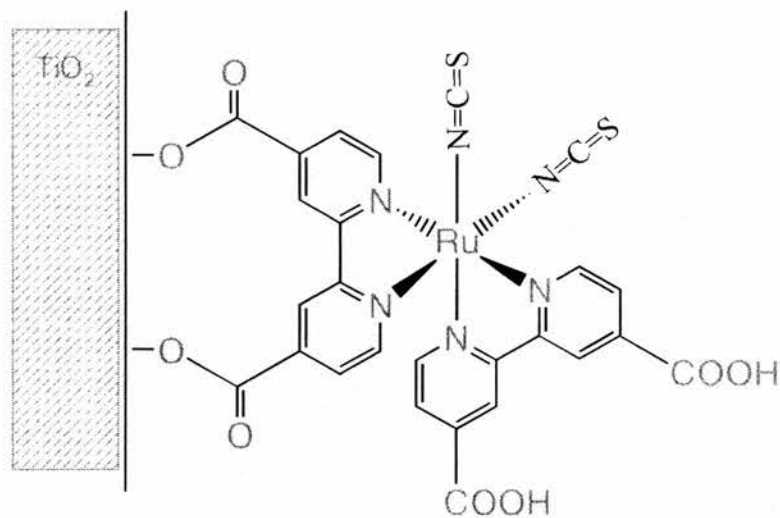


Fig. 1.11. A scheme of the attachment of $Ru(dcpv)_2(SCN)_2$ to the TiO_2 nanocrystalline surface of the Gratzel cell.

Although attempts to use dye-sensitized photoelectrochemical cells in energy conversion have long been made, the efficiency of such devices has been extremely low and practical applications have seemed remote. One problem is that of poor light harvesting. On a smooth surface, a monomolecular layer of sensitizer absorbs less than 1% of incident monochromatic light. Attempts to harvest more light by using multi-layers of dye molecules have in general been unsuccessful. About 10 years ago, a breakthrough in research on solar energy conversion efficiency at dye sensitized photoelectrochemical cells has been accomplished.⁵⁴ The device realised by the Grätzel research group is based on a 10 μm thick, optically transparent film of titanium dioxide particles a few nanometres in size, coated with a mono-layer of charge-transfer dye to sensitize the film for light harvesting (see Fig. 1.11).

Chapter One: Introduction

Because of the high surface area of the semiconductor film and the ideal spectral characteristics of the dye, the device harvests a high proportion of the incident solar energy (46%) and shows exceptionally high efficiencies for the conversion of incident photons to electrical current (more than 80%). The overall light-to-electric energy conversion yield was reported to be 7.1-7.9% in simulated solar light and 12% in diffuse day light. The large current densities, exceptional stability and low cost of the Grätzel cell make practical application feasible.

1.7.2 Semiconductor-solution Interface

In this section, we will discuss the basic theory of understanding the functioning of dye-sensitized solar cells.^{55, 56} Not like the solid state solar cells, the semiconductor employed in dye sensitized cells is in contact with a solution containing an electrolyte and a redox couple, which results in the need of using a different theory⁵⁷ to the previously discussed theory which is valid for the solid-solid interfaces (*p-n* junctions).

The Fermi level in the solution phase can be identified by the chemical potential and is calculated in terms of reversible potential or E^0 . While for most electrochemical purpose it is convenient to refer E^0 to a reference electrode, for semiconductors it is more intuitive to reference them with respect to the vacuum level. When the semiconductor and the solution are brought into contact, the Fermi level of both system must become equal (see the following Fig. 1.12) and this can occur by charge transfer between both phases. In the case illustrated in Fig. 1.12, where the Fermi level of the semiconductor E_F lies above that in solution ($E^0_{Ox/Red}$), electrons

Chapter One: Introduction

will flow from the semiconductor (which becomes reducing, $C_{red} > C_{ox}$) to the solution phase (which becomes negatively charged). However, such reversible behaviour of a semiconductor electrode is rarely found. This lack of equilibration can be ascribed to corrosion of the semiconductor surface (e.g. oxide formation) or an inherently slow electron transfer process across the interface.

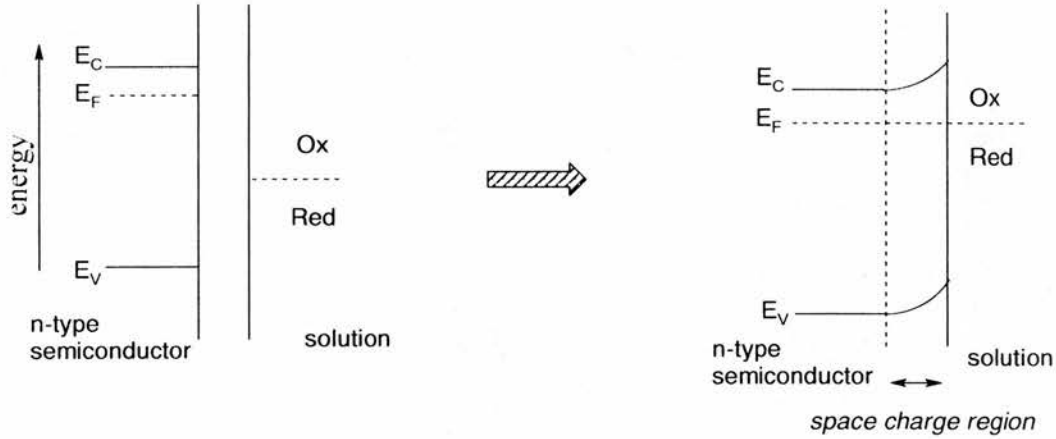


Fig. 1. 12 Schematic representation of energy levels of formation of a junction between an n-type semiconductor and a solution containing a redox couple (Ox / Red). Left: Before contact; Right: After contact and equilibration.

The excess charge is distributed over a layer near the surface, the *space charge region* of thickness:

$$L_D = \sqrt{\frac{\epsilon_0 \epsilon_{sc} kT}{q^2 (n_0 + p_0)}} \quad (1. 11)$$

Chapter One: Introduction

Here ϵ_0 and ϵ_{sc} are the electrical permittivities of the vacuum and the semiconductor, respectively, and q is the charge of the free electron. L_D is called the Debye screening length. The charge distribution is analogous to that found in the diffuse double layer that forms in solution. The resulting electric field that forms in the space charge region is represented by a bending of the bands (Fig. 1.12) right hand side). The space charge region usually has a length of 5 to 1000 nm, depending on the level of doping and applied potential. The bands are bent upward with respect to the level in the bulk semiconductor, when the semiconductor charge is positive with respect to the solution. A created hole-electron pair within the space charge region would then be separated in a similar way to the separation that occurs within the space charge region of a $p-n$ junction. In the case of the illustrated example in Fig. 1.12, an excess hole would move towards to the semiconductor surface and would be available for charge transfer reaction.

When the concentration of majority carriers in the space charge region near the surface is less than in the bulk of semiconductor, the bands bend upward in the case of an n -type semiconductor (Fig. 1. 12). This region is called the *depletion layer*. If, for example, a potential would be applied across this interface so that the space charge region is composed of majority carriers at concentrations higher than in the bulk semiconductor, the bands would bend the other way to the previous case. This is called the *accumulation layer*. A third case exists, when in the region near the surface the concentration of majority carriers exceeds the concentration of majority carriers in the bulk material. This is known as an *inversion layer* and is an extreme case of the *depletion* regime and leads to very strong band bending.

The potential at which no excess charge exists in the semiconductor ($E_F = E^0_{Ox/Red}$) is the potential of zero charge. Under these conditions no electric field is applied and hence no space charge region exists and the bands are flat (no bend). This electrode potential is called *the flat band potential*, E_{fb} . Various methods are available to determine this important characteristic value of a semiconductor. The flat band potential is commonly obtained from measurements of the differential capacity, which is then plotted in a Mott-Schottky plot (capacitance⁻² versus potential). Extrapolation of the linear relationship to zero capacitance⁻² allows the extraction of the E_{fb} values.

1.7.3 The dye-sensitized semiconductor interface

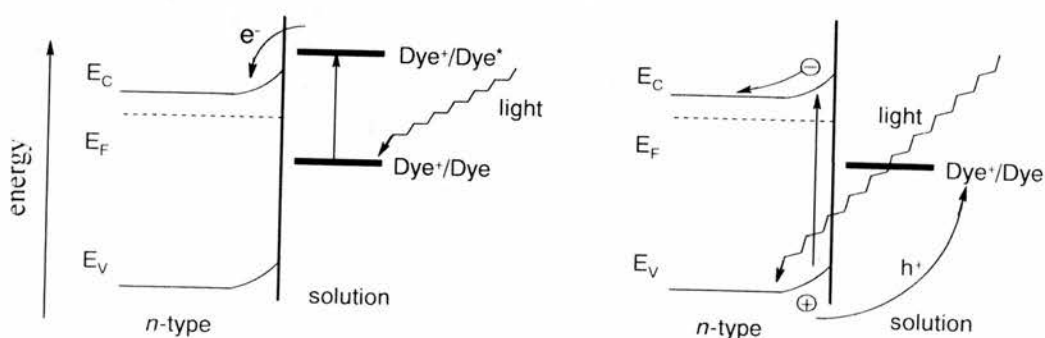


Fig. 1. 13. Electron transition at a dye sensitised semiconductor surface. Left: Light absorption by the dye, followed by an electron injection into the conduction band of the semiconductor (charge separation). Right: Light absorption by the semiconductor results in an undesirable reduction of the dye (hole injection into the dye)

The previous sections have discussed light induced carrier generation by creation of a hole-electron pair within the semiconductor via light absorption by the semiconductor. These two steps (adsorption and charge separation) can be separated

Chapter One: Introduction

by employing a sensitizer adsorbed onto the semiconductor surface (see Fig. 1.13) with the following advantages. Since both processes are now spatially separated, adverse charge recombination will be minimized. As illustrated in Fig. 1.13, the semiconductors with a very large band gap can be employed, the only requirement being that the excited state of the sensitizer ($\text{Dye}^+ / \text{Dye}^*$) is energetically higher than the conduction band level of the semiconductor. The spectral response of the dye-free device is normally very limited since $h\nu \geq E_g$ is required. In contrast, the number of dyes (dyes intrinsically absorb light in the visible spectrum) available is substantial and by appropriate synthetic strategies these can be tuned to produce the desired properties.

The schematics of the dye-semiconductor interface are shown above in Fig. 1.13. The dye absorbs a light photon and is promoted into an excited state. In the case of commonly employed transition metal complexes, this originates from a *metal-to-ligand charge transfer* (MLCT). From this excited state, the dye is now able to inject an electron into the conduction band, thereby becoming oxidized (Dye^+). The injected electron is drawn into the semiconductor by the electric field of the space charge region. In the absence of a suitable redox mediator in solution (not shown in Fig. 1.13), this photo-process would cease when all of the dye (Dye) is consumed. Once more, a hole-electron pair has been created, the electron being in the bulk semiconductor and the hole being the oxidized dye (Dye^+) isolated on the semiconductor surface. In Fig. 1.13 the right hand side shows the case when highly energetic light passes through the absorbed layer of dye and directly excites the semiconductor. The semiconductor now acts like a *p-n* junction, a hole-electron pair is generated within the semiconductor, the electron moves into the bulk whereas the

hole moves toward the electrode surface where it can oxidize the dye. This normally is an unwanted reaction, since it can result in decomposition of the dye. Thus the key additional component required is a redox couple in solution which can equilibrate electrons between a counter electrode and the oxidized dye.

1.7.4 Dye-sensitized photoelectrochemical solar cells

(a) Operating principle⁵⁸

A dye sensitized solar cell can be considered as a hybrid version of photogalvanic cells and solar cells based on semiconductor electrodes. The cell consists of a dye-coated semiconductor electrode and a counter electrode arranged in a sandwich configuration and the inter-electrode space is filled with an electrolyte containing a redox mediator (A/A^{\cdot}). The key reactions taking place in a dye sensitized photoelectrochemical solar cell are shown schematically in Fig. 1.14. Optical excitation of the dye with visible light leads to excitation of the dye to an electronically excited state that undergoes electron transfer quenching, injecting electrons into the conduction band of the semiconductor ($S^* \rightarrow S^+ + e_{cb}^-$). The oxidized dye is subsequently reduced back to the ground state by the electron donor present in the electrolyte filling the pores ($S^+ + A^{\cdot} \rightarrow S + A$). The electrons in the conduction band collect at the back collector electrode and subsequently pass through the external circuit to arrive at the counter electrode where they effect the reverse reaction of the redox mediator ($A + e \rightarrow A^{\cdot}$). The net effect of the visible light irradiation is regeneration of the dye, the redox mediator and the driving of electron through the external circuit. The process thus leads to direct conversion of sunlight to

electricity. If the above cited reactions alone take place, the solar cell will be stable, delivering photocurrent indefinitely. The maximum photovoltage obtainable will be the difference between the Fermi level (conduction band) of the semiconductor under illumination and the redox potential of the mediating redox couple. The photocurrent obtainable is a complex entity depending on the spectral, redox properties of the dye, efficiency charge injection and the structural properties of the semiconductor electrode to collect and channel the electrons through the external circuit.

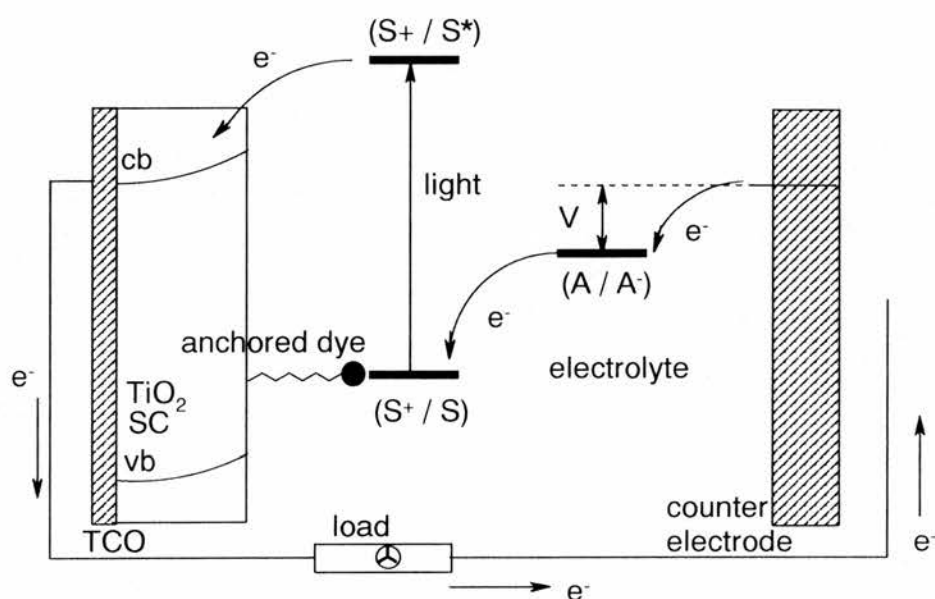


Fig. 1.14. A schematic presentation of key reaction taking place in dye sensitised solar cell

(b) Dye sensitization of semiconductor electrode

Dye sensitization of wide-bandgap semiconductors dates back to the early days of photography, almost a century old now.³⁸ In 1949, Putzeiko and Terenin⁵⁹

Chapter One: Introduction

reported the sensitization of pressed ZnO disk by absorbed rhodamine B, eosin, erythrosine and cyanine dyes. As stated above (*see page 32*), most of these early studies were fundamental in nature, aimed at an understanding of electron-transfer processes involving the valence and conduction bands of a semiconductor immersed in a redox electrolyte. However, the validity of the underlying principles of dye-sensitized solar cells (whether single crystal, sintered disks or high-surface-area porous films was used) illustrated in Fig. 1.14 indeed was built up from the early pioneering studies. Several key observations from these early work should be pointed out:^{38-43, 59}

- The similarity between the photocurrent action spectrum and the absorption spectrum indicates the direct involvement of the dye excited state in the observed photocurrent.
- The dye after excited state electron transfer remains in the oxidized state in the absence of the electron donor and the photocurrent steadily decreases with time.
- Cations of organic dye, particularly of the xanthene family and some metalloporphyrins, are very reactive and undergo structural re-organization, resulting in rapid loss of chemical integrity.
- For sustained observation of the photocurrent, electron donors need to be added to the electrolyte solution. Hydroquinones and iodides were employed as electron donors and the process was labeled as *super-* or *hyper-*sensitization.

It was very quickly realized that, as in the photogalvanic cells, only those dye molecules that are in the immediate vicinity of the electrode contributed to the

Chapter One: Introduction

photocurrent. Reasonably high IPCE values were obtained only in cases where there is a mono- or submono-layer of the dye present on the semiconductor surface. Also most often, the photocurrent saturates at relatively low dye concentration. Several reasons have been identified as the sources for the low efficiency. With the type of organic dyes employed in the majority of the previous work, dye-aggregation occurs even at relatively low concentration of the solution ($\leq 10^{-5}$ M).⁶⁰ The reasons for the low quantum efficiency are not fully understood but several explanations were proposed:

1. Concentration quenching of the excited state via fast energy transfer amongst the dyes or pre-formed dimers (static quenching)
2. Insulating nature of thick dye layers
3. Fast electron trapping and back reaction occurring between excited dye molecules and surface traps not subject to the electric field of the semiconductor space charge region.

(c) Porphyrins complexes as sensitizers

By examining chlorophylls on ZnO electrodes, one of the very early investigations exploring the photosensitization capacity of porphyrins is the work of Tributsch and Calvin⁶¹. Even though the quantum efficiencies up to 0.125 were observed in the presence of phenylhydrazine as the sacrificial electron donor, the measured photocurrent, however, was extremely small (ca. $5\mu\text{A cm}^{-2}$ for monochromatic excitation) due to the very small light harvesting efficiency of a monolayer of the dye on semiconductor single crystal. Quantum efficiencies of the

Chapter One: Introduction

order of 0.3 were obtained by Honda and Miyasaka⁶² who examined the effect of various metal ions in mono-layers of chlorophyll derivatives on SnO₂ electrode deposited using a Langmuir-Blodgett procedure.

Comparing with porphyrins, phthalocyanines show further red-shifted absorption, with the lowest energy band occurring in near IR-region, due to a more extended π -system. Hence they are ideally suited for red-light harvesting for in solar cells. The major problems arising with metallophthalocyanines are their extremely low solubility in solvents of choice for the electrochemical studies and their tendency to aggregate even at concentrations $\leq 1 \mu\text{M}$. Fujishima et al.⁶³ recently studied the dye-sensitizing effect of TiO₂-Pc thin film on the surface of TiO₂ single crystals and he pointed out that the low quantum efficiency of the dye-sensitized photo-oxidation currents is possibly due to the limited diffusion length of excitons and low charge transport.

(d) Polypyridine complexes as sensitizers

As we pointed out above, ruthenium polypyridyl complexes have been of great interest for the sensitization of wide-bandgap semiconductors. Memming and coworkers were the first to explore polypyridyl complexes on SnO₂ electrodes,⁴² followed by similar experiments on [Ru(bpy)₃]²⁺ and related complexes on TiO₂, SrTiO₃ and ZnO electrodes.⁶⁴⁻⁶⁷ Anodic photocurrents corresponding to charge injection from the excited Ru complex to the conduction band of the semiconductor were observed for excitation with photons of energy less than that of the bandgap. Later on, possible catalytic water oxidation to molecular oxygen [Ru(bpy)₃]³⁺ by has

been reported. In aqueous media, the lifetime of the dye cation formed following excited state charge injection, $[\text{Ru}(\text{bpy})_3]^{3+}$ decreases rapidly with increasing pH values.

1.7.5 Comparison to solid state cells

As is the case of solid state solar cells, a semiconductor is used for charge separation in dye sensitized solar cells. In solid state solar cells, an electric field is necessary for efficient charge separation, which is created by a *p-n* junction, whereas in dye sensitized solar cells the charge is spatially separated by utilizing a sensitizer compound. In solid state cells the charges (holes and electrons) need to diffuse in the semiconductor to the back contact, whilst in wet cells only the majority carriers diffuse in the TiO_2 semiconductor and the holes (oxidized dye) remain as fixed charges on the surface. However, the solution diffusion of the charge mediator needs to be taken into account. The most important advantages of wet solar cells are:

- Low cost material: TiO_2 is very cheap and abundant. Solid state solar cells, especially high performance solar cells require high purity semiconductor material which is inherently expensive. The amount of sensitizer needed is low. In the case of polypyridyl ruthenium complexes less than 10mg ruthenium/ m^2 is needed.
- Diffuse light performance: Solid state cells have one significant drawback, they only operate well under direct (perpendicular) irradiation, unless significant effort is made to alter the surface structure. This is partly due to the perfect materials needed, resulting in total reflection phenomena. In the case

of the rough TiO₂ surfaces used in wet solar cells, reflection is minimized and, as a matter of fact, these cells operate best under diffuse lighting conditions.

1.8 AIM OF WORK

The sensitizer compound forms an essential part of a dye sensitized solar cell. It determines its absorption characteristics and spectral response. As illustrated in Figure 1.13, the value for the formal potential of the dye/dye⁺ process is an essential thermodynamic value for describing and understanding the properties of the cell. Photophysical studies⁶⁸⁻⁷² on these kinds of sensitizers have been extensive. However, general electrochemical studies for screening and characterizing the nature of the oxidized states of alternative complexes have not been fully developed. In addition, the polypyridyl complexes have been focused on bipyridyl, terpyridyl and 1,10-phenanthroline ligands, rather than alternative heterocyclic ligands.

For the consideration of the above limitations, we are aiming to develop some new polypyridyl ligands for the solar cells and the electrochemical characterization of these ruthenium complexes based on the new ligands.. The following is a brief research outline of the content of the thesis.

- To study the electrochemical properties of the dye sensitizer of the solar cells for a better understanding of the nature of the oxidized dye.

- To study the electron injection from the dye to the semiconductor by study a dye complex with a variable-length spacer adjusting the distance of the dye to the semiconductor.
- To develop new polypyridyl dyes for solar cells. *Cis*-[Ru(dcpy)₂(SCN)₂] (dcpy = 4,4'-dicarboxylic-2,2'-bipyridyl) is one of the most efficient sensitizer reported up to date.⁷³ An important step for the next generation of solar cells is to prepare sensitizers that have an intense response in the solar spectrum. Based on the ligand modifying theory^{60, 74} that we are going to talk about in chapter 2, we have designed some ligands that meet some of the standards. They are derivatives of 2-(2-pyridyl)benzimidazole (chapter 3) and tris[(2-pyridyl)methyl]amine (chapter 4), as shown in Fig. 1.15.

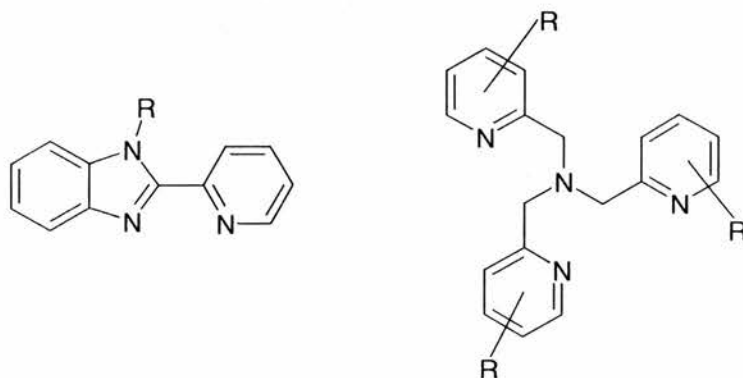


Fig. 1. 15. Derivatives of 2-(2-pyridyl)benzimidazole and tris[(2-pyridyl)methyl]amine.

1.9 REFERENCES

1. <http://www.bp.com/downloads/702/BPwebglobal/BPwebglobal.pdf>, *Statistical Review of World Energy 2001*, p41, J. Browne, March, 2002.
2. C. W. Hamilton, *Americans and Oil in the Middle East*, Huston: Texas, Gulf publishing, 1962.
3. C. Flavin, and O. Tunali, *Climate of Hope : New Strategies for Stabilizing the World's Atmosphere*, Washington, DC : Worldwatch Institute, 1996.
4. J. E. Harries, H. E. Brindley, P. J. Sagoo, R. J. Bantges, *Nature*, 2001, **410**, 6826.
5. R. G. Prinn, J. Huang, R. F. Weiss, D. M. Cunnold, P. M. Fraser, P. G. Simmonds, A. McCulloch, C. Harth, P. Salameh, S. O'Doherty, R. H. J. Wang, L. Porter, B. R. Miller, *Science*, 2001, **292**, 5523.
6. <http://www.epa.gov/globalwarming/climate/index.html>, March, 2002.
7. K. L. Kozloff, and R. C. Dower, *A new powder base: Renewable Energy Policies for the Nineties and Beyond*, World resource institute, 1993.
8. http://www.bp.com/downloads/837/global_oil/global_oil_section.pdf, BP *Statistical Review of World Energy-Oil*, http://www.bp.com/downloads/838/global_ngas/global_ngas_section.pdf, BP *Statistical Review of World Energy-Gas*, March, 2002.
9. B. Sørensen, *Renewable Energy*, 1st ed., Academic Press. London, 1979.
10. K. Lovegrove and K. Weber, *Solar Energy: Power for the New Millennium*, Australian national university, centre for suitable energy systems, 1999.
11. J. Parikh, K. Balakrishnan, V. Laxmi, H. Biswas, *Energy*, 2001, **26**, 949.

12. C. J. Winter, R. L. Sizmann and L. L. Vant-Hall, Springer, Verlag, *Solar Power Plants*, Berlin, Heidelberg, 1991.
13. D. Oliver, H. Miall, F. Nectoux and M. Opperman, *Energy-efficient Futures: Opening the Solar Option*, Earth resources research Ltd., Black rose Press, London, 1983.
14. J. S. Connolly, *Photochemical Conversion and Storage of Solar Energy: Third International Conference on Photochemical Conversion and Storage of Solar Energy*, Academic Press, 1981.
15. T. Ohta and N. Kamiya, *Photochemical Hydrogen Production: Solar-hydrogen Energy System*, Pergamon Press Ltd., Oxford, 1979.
16. R. R Hautala, J. Little and E. Sweet, *Solar Energy*, 1977, **19**, 503.
17. R. G. Salomon, M. F. Salomon and J. L. C. Kachinski, *J. Am. Soc. Chem.*, 1977, **99**, 1043.
18. Farrington Daniels, *Direct Use of the Sun's Energy*, New Haven London: Yale University Press, 1964.
19. S. R. Wenham, M. A. Green and M. E. Watt, *Applied Photovoltaics*, Bridge Printery, Sydney, 1994.
20. M. D. Archer and J. R. Bolton, *J. Phys.Chem.*, 1990, **94**, 8028.
21. M. Gratzel, *Cattech*, 1999, **3**, 5.
22. C. G. Garcia, J. F. de Lima, N. Y. M. Iha, *Coor. Chem. Rev.* 2000, **196**, 219.
23. A. Fujishima, T. N. Rao, *Pure Appl. Chem.*, 1998, **70**, 2177.
24. C. Nasr, S. Hotchandani, W. Y. Kim, R. H. Schemhl and P. V. Kamat, *J. Phys. Chem.*, 1997, **101**, 7480.
25. F. LU, D. W. Gong, J. B. Wang, H. H. Sun and X. Wang, *Phys. Rev., B*, 1996, **53**, 4623.

Chapter One: Introduction

26. E. Becquere, *C. R. Acad. Sci. Paris*, 1839, **9**, 561.
27. D. M. Chapin, C. S. Fuller and G. L. Pearson, *J. Appl. Phys.*, 1954, **25**, 676.
28. J. L. Stone, *Phys. Today*, 1993, **9**, 22.
29. K. J. Close and J. Yarwood, *An Introduction to Semiconductors*, The Pitman Press, Bath, 1971.
30. J. E. Carroll, *Physical Models for Semiconductor Devices*, Edward Arnold Ltd., London, 1974.
31. R. C. Neville, *Solar Energy Conversion, The Solar Cell*, 2nd ed., Elsevier Science B. V., Amsterdam, 1995.
32. J. I. Pankove, *Optical processes in semiconductors*, New York : Dover, 1975
33. L. M. Peter, *Chem. Rev.*, 1990, **90**, 753.
34. A. Hagfeldt and M. Grätzel, *Chem. Rev.*, 1995, **95**, 49.
35. S. Ferrere and B. A. Gregg, *J. Phys. Chem., B*, 2001, **105**, 7602.
36. S. Ruile, O. Kohle, H. Pettersson and M. Grätzel, *New. J. Chem.*, 1998, **25**.
37. A. J. Mcevoy and M. Grätzel, *Sol. Energy Mater. Sol. Cells*, 1994, **32**, 221.
38. J. Moser, *Monatshfte Fur Chemie*, 1887, **8**, 373.
39. H. Tsubomura, M. Matsumura, Y. Nomura and T. Amamiya, *Nature (London)*, 1976, **261**, 402.
40. H. Gerischer, H. Tributsch and Ber. Bunsenges, *Phys. Chem.*, 1968, **72**, 437.
41. A. Terenin and I. A. Akimov, *J. Phys. Chem.*, 1965, **69**, 730.
42. R. Memming and H. Tributsch, *J. Phys. Chem.*, 1971, **75**, 562.
43. K. Hauffe, H. J. Danzmann, H. Pusch, J. Range and H. Volz, *J. Electrochem. Soc.*, 1970, **117**, 995.
44. A. Fujishima and K. Honda, *Nature (London)*, 1972, **238**, 37.
45. F. E. Lytle and D. M. Hercules, *J. Am. Chem. Soc.*, 1969, **91**, 72.

Chapter One: Introduction

46. J. N. Demas and A. W. Adamson, *J. Am. Chem. Soc.*, 1973, **95**, 5159.
47. C. R. Bock, T. J. Meyer and D. G. Whitten, *J. Am. Chem. Soc.*, 1974, **96**, 4710.
48. R. C. Young, F. R. Keene and T. J. Meyer, *J. Am. Chem. Soc.*, 1977, **99**, 2468.
49. G. D. Hager and G. A. Crosby, *J. Am. Chem. Soc.*, 1975, **97**, 7031.
50. G. S. Laurence and V. Balzani, *Inorg. Chem.*, 1974, **13**, 3663.
51. G. Sprintschnik, H. W. Sprintschnik, P. P. Kirsch and D. G. Whitten, *J. Am. Chem. Soc.*, 1976, **98**, 2337.
52. K. Kalyanasundaram, *Coord. Chem. Rev.*, 1982, **46**, 159.
53. P. K. Ghosh and T. G. Spiro, *J. Am. Chem. Soc.*, 1980, **102**, 5543.
54. B. O'Regan and M. Gratzel, *Nature*, 1991, **353**, 737.
55. Y. V. Pleskov, Springer Verlag, *Solar Energy Conversion: A Photoelectrochemical Approach*, Berlin Heidelberg, 1990.
56. S. G. Yan, J. S. Prieskorn, Y. J. Kim, and J. T. Hupp, *J. Phys. Chem., B*, 2000, **104**, 10871.
57. A. J. Bard and L. R. Faulkner, *Photoelectrochemical at Semiconductors*, Chapter 14.5., 629, John Wiley & Sons, Inc., 1980.
58. G. J. Meyer, *J. Chem. Edu*, 1997, **74**, 652.
59. E. K. Putziko, A. Terenin, *Zhur. Fiz. Khim.*, 1949, **23**, 676.
60. K. Kalyanasundaram and M. Gratzel *Coord. Chem. Rev.*, 1998, **177**, 347.
61. H. Tributsch and M. Calvin, *photochem. photobiol.*, 1971, **14**, 95.
62. T. Miyasaka and K. Honda, *Surf. Sci.*, 1980, **101**, 541.
63. H. Yanagi, S. Y. Chan, P. A. Lee. K. W. Nebesny, N. R. Armstrong and A. Fujishima, *J. Phys. Chem.*, 1996, **100**, 5447.

Chapter One: Introduction

64. R. Memming, F. Schröppel and U. Bringmann, *J. Electroanal. Chem.*, 1979, **100**, 307.
65. A. Hamnett, M. P. Dare-Edwards, R. D. Wright, K. R. Seddon and J. B. Goodenough, *J. Phys. Chem.*, 1979, **83**, 3280.
66. W. K. D. Clark and N. Sutin, *J. Am. Chem. Soc.*, 1977, **99**, 4676.
67. A. B. Ellis, S. W. Kaiser and M. S. Wrighton, *J. Phys. Chem.*, **1976**, 80, 1325.
68. K.S. Finnie, J.R. Bartlett and J.L. Woolfrey, *Langmuir*, 1998, **14**, 2744.
69. R. Argazzi, C.A. Bigozzi, G.M. Hasselmann and G. J. Meyer, *Inorg. Chem.*, 1998, **37**, 4533.
70. Y. Tachibana, J.E. Moser, M. Grätzel, D.R. Klug and J. R. Durrant, *J. Phys. Chem.*, 1996, **100**, 20056.
71. T. Hannappel, B. Burfeindt, W. Storck and F. Willig, *J. Phys. Chem. B*, 1997, **101**, 6799.
72. H. Rensmo, S. Sodergren, L. Patthey, K. Westermark, L. Vayssieres, O. Kohle, P.A. Bruhwiler, A. Hagfeldt and H. Siegbahn, *Chem. Phys. Lett.*, 1997, **274**, 51.
73. Md. K. Nazeeruddin, P. Péchy and M. Grätzel, *Chem. Commun.*, 1997, 1705.
74. Md. K. Nazeeruddin, E. Müller, R. Humphry-Baker, N. Vlachopoulos and M. Grätzel, *J. Chem. Soc., Dalton Trans.*, 1997, 4571

CHAPTER TWO

Dye-sensitized Nanocrystalline TiO₂ Solar Cells

2.1 INTRODUCTION

The search for efficient solar energy conversion devices has long been an important area for research.¹⁻⁷ Recently, an order of magnitude increase in solar energy conversion efficiencies at dye-sensitized photo-electrochemical cells has been realized.⁸ This breakthrough was accomplished by attaching ruthenium polypyridyl complexes to high surface area titanium dioxide, TiO₂, electrodes. When operating as photoanodes in a photo-electrochemical cell, these materials efficiently convert visible light to electricity. Research on artificial photosynthetic devices based on this technology provides an opportunity to directly convert light energy into electricity on a molecular level.

Recent studies of dye-sensitized solar cells use invariably mesoporous nanocrystalline films of the semiconductor due to its large surface area for dye absorption. Advances in the photophysics and photoredox chemistry of transition metal complexes have led to identification of numerous examples of coordination complexes as efficient photosensitizers. The early reports of high efficiencies obtained by Grätzel et al⁹⁻¹² using tris- and mixed ligands, such as bipyridine complexes attached to these porous electrodes have been confirmed and extended to a number of ruthenium complexes.^{8, 13-22} While major emphasis is still on optimizing the performance of solar cells based on TiO₂

films (white light conversion efficiency, stability, etc), there have also been exploratory studies on nanoporous films of other semiconducting oxides, particularly on ZnO^{23, 24} and SnO₂.²⁵⁻²⁷

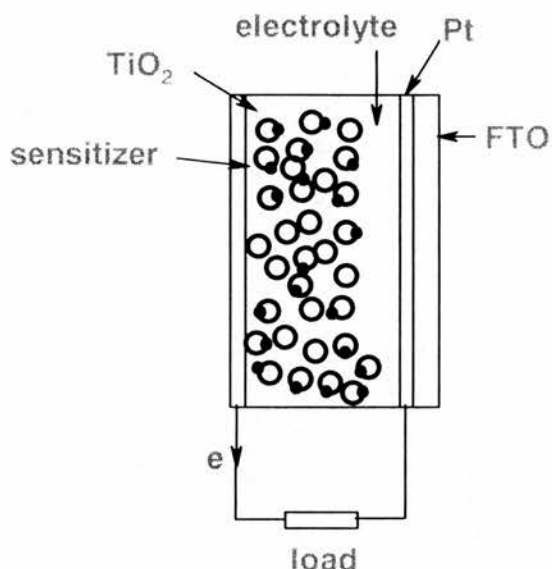


Fig. 2.1 A schematic show of the present generation of dye-sensitized solar cells, FTO is F-doped SnO₂ conducting glass

The solar cell consists of two conducting glass electrodes in a sandwich configuration, with a redox electrolyte separating the two. On one of these electrodes, a layer of TiO₂ (a few micron-thick), is deposited from a colloidal preparation of monodispersed particles of TiO₂. The compact layer is porous with a high surface area, allowing monomolecular distribution of dye molecules. After appropriate heat treatment to reduce the resistivity of the film, the electrode with the oxide layer immersed in the dye solution of interest (typically 2×10^{-4} M in alcohol) for several hours. The porous

oxide layer acts like a sponge and there is very efficient uptake of the dye, leading to intense colouration of the film. The dye-coated electrode is then put together with another conducting glass electrode and the intervening space is filled with an organic electrolyte (generally a nitrile) containing a redox electrolyte (I⁻ / I₃⁻). A small amount of Pt (5 ~ 10 μg cm⁻²) is deposited to the counter electrode to catalyze the cathodic reduction of triiodide to iodide. After making provisions for electrical contact with the two electrodes, the assembly is sealed (see Fig. 2.1).

2.2 KEY COMPONENT OF THE SOLAR CELLS

Understandably, in a multi-component device, the overall performance of the solar cell depends critically on the individual properties of the constituent component and processes:

- (1) The structure, morphology, optical and electrical properties of the nanoporous oxide layer;
- (2) The chemical, redox and photo-physical and photo-chemical properties of the dye;
- (3) The visco-elastic and electrical properties of the redox mediator;
- (4) The redox and optical properties of the redox mediator;
- (5) The electrical and optical properties of the counter electrode.

Those are all the major considerations that need to be taken account of in the design of solar cells. The key processes are: light absorption, charge injection from the excited state of the dye; regeneration of the oxidized dye; electron percolation within the oxide film; dark currents and counter-electrode performance. For devices targeted for commercialization, there are additional factors to consider, such as: long term stability and material cost. Optimal performance is obtainable only when we can understand the factors that control each of these components and our ability to tune to the required configuration. With the involvement of so many parameters, these solar cells are extremely delicate devices to fabricate in a reproducible manner. On the other hand, these parameters allow total flexibility for tuning to specific applications. Indoor applications in electronic gadgets such as watches, calculators, bathroom balances, etc., require higher photo-voltage output at relatively low photocurrent levels upon ambient light exposure to small electrode surfaces. The cells work at ambient temperatures. Outdoor applications employ large area panels composed of modules (typically 10 × 10 cm). Maximum power conversion is envisaged under conditions where the operating temperature and incident solar flux span a wide range.

2.2.1 Titanium Oxide

One of the requirements of dye-sensitized solar cells is the use of a large surface area semiconductor to provide sufficient light absorption with only one adsorbed monolayer of dye. The material of choice was found to be titanium dioxide (TiO₂, anatase). It is cheap, abundant, chemically inert and its properties have been extensively studied,²⁸⁻³⁵

The band gap energy of anatase is 3.2eV^{36} , which makes it unsuitable for solid state solar cell applications ($3.2\text{eV} \cong 387\text{ nm}$). However, for dye sensitized solar cells this is an advantage (the closer the energy level is to that of the excited dye). To obtain a large surface area, nano-sized TiO₂ particles are used (see Fig. 2.2), which usually have diameters of $15 \sim 30\text{ nm}$. These particles are packed into a layer of $2\text{-}10\ \mu\text{m}$ thickness. The layer thickness has to be optimized with respect to light absorption of the film (where thickness is advantageous) and to charge carriers average diffusion length to avoid charge recombination (thin layer is advantageous).

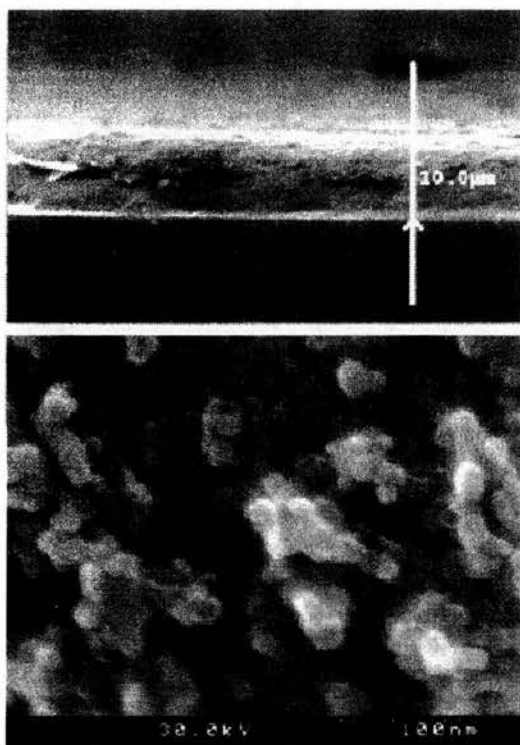


Fig. 2.2. IFESEM micrograph of nano-porous TiO₂ layer. Side and top view. Layer thickness $\approx 10\ \mu\text{m}$, particle diameter $\approx 22\text{nm}$.

It was mentioned earlier that the performance of the solar cells is intimately linked to the material content, chemical composition, structure and morphology of the nanoporous oxide layer. Fortunately, colloid chemistry has advanced tremendously in the last two decades that it is now possible to control the processing parameters, such as precursor chemistry, hydrothermal growth temperature, binder addition and sintering conditions in order to optimize the key parameters of the film, i.e. porosity, pore size distribution, light scattering and electron percolation. Two crystalline forms of TiO₂ are important: anatase and rutile (the third form brookite is difficult to obtain). Anatase is the low-temperature stable form (appears in the form of pyramid-like crystals) and rutile (needle-like) is the dominant form in high temperature preparations, including single crystals. The reduced density of anatase as compared to rutile (3.89 vs 4.26 g cm⁻³) leads to significant differences in many physical properties. Rutile has non-negligible absorption in the near-UV region (350 ~ 400 nm), corresponding to ca. 4% of the incident solar radiation. Excitation within the bandgap leads to the generation of holes in the valence band which are strong oxidants responsible for the long term instability of the solar cell.

For efficient dye distribution, the surface of the membrane film must be large. It is known that the smaller the particle size, the larger will be the surface area of the film. It was mentioned earlier that on surfaces of single crystal electrodes only a few monolayers of the dye can efficiently participate in the excited state charge injection process. The light harvesting from a planar electrode is poor due to the small absorption cross section of a mono-layer of the dye. In highly porous nanotextured films, the available

surface area for dye adsorption can be enormous (with surface roughness factor over 500). This, and the multiple scattering of the light by the small particles leads to near extinction of incident light within a film which is a few microns thick.

Porosity is another factor that needs to be optimized. For the fast regeneration of the oxidized dye and charge transport, the redox electrolyte must be able to penetrate the pores efficiently and be present in places where the dye penetrates. The larger the particle size, the larger will be the porosity of the layer. Larger particles also scatter the incident radiation more effectively and this has been found to be a positive factor in enhancing the red-light response of the sensitizer. So the preparation procedure must be optimized so as to provide an optimal particle size and porosity. Sintering of the particles that form the film is another important step related to electron percolation within the film and reducing of dark currents. Sintering produces low resistance ohmic contacts between the particles. Thus, electrons injected anywhere within the network of particles can hop through several particles and reach the back contact without being lost (trapped) within the oxide layer. The injected electron has to be transported across a large number of colloidal particles and grain boundaries. There will be an increased probability of recombination with increased film thickness. Thus there exists an optimal thickness to obtain maximum photocurrent. Another loss mechanism due to film thickness is a resistance loss leading to a decrease in photo-voltage and fill factor.

Preparation of the nanocrystalline semiconductor films consists of two steps: preparation of a colloidal solution containing mono-dispersed nano-sized particles of the

semiconductor and the preparation of a 1-10 μm thick film with good electrical conduction properties using this colloidal solution. Various steps involved in the preparation of a stock solution of TiO₂ colloid are:

1. precipitation (hydrolysis of Ti-alkoxides using 0.1 M HNO₃)
2. peptization (heating at 80 °C for 8 h) followed by filtering
3. hydrothermal growth / autoclaving (12 h, 200 ~ 250 °C)
4. sonication (ultrasonic bath, 400 W, 15 × 2 s)
5. concentration (450 °C, 30 mbar)
6. binder addition (carboxowax / PEG, M_w 20,000).

Layers are then deposited on conducting glass substrate either using the doctor blade technique or screen printing (see experimental section for further details) followed by sintering (450 °C for 30 min) to burn out the binder.³²

The precipitation process involves the controlled hydrolysis of a Ti(IV) salt, usually an alkoxide, such as Ti(OⁱPr)₄, or a chloride followed by peptization. In order to obtain mono-dispersed particles of desired size, the hydrolysis and condensation kinetics must be controlled. A Titanium alkoxide with bulky groups, such as butoxide hydrolyzes slowly, allowing slow condensation rates. It has been found that, Ti(OⁱPr)₄ suitably modified with acetic acid or acetyl acetonate, gives colloids of higher surface area ($\geq 200 \text{ m}^2 \text{ g}^{-1}$) and small particle diameter (5 ~ 7 nm). The peptization step involves heating of the precipitate for ca. 8 h at 80 °C. The process leads to segregation of the agglomerates

to primary particles. In view of the electrostatic factors that control colloid stability, successful peptization occurs more effectively at pHs further away from the isoelectric point. Particle growth has also been observed to some extent. The precipitate is then filtered through a glass frit to remove larger agglomerates and water added to the filtrate to reach a solution concentration of ca. 5% (w / w)

Autoclaving of these solutions (heating at 200 ~ 250 °C for 12 h) allows the controlled growth of the primary particles and also to some extent the crystallinity. During this hydrothermal growth smaller particles dissolve and fuse to large particle process known as *Ostwald ripening*. The higher the autoclaving pH, the more effective the *Ostwald ripening* is. Aggregation is less efficient at low autoclaving temperatures. The pore size distribution of the film depend on the aggregation and distribution. Average aggregate sizes of 100, 270 and 440 nm, for example, give rise to average pore sizes of 10, 15 and 20 nm, respectively. At higher autoclaving temperatures, more rutile formation occurs, particularly at temperature above 240 °C. Electrodes prepared using colloids autoclaved at or below 230 °C are transparent while those made from colloids autoclaved at higher temperatures are translucent or opaque. Each of these has its own advantages. Solar cells are usually made on a 240 ~ 250 °C autoclaved colloidal solution with a film thickness of 10 μm, whereas for electro-chromic display applications, it is desirable to use a solution autoclaved at 200 °C giving a transparent 3 ~ 4 μm thick film. Sedimentation takes place to some extent during the hydrothermal growth procedure and the precipitates are redispersed using a Ti-ultrasonic horn (15 × 2 s pulses at 400 W). The solution is then concentrated at 45 °C on a rotary evaporator to reach a final concentration

of ca. 11%. An increase in the porosity of the film can be obtained by adding a binder such as polyethylene glycol (M_w 20,000) to the above solution.

The solution is now ready for deposition on the conducting glass substrate. A piece of F-doped SnO₂ glass is used and the solution is deposited by the doctor blade technique to reach a film thickness of 100 μm . In routine work, a piece of Scotch tape at the edges of the support determined the thickness of the film. Commercial powders of TiO₂, such as P-25 and F287 (both Degussa) could also be used in place of the hydrolyzates of titanium alkoxide. P-25 is formed by the hydrolysis of TiCl₄, in a hot flame. The relatively short residence time necessary for the conversion of TiCl₄ to TiO₂ gives a product which has high surface area (ca. 50 m² g⁻¹) and is a mixture of 4:1 anatase to rutile. These TiO₂ powders are dispersed by grinding with water, particle stabilizers (such as acetylacetone or HNO₃) and wetting agents, such as non-ionic surfactant Triton X-100, and spread on the support as with the alkoxide solutions.

The films are then dried in air and then fired at 450 °C in air for 30 min. The film thickness is typically 5 ~ 10 μm and the film density about 1 ~ 2 mg cm⁻². Analysis of the porous films (carbon content) indicate that the binder is totally burnt out. Increase of the firing temperature leads to sintering and pore coarsening. Small pores (≤ 10 nm) decrease substantially and the average pore size increases from 15 nm (400 °C) to 20 nm at 550 °C. Sintering at 350 ~ 450 °C produces electronic contact not only between the particles and the support but also between all the particles constituting the film. Thus a sponge-like structure is obtained and the colloidal TiO₂ film is porous (typically a porosity of 50% is

achieved) from the outer layers to the ITO doping contact. The pores between the colloidal particles are interconnected and can be filled with an electrolyte. A roughness factor, defined as the ratio between the real and the projected surface of these films, of about 1000 has been estimated for 10 μm thick TiO₂ film.

Studies have shown that deposition of a secondary oxide layer to the nano-textured film improves significantly the cell performance. In one procedure the film is impregnated with TiCl₄ by immersing the film in a solution in ice water (conc. 0.2 M) followed by firing at 450 °C for 30 min. Electrochemical deposition of TiO₂ on the nano-textured film can also be carried out by anodic oxidative hydrolysis of TiCl₃. Typically 0.1 ~ 0.35 mg cm⁻² (projected area) of TiO₂ was deposited galvanostatically on top of TiO₂ layer on ITO or Ti sheet.³⁷ One possible effect of the secondary layer is to increase the electron percolation in the film.

The morphology of the oxide layer also affects the dye uptake and also the spectral response in the low energy region. In high surface area films composed of very small TiO₂ particles, the pore size can limit the dye uptake particularly for large size molecules. Feeble coloration is obtained due to low dye uptake that occurs with large supramolecular molecules, such as porphyrin or multinuclear metal centres connected by bridging ligands.³⁷ So, tuning of the pore size is necessary in these cases. The absorption of light by a mono-layer of the dye adsorbed on to a flat semiconductor surface is weak due to the fact that the area occupied by one molecule is much larger than its optical cross section for light capture. High photovoltaic efficiency cannot be obtained in such a

configuration. When the light penetrates the spongy semiconductor in the porous films, it crosses several hundreds of adsorbed dye monolayers thus the mesoscopic films fulfil a function similar to the thylakoid membranes of green leaves.

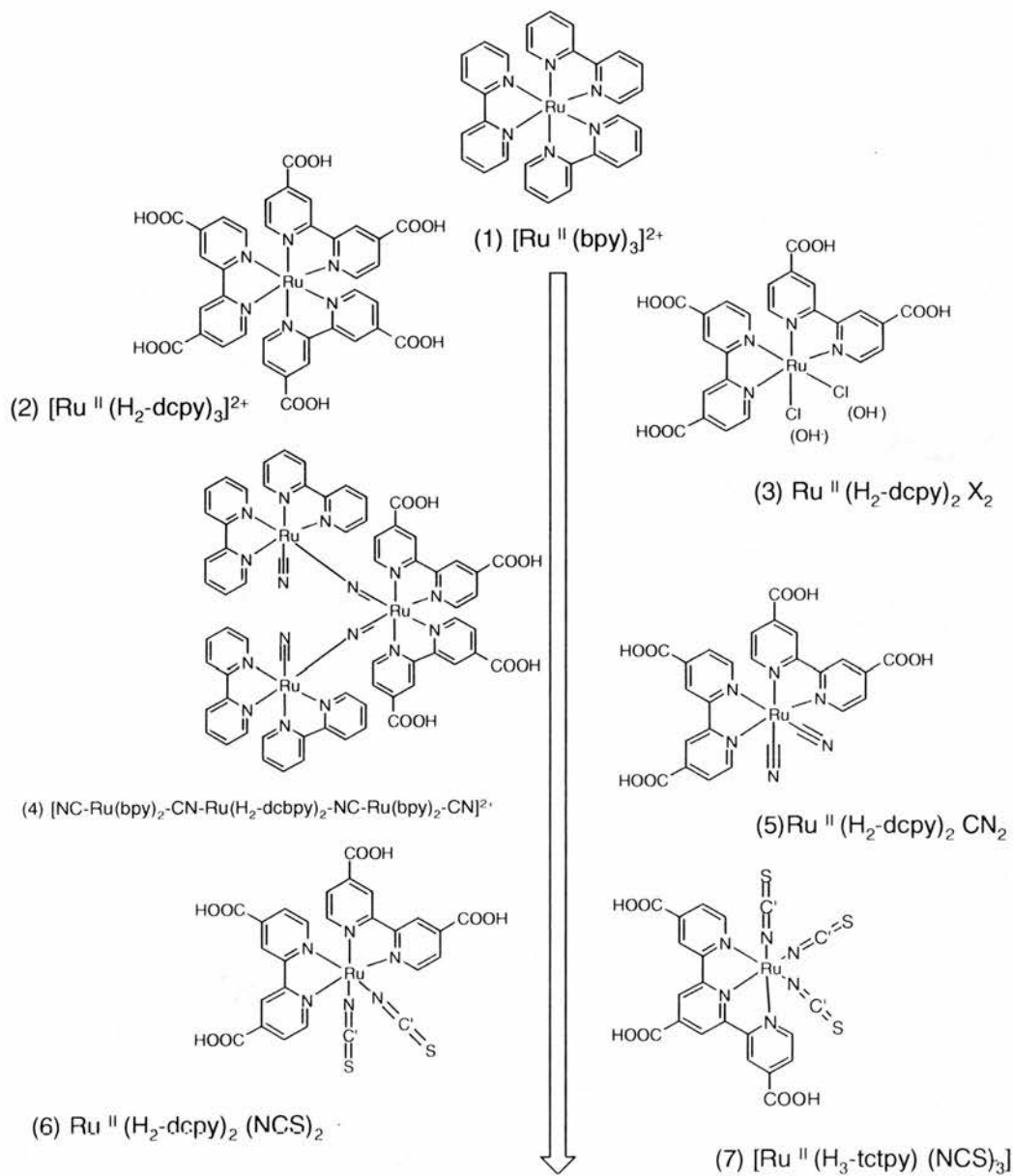


Fig. 2.3. Historical development of sensitizers for solar cells.

2.2.2 Dye Sensitizer

Most sensitizers currently used in solar cell applications are ruthenium polypyridyl complexes. The development of sensitizers over the past two decades is summarized in Fig. 2.3. Over this period, many have specifically been synthesized and tested for solar cell applications, but only those few sensitizers displayed in Fig. 2.3. performed satisfactorily. Most of these sensitizers were ruthenium complexes, some were osmium complexes,³⁸ pure organic dyes³⁹ or other compounds. However, only a small fraction of these dyes performed well as photosensitizers, whilst the majority of the dyes, with a very similar chemical and physical properties, do not. Details on the development of the sensitizer in dye sensitized solar cells are as follows:

- (1) $[\text{Ru}(\text{bpy})_3]^{2+}$: $[\text{Ru}(\text{bpy})_3]^{2+}$ is one of the best studied photosensitizers, partly due to its successful application in homogeneous and heterogeneous water splitting systems⁴⁰⁻⁴². It has never been routinely used as a sensitizer in solar cells, which might be attributable to its ability to only physical adsorption onto the semiconductor surface.⁴² However, since it is a convenient model compound, literature on investigations of $[\text{Ru}(\text{bpy})_3]^{2+}$ in solar cell like applications are available.^{44, 45}

- (2) $[\text{Ru}(\text{H}_2\text{-dcbpy})_3]^{2+}$: Introducing carboxylate groups onto the ligand results in a favourable red shift of the absorption spectrum. Complexes

in which one or more of the bpy ligands of $[\text{Ru}(\text{bpy})_3]^{2+}$ have been replaced, were first synthesized by the group of Wolfgang Sasse in Australia in an attempt to obtain a more efficient sensitizer in water splitting systems.^{46, 47} In the case of nano-porous TiO₂ electrodes, this compound is able to form ester link-ages with the surface hydroxy groups of the TiO₂, thus allowing very efficient attachment onto the surface via formation of chemical bonds⁴⁸.

- (3) $[\text{Ru}(\text{H}_2\text{-dcbpy})_2(\text{OH})_2]$: The replacement of one H₂-dcbpy unit by two negatively charged hydroxyls or chlorides shifts the absorbance bands of the complex by over 100 nm toward the red, thereby increasing the spectral response.¹⁰
- (4) $[\text{NC-Ru}(\text{bpy})_2\text{-CN-Ru}(\text{H}_2\text{-dcbpy})_2\text{-NC-Ru}(\text{bpy})_2\text{-CN}]^{2+}$: With this trimeric complex, a new type of sensitizers was born, in which two bipyridine derivatives and two pseudo-halide ligands, which are able to maintain a strong π -back bond with the metal center, are coordinated to ruthenium.⁴⁹
- (5) $[\text{Ru}(\text{H}_2\text{-dcbpy})_2(\text{CN})_2]$ ^{49, 50}: Developed at about the same time as the latter trimeric sensitizer and exhibits very similar efficiencies.

- (6) [Ru(H₂-dcbpy)₂(NCS)₂]^{20, 51-54}: First reported in 1991, this is currently (2002) still the most commonly-used sensitizer. It provides an overall solar conversion efficiency of over 10%. Use of the ambidentate thiocyanate (NCS⁻) ligand gives rise to three different thiocyanate linkage isomers, which cannot be completely separated. The major product is N-bonded isothiocyanato complex. The majority of the experimental work reported in this chapter is concerned with this complex.
- (7) [Ru(H₃-tctpy)(NCS)₃]⁻ This dye that was reported⁵⁵ to outperform [Ru(H₂-dcbpy)₂(NCS)₂]. Several attempts have been found in the literature to vary the structure of the bipyridine ligand and to replace one or two bipyridines by terpyridine.⁵⁶⁻⁵⁸

2.2.3. Anchoring Groups

There are various ways in which molecular organization can take place on host surfaces: (1) covalent attachment brought about by directly linking groups of interest or via agents; (2) electrostatic interactions, brought about via ion exchange, ion-pairing or donor-acceptor interactions; (3) hydrogen bonding, especially in biological systems; (4) hydrophobic interactions leading to self-assembly of long chain fatty acid derivatives; (5) Van der Waals forces involved in physisorption of molecules on solid surfaces; and (6) physical entrapment inside the pores or cavities of hosts such as cyclodextrins, micelles,

etc. Most of the functionalized molecules that were used for the solar cells are of the first kind. When molecules are chemically derivatized onto surfaces, their translational mobility is considerably reduced. This reduction in dimensionality has important consequences in reaction kinetics.

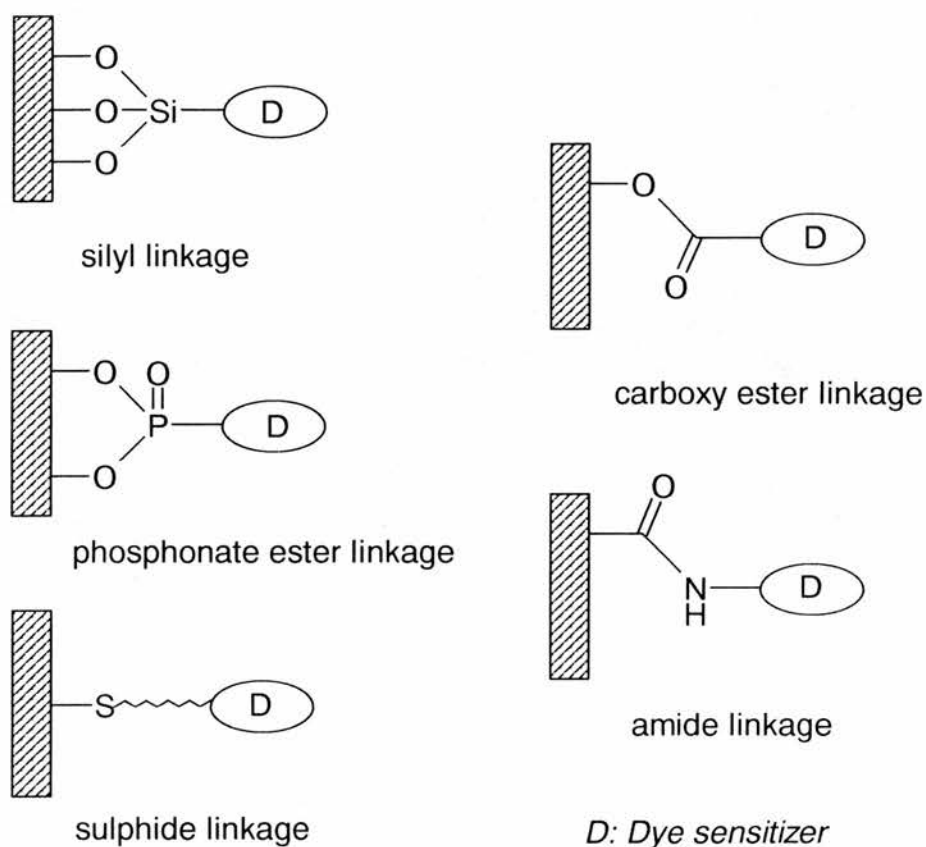


Fig. 2.4. *The possible ways the dye binding to the oxide surfaces*

For improved performance of solar cells, the molecular components have to be structurally modified for attachment to the host matrix, semiconductor. Groups such as silanyl (-O-Si-), amide (-NH-C(O)-), phosphonato (-O-(HPO₂)-), carboxyl (-O-C(O)-)

have been shown to form stable linkages (as shown in Fig 2.4). In most of these cases, reactive elements react spontaneously with surface hydroxyl groups on the oxide surface to form linkages that exhibit good stability.

Carboxylic and phosphonic acid derivatives of photo- and redox active molecules readily react with oxide surfaces to form the corresponding esters. Amide linkages are obtained via the reaction of amine derivatives (RNH₂) and dicyclohexyl carbodiimide (R-N=C=N-R) on oxides. In aqueous medium the stability of some of the linkages can be limited to a certain pH range due to associated protolytic equilibria, e.g. carboxy-esters to $\text{pH} \leq 4.5$ and phosphonato-esters to $\text{pH} \leq 8.5$.⁵⁹ In aqueous solutions at higher pH, hydrolysis and de-chelation of the anchoring group from the surface can occur. Most often these reactions take place sufficiently slowly that the effect of de-chelation are manifested only in limited long term stability tests. The pH range over which the devices can be used in aqueous media is rather limited for this reason. Other linkages have been used, for example, the known affinity of Au, Ag surfaces to sulfur compounds have been used to anchor long chain thiols (RSH) onto electrode surfaces. However, in the recent work, carboxyl and phosphonic linkages have been most frequently used for the binding of the dye to the semiconductor electrode.

2.2.4 Redox Couple

After photoexcitation of the dye, electrons are injected through the bidentate carboxylate-titanium linkage (assuming the standard dye is used, the link will be *via* its

4,4'-dicarboxyl-2,2'-bipyridyl ligand). The linkage constitutes a strong coupling to the Ti (3d) conduction band orbital. The injection time is very fast, in the femto-second time region. After injection, the electron diffuses through the network of nanocrystalline particles to the back-contact. The oxidized dye is regenerated by the redox couple in the electrolyte. The redox couple most used today is I⁻ / I₃⁻.

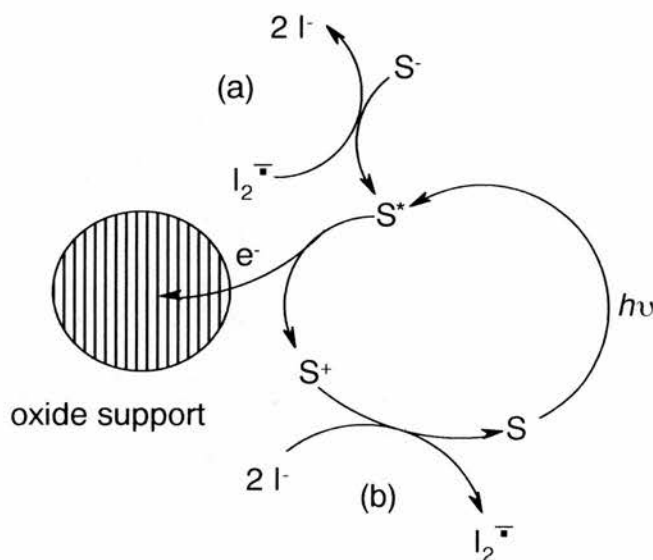


Fig. 2. 5. Reaction pathways with which iodide ions can interact with (a) excited sensitizer (S^*) or (b) oxidized sensitizer (S^+) at the oxide surface

The use of a redox couple is often useful for preventing back electron transfer as it quickly intercepts the oxidized sensitizer with electron transfer. Such redox couples have been employed in the photosensitized water splitting reaction and photoelectrochemical solar cells.⁶⁰⁻⁶² To compete with the back electron transfer between the oxidized sensitizer and the injected electron, it is necessary to employ high concentrations (>0.1 M) of redox couple in these systems.⁶³ However, since the redox couples are also capable

of interacting with the excited sensitizer, it can create a competing deactivation pathway for the excited sensitizer. (Fig. 2.5)

2.3 OCTAHEDRAL COMPLEXES

(a) *Valence Bond Theory*

In general, a molecular orbital is constructed from atomic orbitals of the appropriate symmetry. However, instead of describing an orbital in terms of a linear combination of all possible atomic orbitals, it is sometimes convenient to form a mixture of orbitals on one atom and then use the *hybrid orbitals* to construct localized orbitals.⁶⁴ In CH₄ for instance, each C—H bond can be regarded as formed by the overlap of an H1s orbital and a hybrid orbital composed of C2s and C2p orbitals, thus forming four equivalent *sp³-hybrid orbitals*.

To form hexacyano ruthenium [Ru(CN)₆]⁴⁺, the first three of the five d-orbitals will be doubly occupied, so that two d-orbitals will become vacant. Subsequently these two 4d-orbitals will be hybridized with the 5s- and 5p-orbitals. Each cyanide molecule donates an electron pair for bonding to the coordination center, thus resulting in six equivalent *d²sp³-hybrid orbitals* (see Fig. 2.6).

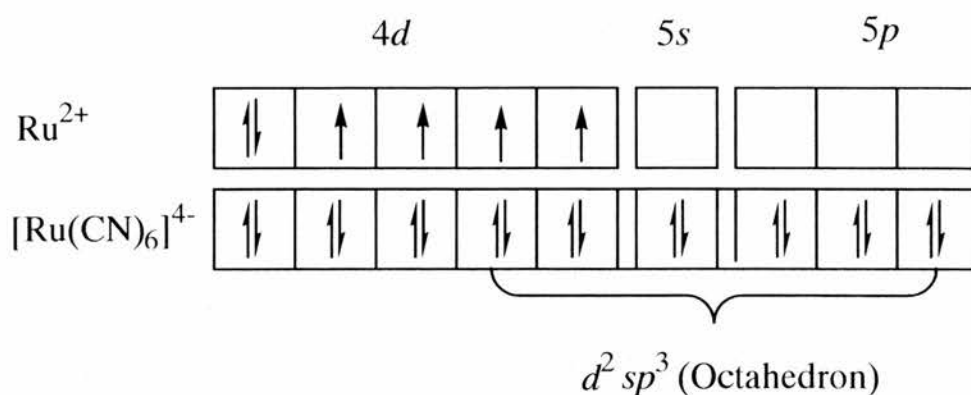


Fig. 2.6 Orbital hybridization in case of an octahedral ruthenium complex

(b) Molecular Orbital and Ligand Field Theory

Ligand field theory, which is a particular application of molecular orbital theory, provides a simple conceptual model to interpret electronic spectra.⁶⁴ In an octahedral complex each ligand has a single valence orbital directed toward the central metal atom with local symmetry (rotational symmetry) with respect to the M—L axis.

As illustrated in Fig. 2.7, in an octahedral d-metal complex, the d_z^2 and $d_{x^2-y^2}$ orbitals (de-generated or hybridized into two e_g orbitals) point along the axes directly toward the ligands and thus are repelled more strongly by the negative charge of ligands than electrons in the d_{xy} , d_{zx} and d_{yz} orbitals, which are triply degenerated into three equal t_{2g} orbitals. Due to the energetically unfavorable configuration of the e_g subset, it is increased in energy, concurrently the energy of the t_{2g} subset is lowered, resulting in zero net change. Both subsets are split by Δ_0 , called the *ligand field splitting parameter*.

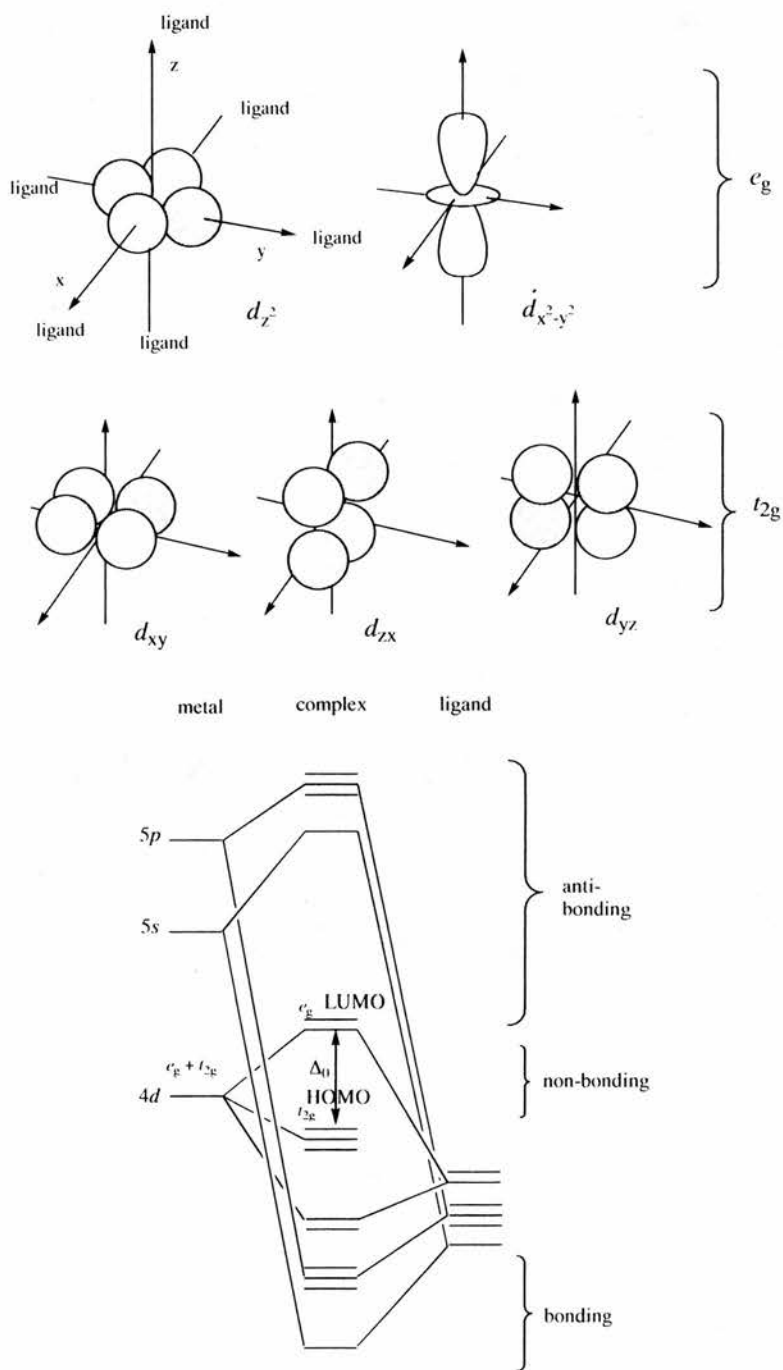


Fig. 2.7. Splitting of the d-orbitals in the octahedral ligand field into two energetically non-equivalent subsets, t_{2g} and e_g . Δ_0 = octahedral ligand field splitting parameter.

Shaded area shows frontier orbitals.

(c) π back-bonding

If the ligands in a complex have orbitals with local π symmetry with respect to the M—L axis, then they may form π molecular orbitals with the t_{2g} metal orbitals. A π -acceptor ligand means a ligand that usually has filled π -orbitals at lower energies than the metal t_{2g} orbitals and low energy empty π orbitals that are available for occupation. Typically, the π acceptor orbitals are vacant antibonding orbitals on the ligand, as in CO and bipyridine. If these vacant π^* ligand orbitals are close in energy to the metal t_{2g} orbitals and the metal-ligand π overlap is strong, some electron density will be delocalized from the metal to the ligand. As illustrated in Fig. 2.8, this type of bonding results in a decrease in energy of the metal character t_{2g} orbital and as a net result Δ_0 is increased by the π -acceptor interaction. Conversely, if a ligand has filled π orbitals and the metal t_{2g} orbitals are predominantly empty, bonding between the filled π and partly empty t_{2g} orbitals can be established, resulting in a decrease of the Δ_0 value. These kind of ligands are called π -donor ligands (such as Cl⁻, I⁻ and H₂O). Thus, ligands which are able to form strong π bonds and are good π acceptors form very stable complexes when coordinated to a metal center. Schematic molecular orbital diagrams, as shown in Fig. 2.7 and 2.8, are a very valuable tool for interpretation of electronic spectra. And, *vice versa*, electronic spectra can provide much insight into orbital structure and bonding of complexes. For instance, the ruthenium bipyridine complexes used in dye sensitized solar cells are dominated by very strong MLCT transitions in the visible spectrum. Such transitions involve an electron from the metal t_{2g} orbital to be promoted into the empty π^*

orbital of the bipyridine ligand and results in a momentary spatial charge separation. Hence, its name "*metal-to-ligand charge transfer*" is derived. The intensity of this band in the spectrum reflects the quality of orbital overlap between the metal and ligand orbitals (see Fig. 2.8 left), whereas the position of the transition is a measure of the energy between both orbital levels.

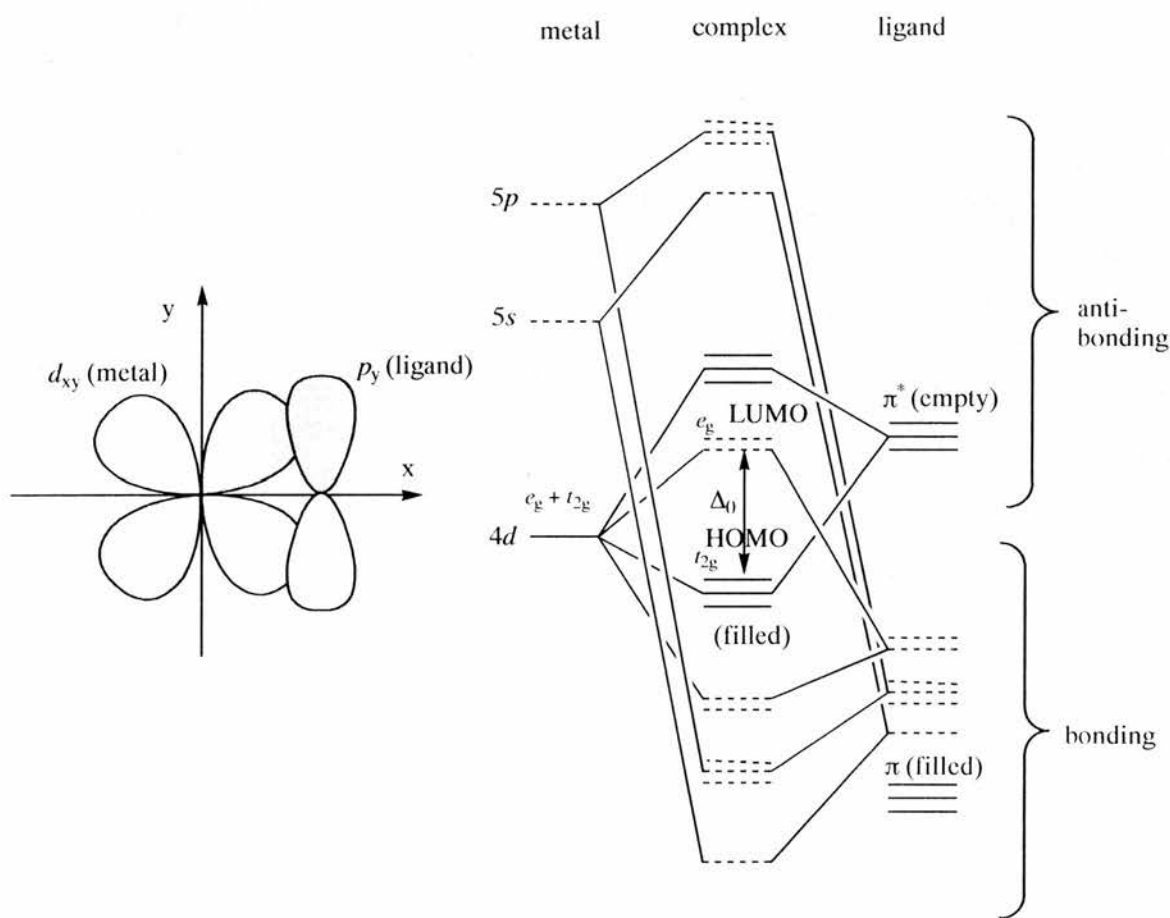


Fig. 2.8. π -back bonding in an octahedral metal complex

2.4 MOLECULAR ENGINEERING OF THE DYE-SENSITIZERS

2.4.1 General considerations

According to historic development of the dye sensitizer and the people who have engaged in the molecular engineering of the dyes, there are several key criteria that are preferably met for the dyes to serve as efficient photosensitizers in solar cells.

(a) Spectral properties

Obviously one would like to use a dye that has near black body absorption, *i.e.*, a dye that absorbs all of the visible, near-IR photons of the sunlight incident on earth. Fortunately, transition metal complexes derived using the ligand systems mentioned earlier all exhibit strong absorption bands in the spectral region of interest. The dominant electronic transitions contributing to the molar absorbance are of MLCT character for polypyridines and $\pi - \pi^*$ transitions for the porphyrins and phthalocyanines. Unlike *d-d* transitions, charge transfer $\pi - \pi^*$ transitions are fully allowed by the selective rules. Sufficient knowledge is available to modulate the energies and intensities of the low-lying elicited states. Some examples of design strategies leading to identification of photosensitizers are elaborated below, using Ru-polypyridyl complexes as model candidates.

For dyes that are adsorbed or covalently bound to the oxide surface, the light-induced electron transfer is non-diffusional. Hence it suffices to have the excited state lifetime to be in the order of tens of nano-seconds. Where there are several forms of excited state available, kinetics and thermodynamics decide if charge injection occurs from some or all of them. When the excited state charge injection is kinetically slow, other processes in the excited state manifold such as non-radiative decay, cross-over to metal-centered excited states (which can lead to photo-substitution) becomes important in determining the efficiency of charge injection and stability of the dye.

(b) Redox properties in the ground and excited state

These are used to ensure fast charge injection and regeneration of the oxidized dye. Efficient charge injection from the electronically excited state of the dye into the conduction band of TiO₂ depends on the redox potential of the dye in the excited state, $E(S^+ / S^{\circ})$. In cases where the reorganization energy for the formation of oxidized dye is small (as is often the case with polypyridine and porphyrin complexes), the excited state reduction potential $E(S^+ / S^{\circ})$ is given by:

$$E(S^+ / S^{\circ}) = E(S^+ / S) + E(S^{\circ}) \quad (2. 1)$$

where $E(S^{\circ})$ and $E(S^+ / S^{\circ})$ represent the excited state energy and the oxidation potential of the dye in the ground state, respectively. Electron transfer reactions involving semiconductor valence and/or conduction bands have been described by the same

Marcus-type formalisms used for electron transfer reactions of solution redox species, particularly for the dependence of the rate on the driving force associated with respective electron transfer steps. Strictly speaking the above approach assumes that the redox partners are vibrationally relaxed. This condition is met for the reverse electron transfer reaction, which are usually slow. But the forward electron-transfer / charge injection step, often occurs in the *ps* timescale, so it's assumption of vibrational equilibration may not be valid.

Obviously one would like to use a dye that absorbs nearly all of the sunlight incident on the earth, like a black body absorber. Generally, however, the sensitizer has only a single energy gap. The mismatch of this gap of the solar spectrum is a major limitation on the overall solar cell efficiency. It is interesting to speculate on the threshold wavelength, if any, for optimal light harvesting. The solar spectrum has its maximum intensity in the IR region (ca. 1200 nm) and so it is desirable to shift this threshold to as low energy as possible. The energy content of the photon, however, decreases as we move further into the IR region. There are two key electron transfer steps (primary charge injection and regeneration of the dye) that must occur very rapidly for solar cells to have high quantum efficiency and long term stability (turnovers). Studies have shown that one needs to provide at last *ca.* 200 mV driving force for each of these reactions to take place with optimal efficiency. In view of this, for a cell that uses a single photon to drive a single electron through the external circuit (as the present case), an optimal threshold for maximum power conversion would be around 850 nm (*ca.* 1.45 eV). Solar cells using low energy photons can deliver higher currents, but only with low photovoltages (*vice*

versa for the high energy case). There are many applications that demand higher voltage output at low light flux. The possibility to design efficient solar cells that work in the blue, green or red part of the solar spectrum opens up interesting applications, as in fashion watches where the photoactive element embedded in the dial can have different colours.

(c) Introduction of anchoring groups

The anchoring groups are employed to ensure uniform distribution of the dye on the oxide surface and to promote electronic coupling of the donor levels of the dye with the acceptor level of the semiconductor. They can operate by physical adsorption (perhaps via H-bonding) or chemical bond formation to the surface by unidentate, chelating or bridging mode of attachment.

There have been reports of cases where chelation of dyes on oxide surfaces leads to strong colouration (development of new charge-transfer absorption band) and the resulting surface-bound complexes act as photosensitizers.⁵⁹ The carboxylic acid groups, for example, while ensuring efficient adsorption of the dye on the surface of the amphoteric oxide TiO₂, promote electronic coupling between the donor levels of the excited dye (a MO which is largely π^* of the ligand in character) and the acceptor levels of the semiconductor (*3d* wave function / conduction band of TiO₂). Electronic excitation in this band leads to extremely rapid and efficient injection of electrons onto the conduction band of the semiconductor. A lower limit for the rate constant of interfacial

electron transfer was determined as 10^8 s^{-1} and the back electron transfer was found to occur with a specific rate of $2.8 \times 10^5 \text{ s}^{-1}$. The injected electrons in the conduction band readily reduce electron acceptors such as methyl viologen efficiently in the same manner as when they are produced by bandgap excitation of the semiconductor. In the case of $[\text{Ru}(\text{dcpv})_2(\text{CN})_2]$, surface chelation is indicated by red-shift in the photocurrent action spectra-maximum observed at 515 nm while it is at 493 nm in solution. For the corresponding bis-chloro complexes, the photocurrent action spectrum has a maximum at 566 as compared to 534 nm observed in solution.⁶⁵

In addition, there are some other factors, such as choice of counterions and degree of protonation (overall charge), choice of peripheral groups and choice of ambidentate ligands, which might affect the performance of the solar cells. Counter ions and the degree of protonation are selected to ensure sufficient solubility in organic or aqueous solvents and in order to control the proton and water content in the pores during the loading of the dye.

2.4.2 Tuning of the t_{2g} and π^* levels in polypyridyl complexes

Spectroscopic and electrochemical studies of polypyridine complexes have clearly established that the first oxidation and reduction potentials are good indicators of the electronic levels of the donor and acceptor MOs. The MLCT transition energy can be reduced either by tuning of the metal-based MO (t_{2g} tuning) or by tuning the polypyridine acceptor based MO (π^* tuning). The t_{2g} energy level is determined largely by the electron

density at the metal center and it can be controlled by the nature of the auxiliary ligand such as CN⁻, Cl⁻ or SCN⁻. Concerning π^* energy level of the ligand, electron-donating substituents (such as -NMe₂ or -OMe) on the polypyridine raise the π^* level and thereby decrease the energy associated with the MLCT transition. Electron-withdrawing groups (such as -COOH) lower the level.

This tuning of redox levels concept can be demonstrated with a graded series of metal complexes with different peripheral substituents. Consider, for example, the spectral and redox properties of a series of mixed ligand complexes of the type [Ru(dcbpy)₂(X)(Y)], where X and Y are electron-rich monodentate non-chromophoric ligands or bidentate polypyridine ligands.⁶⁶ The dicarboxy-bipyridine ligand were chosen as the anchoring ligand and also to ensure sufficient visible light absorption. In all these complexes, the lowest excited state is Ru → dcbpy MLCT. The auxiliary ligands allow tuning of the energy of the Ru → dcbpy CT transition by increasing the charge density at the metal centre. Increasing the charge density at Ru raises the energy of the donor (*t*_{2g}) level, thereby decreasing the energy of the associated MLCT transition. If we take three representative cases of [Ru(ddbpy)₃]²⁺, [Ru(ddbpy)₂(DEA-bpy)]²⁺ and [Ru(ddbpy)₂(ph-py)₂]²⁺, there is a gradual lowering of the energy of the MLCT state due to the presence of electron-rich ligands 4,4'-diethylamino-bpy (DEA) and an *ortho*-metalating ligand phenylpyridine (ph-py). The lowering of the energy of the MLCT state is accompanied by a gradual decrease in emission quantum yield and shorter excited state lifetimes. Quantitative analysis for about 20 mixed ligands complexes showed that the enhanced decay of the excited state is due to enhanced radiationless decay. The rate parameters can

be quantitatively explained in terms of the energy gap law,⁶⁷ while states that non-radiative decay processes become more important decay channels with lowering of the energy of the lowest excited state.

2.5 KINETICS OF THE DYE-SENSITIZED SOLAR CELLS

In the previous sections we have talked about the key components, mainly the dye sensitizers and nano-structured semiconductor, TiO₂. This information is combined to give a cell of the kind shown in Fig. 2.1. The cell is constructed in a sandwich configuration. The working electrode is nano-porous TiO₂ placed on a conducting glass slide support, and only separated by a 50-100 μm thick layer of electrolyte solution (acetonitrile) from the counter electrode. The dye is adsorbed (usually chemisorbed) onto the TiO₂ surface. The counter electrode is also made of conducting glass with a thin transparent layer of platinum sputtered onto it to reduce over-potentials. Since both electrode materials are transparent, illumination might occur from either the front (through counter electrode) or from the back (through the working electrode). The latter case is preferred, as it reduces the diffusion length of the generated carrier to the back contact.

A light photon enters the cell and transverses it until it is absorbed by a dye molecule. The dye will then be promoted into its excited state (Dye^{*}) from where it is now energetically able to inject an electron into the TiO₂ conduction band. The electron can flow into an external circuit through a load (resistor) in order that the energy can be

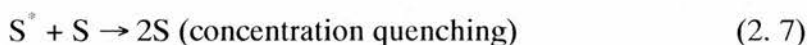
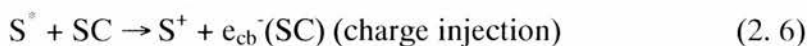
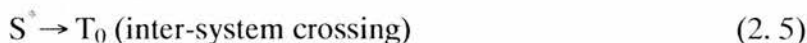
utilized. After this, the electron, which now carries less energy, enters the cell via the counter electrode. From the counter electrode/electrolyte interface it is transported via a charge mediator (commonly the iodide/triiodide couple, present in very high concentrations of about 0.5M / 0.05M) to the working electrode. This process is diffusion controlled. The remaining oxidized dye (Dye⁺) on the TiO₂ surface is then reduced back to its original state by the redox mediator ($R^- + \text{Dye}^+ \rightarrow R + \text{Dye}$), which completes the cycle.

2.5.1 Operating Principles

(a) Principles of Operation

The generally accepted model for dye sensitization of wide gap semiconductors is shown in *scheme 1*. In this model, a molecule of dye-sensitizer absorbs a photon from the light and becomes excited, k_1 . The excited dye injects an electron into the semiconductor conduction band from a normal distribution of donor levels and becomes oxidized, k_{inj} . The electron is swept to the semiconductor bulk by the surface electric field and flows through an external cell to perform useful work. The oxidized dye is reduced by an electron donor present in the electrolyte, k_2 . Reduction of the oxidized donor occurs at the counter electrode and the solar cell is therefore regenerative. Radiative and nonradiative decay of the excited state, k_0 , and recombination of the photoinjected electron with the oxidized dye sensitizer or the oxidized electron donor, k_{er1} , represent loss mechanisms. Following the light absorption of the ruthenium complex, for example, the rate constant

of the electron injection into the conduction band of nanocrystalline TiO₂ is in the sub-ps to ps range. The rate constant for the back electron transfer, however, is much smaller, typically τ ca. 1 μ s. Reactions 2.2 ~ 2.8 below are some of the key reactions that we will consider.

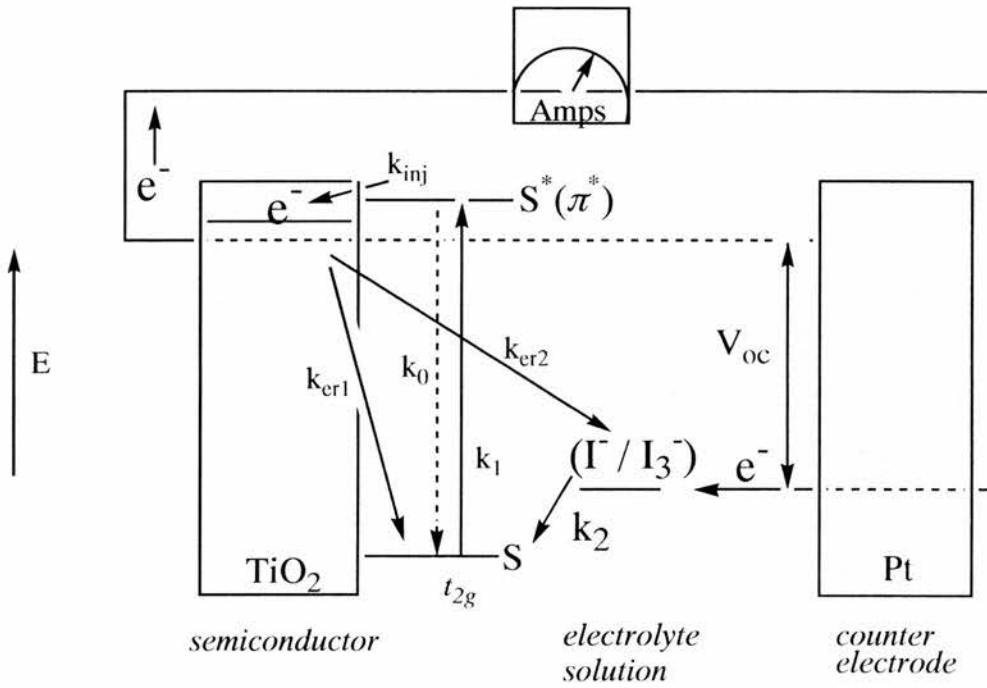


(b) Side Reactions

Several reactions need to be considered which may lower the performance of dye-sensitized solar cells. These reactions are:

- Excited state decay: Electron injection (k_{inj}) or regeneration of Dye⁺ by R⁻ needs to be faster than the decay rate (k_0).
- Electron recombination with dye⁺: Electron in the TiO₂ conduction band recombines (k_{er1}) with the oxidized dye (Dye⁺) on the TiO₂ electrode surface.
- Electron recombination with R: Electron in the TiO₂ conduction band recombines (k_{er2}) with oxidized form of redox mediator (R).

- Bleaching of dye: If the oxidized form of dye (Dye⁺) is not stable on the time scale over which it is reduced back to its ground state (Dye), it will decompose and hence, the cell will bleach.



Scheme 1. Schematic representation of electron transitions in a dye sensitized solar cell. k_0 = rate constant for decay of excited state ($S^* \rightarrow S$). k_{inj} = rate constant for electron injection into TiO₂ ($S^* \rightarrow e^-_{TiO_2}$). k_{er1} = rate constant for electron recombination with oxidized dye ($e^- + S^+$). k_{er2} = rate constant for electron recombination with redox mediator ($e^- + I_3^-$)

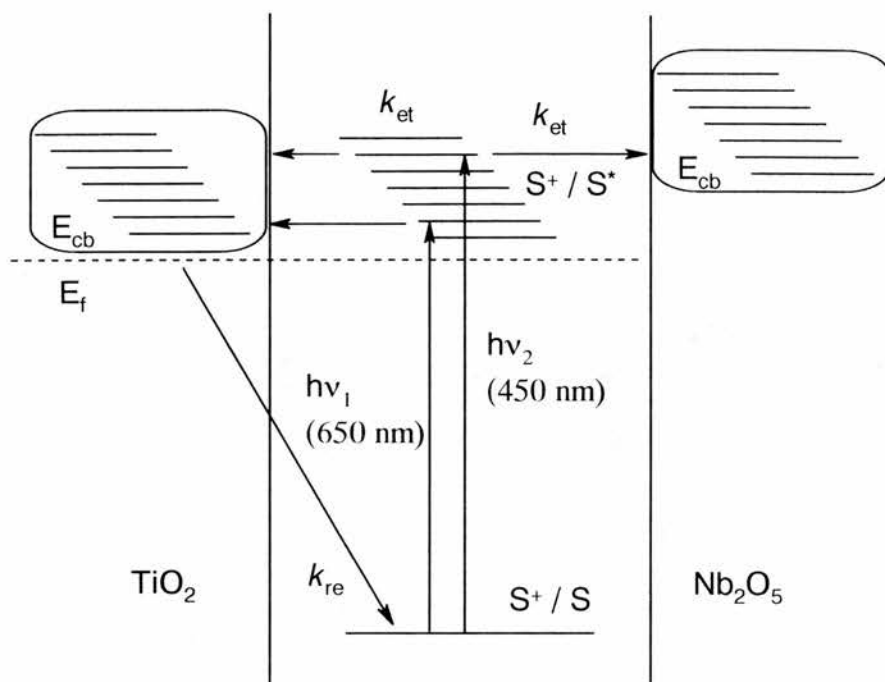
2.5.2 Charge Injection from the Dye to the Semiconductor TiO₂

Fig. 2.9. Schematic representation of excited state injection into a continuum of acceptor states (conduction band) of the semiconductor in dye-sensitized solar cell for excitation at two different excitation wavelengths (450 and 650 nm).

The direct probing of dye sensitization mechanism was first reported in 1976 by time-resolved fluorescence decay study of dye adsorbed on to silver halides,⁶⁸ nano-seconds time resolution was detected then. The time resolution was increased to the ps range in 1980 with measurements by Nakashima, Yoshihara and Willig⁶⁹ on fluorescence decay kinetics of rhodamine B on aromatic hydrocarbon crystals. In the last few years there have been many direct kinetic measurements of the key processes taking place on

nanocrystalline films by spectroscopic and electrochemical techniques,⁷⁰⁻⁷² the former with fs time-resolution.

If we assume that the observed decrease in the luminescence lifetime on the oxide surfaces is entirely due to charge injection and that the other radiative and non-radiative decay processes of the dye on surface occur at the same rate as in a neat solvent, the charge injection rate can be deduced from the expression:

$$(1 / \tau_{\text{ads}}) = (1 / \tau_{\text{solv}}) + k_{\text{inj}} \quad (2.9)$$

where τ_{ads} and τ_{solv} refer to the excited state lifetime in the adsorbed state on the oxide semiconductor and in a neat solvent, respectively and k_{inj} is the specific rate constant for the charge injection process. Clearly when extensive quenching takes place, $\tau_{\text{ads}} \ll \tau_{\text{solv}}$ and $(1 / \tau_{\text{ads}}) \approx k_{\text{inj}}$.

Recent studies with different sensitizers anchored on to nanocrystalline TiO₂ and other semiconductors have shown that the forward electron transfer (injection of electrons into the conduction band by the electronically excited state of the dye) is extremely rapid (a few ps or much less).^{73, 74} In a majority of the cases ultra-fast decay of the excited state is directly linked to charge injection. The dye cation radical is formed with a yield of nearly 100%. The subsequent recombination reactions occur over a much longer timescale (several μs or longer). Thus the conditions are ideal for light induced electron transfer to occur with high quantum efficiency. But it should be emphasized that,

observing ultra-fast decay ($< \text{ps}$) of the excited state of the sensitizer on the semiconductor itself is not a direct proof that the quenching process is only via electron-transfer. There are many documented cases where the measured photocurrent yield is quite negligible yet the excited state decay is extremely rapid. Only in very few cases the yield of redox products (sensitizer cation) has been measured directly in fast transient absorbance studies.

Ultra-fast charge injection rates (in the fs range) measured recently for several sensitizers adsorbed on to TiO₂ raises fundamental questions as to whether the electron transfer does take place from unrelaxed excited states. Ultra fast electron transfer implies ultra-fast charge separation and a slow back reaction. In a number of cases, the excited state charge injection process has been found to be independent of temperature down to 4 K, indicating that the electron-transfer is not an activated process and hence not subject to the kind of dynamical picture that would emerge from classical treatments using the Marcus- Levich equation. Fig. 2.9 shows schematically one possible scenario for such ultra-fast electron transfer involving anchored dyes. In classical electron transfer quantitatively treated under Marcus-Levich-Jortner-Gerischer type formalism, optical excitation is followed by rapid vibrational relaxation (fast redistribution of vibrational energy amongst the sensitizer molecules). In a situation where the photo-excited dye is strongly coupled to the surface, the level matching (in Marcus theory) that ensures energy conservation during electron transfer involves not simply molecular (vibrational) energy level as in solution reactions, but rather a continuum of electronic energy levels that exist in the semiconductor. In such a case, when the donor system is coupled to an electronic

continuum and nuclear degrees of freedom are neglected, the rate constant for transfer is given by the golden rule expression:

$$k_{\text{inj}} = \frac{2\pi}{h} |V|^2 \rho \quad (2.10)$$

where $|V|$ is the electron coupling matrix element and ρ is the density of electronic acceptor states in the semiconductor. The subsequent dephasing which traps the electron can occur on an ultra-fast timescale if the electronic state is high in energy (*i.e.* above the band-edge) and the electronic coupling between the dye and the semiconductor is large. Thus the injection efficiency is primarily attributed to strong electronic coupling.

Willig has described the ultra-fast charge injection process as electron transfer by electron tunneling but with a finite reaction time.⁷⁵ The finite reaction time allows for the motion of the vibrational wave packet in the time span between the generation of the excited reactant state and the appearance of product states. The reverse electron transfer of the electrons wave packet representing the initially formed hot electron in the semiconductor is considered virtually impossible, since this wave packet spreads in time and moves away from the reaction distance. After a series of inelastic and elastic events, the injected electron can return to the interface; however, the wave packet representing the electron will now be completely different; it will have lost energy, changed momentum, etc.

In order to investigate if there is a wavelength dependence of the monochromatic injection efficiency for the excited state charge injection process, Moser has recently examined⁷⁶ the behavior of the standard dye [Ru(dcbpy)₂(SCN)₂] on two oxides surface (TiO₂ and Nb₂O₅), and [Ru(bmip)(dcbiq)(SCN)] on TiO₂. [bmip, 2,6-bis(1-methylbenzimidazol-2-yl)pyridine, dcbiq, 4,4'-dicarboxy-2,2'-biquinone]. Nb₂O₅ has the same bandgap energy as TiO₂ (3.2 eV) but has its conduction band located 0.2 ~ 0.3 eV more negative with respect to that of TiO₂. For excitation with 650 nm photons, photo-induced charge injection from the bis(thiocyanato) complex can occur on TiO₂ (due to its more favorable location of E_{cb}, with respect to E(S^{*})) but not on Nb₂O₅ (see Fig. 2.9). For excitation at 450 nm, charge injection can take place on both these oxide semiconductors. An analogous situation is present when one compares the photo-induced charge injection on TiO₂ for the two Ru dyes cited above. For the same acceptor (TiO₂), the donor levels are differentiated by nearly 0.5 V. The excited state redox potential of the 4,4-dicarboxy-2,2'-biquinoline dye is located just below the conduction band-edge of TiO₂. Optical excitation of the dcbq complex with a low energy photon (650 nm) can lead to charge injection while similar excitation of the dcbpy complex yields none. Thus there are now preliminary indications that charge injection indeed can take place from a hot, vibrationally unrelaxed excited state and this in turn, in select cases, results in a wavelength dependent injection yields.

2.5.3 Back Electron Transfer

A key feature of the nanocrystalline TiO₂ solar cells with ruthenium carboxyl bipyridine based sensitizers is relatively slow back electron transfer (≤ 100 ns) after forward electron injection. Several orders of magnitude difference in the forward and reverse electron transfer rates allow processing of the charge separated products very efficiently: reduction of the oxidized form of the dye by the redox mediators and percolation of the injected charges in the mesoporous layer to arrive at the back contact. In nanocrystalline films, there is hardly any space charge layer and the reverse electron transfer is a thermodynamically well-defined process. For Ru-bpy complexes, with E (Ru^{3+ / 2+}) located between 0.8 and 1.2 eV and an E_{cb} (TiO₂) of ca. -0.8 eV, the driving force for the back electron transfer exceeds 1.6 eV. Such a large driving force should make the reaction kinetics fall deep in the inverted region in the classical Marcus description. Measurements of rate constants for the reverse electron transfer in question by Moser and Grätzel over a wide range of temperature range indicated it to be invariant.⁷⁶

Salafsky et al.⁷⁷ recently used transient microwave reflectivity on a dye-TiO₂ nanocrystal system to monitor the dynamics of photo-injected charge in the semiconductor. The electron decay from the nanocrystals is monitored following photo-injection by a dye and reduction of the dye cation by an electron donor. In an I⁻ / I₃⁻ ethylene carbonate:propylene carbonate electrolyte like that used in dye-TiO₂ photoelectrochemical cells, this decay process represents a short-circuit pathway in the

cell, the long lifetime for injected charge could explain the high efficiency of charge collection in such devices.

2.5.4 Regeneration of the Oxidized Dye

The preferred process for the injected electron in the conduction band, on thermodynamic grounds, is to return to the oxidized sensitizer. Naturally, this reaction is undesirable, since such back reactions generate only heat and not electrical current. For efficient processing of the charge separated products, it is of interest to develop systems where there is an order of magnitude difference in the forward and back electron transfer rates. Fortunately, in the present case, these rates differ by more than a million. In contrast to the charge injection step which occurs in few *ps* or less, the back reaction of the electrons of TiO₂ with the oxidized Ru complex is extremely slow, occurring typically in the μs time domain. The process involves a *d*-orbital localized on the Ru metal whose electronic overlap with the TiO₂ conduction band is small. This together with the fact that the driving force for the back electron transfer is large enough to place it in the inverted Marcus region explains the relatively slow back electron transfer. Thus, in analogy to natural photosynthesis, light induced charge separation is achieved on kinetic grounds, the forward electron transfer being orders of magnitude faster than the back reaction. As a consequence, the presence of a local electrostatic field is not required to achieve good efficiencies for the process. This distinguishes nanocrystalline devices from conventional photovoltaic cells in that the successful operation of the latter is contingent upon the presence of a potential gradient within the *p-n* junction.

For stable operation of the solar cell and maximal power output, the oxidized dye must be reduced back to the ground state as rapidly as possible by a suitable electron donor. Since the maximum photovoltage obtainable is related to the position of the mediator redox potential, it is preferable to choose a couple whose potential is as close to the $E(S^+ / S)$ as possible. As with the charge injection step, the choice of the mediator should be such that there is enough driving force (≥ 250 mV) for the dye reduction step to have the optimal rate. Thirdly, for stable performance of the solar cell for months, the redox couple must be fully reversible, have no significant absorption of the visible light region, and be stable in the oxidized, reduced forms. The I^- / I_3^- couple is currently being used as the redox mediator of choice. The electrolyte containing the mediator could be replaced by a *p*-type semiconductor, *e.g.* cuprous thiocyanate, CuSCN and cuprous iodide CuI or a hole-transmitting solid, such as the amorphous organic compounds used in electro-luminescence devices.⁷⁹ Murakoshi et al.⁸⁰ have reported on the possibility of using polypyrrole as a hole-transport layer for dye-sensitized TiO₂ solar cell, but the polypyrrole is still quite light-absorbing.

2.5.5 Dark Current

Dark currents significantly reduce the maximum cell voltage obtainable. The oxide layer is an inter-connected network of particles with high porous interior. The dyes can penetrate everywhere and adsorb over a large surface area. Surface concentrations of the Ru complexes as high as 10^{-7} mol cm⁻² on a 10 μ m thick films are achieved, generally

indicating a very dense packing of the sensitizer. However, there still exists enough naked sites. The redox mediator also must penetrate the same domain so as to be present in the immediate vicinity of the photosensitizer. If the redox mediator gets to the back contact, dark currents arise from the reduction of the redox mediator by the collector electrode with the oxide layer:



In principle, this charge recombination can occur at surfaces other than that of TiO₂. Due to the porous nature of the TiO₂ film, it can also occur at the back conducting glass (ITO) electrode. In reality, the reaction occurs at the TiO₂ particle / redox electrolyte interface due to the relatively large surface area of the nanocrystalline film.

Dark currents can be suppressed by co-adsorption of saturated hydrocarbons with anchoring groups that isolate the uncovered oxide surfaces from interactions with I₃⁻, for example, chenodeoxycholic acid. The concentrations of sensitizer and the additives in the coating solution have to be adjusted for high sensitizer loading and at the same time complete isolation (coverage) of non-accessible surface sites—a catch-22 situation for optimization. Several alternate approaches to co-adsorption of additives are also being examined. In one approach, long alkyl chain substituents are introduced at the polypyridine units (not carrying the anchoring groups). Lateral interactions of the alkyl chains and formation of a hydrophobic interface stabilizes the adsorbate from water-induced desorption. A variant of this is the use of bulky, sterically hindering groups such

as *t*-butylphenyl. Another approach is to introduce electropolymerizable groups such as pyrrolic units at the polypyridine ligands. The corresponding Ru complexes can be adsorbed on to TiO₂ and then photopolymerised in the presence of free pyrrole at electrode potentials positive of the flat-band.

In order to reduce the dark current, an oxide underlayer is deposited. Alternatively, exposure of the dye-coated electrode to a solution of a pyridine derivative (donor) such as 4-*t*-butylpyridine was found to improve dramatically the fill factor (ff) and the open-circuit voltage (V_{oc}) of the device without affecting the short-circuit photocurrent (i_{sc}) in a significant fashion. For example, the untreated electrode gave $i_{sc} = 17.8 \text{ mA cm}^{-2}$, $V_{oc} = 0.38 \text{ V}$ and $ff = 0.48$, corresponding to an overall conversion efficiency (η) of 3.7%. After the electrode is dipped in 4-*t*-butylpyridine, V_{oc} increases to 0.66, ff to 0.63 and η to 8.5%.⁵⁹ The increase in the open circuit voltage and the fill factor is due to the suppression of the dark current at the semiconductor / electrolyte junction. The effect of the substituted pyridine can be rationalized in terms of its adsorption at the TiO₂ surface, blocking the surface states that are active intermediates in the heterogeneous charge transfer.

2.5.6 Counter Electrode Performance

Solar cell studies employ usually a F-doped SnO₂ as the conducting glass electrodes. Such electrodes are known to be poor choice for efficient reduction of triiodide. To reduce the overvoltage losses, a very fine Pt-layer or islands of Pt is

deposited on to the conducting glass electrode. This ensures high exchange current densities at the counter electrode and thus the processes at the counter electrode do not become rate limiting in the light energy harvesting process.

2.5.7 Summary of the Kinetics

On the basis of different measurements, it is possible to indicate the orders of magnitude for the rate constants of electron transfer steps involved:

1. Electron injection into TiO₂: following the light absorption of the Ru complex, the electron injection into the conduction band is in the sub-*ps* to *ps* range.
2. Back electron transfer: the rate constant for the back electron transfer (dark reduction in the absence of externally added electron donors) however is much smaller for several reasons, typically τ ca. 1 μ s.
3. Reduction of triiodide by e_{cb}⁻: another important recombination process is the reduction of I₃⁻ in the electrolyte by conduction band electrons. The exchange current density, j_0 of the reverse saturation current of this process has been measured in the range $10^{-11} \sim 10^{-9}$ A cm⁻², depending on the electrolyte. Surface treatment of the electrode can alter these values drastically.

4. The exchange current density for the reduction of triiodide at the counter electrode ITO coated with a catalytic amount of Pt, has been measured to be 0.01 ~ 0.2 A cm⁻².
5. Reduction of the oxidized dye by iodide occurs on a timescale of 10⁻⁸ s.

2.6 EXPERIMENTAL

Chemicals and materials All the chemicals, RuCl₃·3H₂O (Aldrich), 4,4'-dimethyl-2,2'-bipyridine (Aldrich), titanium isopropoxide (Aldrich), polyethylene glycol (Fluka), ITO conducting glass (Nippon sheet glass coated with fluorine-doped SnO₂, Pilkington) and tritonX-100 (Aldrich) were used as received except. Water was triply distilled.

Instrumental and General Techniques NMR spectra were recorded using a Varian Gemini-200 Spectrometer (200 MHz) and a Bruker AM300 NMR Spectrometer (300 MHz). Electronic spectra were recorded on a Perkin-Elmer Lambda 5 spectrometer against a background of pure solvent. Infrared spectroscopy were obtained on a Perkin-Elmer 1710 fourier transform spectrophotometer. Elemental analysis were carried out on a Carlo-Erba 1106 elemental analyzer. Melting point were determined on a Reichert hot-stage microscope. All the melting points are uncorrected.

TiO₂ semiconductor electrode was prepared by the doctor blade method. TiO₂ solution was dispersed on a conducting glass sheet evenly. A blade which was tightly

hold by a moving machine was adjusted to the desired thickness of the semiconductor surface and moved slowly across the surface. The glass sheet with the wet surface was allowed to dry for about 15 min and then was put in the oven for 30 min at 450 °C.

Electrochemistry Cyclic Voltammetry was carried out with a Pine Instruments RDE 4 (EG & G, Wokingham, UK) potentiostat. The CV's were obtained in dimethylformamide with 0.1 M tetrabutylammonium hexafluorophosphate (Bu₄NPF₆) as supporting electrolyte. The working electrode was platinum, the counter electrode was platinum wire and the reference was a SCE.

2.6.1 Dye-sensitizer Synthesis

(1) Preparation of 4,4'-dicarboxy-2,2'-bipyridine⁸¹

4,4'-dimethyl-2,2'-bipyridine (5.0 g, 27 mmol) was dissolved in concentrated H₂SO₄ (100 cm³). After the solution was cooled to 0 °C, CrO₃ (18.0 g, 180 mmol) was added in small portions during 1 h. The mixture which turned blue-green was heated to 75 °C for 4 h, stirred 10 h at room temperature, and finally poured into a mixture of ice/water. The green precipitate was separated by filtration and washed with water several times. The green powder was then suspended in water, and KOH was added under vigorous stirring until the solution was basic. The blue insoluble powder was filtered off and washed with water. The aqueous solution was acidified

with HCl to precipitate the diacid which was filtered, washed with water, methanol, ether. The diacid is insoluble in most organic solvents.

The diacid then was refluxed for 4h in pure SOCl₂ (40 ml), thionyl chloride, which was stripped off under reduced pressure to yield a yellow residue which was recrystallized from cyclohexane. The residue was refluxed for 8 h in methanol with 10 ml concentrated H₂SO₄. Then the reaction mixture was poured into icy water. The precipitate was isolated by filtration and then dissolved in methanol and aqueous NaOH with stirring. After removing the methanol, the mixture was acidified with 37% HCl. The precipitate after acidification was filtered, washed with water, methanol, and then diethyl ether, and dried in air to give the pure diacid. White powder, 5.4g, 80% yield. ¹H NMR (300 MHz, D₂O / NaOD): 8.76 (d, 6H), 8.38 (s, 3H), 7.85 (dd, 5H).

*(2) Preparation of cis-(4,4'-dicarboxy-2,2'-bipyridine)₂RuCl₂*¹⁰

Cis-(4,4'-dicarboxy-2,2'-bipyridine)₂RuCl₂ was obtained by refluxing under argon 110 mg (0.42 mmol) of RuCl₃·3H₂O (Aldrich) and 210 mg (0.86 mmol) of 4,4'-(CO₂H)₂-2,2'-bipyridine (bcpy) in 30 mL of DMF for 8 h. After cooling, traces of RuL₃ were filtered. Most of the DMF solvent was evaporated under vacuum, and *cis*-Ru^{II}L₂Cl₂ was precipitated with acetone. The crystals were filtered off and dried in vacuum, 70 % yield. UV-Vis: 315 nm (ε = 3.50 × 10⁴ M⁻¹ cm⁻¹), 398 nm (ε = 1.35 × 10⁴ M⁻¹ cm⁻¹), 537 nm (ε = 1.35 × 10⁴ M⁻¹ cm⁻¹).

(3) Preparation of *cis*-(4,4'-dicarboxy-2,2'-bipyridine)₂Ru(SCN)₂¹³

RuL₂Cl₂ (117.5 mg, 0.178 mmol) was dissolved in 20 cm³ of DMF solvent under reduced light. To this solution 10 ml of 0.1 M aqueous NaOH solution was added in order to deprotonate the carboxyl groups. Sodium thiocyanate (165 mg, 2.13 mmol) was separately dissolved in 2 cm³ water and subsequently added to the above solution. The reaction mixture was then heated to reflux for 10 h under argon atmosphere. The solvent was removed and the resulting solid was dissolved in water and filtered through a sintered glass crucible. The pH value of the filtrate was lowered to 2.5 by adding dilute HClO₄, and the filtrate was placed in a refrigerator overnight. After reaching room temperature, the solid was isolated by suction filtration, washed well with H₂O / acetone solution, ether and air-dried, 60 % yield. UV-Vis, 410 nm ($\epsilon = 0.95 \times 10^4 \text{ M}^{-1} \text{ cm}^{-1}$), 558 nm ($\epsilon = 1.00 \times 10^4 \text{ M}^{-1} \text{ cm}^{-1}$). IR, 1727 cm⁻¹ (νCO_2^-), 2110 cm⁻¹ (νCN , N-bonded), 2050 cm⁻¹ (νCN , S-bonded). ¹H NMR (300 MHz, D₂O/NaOD), *cis*: 9.45 (d, 6H), 8.90 (d, 3H), 8.70 (d, 3H), 8.18 (dd, 5H), 7.75 (d, 6H), 7.40 (dd, 5H), *trans*: 9.70 (d, 6H), 8.45 (s, 3H), 8.12 (dd, 3H), (The mole ratio of *cis* and *trans* isomers can be determined from the integration of NMR, *cis* : *trans* = 19 : 1). Anal. Calcd for RuC₂₆H₁₆N₆O₈S₂·4H₂O: C, 40.15; H, 3.11; N, 10.81. Found: C, 40.31; H, 3.03; N, 10.65.

2.6.2 Hydrolysis of Titanium Isopropoxide

(1) Acidic conditions³²

Titanium isopropoxide (60 cm³, Aldrich) is hydrolysed at room temperature by its dropwise addition to 300 cm³ of about 0.1 mol L⁻¹ nitric acid solution under vigorous stirring. A white precipitate is formed instantaneously. Immediately after the hydrolysis, the slurry is heated to about 80 °C and stirred vigorously for 8 h in order to achieve the peptisation (i.e., destruction of the agglomerate and redispersion into primary particles). The solution is then filtered through a glass frit to remove nonpeptized agglomerate as well as dust. Water is then added to the filtrate to adjust the final concentration to about 5% in weight.

The growth of these particles up to 10-25 nm is achieved under hydrothermal conditions in a autoclave heated for 12 h between 200 and 250 °C. Sedimentation takes places during the autoclaving and the particles are redispersed and the concentration of the solution is modified to about 10% in weight by evaporation. To prevent the film cracking and thus render the synthesis of 10 µm thick film possible, polyethylene glycol is added in a proportion of 30~50 % of the TiO₂ weight.

(2) Basic conditions⁸²

Titanium (IV) isopropoxide (60 cm³, Aldrich) was rapidly added to distilled water and then stirred for 1h. A white precipitate formed immediately upon addition

of the titanium oxide. The resultant colloid was filtered using a glass frit and washed three times with 50 cm³ of distilled water. The filter cake was added to a Teflon-lined titanium autoclave containing 30 cm³ of a 0.7 mol L⁻¹ ammonium hydroxide solution to form a white slurry. The pH value of the colloidal solution after addition of base was measured to be between 7 and 8 with pH paper. Syntheses with ammonium hydroxide did not bring about complete peptization even after heating at 120 °C for periods up to 16 h, and resulted in a milky-white non-viscous solution.

The suspensions, which resulted from peptization, were treated hydrothermally in the autoclave at temperature 220 °C for 12h. Following growth, the resultant colloidal suspensions were milky-white and had a faint fishy odour. The pH value of the resultant colloidal was measured to be 13.5. These suspensions were concentrated to form aqueous solution containing about 45% solids. Films were made from these suspensions by adding the surfactant TritonX-100 (Aldrich). The resultant solution contained 0.1 wt (%) surfactant with respect to the titanium oxide. The films were deposited using a simple doctor-blade technique onto a plain ITO conducting glass (Nippon sheet glass coated with fluorine-doped SnO₂, Pilkington) substrate. The films were heated at 450 °C for 45 min.

2.6.3 Cell Preparation

*(1) TiO₂ electrode preparation*⁸³

A commercially available glass plate coated with a conductive layer of fluorine-doped SnO₂ was cut (2.5 × 2.5 cm) and used as the starting materials for the electrodes. A volt-ohm meter should be used to check which side of the glass is conductive. Four pieces of Scotch adhesive tape are applied to the face of the conductive glass plate to mask a 1-2 mm strip at three of the four edges, and a 4-5 mm strip is masked on the fourth side. Half of the tape extends from the edge of the table to secure the glass. This tape will form a mould or channel 40-50 μm deep into which the TiO₂ solution can flow, while masking a strip of the conductive glass so that an electrical contact can later be made. Three drops of TiO₂ solution are distributed uniformly on the plate by sliding a glass rod over the plate. The film is then allowed to dry in air and the tape is then carefully removed. The film is annealed and sintered in an air stream at 450 °C for 30 min.

(2) Counter electrode preparation

Following the same procedure as that for the preparation of the working electrode except that a drop of H₂PtCl₆ (Aldrich, 10⁻³ M) solution in acetonitrile was spreading over the conducting ITO glass and sintered at 300 °C for 15 min.

*(2) Coating of the nanocrystalline with the dye*⁸⁴

Coating of the TiO₂ surface with the dye was carried out by soaking the film for at least 3 h in about 10⁻⁴ mol L⁻¹ solution of the ruthenium complex in dry

ethanol. The dye coating was done immediately after the high temperature annealing in order to avoid the rehydration of the TiO₂ surface or the capillary condensation of water vapor from ambient air inside the nanopores of the film. The electrode is dipped into the dye solution while it is still hot, i.e., its temperature was ca 80 °C. It was stored in dry ethanol or immediately wetted with redox electrolyte solution for testing. The amount of adsorbed dye was determined by desorbing the dye from the TiO₂ surface into solution of 10⁻⁴ mol L⁻¹ NaOH in ethanol and measuring the absorption spectrum.

2.7 RESULTS AND DISCUSSIONS

2.7.1 Synthesis

a) Synthesis of TiO₂ colloid

As we described above, TiO₂ colloid solution was obtained by the hydrolysis of Titanium (IV) isopropoxide in either an acidic or a basic condition. The X-ray diffraction pattern for nanocrystalline titanium dioxide colloids of anatase crystal phase got from hydrolysis of titanium isopropanol in acidic and basic condition are illustrated by Fig. 2.10. As we can see from the x-ray spectra, the crystal structure of TiO₂ nanocrystalline hydrolyzed both from basic and acid conditions are anatase, which is the more effective than rutile in structure for solar

cell, according to the investigation from Grätzel research group. TiO₂ electrode was prepared from such colloid following a procedure of autoclaving, sintering.

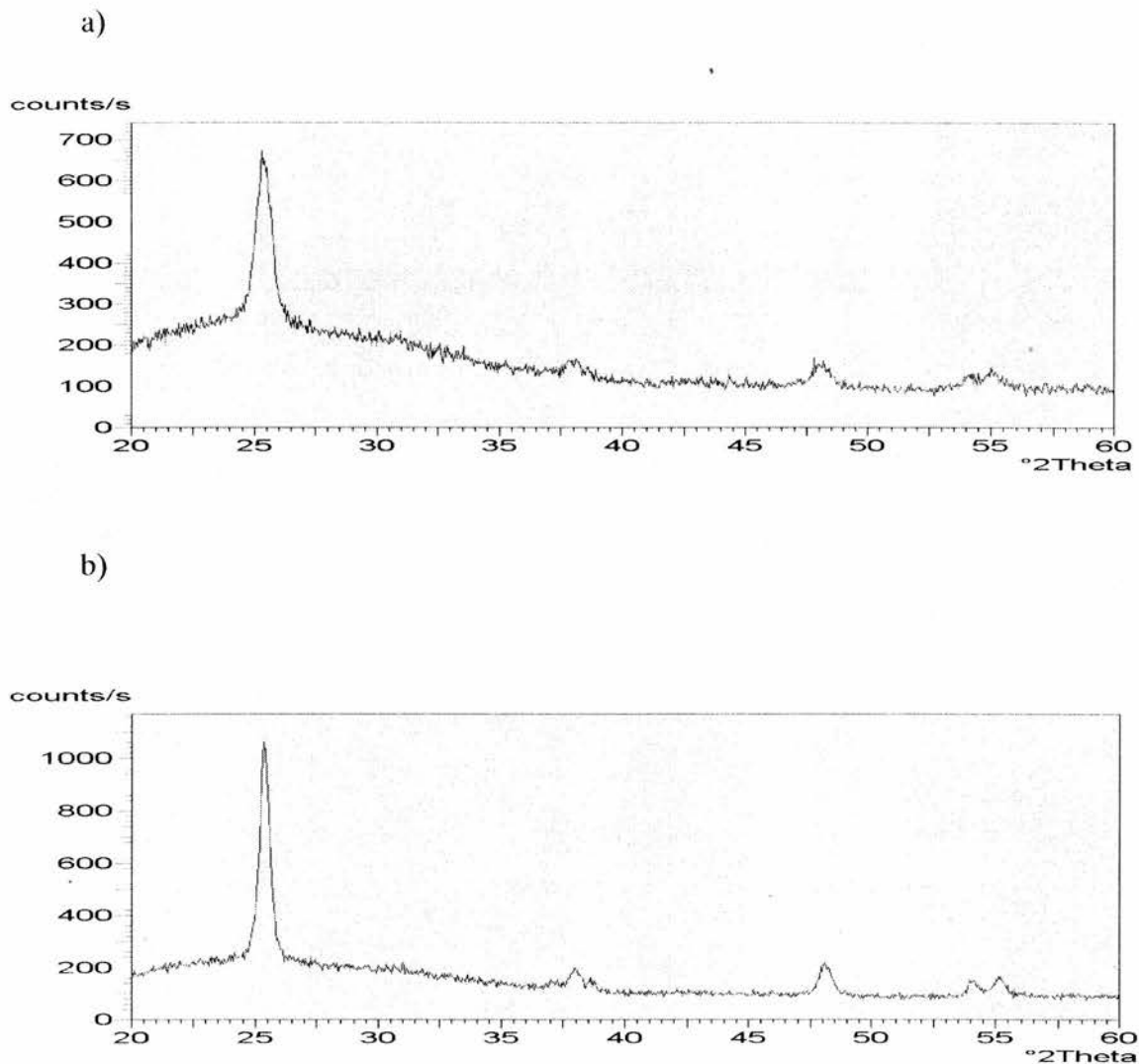
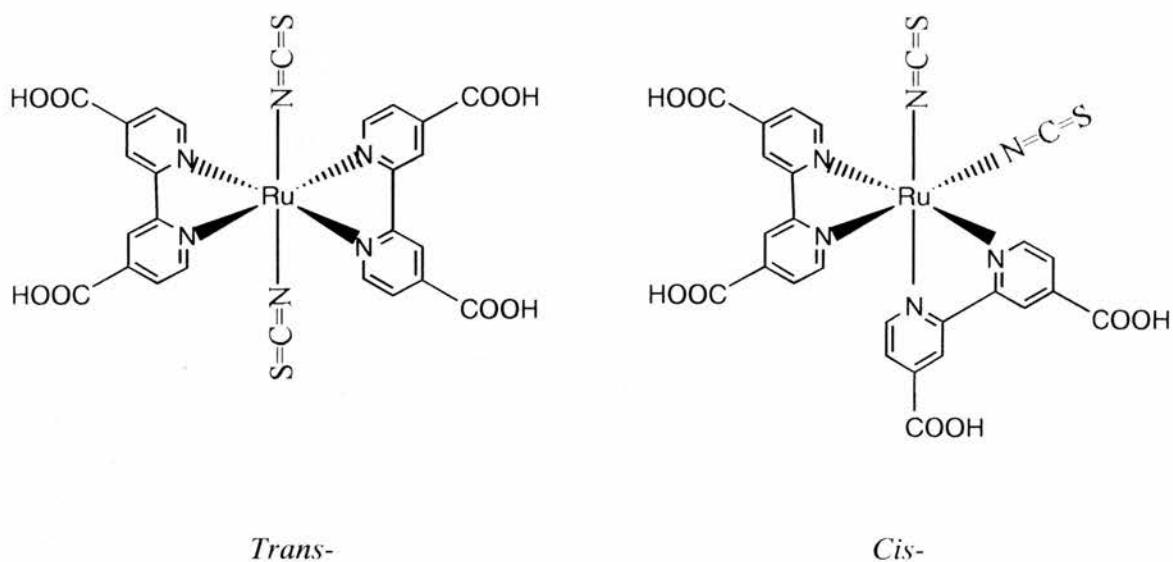


Fig. 2. 10. X-ray diffraction pattern for nanocrystalline titanium dioxide colloids after autoclaving at 220⁰C for 12h and then heated at the temperature of 450⁰C for 1h. All peaks in the XRD pattern can be identified as the anatase crystal phase of titanium, which is the product of the hydrolysis of titanium isopropanol on a) acidic, b) basic condition.

Synthesis of the dye sensitizers

The dye sensitizer Ru(4,4'-dicarboxy-2,2'-bipyridine) obtained was a mixture of *cis*- and *trans*- two isomers, however, with *cis*-Ru(dcbpy)₂(SCN)₂ as a dominated product after refluxing Ru(dcbpy)₂Cl₂ with KSCN in DMF for 8 h.



The structure and the ratio of the isomers were determined by ¹H NMR spectroscopy. As we can see, for the *trans*-isomer, with all the pyridines facing each other, the chemical shifts surroundings for the protons of each pyridine ring is the same. The pyridyl groups of the *cis*-isomer, however, are different story, with one facing another pyridine ring, and the other facing the thiocyanato group. The ¹H NMR spectrum of the dye is shown in Fig. 2.11, and the ratio of the *cis*- and *trans*- isomers was calculated from the integration of the protons (about *cis* : *trans* = 19:1). The H₆ of the pyridine rings facing the thiocyanate can have a difference of the chemical shift up to 1.84 ppm from H₆ of the pyridine rings facing each other.

In addition, there are two possibilities in the way the thiocynato group could be bonded to the ruthenium center. It could be either nitrogen bonded or sulfur bonded. The structure was determined by IR spectroscopy, with a characteristic peak at 2110 cm⁻¹ for the N-bonded isomer and 2050 cm⁻¹ for the S-bonded.¹³ Our sample has a dominant peak at 2110 cm⁻¹ with a shoulder at 2050 cm⁻¹ (page 102), indicating that the N-bonded thiocyanate is the thermodynamically favoured form.

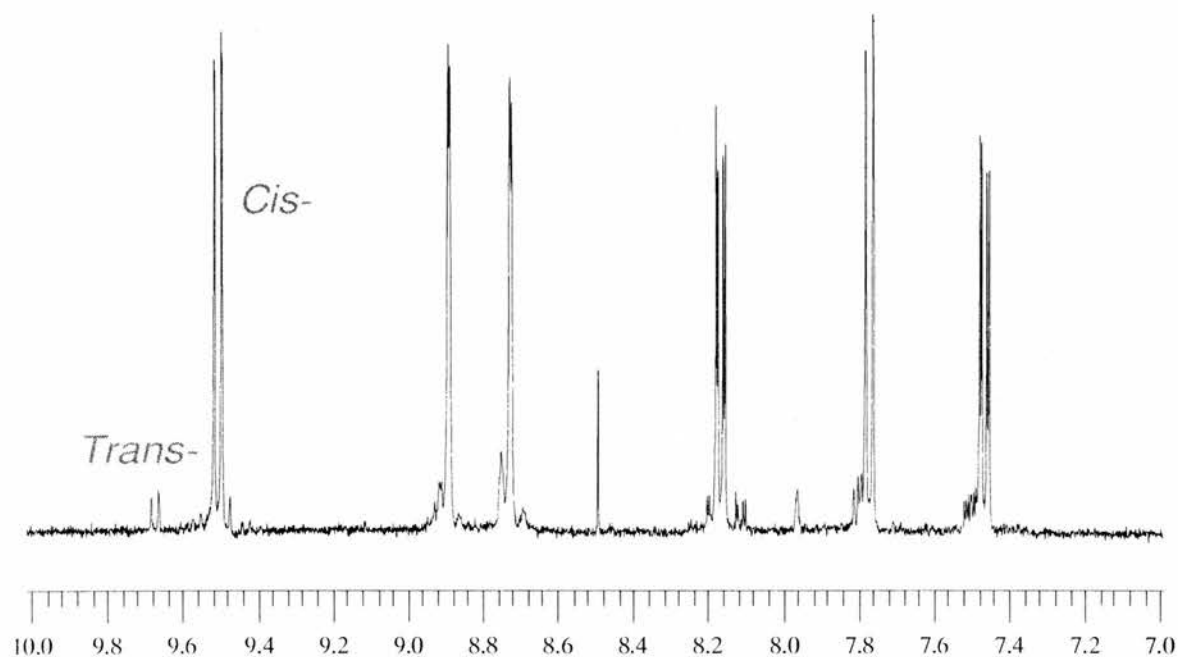


Fig. 2. 11. ¹H NMR spectrum of (4,4'-dicarboxy-2,2'-bipyridine)₂Ru(SCN)₂ measured in D₂O / NaOD

2.7.2. Electronic Absorption Spectra

In general, a good dye sensitizer should act alike a black body, that is, absorb light of almost the whole spectrum region. Fortunately, the standard dye Ru(dcbpy)₂(SCN)₂

has optimal absorbance at the wavelength of both 410 nm ($\epsilon = 0.95 \times 10^4 \text{ M}^{-1} \text{ cm}^{-1}$, MLCT), 558 nm ($\epsilon = 1.00 \times 10^4 \text{ M}^{-1} \text{ cm}^{-1}$, MLCT), which almost covers the whole visible light region. (Fig. 2.12) The most intense transition is found at ca. 320 nm, with molar absorbance of up to $58,400 \text{ M}^{-1} \text{ cm}^{-1}$. This transition is assigned to a ligand (dcbpy) based $\pi \rightarrow \pi^*$ process, since the free ligand shows a transition at the same energy. Two MLCT bands, $\text{Ru}(d_\pi) \rightarrow \text{dcbpy}(\pi^*)$, of almost identical intensity, shape and absorbance are found in the visible region. The observation of two bands is a result of the energetic closeness of the π_1^* and π_2^* dcbpy orbitals. The band at lower energies is a $d \rightarrow \pi_1^*$ transition; the band at higher energies is the direct $d \rightarrow \pi_2^*$ transition into the next higher unoccupied orbital.⁸⁵

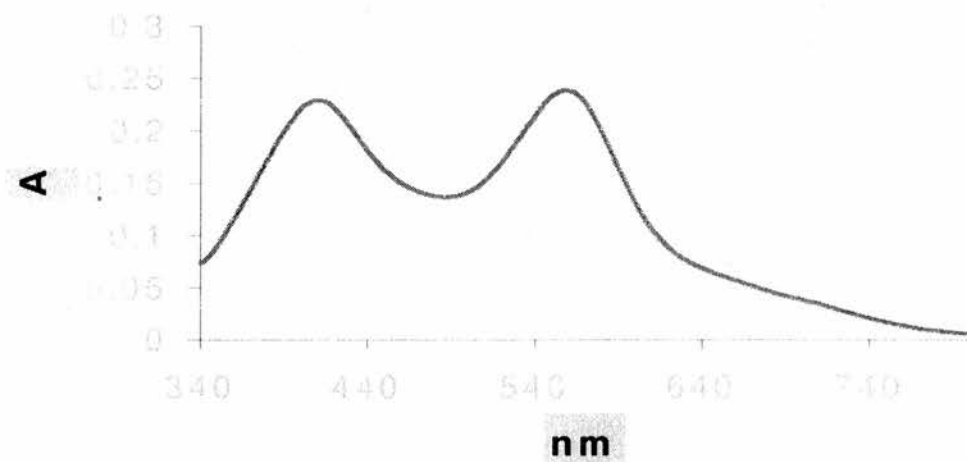


Fig. 2.12. UV-Vis spectrum of $\text{Ru}(\text{dcbpy})_2(\text{SCN})_2$ measured in methanol

2.7.3 Electrochemistry

a) Oxidation of Ru(dcpv)₂Cl₂

Voltammetric data obtained for the oxidation of Ru(dcpv)₂Cl₂ complex in DMF at a platinum electrode with Bu₄NPF₆ (0.1 M) as the supporting electrolyte are summarized in Table 2.1. A reversible and an irreversible oxidation process of the metal center were observed, which could be assigned to the oxidation of Ru²⁺ / Ru³⁺ and Ru³⁺ / Ru⁴⁺ respectively.

Table 2.1. Voltammetric data obtained for the oxidation of Ru(dcpv)₂Cl₂ complex in DMF at a platinum electrode. (ν = scanning rate, E_p = peak potential, $\Delta E_p = E_p^{ox} - E_p^{red}$, $E_{1/2} = E_p^{ox} + E_p^{red}$).

Cyclic voltammetry					
ν / mVs^{-1}	$E_p^{ox} / \text{mV (1)}$	E_p^{red} / mV	$\Delta E_p / \text{mV}$	$E_{1/2} / \text{mV}$	$E_p^{ox} / \text{mV (2)}$
20	196	128	68	162	666
40	196	130	66	163	635
80	198	128	70	163	666
100	202	130	72	166	678
200	202	122	80	162	748

As it is shown in Fig. 2.13, the first voltammetric oxidation of Ru(dcpy)₂Cl₂ represents an almost ideal example of a chemically and electrochemically reversible process, while further oxidation of the dye become irreversible:

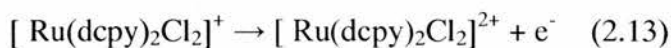


Fig. 2.13 shows that a series of cyclic voltammograms carried out in DMF on a platinum working electrode as a function of scanning rate (ν). As expected for a reversible process, the $E_{1/2}$ value is independent of the scan rates.

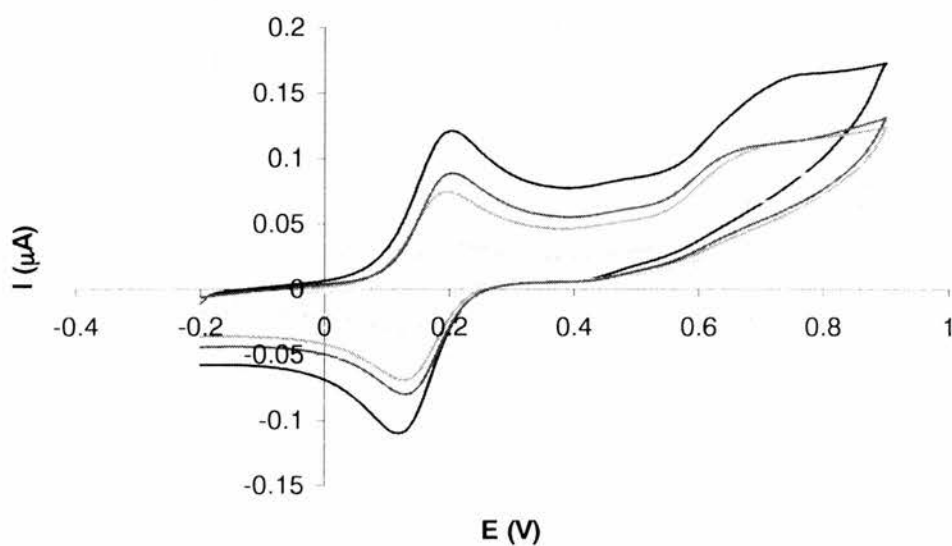


Fig. 2.13. Oxidation of 0.5 mM Ru(dcpy)₂Cl₂ in DMF at a platinum electrode as a function of scan rate ($\nu = 20, 40, 80, 100, 200 \text{ mVs}^{-1}$ respectively).

b) Oxidation of Ru(dcpy)₂(SCN)₂

The oxidation process of Ru(dcpy)₂(SCN)₂ at a platinum electrode in DMF, however, is irreversible, when carried out at a scanning rate of 100 mVs⁻¹. Nazceruddin¹³ *et al.* have reported a value for the standard potential for oxidation of Ru(dcpy)₂(SCN)₂ of +0.85V vs. SCE (corrected to +0.47V vs. Fc/Fc⁺) in acetonitrile. Furthermore, he pointed out that the oxidation process was described as highly reversible, indicating high stability of the oxidized sensitizer, at least on the cyclic voltammetric time scale.

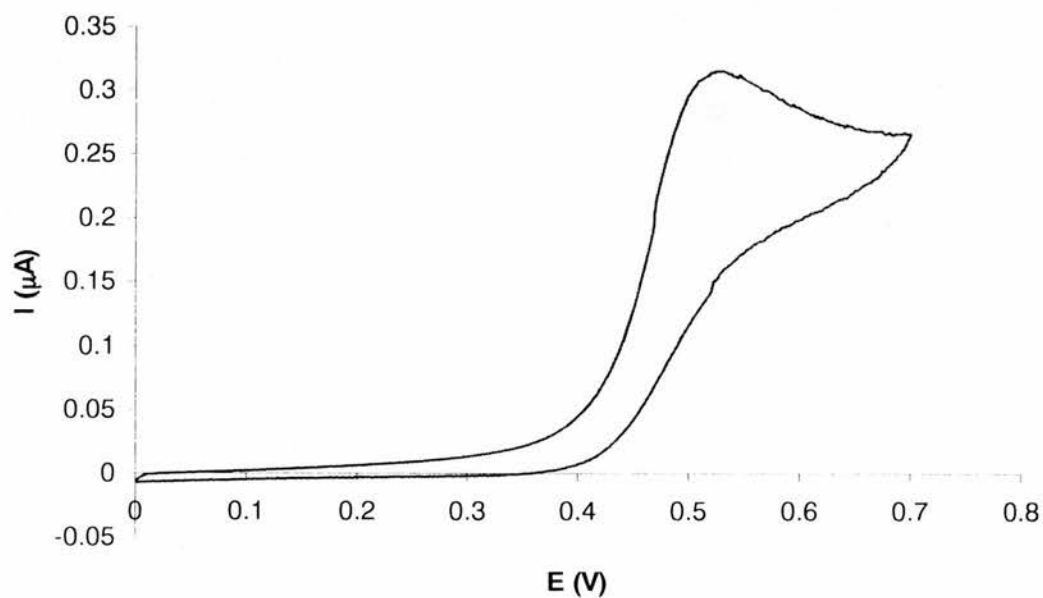


Fig. 2.14. Oxidation of 0.5 mM Ru(dcpy)₂(SCN)₂ in DMF at a platinum electrode, scan rate was $v = 100 \text{ mVs}^{-1}$.

Pure Ru(dcpy)₂(SCN)₂, however, was sparsely dissolvable in MeCN, the concentration of the final solution falls in the region of 10⁻⁴ to 10⁻⁵ M. The E_{1/2} value of this oxidation process was found to be +0.467 V vs. F_c⁺/F_c, which agrees with the data that obtained by Nazeeruddin.¹³

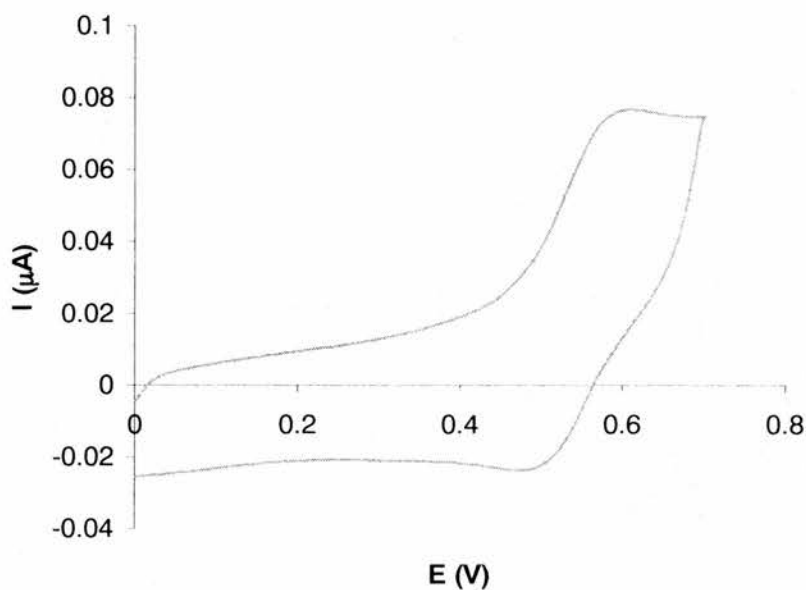


Fig. 2.15. Cyclic voltammetric oxidation of Ru(dcpy)₂(SCN)₂ in MeCN at a platinum electrode, scan rate was $\nu = 100 \text{ mVs}^{-1}$.

c) Reduction of Ru(dcpy)₂(SCN)₂

Two well defined processes of were observed in the cyclic voltammetric reduction of Ru(dcpy)₂(SCN)₂ in DMF at a platinum electrode with E_{1/2} = -1.11 and -1.15 V respectively, corresponding to the reduction of the two dcpy's of the complex.

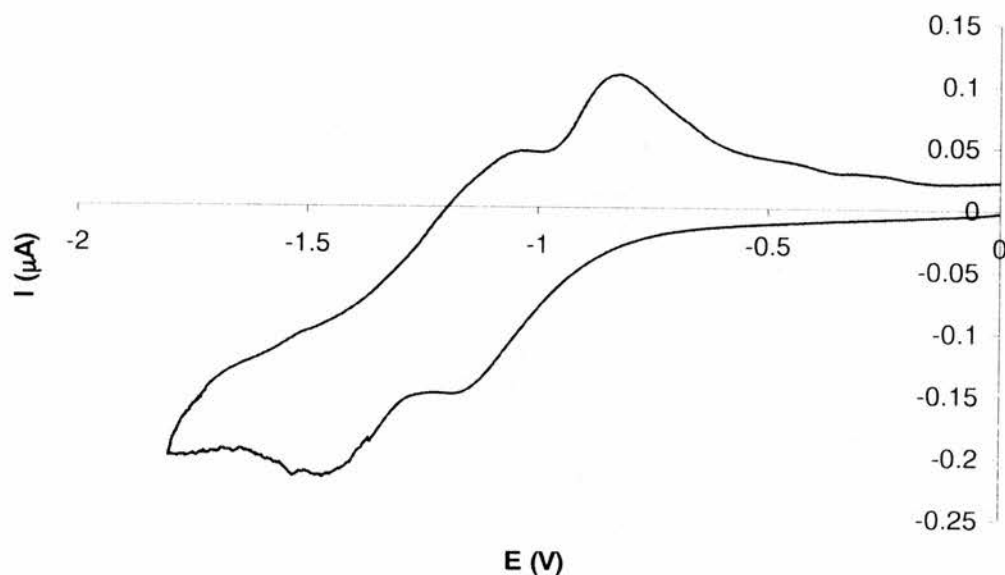
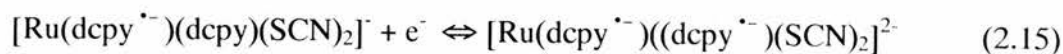
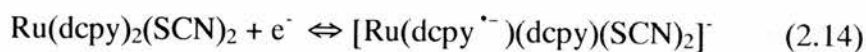


Fig. 2.16 Reduction of 0.5 mM Ru(dcpv)₂Cl₂ in DMF at a platinum electrode, scan rate was 100 mVs⁻¹.

2.7.4 Surface Chemistry

1) IR spectroscopy

When absorbed on the TiO₂ surface, the binding group and the surface form an ester bond which is indicated by the infrared resonance spectroscopy at 1616 cm⁻¹ and 1728 cm⁻¹ (ν CO₂), as shown in Fig 2.17.

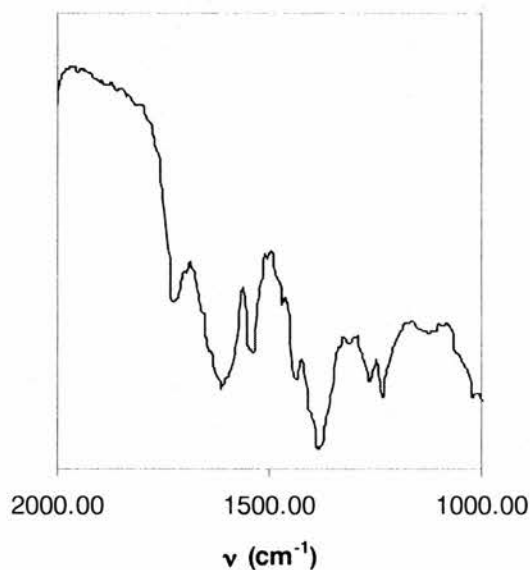


Fig. 2.17 *Infrared spectrum of Ru(dcpy)₂(SCN)₂ on TiO₂ semiconductor electrode*

2) *UV-Vis absorption*

According to Goodenough,⁸⁵ when the dehydrative coupling reaction between the sensitizer happens, 4,4'-dicarboxyl-2,2'-bipyridine for example, the surface hydroxyl groups on rutile TiO₂ would yield a ester linkage on the surface with enhanced electronic coupling between the π^* orbital of the bipyridine ring and the Ti 3d orbital manifold of the semiconductor.

Comparing with the electronic absorption of the dye in free solution, the two MLCT transitions overlap from 350 nm to 600 nm when it is coated with the semiconductor electrode. It looks more like the IPCE spectrum,¹³ indicating that the light absorption improvement in the whole visible light region when the dye is bound to the surface.

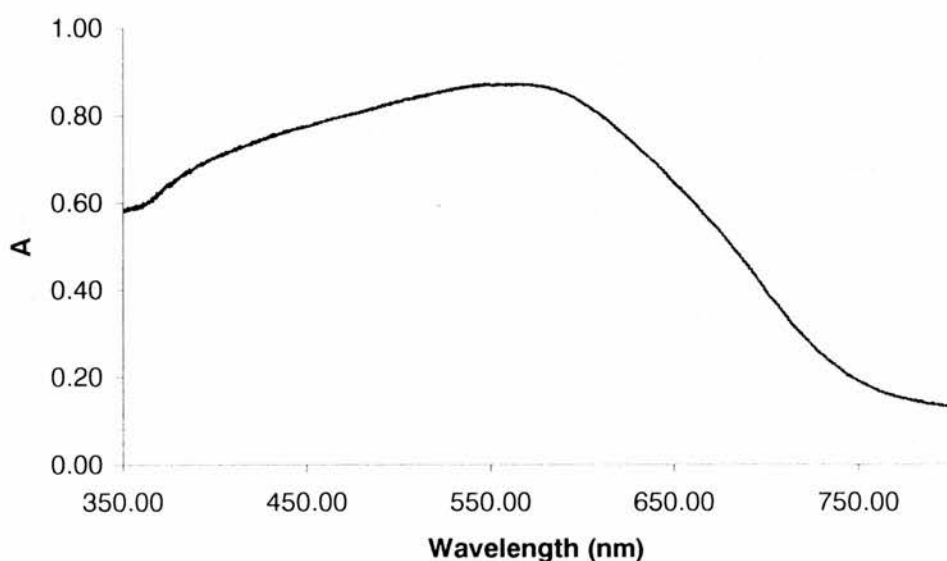


Fig. 2.18 *UV-Vis absorption of Ru(dcpy)₂(SCN)₂ on TiO₂ semiconductor electrode, measured in ethanol at 25 °C*

2.7.5 Solar Cell Performance

The general procedure for constructing the cell was similar to previously reported methods.³ It is important to correct the IPCE for the light harvesting efficiency (see below), and then to correct for the absorption of the ITO and the electrolyte.

As we discussed before, the efficiency of the solar cell is often measured by the incident photon to current conversion efficiency (IPCE), the ratio of the number of electrons flowing through the external circuit to the number of incident photons. For a given area of cell the IPCE can then be expressed as follows:

$$IPCE = 1250 i_{\text{corrected}} (\mu\text{A}) / [\lambda (\text{nm}) P(\mu\text{W})] \quad (2.16)$$

Where I_{corr} is the dark-current corrected maximum (short-circuit) photocurrent at and P is the incident light intensity. The IPCE tested is shown below. The result (37% maximum at 545 nm) was not as good as expected by building the test equipment in the Physics, St Andrews, comparing with that (85% at 560 nm) achieved in Grätzel¹³ research group. Corrections due to reflection losses etc may be required. Further experiments will be carried out in Imperial College, London.

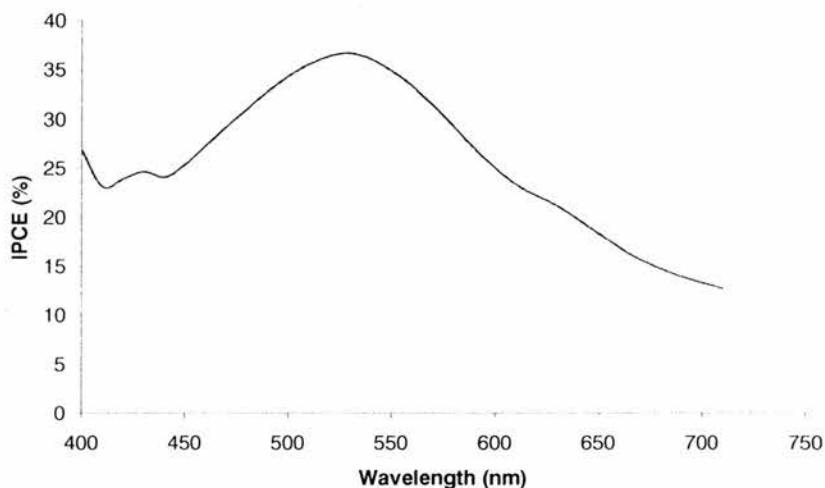


Fig. 2.19 IPCE spectrum of $Ru(dcpy)_2(SCN)_2 TiO_2$ semiconductor solar cell, $V_{oc} \approx 500$

$mV, I_{sc} \approx 200\mu A.$

2.8 CONCLUSIONS

In this chapter, Ru(dcpy)₂(SCN)₂ was synthesized and its electronic absorption and electrochemical behaviours have been discussed. Solar cell based on this dye and TiO₂ semiconductor has been built up and its performance has been tested. Ru(dcpy)₂(SCN)₂ is quite stable and inert to the air and moisture so the solar cells with such a dye are capable of different uses and will have long life circles.

2.9 REFERENCES:

1. G. Tollin, *J. Phys. Chem.*, 1976, **80**, 2274.
2. M. Almgren, *Photochem. Photobio.*, 1978, **27**, 603.
3. M. Calvin, *Acc. Chem. Res.*, 1978, **11**, 369.
4. D. G. Whitten, *Acc. Chem. Res.*, 1980, **13**, 83.
5. K. I. Zamaraeu and V. N. Parmon, *Russ. Chem. Rev.*, 1980, **49**, 695.
6. M. Grätzel, *Acc. Chem. Res.*, 1981, **14**, 376.
7. J. H. Fendler, *J. Phys. Chem.*, 1985, **89**, 2730.
8. B. O'Regan and M. Gratzel, *Nature*, 1991, **353**, 737.
9. J. DeSilvestro, M. Grätzel, L. Kavan, J. Moser and J. Augustynski, *J. Am. Chem. Soc.*, 1985, **107**, 2988.
10. P. Liska, N. Vlachopoulos, M. K. Nazeeruddin, P. Comte and M. Grätzel, *J. Am. Chem. Soc.*, 1988, **110**, 3686.
11. N. Vlachopoulos, P. Liska, J. Augustynski and M. Grätzel, *J. Am. Chem. Soc.*, 1988, **110**, 1216.
12. M. K. Nazeeruddin, P. Liska, J. Moser, N. Vlachopoulos and M. Grätzel, *Helv. Chim. Acta.*, 1990, **73**, 1788.
13. Md. K. Nazeeruddin, A. Kay, I. Rodicio, R. Humphry-Baker, E. Muller, P. Liska, N. Vlachopoulos and M. Grätzel, *J. Am. Chem. Soc.*, 1993, **115**, 6383.
14. K. Kalysnasundaram, M. K. Nazeeruddin, M. Grätzel, G. Viscardi, P. Savarino and E. Barni, *Inorg. Chim. Acta.*, 1992, **198**, 831.

15. K. Matsui, M. K. Nazeeruddin, R. Humphry-Baker, M. Grätzel and K. Kalysnasundaram, *J. Phy. Chem.*, 1992, **96**, 10590.
16. O. Kohle, S. Ruile and M. Grätzel, *Inorg. Chem.*, 1996, **35**, 4779.
17. S. Ruile, O. Kohle, P. Péchy and M. Grätzel, *Inorg. Chim. Acta.*, 1997, **261**, 129.
18. R. Amadelli, R. Argazzi, C. A. Bignozzi and F. Scandola, *J. Am. Chem. Soc.*, 1990, **112**, 7099.
19. R. Argazzi, C. A. Bignozzi, T. A. Heimer, F. N. Castellano and G. J. Meyer, *Inorg. Chem.*, 1994, **33**, 5741.
20. M. K. Nazeeruddin, S. M. Zakeeruddin, R. Humphry-Baker, S. I. Gorelsky, A. B. P. Lever and M. Grätzel, *Coord. Chem. Rev.*, 2000, **208**, 213.
21. T. Renouard and M. Grätzel, *Tetrahedron*, 2001, **57**, 8145.
22. M. K. Nazeeruddin, P. Péchy, T. Renouard, S. M. Zakeeruddin, R. Humphry-Baker, P. Comte, L. Cevey, E. Costa, V. Shklover, L. Spiccia, G. B. Deacon, C. A. Bignozzi and M. Grätzel, *J. Am. Chem. Soc.*, 2001, **123**, 1613.
23. G. Redmond, D. Fitzmaurice and M. Grätzel, *Chem. Mater.*, 1994, **6**, 686.
24. H. Rensmo, K. Keis, and H. Lindström, *J. Phys. Chem.* 1997, **101B**, 1598. (X)
25. D. Liu, G. Hug and P. V. Kamat, *J. Phys. Chem.*, 1995, **99**, 16768.
26. C. Nasr, D. Liu, S. Hotchandani and P. V. Kamat, *J. Phys. Chem.*, 1996, **100**, 11054.
27. P. V. Kamat, I. Bedja, S. Hotchandani and L. K. Patterson, *J. Phys. Chem.*, 1996, **100**, 4900.

28. R. Argazzi, C.A. Bignozzi, T.A. Heimer, F.N. Castellano and G.J. Meyer, *J. Am. Chem. Soc.*, 1995, **117**, 11815.
29. L. Kavan, P. Krtil and M. Grätzel, *J. Electroanal. Chem.*, 1994, **373**, 123.
30. L. Kavan, M. Grätzel, J. Rathousky and A. Zukal, *J. Electrochem. Soc.*, 1996, **143**, 394.
31. R. Knödler, J. Sopka, F. Harbach and H.W. Grünling, *Sol. Energy Mater. Sol. Cells*, 1993, **30**, 277
32. V. Shklover, M. K. Nazeeruddin, S.M. Zakeeruddin, C. Barbe, A. Kay, T. Haibach, W. Steurer, R.Hermann, H.U. Nissen and M. Grätzel, *Chem. Mater.*, 1997, **9**, 430.
33. F. Cao, G. Oskam, G.J. Meyer and P.C. Searson, *J. Phys. Chem.*, 1996, **100**, 17021.
34. F. N. Castellano, J.M. Stipkala, L.A. Friedman and G.J. Meyer, *Chem. Mater.*, 1994, **6**, 2123.
35. J. B. Goodenough, in "*Solid State Chemistry: A Contemporary Overview*", chapter 6, 113-137, editor: S.L. Holt, J.B. Milstein and M. Robbins, *Advances in Chemistry Series*, American Chemical Society, Washington, D.C., 1980.
36. A. Hagfeldt and M. Grätzel, *Chem. Rev.*, 1995, **95**, 49.
37. K. Kalyanasundaram and M. Grätzel, *Coord. Chem. Rev.*, 1998, **77**, 347.
38. G. Smestad, C. Bignozzi and R. Argazzi, *Sol. Energy Mater. Sol. Cells*, 1994, **32**, 259.
39. H. Tsubomura, M. Matsumura, Y. Nomura and T. Amamiya, *Nature (London)*, 1976, **261**, 402.

40. H. D. Abruña, A.Y. Teng, G.J. Samuels and T.J. Meyer, *J. Am. Chem. Soc.*, 1979, **101**, 6745.
41. S. Chardonnoibat, S. Cosnier, A. Deronzier and N. Vlachopoulos, *J. Electroanal. Chem.*, 1993, **352**, 213.
42. T. Ohta, *Photochemical Hydrogen Production*, Press Ltd., Oxford, 1979, 115.
43. W.E. Ford, J.M. Wessels and M.J. Rodgers, *J. Phys. Chem. B*, 1997, **101**, 7435.
44. F.N. Castellano, T.A. Heimer, M.T. Tandhasetti and G.J. Meyer, *Chem. Mater.*, 1994, **6**, 1041.
45. F.N. Castellano and G.J. Meyer, *J. Phys. Chem.*, 1995, **99**, 14742.
46. J. Ferguson, A.W.H. Mau and W.H.F. Sasse, *Chem. Phys. Lett.*, 1979, **68**, 21
47. P.A. Lay and W.H.F. Sasse, *Inorg. Chem.*, 1984, **23**, 4123.
48. K. Murakoshi, G. Kano, Y. Wada, S. Yanagida, H. Miyazaki, M. Matsumoto and S. Murasawa, *J. Electroanal. Chem.*, 1995, **396**, 27.
49. C. A. Bignozzi, R. Argazzi, J. R. Schoonover, K. C. Gordon, R. B. Dyer and F. Scandola, *Inorg. Chem.*, 1992, **31**, 5260.
50. M. Alebbi, C. A. Bignozzi, T. A. Heimer, G. M. Hasselmann and G. J. Meyer, *J. Phys. Chem. B*, 1998, **102**, 7577.
51. R. J. Ellingson, J. B. Asbury, S. Ferrere, H. N. Ghosh, J. R. Sprague, T. Q. Lian and A. J. Nozik, *J. Phys. Chem. B*, 1998, **102**, 6455.
52. S. Y. Huang, G. Schlichthorl, A. J. Nozik, M. Grätzel and A. J. Frank, *J. Phys. Chem. B*, 1997, **101**, 2576.
53. L. Kavan, M. Grätzel, S.E. Gilbert, C. Klemenz and H. J. Scheel, *J. Am. Chem. Soc.*, 1996, **118**, 6716.

54. H. Sugihara, L. P. Singh, K. Sayama, H. Arakawa, M. K. Nazeeruddin and M. Grätzel, *Chem. Lett.*, 1998, **10**, 1005.
55. M. K. Nazeeruddin, P. Péchy and M. Grätzel, *J. Chem. Soc., Chem. Commun.*, 1997, **18**, 1705.
56. S. M. Zakeeruddin, M. K. Nazeeruddin, P. Pechy, F. P. Rotzinger, R. Humphry-Baker, K. Kalyanasundaram, M. Grätzel, V. Shklover and T. Haibach, *Inorg. Chem.*, 1997, **36**, 5937.
57. M. K. Nazeeruddin, E. Muller, R. Humphry-Baker, N. Vlachopoulos and M. Grätzel, *J. Chem. Soc., Dalton Trans.*, 1997, **23**, 4571.
58. H. Nusbaumer, J. E. Moser, S. M. Zakeeruddin, M. K. Mohammad, K. Nazeeruddin and M. Grätzel, *J. Phys. Chem. B*, 2001, **105**, 10461.
59. Y. I. Kim, S. J. Atherton, E. S. Brigham and T. E. Mallouk, *J. Phys. Chem.*, 1993, **77**, 11802.
60. W. J. Dressick, T. J. Meyer, B. Durham and D. P. Rillema, *Inorg. Chem*, 1982, **21**, 3451.
61. G. B. Saupe, T. E. Mallouk, W. Kim and R. H. Schmehl, *J. Phys. Chem. B*, 1997, **101**, 2508.
62. C. Nasr, S. Hotchandani and P. V. Kamat, *J. Phys. Chem. B*, 1998, **102**, 4944.
63. D.F. Shriver, P.W. Atkins and C.H. Langford, "*Inorganic Chemistry*", 2nd ed., Oxford University Press, 1996.
64. H. Frei, D. J. Fitzmaurice and M. Grätzel, *Langmuir*, 1995, **11**, 4193.
65. K. Kalyanasundaram and M. K. Nazeeruddin, *Chem. Phys. Lett.*, 1992, **193**, 292.

66. T. J. Meyer, *Acc. Chem. Res.*, 1989, **22**, 163.
67. D. N. Furlong, D. Wells and W. H. F. Sasse, *J. Phys. Chem.*, 1986, **90**, 1107.
68. N. Nakashima, K. Yoshihara and F. Willig, *J. Chem., Phys.*, 1980, **73**, 3553.
69. F. Willig, R. Eichberger, N. S. Sundaresan, B. A. Parkinson, *J. Am. Chem. Soc.*, 1993, **115**, 1930.
70. Y. Tachibana, J. E. Moser, M. Grätzel, D. R. Klug and J. M. Durrant, *J. Phys. Chem.*, 1996, **100**, 20056.
71. I. Martini, J. H. Hodak, G. V. Hartland, *J. Phys. Chem.*, 1998, **102B**, 607.
72. A. Kay, R. Humphry-Baker and M. Grätzel, *J. Phys. Chem.*, 1994, **98**, 952.
73. B. O'Regan, J. Moser, M. A. Anderson and M. Grätzel, *J. Phys. Chem.*, 1990, **94**, 8720.
74. T. Hannappel, B. Burfeindt, W. Storck, F. Willig, *J. Phys. Chem.*, 1997, **101B**, 6799.
75. J. E. Moser and M. Grätzel, *Chimia*, 1998, **52**, 160.
76. J. E. Moser and M. Grätzel, *Chem. Phys.*, 1993, **176**, 493.
77. J. S. Salassky, W. H. Lubberhuizen, E. Van Faassen and R. E. I. Schropp, *J. Phys. Chem.*, 1997, **101B**, 766.
78. B. O'Regan and D. T. Schwartz, *Chem. Mater.*, 1996, **7**, 1349.
79. K. Murakoshi, R. Kogure, Y. Wada, S. Yanagida, *Chem. Lett.*, 1997, 471.
80. N. Garelli, P. Vierling, *J. Org. Chem.*, 1992, **57**, 3046.
81. S. D. Burunside, V. Shklover, C. Barbe, P. Comte, F. Arendse, K. Brooks, M. Grätzel, *Chem. Mater.* 1998, **10**, 2419.
82. G. P. Semestad, M. Grätzel, *J. Chem. Edu.*, 1998, **75(6)**, 752.
83. G. Navon and N. Sutin, *Inorg. Chem.*, 1974, **13**, 2159.

84. M. G. Posse, N. E. Katz, L.M. Baraldo, D. D. Polonuer, C. G. Colombano and J. A. Olabe, *Inorg. Chem.*, 1995, **34**(7), 1830.
85. S. Anderson, E. C. Constable, M. P. Dare-Edwards, J. B. Goodenough, A. Hamnett, K. R. Seddon and R. D. Wright, *Nature*, 1979, **280**, 571.

CHAPTER THREE

Ruthenium Complexes of Polypyridyl Benzimidazole

3.1 INTRODUCTION

Dye-sensitizers for solar cells have focused on the ruthenium complexes of bipyridyl¹⁻⁸ and terpyridyl⁹⁻¹³ ligands. The photophysical and photochemical properties of group (VIII, 8) metal complexes using those ligands have been thoroughly investigated during the last three decades.^{14, 15} The main thrust behind these studies is to understand the energy and electron transfer processes in the excited state and to apply this knowledge to potential practical applications such as solar energy conversion. Ruthenium(II) complexes containing 4,4'-dicarboxy-2,2'-bipyridyl ligand have been used extensively as charge-transfer sensitizers on nanocrystalline TiO₂ films. The photoexcitation of the metal-to-ligand charge transfer (MLCT) of the absorbed dye leads to injection of electrons into the conduction band. The efficiency of this electron transfer process has been reported to be 95% for monochromatic light.³

The MLCT transitions of the polypyridyl complexes of ruthenium can be tuned by introducing a ligand with a low lying π^* molecular orbital such as 2,2'-biquinoline¹⁶ and 2,3-dipyridylpyrazine.¹⁷ A very good example is the very efficient electronic coupling between the π^* orbital of the dcbpy (4,4'-dicarboxy-2,2'-bipyridyl) ligand and the 3d orbital of the TiO₂ semiconductor.¹⁸ Near-unity incident photon-to-current conversion

efficiency (IPCE) of these complexes was achieved. In ruthenium(II) complexes containing such ligands the MLCT transitions are considerably red shifted, thus absorbing more of the visible solar spectrum. Another way to achieve this goal is to destabilize the metal t_{2g} orbital with a stronger donor ligand. With suitable ligands it is possible to shift the metal-centred oxidation potential in such complexes over a range of 1 V.¹⁹ Excessive tuning of the π^* and t_{2g} levels does not necessarily lead to a good sensitizer. This is because with a lower π^* energy, the excited state is not sufficiently energetic to enable electron transfer into the conduction band of the TiO₂ semiconductor. If the t_{2g} is raised too much, latter case the easily oxidized complex cannot be reduced back by a suitable electron relay such as the usual iodine/iodide couple (*see scheme 1, chapter 2, P₈₇*).

By employing the above-mentioned concepts, Meyer²⁰ and co-workers have tuned the MLCT transitions from *ca.* 450 nm to *ca.* 568 nm in ruthenium complexes containing three different bidentate ligands. However, there are only a few reports on MLCT and redox tuning of terpyridine and substituted terpyridine complexes of ruthenium. The main reason for such a limited study on terpyridine complexes is the lack of synthetic routes for substituted terpyridines and the short excited state lifetime of these complexes.²¹

Unlike the terpyridine ligand, 2-(2-pyridyl)benzimidazole acts as a hybrid ligand having present both a strong σ -donor (benzimidazole unit) and a π -acceptor (pyridine ring). Thus, by an appropriate choice of substituents on the uncomplexed imidazole nitrogen, it is now possible to tune the ground and excited state of the ligand to provide

the grafting functionalities to the oxides surface, ensuring intimate electronic coupling between the excited state of the sensitizer and the conduction band.

3.2 LIGAND MODIFICATION

The rapid development of both chemical sensors and non-linear optical materials will further increase the demand for ligands which do not only have the appropriate coordinative capabilities, but also allow for easy-to-achieve modifications by additional functionalities. For example, modifying ligands so as to induce self-assembly can form a phase boundary through which the back electron transfer might be impeded. Sprintschink et al. reported that such monolayer assemblies containing surfactant ester derivatives of $[\text{Ru}(\text{bpy})_3]^{2+}$ complex catalyzed the photo-dissociation of water.²²

As a consequence, a well-thought-of strategy for designing a particular class of ligands will from the very beginning incorporate a functionality that may serve as a linkage group. There have been reports of the modification of 2-(2-pyridyl)benzimidazole to give bridged derivatives (Fig. 3.1), *i.e.* 2,2'-bis(2-pyridyl)benzimidazole and 1,2-bis[2-(2-pyridyl)benzimidazolyl]ethane.²³ Coordination of the bridged ligands to two ruthenium(II) ions results in a low-energy shift and a shorter lifetime of the MLCT luminescence. The same spectroscopic shift in the ruthenium complexes was observed when the proton to the nitrogen of 2,6-bis(benzimidazol-2-yl)pyridine was replaced by a methyl or hexadecyl group.¹⁸

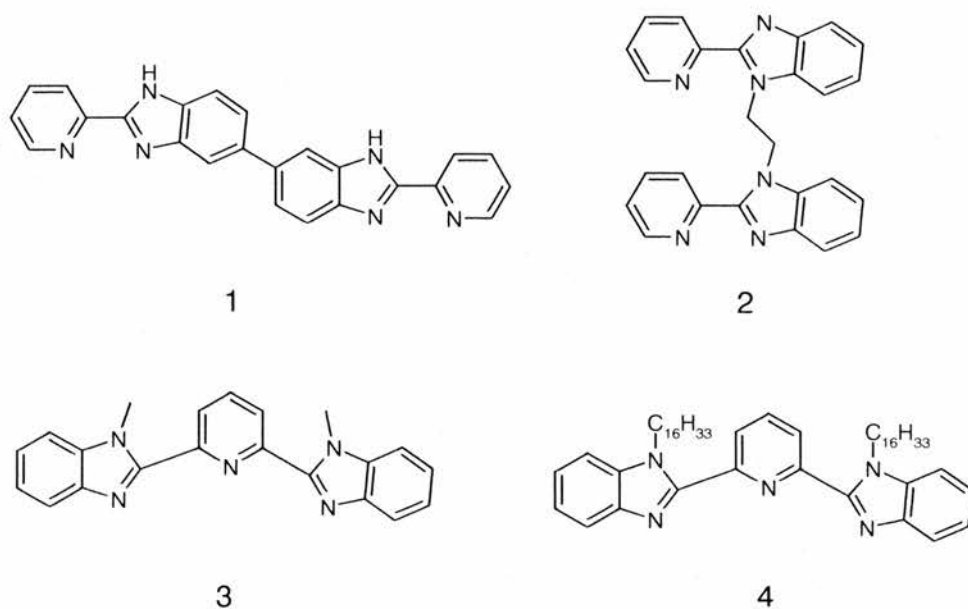
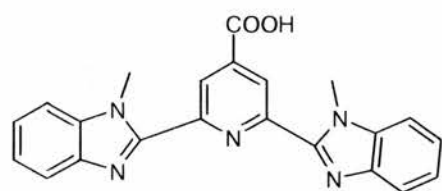


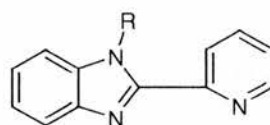
Fig. 3.1. (1) 2,2'-bis(2-pyridyl)benzimidazole, (2) 1,2-bis(2-(2-pyridyl)benzimidazolyl)ethane, (3) 2,6-bis(1-methylbenzimidazol-2-yl)pyridine, (4) 2,6-bis(1-hexadecylbenzimidazol-2-yl)pyridine

Complexes of such ligands cannot be attached to the surface of oxide semiconductors without further modification of the ligands or help from other ligands which bear a functional group such as carboxylic or phosphoric acid. These groups would most likely be introduced to the pyridyl ring of the imidazole derivatives, serving as the linkage between the dye sensitizer and the semiconductor. These groups also tune the ligand to have the properties of being both a strong σ -donor and a π -acceptor (the electron withdrawing effect of the carboxyl group, Fig. 3.2). In this chapter, we report the

ruthenium(II) complexes of modified benzimidazole ligands, in which the linkage was introduced at the uncomplexed benzimidazole nitrogen of the ligands.



5



6: R = CH₂COOH,

7: R = CH₂CH₂COOH

8: R = CH₂CH₂CH₂COOH

Fig. 3.2. (5) 2,6-bis(1-methylbenzimidazol-2-yl)-4-carboxypyridine, (6) 1-acetic-2-(2-pyridyl)benzimidazole, (7) 1-propionic-2-(2-pyridyl)benzimidazole, (8) 1-butyric-2-(2-pyridyl)benzimidazole

3.3 CHARGE SEPARATION

As we have mentioned before, when the dye connected to the semiconductor electrode absorbs a photon from sunlight, An electron is transferred from the ruthenium(II) center to the ligand (MLCT) and then pumped into the TiO₂ nanocrystalline electrode. As a result, the ruthenium(II) polypyridyl complex is oxidized to the ruthenium(III) oxidation state, which will be reduced again by iodide (I₃⁻) in the electrolyte to the ground state and the cycle is repeated. At the same time, it is possible that a back electron transfer process takes place either from the excited dye-sensitizer (S^{*})

or from the semiconductor electrode to the ground state of the dye (S_0), equations (3.3) and (3.4) respectively. These represent detrimental processes which may reduce the efficiency of a regenerative solar cell (Fig. 3.3).

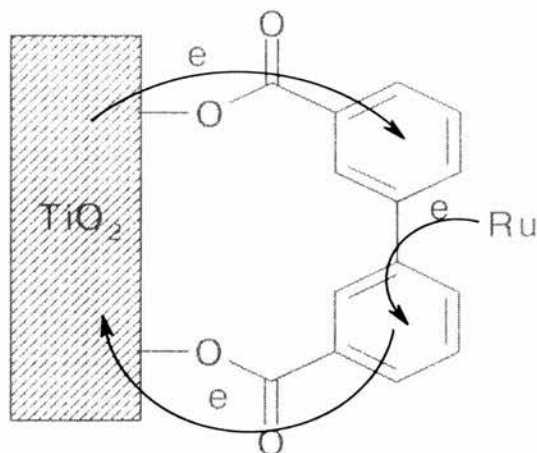
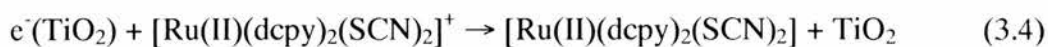
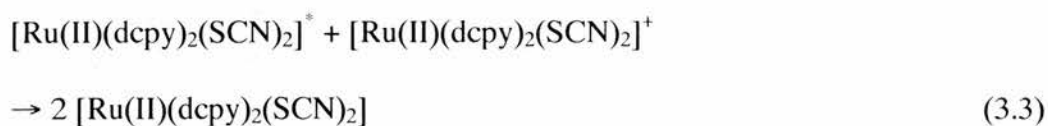
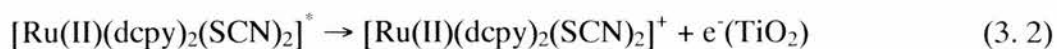


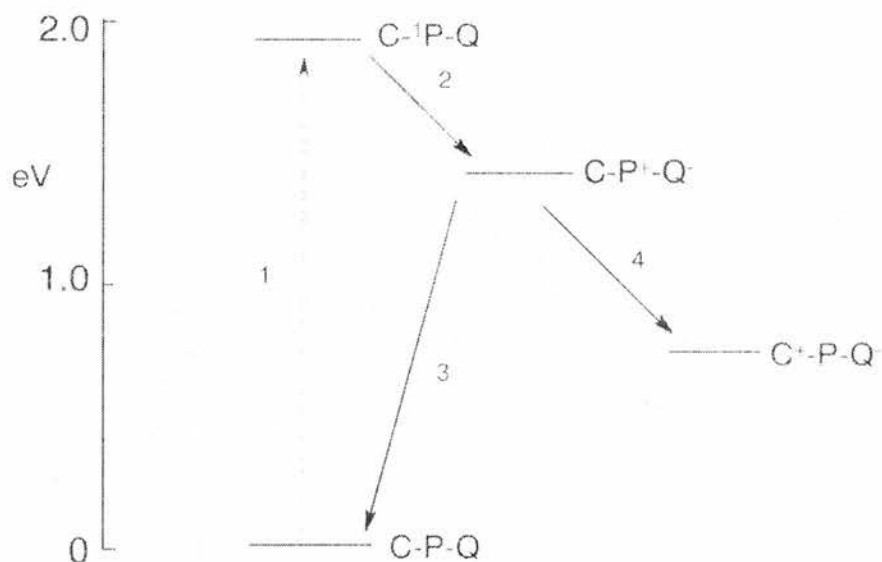
Fig. 3.3. An illustration of metal-to-ligand electron transfer (MLCT), electron collection of the semiconductor from the excited dye and back electron transfer process from the semiconductor to the dye sensitizer



In the natural photosynthesis system, one of the remarkable features of reaction centers is their ability to use excitation energy to quickly separate charge with high quantum yield over large distance, while retarding energy wasting charge recombination to the ground state. This is achieved at least in part by a multi-step electron-transfer sequence. Charge is separated by a series of short-range, fast and efficient electron-transfer steps to yield a final charge-separated state that is long-lived, because the negative and positive charges are spatially and electronically well isolated. For artificial photosynthetic applications, the importance of this charge-separation is that it provides a molecular basis for the conversion of photons into potential energy. The carotenoid-porphyrin-quinone(C-P-Q) system, for example, undergoes a photo-driven two-step electron transfer reaction which results in the generation of a high energy, charge-separated state with lifetimes on the microsecond time scale in a certain kind of situation.²⁴ This system mimics the initial charge separation steps of photosynthesis. Excitation of the porphyrin moiety yields the porphyrin first excited singlet state C^1P-Q (Scheme 3.1, step 1), which donates an electron to the quinone to produce an initial charge separated state $C-P^+-Q^-$ (step 2). This state has two possible pathways for decay. Charge recombination (step 3) is a facile reaction, which yields the ground state. Such back-electron-transfer reactions are to be avoided in photosynthesis or other energy conversion systems because they degrade the chemical potential stored in the charge-separated state to heat. In the triad, a second electron transfer reaction (step 4) competes with step 3 to yield a final charge-separated state C^+-P-Q^- . This state lives from hundreds of nanoseconds to microseconds. A lifetime on the microsecond time scale is long

enough to allow harvesting of the potential energy stored in the charge-separated state by reaction with other species in solution or at a phase boundary.²³

Scheme 3.1



A particular advantage of interfacial charge-separated states at semiconductor materials is that the injected electron can be collected as an electrical response. This forms the basis for new applications that exploit both the electronic and optical properties of the sensitized materials, such as charge storage, displays, chemical sensing and optical switching.

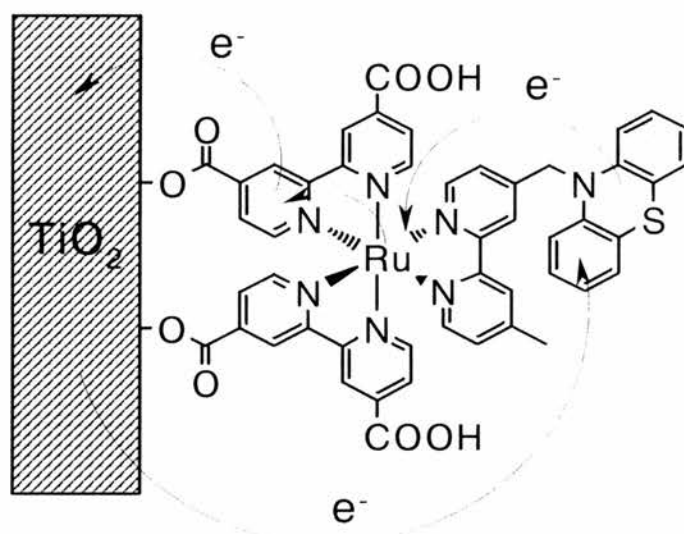


Fig. 3.4. Charge transfer process between the dye sensitizer $\text{Ru}(\text{dcpy})_2(\text{bpy-PTZ})$ and the TiO_2 semiconductor electrode.

To achieve a charge-separated state to improve the efficiency of energy transferring, some work has been done for slowing the charge recombination process.²⁵⁻²⁸ One strategy to increase charge-separation lifetimes is to explore the performance of a more complex molecular sensitizer with a covalently-bound electron donor to develop a clear picture of the interfacial electron transfer processes which dictate charge separation efficiencies. This strategy was explored with the sensitizer $\text{Ru}(\text{dcpy})_2(\text{bpy-PTZ})$,²⁶ where PTZ stands for phenothiazine, shown in Fig. 3.4. With both donors and acceptor present, this complex begins to mimic some of the functional elements of the reaction center of photosynthesis. It was reported that less than 20 ns after excitation of the surface-anchored $[\text{Ru}(\text{II})(\text{dcpy})_2(\text{bpy-PTZ})]$ sensitizer, an electron is injected into TiO_2 and the

PTZ group reduce the metal center. The net effect is to shift the hole from ruthenium to the pendant PTZ group by rapid intramolecular electron transfer. These excited electron-transfer reactions produce interfacial charge-separated pairs that are remarkably long-lived, $\text{TiO}_2(e^-)|\text{-Ru}^{\text{II}}\text{-PTZ}^+$, where the electron is in the conduction band of the solid and the hole is localized on PTZ.

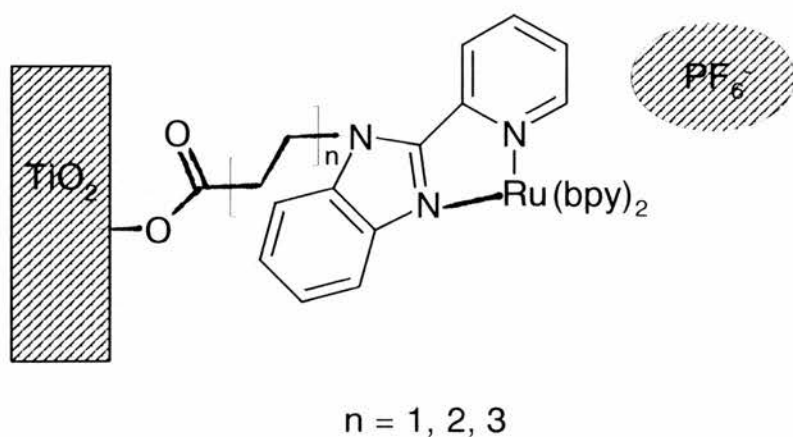


Fig. 3.5. The way the ruthenium(II) complexes of 2-(2-pyridyl)benzimidazole derivatives of different chain-length bind to the TiO_2 semiconductor electrode.

Another strategy is that the distance between the semiconductor electrode and the dye-sensitizer can be optimized by introducing a bridging group between them, *i.e.* $-\text{CH}_2$, or $-\text{C}_6\text{H}_4$. In such a way, a charge-separated state can also be achieved after an electron is injected from the donor to the acceptor. For this reason, we have developed a series of ruthenium polypyridyl complex with pyridylbenzimidazole derivatives of variable chain-

length, which introduce anchoring groups capable of attaching to the TiO₂ nanocrystalline electrode surface (Fig. 3. 5).

3.4 EXPERIMENTAL

Chemicals and materials RuCl₃ · 3H₂O (Aldrich), 2-(2-pyridyl)benzimidazole (Aldrich), 2,2'-bipyridine (Aldrich), ethyl bromoacetate (Aldrich), ethyl acrylate (Fluka), ethyl bromobutylate, butyllithium (Aldrich), tetra-*n*-butylammonium hexafluorophosphate (Fluka, electrochemical grade) and DMF (Aldrich) were used as they were received. THF was refluxed from potassium.

Measurements Cyclic voltammograms was recorded using an EG and G PARC 273 A potentiostat/galvanostat controlled by version 4.11 of the Electrochemistry Research Software running on a PC. All the experiments were carried out in degassed HPLC grade acetonitrile solution containing ruthenium complexes (5×10^{-4} M) and TBAP (0.1 M) as a supporting electrolyte. The measurement was carried out using a Pt wire as the counter electrode. The Reference electrode, separated from the voltammetric cell by a salt bridge, was Ag / AgNO₃ (0.01 M in CH₃CN). The electronic spectrum was recorded on Perkin-Elmer Lambda-14 UV-Vis spectrometer using 1 cm quartz cell.

Luminescence spectrometer Measurements are performed by exciting the sample with a brief light pulse. The apparatus consists of a light source (laser LED) which excites the sample at 390 nm. The sample re-radiates, and the light is detected at a

wavelength of 650 nm set by a mono-chromator. Signal from the excitation source begins to charge a capacitor within the time to amplitude converter (TAC). The fluorescence from the sample arrives at the photomultiplier tube at a later time, and stops the charging. The charge accumulated is converted directly into a potential difference and is now sent as a pulse to a multi channel analyser where it is allocated a channel related to its magnitude. This channel relates directly to a period of time. The signal from the TAC passes down standard coaxial cable of length 1-2 m and to the MCA, a PCI device with several available inputs, although only one is used in this experiment. Each voltage-amplitude is assigned with a particular channel of a certain time period. The software interface, Maestro 3.10 for Windows, plots a graph of time (x axis) against number of pulses (y axis), which can be plotted logarithmic. Spectrophotometer with laser excitation and micro-channel plate photo-multiplier detector provides an instrument response of 100 ps. The collected decay was in the microsecond range and the spectrum was fitted by Origin software with second order exponential decay. The average lifetime was calculated from the eq. 3.7, where A_i is the pre-exponential coefficient.

$$\tau = \frac{\sum_{i=1}^n A_i \tau_i}{\sum_{i=1}^n A_i} \quad (3.7)$$

Film Preparation TiO₂ solution was prepared by following the same procedure that has been described in the Chapter 2. The UV, IR, CV studies of the dye absorbed on the TiO₂ semiconductor electrode were carried out on the ITO coated conducting glasses. The glass slides were washed with KOH ethanol solution and cut into

9 mm × 9 mm pieces which allows to be inserted into a 10 mm × 10 mm optical path length, quartz fluorescence cell. The TiO₂ solution was dispersed on the glass that was tightened by scotch tape at the four edges and rod over with a glass rod. The wet TiO₂ electrode was dried in air for 15 min and then was sintered at 450 °C for 30 min. The electrode was immersed into the dye ethanol solution (typically 10⁻⁴ M) where it was cooled down to 80 °C for 16 h. IR and UV was tested with a TiO₂ semiconductor electrode as the background. CV was carried out by using the semiconductor electrode as the working electrode, Pt wire as the counter and Ag / AgNO₃ (0.01 M in CH₃CN) as the reference electrode. Nanocrystalline ZrO₂ solution and films were prepared by following the same method as that of TiO₂.

3.4.1 Synthesis of ligands

(1) ethyl 2-(2'-pyridyl)benzimidazole-1-methylcarboxylate

Method A To a suspension of 2-(2-pyridyl)benzimidazole (2 g, 10.2 mmol) in 10 ml DMF was added Cs₂CO₃ (0.33 g, 1 mmol) and K₂CO₃ (1.41 g, 10.2 mmol). After stirring for 5 min, ethyl bromoacetate (1.30 ml, 11.5 mmol) was added dropwise. The mixture was stirred for 24 h and then evaporated to dryness. The residue was extracted with ethyl acetate (100 ml) and then washed with water (3 × 30 ml) and brine (3 × 30 ml), dried in anhydrous Na₂SO₄ overnight and the solvent was evaporated. The product was recrystallized from ethyl acetate/hexane to afford the product (1.5 g, 52 %).

Method B 2-(2-pyridyl)benzimidazole (2 g, 10.2 mmol) was dissolved in 20 ml anhydrous THF under N₂. The solution was cooled to minus 78 °C and butyllithium (4.5 ml × 2.5 mol L⁻¹, 11.0 mmol) was added with stirring. After addition, the mixture was kept at -78 °C for 3 h and then ethyl bromoacetate (1.30 ml, 11.5 mmol) was added dropwise. It was allowed to warm to room temperature and then refluxed for 3h under anhydrous conditions. The mixture was poured into 50 ml water and extracted with ethyl acetate (3 × 50 ml). The organic phase was washed with water (3 × 30 ml) and brine (3 × 30 ml), dried in anhydrous Na₂SO₄ overnight and the solvent was evaporated. The product was recrystallized from ethyl acetate/hexane (2.0 g 70 %). ¹H NMR (CDCl₃) δ 9.34 (d, 1 H), 8.74 (d, 1 H), 8.31 (t, 1 H), 8.12 (t, 1 H), 7.6 (m, 4 H), 5.78 (s, 2 H), 4.22 (q, 2 H), 1.21 (t, 3 H). Anal. Calcd for C₁₄H₁₁N₃O₂: C, 68.33; H, 5.34; N, 14.94. Found: C, 68.34; H, 5.57; N, 14.92.

(2) 2-(2'-pyridyl)benzimidazole-1-methylcarboxylic acid (*pbimC*₂)

Ethyl 2-(2'-pyridyl)benzimidazole-1-methylcarboxylate (1.0 g, 3.6 mmol) was dissolved in 25 ml 75 % aqueous ethanol solution. To the solution NaOH (1.5 g, 37.5 mmol) was added and the mixture was warmed at low steam for 40 min. After the reaction, the mixture was cooled down and 50 ml cold water was added and the pH value of the solution was adjusted to 2. The precipitate was filtered and washed with water, acetone and diethyl ether (0.88 g, 97 %). White powder, m.p. 248 ~ 249 °C. ¹H NMR (DMSO-*d*₆) δ 8.68 (s, 1 H), 8.40 (d, 1 H), 8.00 (t, 1 H), 7.70 (dd, 2 H), 7.50 (t, 1 H), 7.30

(q, 2 H), 5.62 (s, 2 H). Anal. Calcd for $C_{16}H_{15}N_3O_2$: C, 66.40; H, 4.34; N, 16.60. Found: C, 66.10; H, 4.00; N, 16.53.

(3) 2-(2'-pyridyl)benzimidazole-1-ethylcarboxylic acid (*pbimC₃*)

2-(2-pyridyl)benzimidazole (2.0 g, 10.2 mmol) and ethyl acrylate (1.3 ml, 12 mmol) was dissolved in 10 ml anhydrous DMF under N_2 . To this solution 1,3,4,6,7,8-hexahydro-2H-pyrimido[1,2-a]-pyrimidine was added and were heated at 60 °C for 24 h while stirring. After reaction, cold water (50 ml) was added. The precipitate was filtered, washed with water. The crude product was dissolved in 25 ml 75% aqueous ethanol and NaOH (2.0 g, 50 mmol) was added. The mixture was heated at low steam for 40 min and cold water (50 ml) was added after reaction upon cooling. The solution was adjusted to pH = 2 with hydrochloric acid and the precipitate was filtered, washed with water, acetone and diethyl ether, air dried (1.78 g, 87% yield). White powder, m.p. 236 ~ 237 °C. 1H NMR (DMSO- d_6) δ 8.85 (d, 1 H), 8.43 (d, 1 H), 8.12 (t, 1 H), 7.82 (dd, 2 H), 7.64 (t, 1 H), 7.40 (q, 2 H), 5.10 (t, 2 H), 3.00 (t, 2 H). Anal. Calcd for $C_{15}H_{13}N_3O_2$: C, 67.40; H, 4.87; N, 15.73. Found: C, 67.10; H, 4.69; N, 15.29.

(4) 2-(2'-pyridyl)benzimidazole-1-propylcarboxylic acid (*pbimC₄*)

2-(2-pyridyl)benzimidazole (2.0 g, 10.2 mmol) was dissolved in 10 ml DMF under N_2 . To this solution K_2CO_3 (2.0 g, 14.5 mmol) and trace of BuN_4I were added. The mixture was stirred for 5 min and ethyl bromobutyrate (1.8 ml, 12 mmol) was added

dropwise and then stirred for 24 h at room temperature. After reaction, cold water (50 ml) was added and the precipitate was filtered, washed with water. The crude product was dissolved in 25 ml 75% aqueous ethanol and NaOH (2.0 g, 50 mmol) was added. The mixture was heated at low steam for 40 min and cold water (50 ml) was added after reaction upon cooling. The solution was adjusted to pH = 2 with hydrochloride acid and the precipitate was filtered, washed with water, acetone and diethyl ether, air dried (1.8 g, 62% yield). White powder, m.p. 196 ~ 198 °C. . ¹H NMR (DMSO-*d*₆) δ 8.90 (d, 1 H), 8.40 (d, 1 H), 8.15 (t, 1 H), 7.96 (d, 1 H), 7.85 (d, 1 H), 7.70 (t, 1 H), 7.50 (q, 2 H), 4.88 (t, 2 H), 2.30 (t, 2 H), 2.05 (q, 2 H). Anal. Calcd for C₁₆H₁₅N₃O₂: C, 68.32; H, 5.34; N, 14.95. Found: C, 68.08; H, 4.97; N, 14.88.

3.4.2 Synthesis of the complexes

(4) *Cis-[Ru(bpy)₂Cl₂]·2H₂O*

RuCl₃·3H₂O (3.0 g, 11.5 mmol), bipyridine (3.61 g, 23.1 mmol) and LiCl (1g, 23.6 mmol) were refluxed in DMF under argon for 8 h. The reaction mixture was cooled to room temperature and 100 ml acetone was added. The resultant solution was cooled at 0 °C overnight. The precipitate was filtered and washed with water (3 × 10 ml) and diethyl ether (3 × 20 ml). The product was dried by suction, 68 % yield⁵.

(5) $[(bpy)_2Ru(pbimH)](PF_6)_2$

$Ru(bpy)_2Cl_2 \cdot H_2O$ (1.0 g, 1.9 mmol) and 2-(2-pyridyl)benzimidazole (0.37 g, 1.9 mmol) were dissolved in 25 ml ethanol and refluxed for 4 h under argon. After reaction, the solution was cooled to room temperature and excess KPF_6 aqueous solution was added. The precipitate was collected by filtration and the crude product was recrystallized from methanol/acetone (1.64 g, 95 %)⁵. UV-Vis (λ_{max}) 460 nm ($\epsilon = 7500 M^{-1} cm^{-1}$). 1H NMR (DMSO- d_6) δ 8.95 (t, 3H), 8.87 (d, 1H), 8.72 (d, 1H), 8.39 (t, 2 H), 8.28 (p, 2 H), 8.22 (t, 1H), 8.10 (d, 1H), 7.98 (d, 1H), 7.95 (d, 1H), 7.92 (d, 2 H), 7.88 (d, 1 H), 7.73 (t, 1 H), 7.67 (br, 3 H), 7.62 (t, 1 H), 7.52 (t, 1 H), 7.19 (t, 1 H), 5.82 (d, 1 H). Anal. Calcd for $RuC_{32}H_{25}F_{12}N_7P_2$: C, 42.77; H, 2.78; N, 10.91. Found: C, 42.79; H, 2.25; N, 10.73.

(6) $[(bpy)_2Ru(pbimC_2)](PF_6)_2$

$[(bpy)_2Ru(pbimC_2)](PF_6)_2$ was prepared by following the same procedure as that for the preparation of $[(bpy)_2Ru(pbimH)](PF_6)_2$ except that 2-(2'-pyridyl)benzimidazole-1-methylcarboxylic acid was used as the starting material, 93% yield. 1H NMR (DMSO- d_6) δ 8.85 (t, 3H), 8.76 (d, 1H), 8.46 (d, 1H), 8.22 (t, 1 H), 8.10 (br, 4 H), 7.97 (d, 1H), 7.91 (d, 1H), 7.82 (d, 1H), 7.72 (br, 3H), 7.48 (br, 6 H), 7.17 (t, 1 H), 5.68 (t, 1 H), 5.56 (s, 2 H). Anal. Calcd for $RuC_{34}H_{27}F_{12}N_7O_2P_2$: C, 42.69; H, 2.84; N, 10.25. Found: C, 42.78; H, 2.60; N, 10.66.

(7) $[(bpy)_2Ru(pbimC_3)](PF_6)_2$

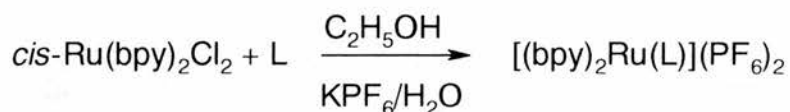
$[(bpy)_2Ru(pbimC_3)](PF_6)_2$ was prepared by following the same procedure as that for the preparation of $[(bpy)_2Ru(pbimH)](PF_6)_2$ except that 2-(2'-pyridyl)benzimidazole-1-ethylcarboxylic acid was used as the starting material, 96% yield. 1H NMR (DMSO- d_6) δ 8.83 (dd, 3H), 8.72 (d, 1H), 8.68 (d, 1H), 8.18 (br, 5 H), 7.99 (d, 1 H), 7.90 (d, 1H), 7.82 (d, 1H), 7.73 (br, 3H), 7.50 (br, 6 H), 7.08 (t, 1 H), 5.69 (t, 1 H), 5.14 (t, 2 H), 3.00 (t, 2H). Anal. Calcd for $RuC_{35}H_{29}F_{12}N_7O_2P_2$: C, 43.30; H, 2.99; N, 10.10. Found: C, 42.95; H, 2.65; N, 10.02.

(8) $[(bpy)_2Ru(pbimC_4)](PF_6)_2$

$[(bpy)_2Ru(pbimC_4)](PF_6)_2$ was prepared by following the same procedure as that for the preparation of $[(bpy)_2Ru(pbimH)](PF_6)_2$ except that 2-(2'-pyridyl)benzimidazole-1-propylcarboxylic acid was used as the starting material, 90% yield. Red microcrystal, m.p. 200 ~ 202 °C. 1H NMR (DMSO- d_6) δ 8.87 (br, 4H), 8.71 (d, 1H), 8.20 (br, 5 H), 7.98 (d, 1 H), 7.88 (d, 1 H), 7.80 (d, 2 H), 7.72 (d, 1 H), 7.67 (d, 1 H), 7.52 (br, 6 H), 7.05 (t, 1 H), 5.65 (t, 1 H), 4.90 (t, 2 H), 2.30 (t, 2 H), 2.05 (q, 2 H). Anal. Calcd for $RuC_{36}H_{32}F_{12}N_7O_3P_2$: C, 43.50; H, 3.22; N, 9.87. Found: C, 43.50; H, 2.85; N, 9.84.

3.5 RESULTS AND DISCUSSIONS

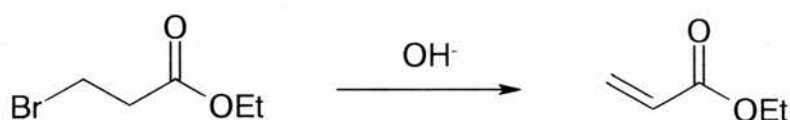
3.5.1 Synthesis



The mono-substituted complexes $[(\text{bpy})_2\text{Ru(L)}](\text{PF}_6)_2$ (where L = derivatives of 2-(2-pyridyl)benzimidazole) were prepared by reaction of the free ligand with *cis*- $[\text{Ru}(\text{bpy})_2\text{Cl}_2]$. Isolation of the mono-substituted products was achieved by addition of KPF_6 aqueous solution to the reaction mixture. Purification of the crude products was accomplished in most cases by recrystallization from dry methanol/acetone. The final products tend to be insoluble in most solvents including water, but dissolved well in acetone.

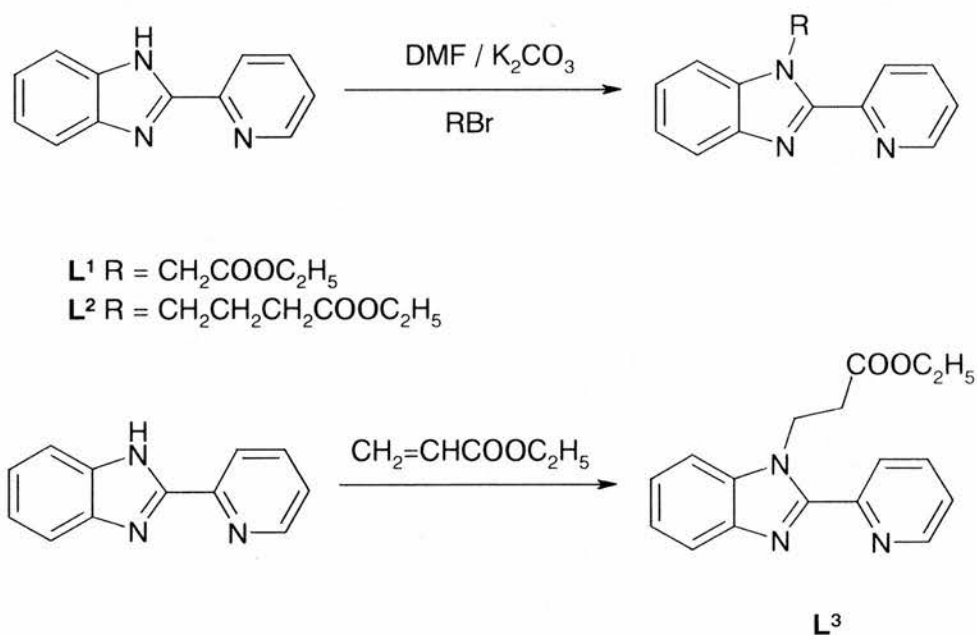
First of all, we tried to prepare $[\text{Ru(L)}_3](\text{PF}_6)_2$ complexes, but disappointingly, we failed because the product was so unstable that it decomposed during the isolation and purification steps. It is possible that the carboxylic acid group is coordinated with the ruthenium center and thus complexes of such composition would be easily oxidized in the air. With $[\text{Ru}(\text{bpy})_2\text{Cl}_2]$ as the starting material, the synthesis of the $[(\text{bpy})_2\text{Ru(L)}](\text{PF}_6)_2$, however, is more readily controlled. There would only be the coordination of the two nitrogen atoms of the ligand with the ruthenium because there are only two positions available in $[\text{Ru}(\text{bpy})_2\text{Cl}_2]$ for coordination.

The synthesis of the carboxylic derivatives of 2-(2-pyridyl)benzimidazole involves the deprotonation of the nitrogen, so strong base was used. Ethyl 2-(2'-pyridyl)benzimidazole-1-methylcarboxylate (L^1) was prepared while reacting 2-(2-pyridyl)benzimidazole with ethyl bromoacetate in DMF solution with potassium carbonate as the base. The reaction was successful in all cases except for the preparation of Ethyl 2-(2'-pyridyl)benzimidazole-1-ethylcarboxylate (L^2), which was run under the same reaction conditions with ethyl bromopropionate as the starting material. It is proposed that with potassium carbonate as the base, ethyl bromopropionate would undergo an elimination reaction.



Instead, L^2 was prepared by reacting 2-(2-pyridyl)benzimidazole with ethyl acrylate, undergoing a Michael addition reaction with 1,3,4,6,7,8-hexahydro-2H-pyrimido[1,2-a]-pyrimidine as the catalyst. The synthesis of the ligands is shown in the following scheme:

Scheme 3.2

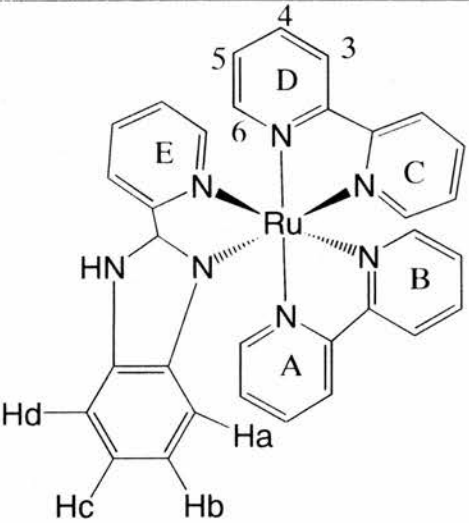


3.5.2 ^1H NMR study of the complexes

1) ^1H NMR 1D spectra

^1H NMR of $(\text{bpy})_2\text{Ru}(\text{Hpbim})(\text{PF}_6)_2$ in DMSO-d_6 is shown in Fig. 3.6. The chemical shift assignment of the protons of the complex $(\text{bpy})_2\text{Ru}(\text{Hpbim})(\text{PF}_6)_2$ is listed in Table 3. 1.

Table 3.1 ^1H chemical shift assignment of $[(\text{bpy})_2\text{Ru}(\text{pbimH})](\text{PF}_6)_2$ in $\text{DMSO-}d_6$

	3 H	4 H	6 H	5 H	Benzene
	δ 8.85 ($\text{H}_{\text{B}3}$, $\text{H}_{\text{A}3}$, $\text{H}_{\text{D}3}$, 8.75 (d, $\text{H}_{\text{C}3}$, 8.59 (d, $\text{H}_{\text{E}3}$)	δ 8.25 ($\text{H}_{\text{E}4}$, $\text{H}_{\text{B}4}$, 8.14 ($\text{H}_{\text{A}4}$, $\text{H}_{\text{D}4}$, 8.09 (t, $\text{H}_{\text{C}4}$)	δ 7.96 (d, $\text{H}_{\text{B}6}$, 7.84 (d, $\text{H}_{\text{C}6}$), 7.82 (d, $\text{H}_{\text{D}6}$), 7.78 ($\text{H}_{\text{A}6}$, H_{d}) δ 7.73 (d, $\text{H}_{\text{E}6}$)	δ 7.60 (t, $\text{H}_{\text{B}5}$, 7.53 ($\text{H}_{\text{E}5}$, $\text{H}_{\text{A}5}$, $\text{H}_{\text{C}5}$, 7.49 (t, $\text{H}_{\text{D}5}$,	δ 7.40 (t, H_{c}), 7.08 (t, H_{b}), 5.68 (d, H_{a})

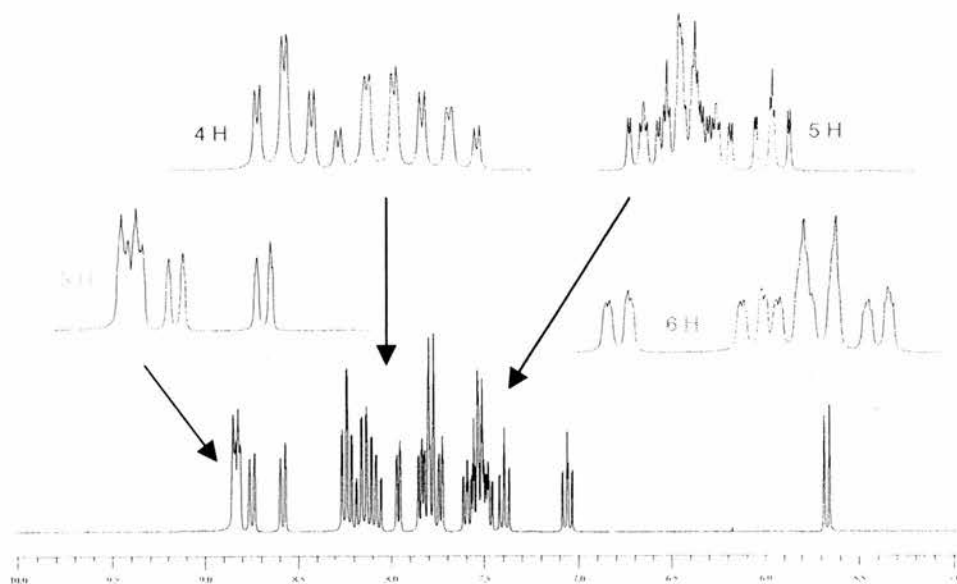


Fig. 3.6 ^1H NMR of $[(\text{bpy})_2\text{Ru}(\text{pbimH})](\text{PF}_6)_2$ in $\text{DMSO-}d_6$ (below) and with expanded regions of the pyridyl protons (above)

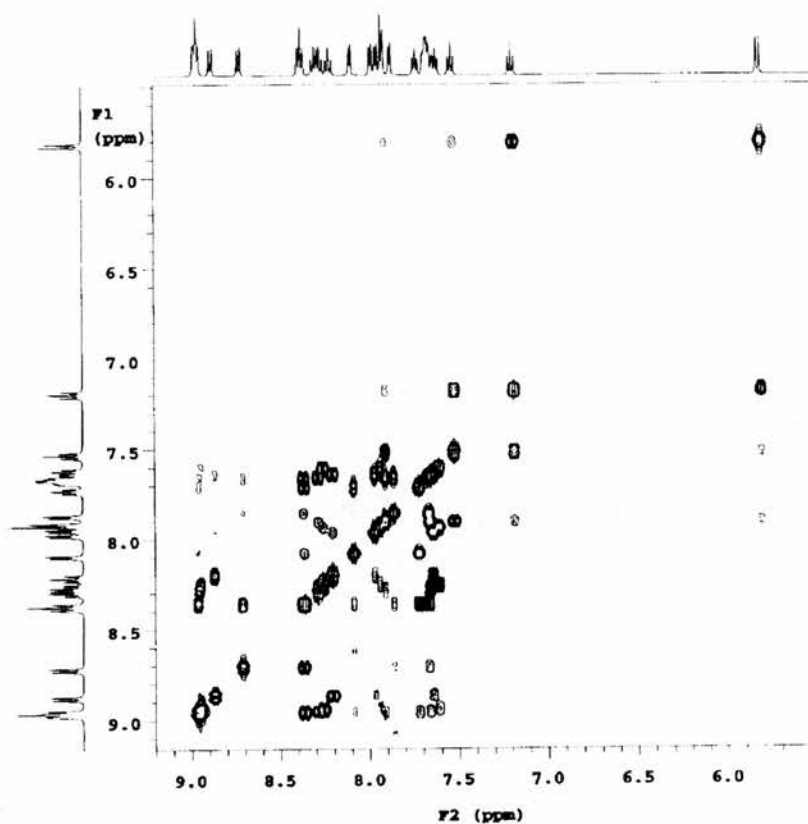


Fig. 3.7 ^1H - ^1H COSY of $[(\text{bpy})_2\text{Ru}(\text{pbimH})](\text{PF}_6)_2$ in MeCN.

2) ^1H - ^1H NOESY and COSY 2D spectra

The assignment of the chemical shift of the protons was determined by ^1H - ^1H COSY (Fig. 3.7) and NOESY (Fig. 3.8) 2D spectroscopy. The correlation of each proton was observed in the ^1H - ^1H COSY spectrum, which distinguishes the protons in

different positions (3 H, 4 H, 5 H, 6H) on different pyridine rings (A, B, C, D, E) as defined in the structure in Table 3.1. The chemical shifts of the protons on the pbim benzene rings, however, separate at higher field, especially H_a at 5.68 ppm because of the ring current effect with the benzene ring facing the pyridine A in the complex.

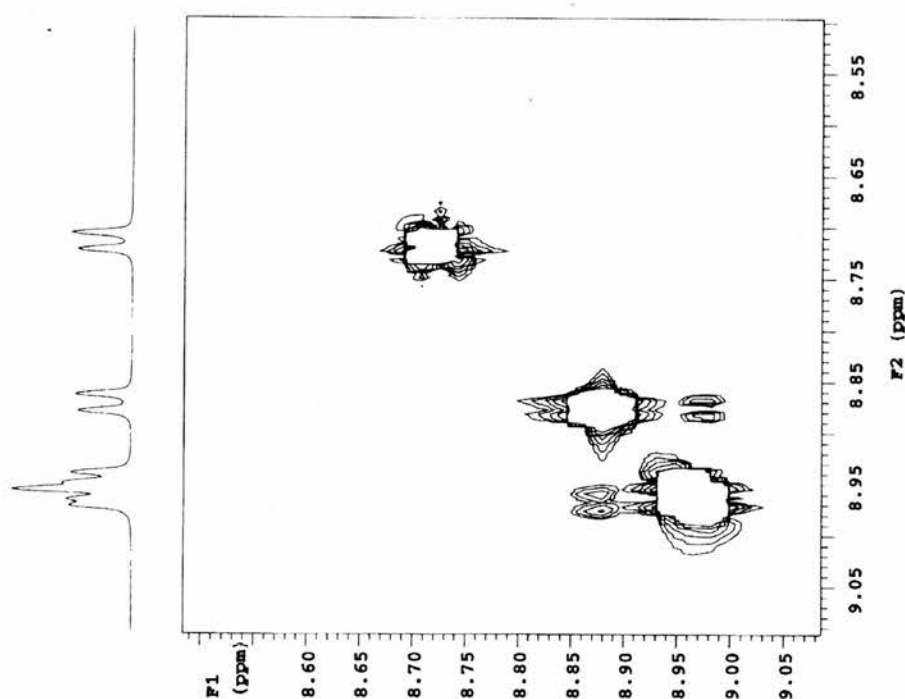


Fig. 3.8 ^1H - ^1H NOESY of $[(\text{bpy})_2\text{Ru}(\text{pbimH})](\text{PF}_6)_2$ in $\text{DMSO-}d_6$

First of all, we can determine the chemical shift of the protons on the benzene ring of pbimH since they are far apart from other protons from the COSY spectrum. H_a is upshifted at 5.68 ppm because of the ring current we mentioned earlier which arises when pbimH is coordinated to the ruthenium center. By reading across to the left (or down)

from the H_a (5.68 ppm) peak in the COSY spectrum, we can immediately assign H_b, H_c and H_d peaks. The chemical shifts of the bipyridine protons separate in groups as 3H, 4H, 6H and 5H (as shown in the upper part of Fig. 3.7), and each group contains the protons from the bipyridine rings and the pyridine ring from pbimH. Bipyridine H₃ and H_{3'} coupling was observed in the NOESY spectrum, which holds a key to the assignments of the all the rest of protons by walking around the pyridine rings from the COSY spectrum (Fig. 3.8). The only H₃ signal (δ 8.70, measured in MeCN) without a cross peak must be E₃, so from the COSY spectrum we can determine all the E ring proton assignments. The unique signal at δ 8.87 must correspond to the unique pyridine ring C trans to the benzimidazole group. Then we can use the COSY to assign all the C and D protons. A similar process yields A and B assignments.

3) Effect of ring current

Shown in Fig. 3.9 are the ¹H NMR spectra of the free ligands. When the proton was replaced by the CH₂COOH group, as we can see from the spectra, H_d moves upfield because of the electron withdrawing nature of the carboxylic acid group. H_a moves dramatically upfield when pbimH is coordinated with the ruthenium metal centre (see Fig. 3.7), influenced predominantly by the ring current effect of a nearby ring. This is understandable when a Chem3D model is examined. The same effects have been observed for all the 6H protons of the pyridine rings, which are facing the rings nearby respectively, while most of the 3Hs and 4Hs move downfield in the complex with the pyridine rings become electron deficient when coordinated.

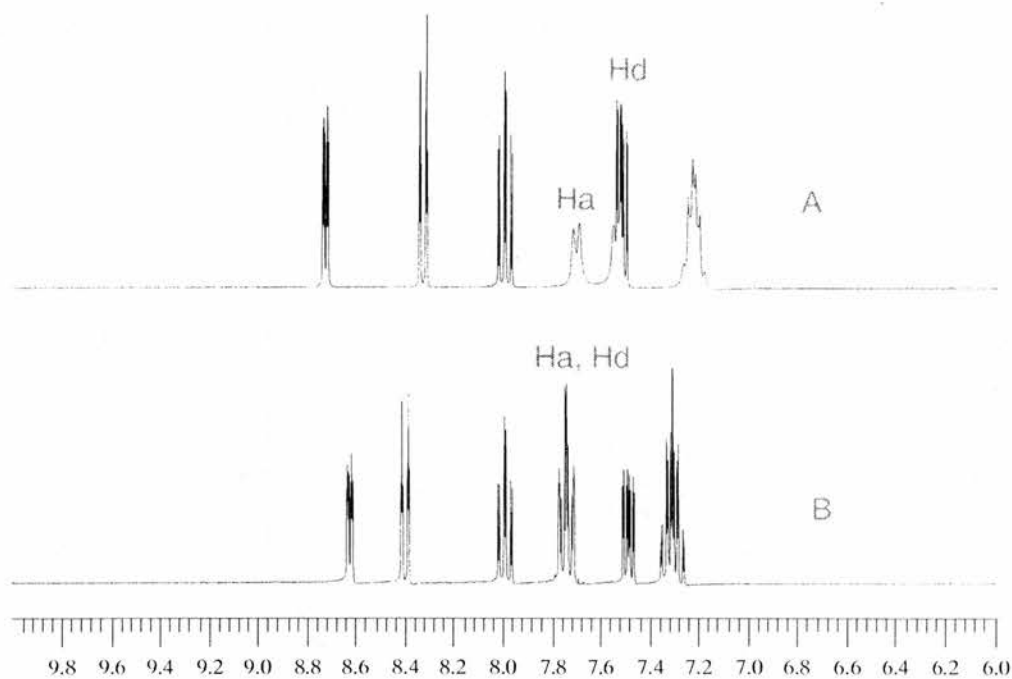


Fig. 3. 9. ^1H NMR (aromatic region) of A) *pbimH*; B) *pbimC*₂ in *DMSO-d*₆

3.5.3 Electronic absorption and luminescence spectra

Data from the absorption spectra for the complexes obtained in acetonitrile in the visible region are summarized in Table 3. 2. The low energy absorption band at about λ_{max} (455 nm) could be assigned to the π^* (bpy) $\leftarrow d\pi$ (Ru) metal to ligand charge transfer transition. The higher energy bands, 240 and 285, 315 nm, are the pyridylbenzimidazole and bipyridyl intraligand $\pi-\pi^*$ transitions respectively. The visible absorption band of the *pbim* complex is blue-shifted relative to that of $[\text{Ru}(\text{dcpv})_2(\text{SCN})_2]$ ($\lambda_{\text{max}} = 537$ nm). The absorption spectrum of $[(\text{bpy})_2\text{Ru}(\text{L})](\text{PF}_6)_2$ is shown in Fig. 3.10.

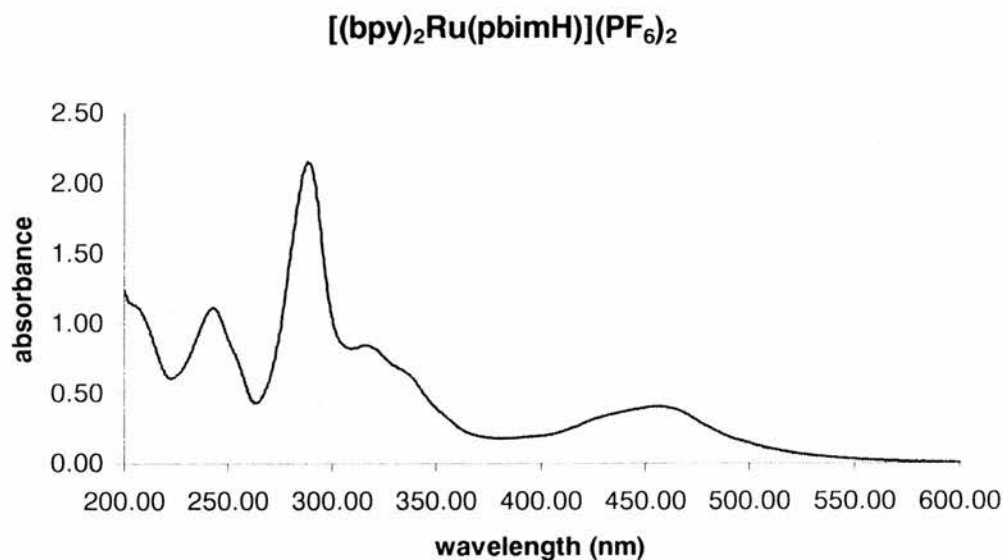


Fig. 3.10. UV-Vis absorption spectrum of $[(bpy)_2Ru(pbimH)](PF_6)_2$ (5×10^{-5} M) in acetonitrile

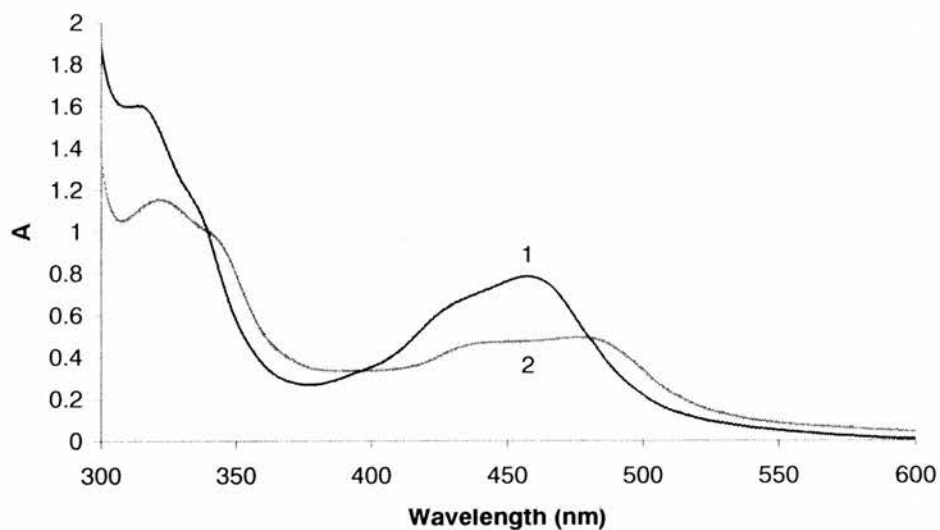


Fig. 3. 11 Absorption spectra of $[(bpy)_2Ru(pbimH)](PF_6)_2$ in ethanol/ H_2O (20:1) (1) without and () with the presence of NaOH at 25 °C

Table 3. 2 Data from UV absorption and emission spectra of the Ru(bpy)₂(pbimH)(PF₆)₂ complex and its derivatives measured in CH₃CN

	λ_{\max} , nm (ϵ , M ⁻¹ cm ⁻¹)	Emission (nm) (Free solution)	Emission (nm) (On TiO ₂)
Ru(bpy) ₂ (Hpbim)(PF ₆) ₂	242 (22400), 285 (42800), 315 (17200), 455 (8400)	653	-
Ru(bpy) ₂ (pbimC ₂)(PF ₆) ₂	243 (21600), 287 (45200), 315 (18400), 458 (9600)	662	643
Ru(bpy) ₂ (pbimC ₃)(PF ₆) ₂	243 (22500), 283 (46500), 314 (18800), 457 (15400)	661	648
Ru(bpy) ₂ (pbimC ₄)(PF ₆) ₂	240 (28000), 280 (48800), 315 (19200), 457 (10600)	653	647

The absorption spectra of [(bpy)₂Ru(pbimH)](PF₆)₂ in ethanol/H₂O (20:1) with and without the presence of base are shown in Fig. 3.11. The pK_a value of [(bpy)₂Ru(pbimH)](PF₆)₂ (10⁻⁴ M) tested in ethanol/H₂O (20:1) was 5.50, slightly acidic. When 100 μ l of 0.01 M NaOH was introduced into the solution, as shown below, the shoulder at 315 nm became a full peak at 325 nm, indicating the concentration of

deprotonated form of pbimH increased. The peak position at 455 nm in the visible light region decreased while a new peak at 440 nm started to take shape, however, leading to lower energy shifts of the absorption maxima on deprotonation of the coordinated pbimH ligand. Similar phenomena were observed by Haga²⁹ when pimH (2-(2-pyridyl)imidazole) and biimH (2,2'-biimidazole) were used as the coordinating ligands upon deprotonation.

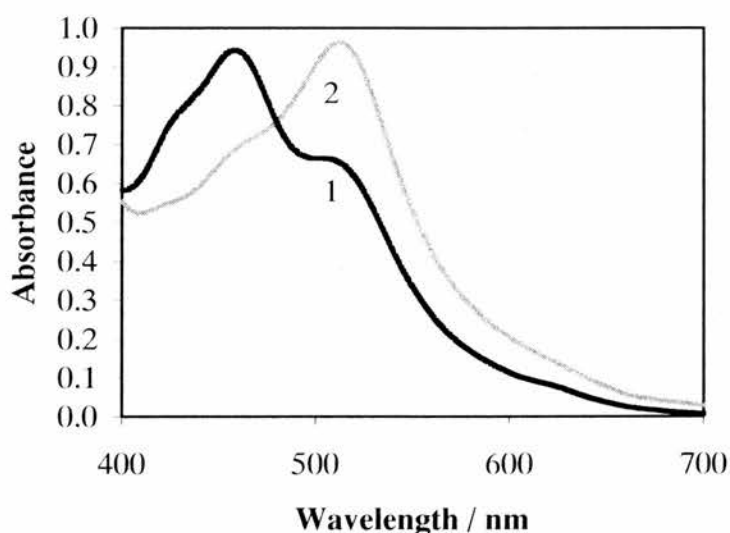


Fig. 3.12 Changes in UV-Vis spectrum of pbimH complex when exposed to TiO₂ in ethanol / 1mM HCl solution, (1) in the absence and (2) in the presence of TiO₂.

Changes in the UV-Vis spectrum of pbimH complex were observed when exposed to TiO₂ in ethanol/1mM HCl solution (Fig. 3.12). When TiO₂ was added to the solution and exposed to the light for 12 h, there was an increase in the band at $\lambda_{\text{max}} = 513$ nm at the expense of the 458 nm band. One would suggest that TiO₂ catalyses the photodecomposition of pbimH of the complexes when exposed to the light. The solution

became a much darker red indicating that the proton of the free nitrogen (uncoordinated) of the pbim was deprotonated by TiO_2 . Once the nitrogen is deprotonated, it becomes more electron rich thus less energy is needed for the MLCT transition and so it appears in the spectra that the maximum absorption is red-shifted. While T. J. Meyer³⁰ pointed out that it is possibly due to the decomposition of the complex and the formation of the $[\text{Ru}(\text{bpy})_2(\text{EtOH})_2]^{2+}$, leading to the absorption at lower energy.

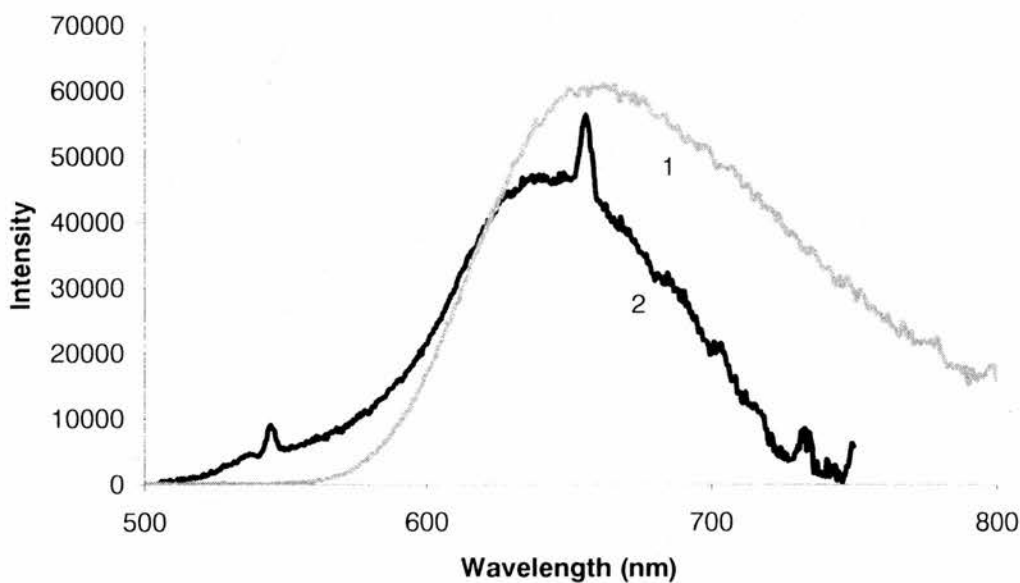


Fig. 3.13 Emission spectra of $[(\text{bpy})_2\text{Ru}(\text{pbimC}_2)](\text{PF}_6)_2$ ($5 \times 10^{-5} \text{ M}$) in MeCN at $T = 298 \text{ K}$ when excited at 400 nm , (1) free solution and (2) absorbed on TiO_2 .

Data from the luminescence spectra of $[(bpy)_2Ru(pbimH)](PF_6)_2$ and its alkylated derivatives are shown in Table 3.2. The emission maxima are almost identical, near 660 nm in free solution and about 645 nm adsorbed on a TiO_2 film, when excited at 400 nm at room temperature (Fig. 3.13)

3.5.4 Electrochemistry

1) Oxidation

Since the electrochemical behavior of the ruthenium 2-(2-pyridyl)benzimidazole (pbimH) complexes and its derivatives are quite similar, we will choose $[(bpy)_2Ru(pbimC_2)](PF_6)_2$ as an example for the description for all the complexes that we will mention in this section. Voltammetric data obtained for the oxidation of the $[(bpy)_2Ru(pbimC_2)](PF_6)_2$ complex in acetonitrile at a platinum electrode with Bu_4NPF_6 (0.1 M) as the supporting electrolyte are summarized in Table 3.3. A reversible oxidation process of the metal center has been observed ($\Delta E_p \sim 78$ mV, close to that observed for ferrocene in the same solution), corresponding to the oxidation of Ru^{2+} to Ru^{3+} .

The complex $[(bpy)_2Ru(pbimC_2)](PF_6)_2$ became oxidized at a potential of +0.85 V and became reduced at +0.77 V vs F_c / F_c^+ , when the experiment was carried out in acetonitrile at a platinum electrode. Its cyclic voltammogram is shown in Fig. 3.14, with ferrocene added as the potential calibrator. The oxidation of the complex is a reversible process, and one electron is released from this electrochemical oxidation. Voltammetric

data obtained for the oxidation of derivatives are shown in Table 3.4. All the complexes have the same one-electron oxidation process as that of $[(bpy)_2Ru(pbimC_2)](PF_6)_2$, and all are reversible. A plot of i_p^{ox} versus $v^{1/2}$ from cyclic voltammograms (i_p^{red} = reduction peak current, v = scan rate) is linear over the scan rate range of 10 to 900 mVs^{-1} was shown in Fig. 3.15, indicating the oxidation of the complex at the electrode was a diffusion-controlled process.

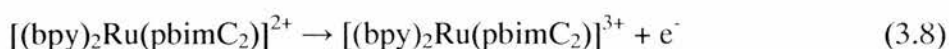


Table 3.3. Voltammetric data obtained for the oxidation of $[(bpy)_2Ru(pbimC_2)](PF_6)_2$ (1 mM) complex in acetonitrile at a platinum electrode. (v = scan rate, E_p = peak potential, $\Delta E_p = E_p^{ox} - E_p^{red}$, $E_{1/2} = E_p^{ox} + E_p^{red}$).

v / mVs^{-1}	E_p^{ox} / mV	E_p^{red} / mV	$\Delta E_p / mV$	$E_{1/2} / mV$
10	856	766	90	811
20	852	770	82	808
40	846	768	78	807
60	848	768	80	808
80	846	768	78	807
100	848	768	80	808
400	864	750	114	807
900	900	718	182	809

Table 3.4. Voltammetric data obtained for the oxidation of ruthenium 2-(2-pyridyl)benzimidazole complexes (1 mM) in acetonitrile at a platinum electrode. The scan rate was at 100 mVs^{-1} . Potential referred to added Ferrocene ($\Delta E_p = 78 \text{ mV}$).

Compound	$E_p^{\text{ox}} / \text{mV}$	$E_p^{\text{red}} / \text{mV}$	$E_{1/2} / \text{mV}$
$\text{Ru}(\text{bpy})_2(\text{Hpbim})(\text{PF}_6)_2$	825	747	786
$\text{Ru}(\text{bpy})_2(\text{pbimC}_2)(\text{PF}_6)_2$	848	768	808
$\text{Ru}(\text{bpy})_2(\text{pbimC}_3)(\text{PF}_6)_2$	820	746	783
$\text{Ru}(\text{bpy})_2(\text{pbimC}_4)(\text{PF}_6)_2$	809	733	771

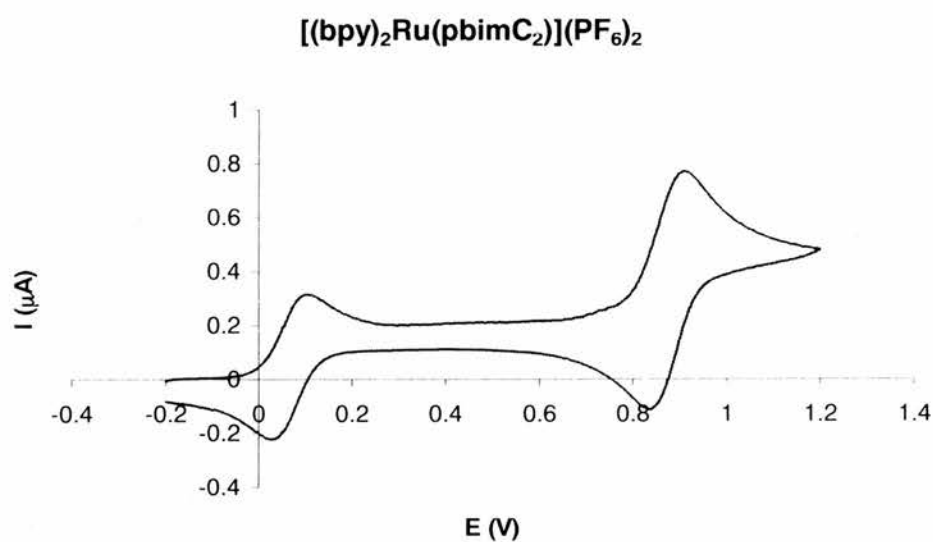


Fig. 3.14 Voltammetric oxidation of $[(\text{bpy})_2\text{Ru}(\text{pbimC}_2)](\text{PF}_6)_2$ (1 mM) complex in acetonitrile at a platinum electrode. Scan rate was at 100 mVs^{-1} .

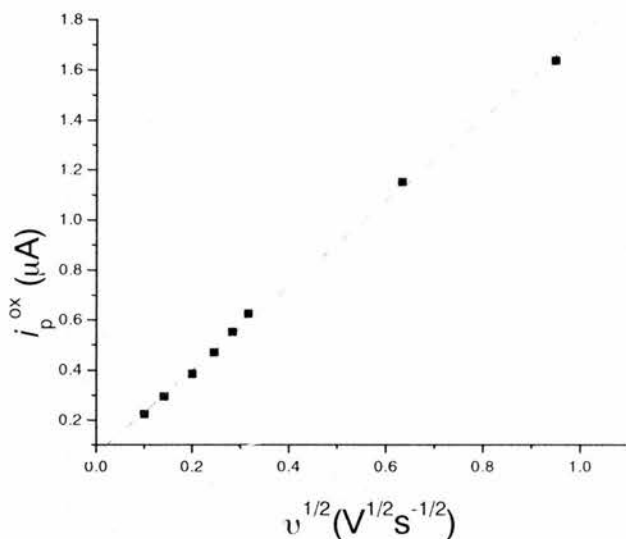


Fig. 3.15 Plot of i_p^{ox} versus $v^{1/2}$ from cyclic voltammograms (i_p^{ox} = oxidation peak current, v = scan rate) over the scan rate range of 10 to 900 mVs^{-1}

As we can see from Table 3.4, the tendency of the pbim complexes to be oxidized at the electrode is $[(bpy)_2Ru(pbimC_4)](PF_6)_2 > [(bpy)_2Ru(pbimC_3)](PF_6)_2 (\approx [(bpy)_2Ru(pbimH)](PF_6)_2) > [(bpy)_2Ru(pbimC_2)](PF_6)_2$. This is because of the electron withdrawing nature of the carboxylic acid group $-CH_2COOH$. The electron density of the metal center is lower than that of $[(bpy)_2Ru(pbimH)](PF_6)_2$ and thus it is more difficult to be oxidized. For complex $[(bpy)_2Ru(pbimC_4)](PF_6)_2$, however, because the carboxylic group is further away, $-CH_2CH_2CH_2COOH$ becomes electron donating than withdrawing, which increases the electron density of the metal center. Hence a lower potential is needed for the oxidation of the ruthenium center. For $[(bpy)_2Ru(pbimC_3)](PF_6)_2$, it seems the functional group $-CH_2CH_2COOH$ has a balanced way of electron withdrawing and

donating ability thus has a neutral effect on the metal. The effects are rather small due to the transmission of the electron-withdrawing group effect through the alkyl chain.

2) *Reduction*

As shown in Fig. 3.16, three reversible reduction processes of the ligands in the complex $[(bpy)_2Ru(pbimC_2)](PF_6)_2$ were observed in the cyclic voltammogram. The first two potential peaks corresponding to the reduction of the bipyridine groups, and the last one to that of 2-(2-pyridyl)benzimidazole:

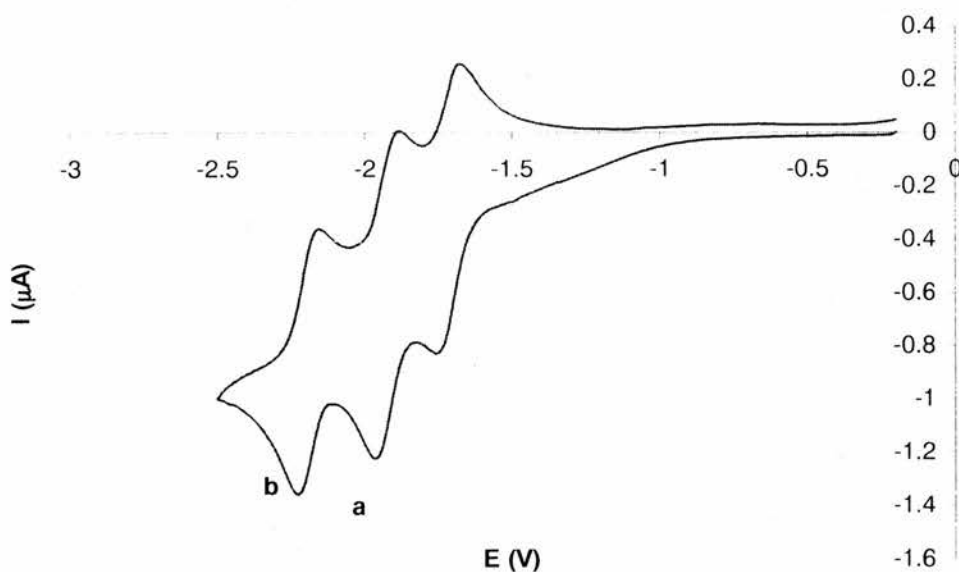


Fig. 3.16. Reduction of $[(bpy)_2Ru(pbimC_2)](PF_6)_2$ (1mM) in acetonitrile at a platinum electrode. Scan rate was at 100 mVs^{-1} .

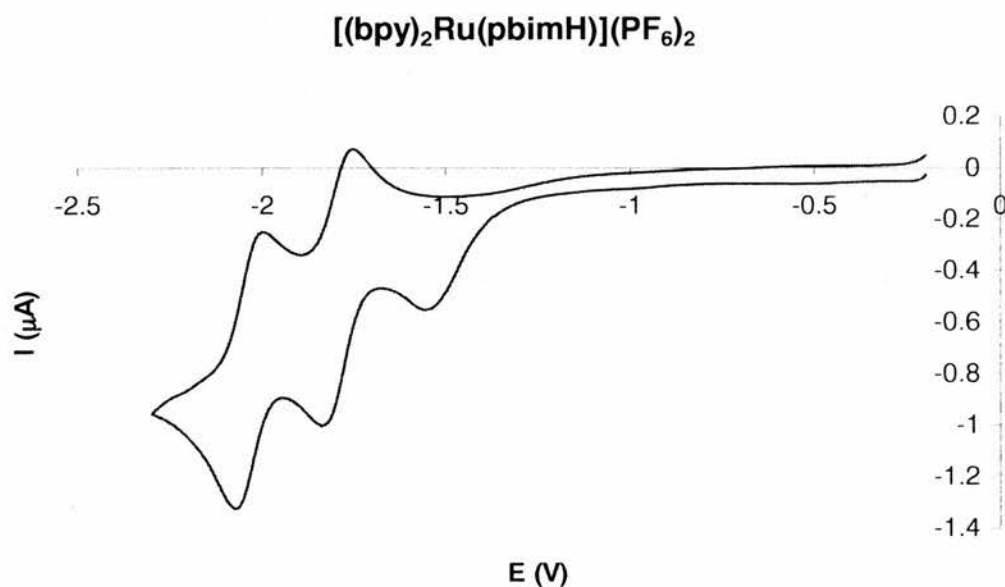
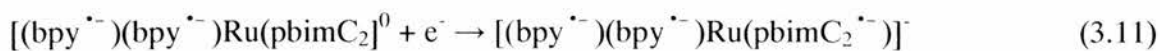
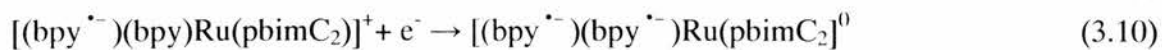
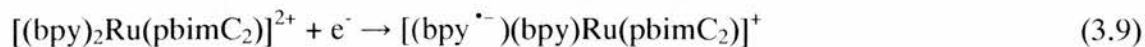


Fig. 3.17. Reduction of $(bpy)_2Ru(pbimH)(PF_6)_2$ (1mM) in acetonitrile at a platinum electrode. Scan rate was at 100 mVs^{-1} .

[†] Note that this is a likely overall reaction. It is impossible to decide whether deprotonation occurs before or after electron transfer.

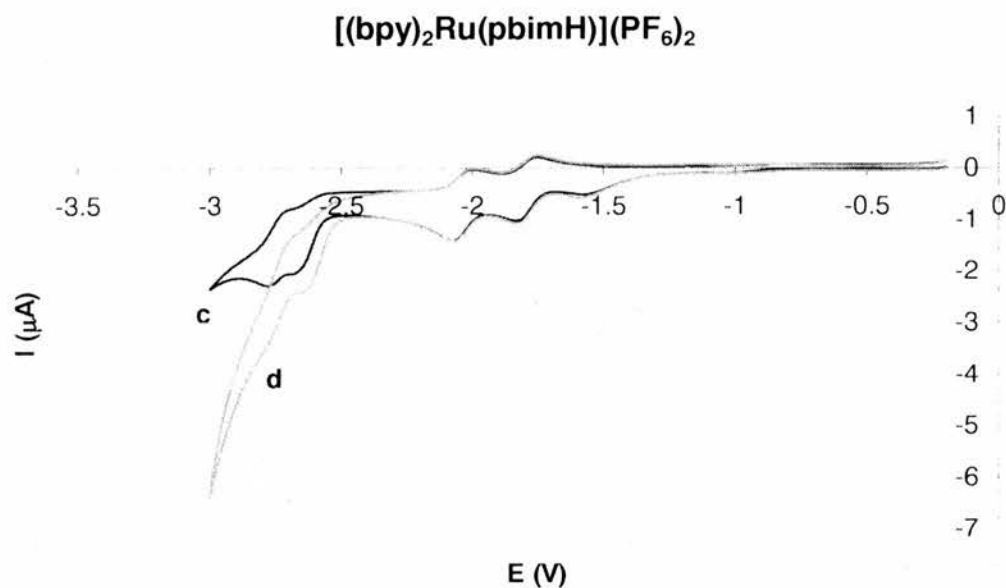


Fig. 3.18. Reduction of $[(bpy)_2Ru(pbimH)](PF_6)_2$ (1mM) in acetonitrile at a platinum electrode before (c) and after (d) water was added. Scan rate was at 100 mVs^{-1} .

The reduction of the other complexes is quite similar except for that of $[(bpy)_2Ru(Hpbim)](PF_6)_2$ (Fig. 3.17), in which the first reduction process is irreversible. This was not seen in the original work by Haga as the scan was reversed before this potential. Additional waves at -0.7 to -1.2 V vs Ag / Ag^+ were noted by Haga (in a footnote) for this complex. He claimed that these waves disappeared when dry alumina was added to the cell and proposed that water induced a reduction process involving NH reduction.²⁹ The corresponding complex $[RuL_2]^{2+}$, L = 2,6-bis(benzimidazole)pyridine, has complex electrochemistry with one irreversible wave at -1.70 V vs Ag / Ag^+ .³¹ The pbim complex is also sensitive to the presence of species such as added organic bases which are capable of hydrogen bonding to the pbim NH group³² but we do not feel that

this is relevant. When we added water, the peak at -1.6 V remained the same, the peak at -2.6 V became irreversible (Fig. 3.18). We suggest that the reduction of pbimH happens at -2.5 to -3.0 V vs. F_c / F_c^+ , and when water was added, the reduction of pbimH is simply superimposed on the current for water reduction at the electrode. We now propose the explanation that perhaps related to the deprotonation of the pbimH according to Wolfbauer³³ for $[Ru(dcbpy)_2(SCN)_2]$ (eq. 3.12).

Table 3.5. Voltammetric data obtained for the reduction of the ruthenium 2-(2-pyridyl)benzimidazole complexes (1 mM) in acetonitrile at a platinum electrode. The scan rate was at 100 mVs^{-1} .

Compound	Redox potential (V) vs. F_c / F_c^+		
	$E_p^{\text{red}} (E_p^{\text{ox}})$	$E_p^{\text{red}} (E_p^{\text{ox}})$	$E_p^{\text{red}} (E_p^{\text{ox}})$
	$E_{1/2}$	$E_{1/2}$	$E_{1/2}$
Ru(bpy) ₂ (pbimH)(PF ₆) ₂	-1.617 (-)	-1.901 (-1.815)	-2.133 (-2.061)
		-1.853	-2.097
Ru(bpy) ₂ (pbimC ₂)(PF ₆) ₂	-1.820 (-1.744)	-2.030 (-1.950)	-2.292 (-2.222)
	-1.782	-1.990	-2.257
Ru(bpy) ₂ (pbimC ₃)(PF ₆) ₂	-1.808 (-1.730)	-2.006 (-1.926)	-2.254 (-2.180)
	-1.701	-1.898	-2.217
Ru(bpy) ₂ (pbimC ₄)(PF ₆) ₂	-1.805 (-1.731)	-2.003 (-1.933)	-2.259 (-2.179)
	-1.768	-1.968	-2.219

Voltammetric data obtained from the reduction of the complexes is shown in Table 3.5. As we can see, the third reduction process of $[\text{Ru}(\text{bpy})_2(\text{pbimC}_2)](\text{PF}_6)_2$ is slightly more negative because of the electron withdrawing effect from the carboxylic acid group, while the difference of redox potentials of the bpy are less obvious.

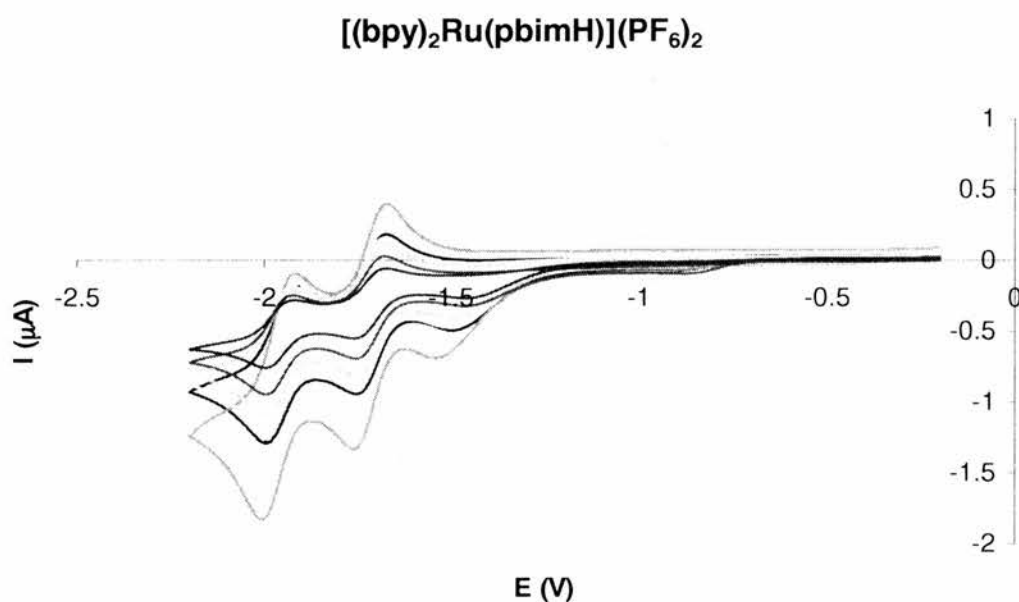


Fig. 3.19. Reduction of $[(\text{bpy})_2\text{Ru}(\text{pbimH})](\text{PF}_6)_2$ (1mM) in acetonitrile at a platinum electrode with different scan rates: 20, 40, 60, 80, 100 and 400 mVs^{-1} .

The cyclic voltammograms of $[(\text{bpy})_2\text{Ru}(\text{pbimH})](\text{PF}_6)_2$ in acetonitrile at a platinum electrode with different scan rates from 20 to 400 mVs^{-1} are shown below (Fig. 3.19). Voltammetric data obtained from the reduction processes of the complex are summarized in Table 3.6. A plot of i_p^{red} versus $v^{1/2}$ from cyclic voltammograms ($i_p^{\text{red}} =$

reduction peak current, v = scan rate) is linear over the scan rate range of 20 to 400 mVs^{-1} implying that the process is diffusion controlled and not due to an adsorbed species. (Fig. 3.20)

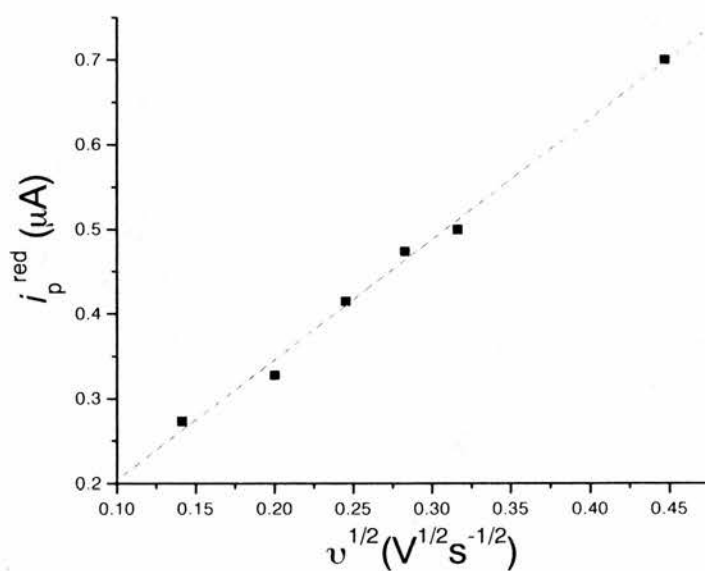


Fig. 3.20. plot of i_p^{red} versus $v^{1/2}$ from cyclic voltammograms (i_p^{red} = reduction peak current, v = scan rate) over the over the scan rate range of 20 to 400 mVs^{-1} at the first irreversible processes.

Table 3.6. Data obtained from the reduction of $[(bpy)_2Ru(pbimH)](PF_6)_2$ in acetonitrile at a platinum electrode with different scan rates from 20 to 400 mVs^{-1} .

v (mV/s)	Redox potential (V) vs. F_c / F_c^+		
	$E_p^{red} (E_p^{ox})$	$E_p^{red} (E_p^{ox})$	$E_p^{red} (E_p^{ox})$
	$E_{1/2}$	$E_{1/2}$	$E_{1/2}$
20	-1.600 (-)	-1.898 (-1.813)	-2.136 (-2.063)
		-1.856	-2.099
40	-1.601 (-)	-1.893 (-1.819)	-2.135 (-2.065)
		-1.856	-2.100
60	-1.633 (-)	-1.895 (-1.819)	-2.135 (-2.061)
		-1.857	-2.098
80	-1.653 (-)	-1.895 (-1.819)	-2.139 (-2.065)
		-1.857	-2.102
100	-1.635 (-)	-1.897 (-1.813)	-2.135 (-2.057)
		-1.855	-2.096
400	-1.681 (-)	-1.899 (-1.817)	-2.145 (-2.061)
		-1.858	-2.103

Further experiments on the reduction of $[(bpy)_2Ru(pbimH)](PF_6)_2$ in acetonitrile were carried out at Au (0.01 cm^2) and carbon (0.07 cm^2) electrodes. In both cases, only two reversible reduction processes were observed from -1.0 to -2.5 V (Fig. 3.22). The first irreversible peak which was observed when Pt electrode was used as the working

electrode disappeared. We propose that it is the adsorption of the first reduced species $[(bpy^{\cdot-})(bpy)Ru(pbimH)]^+$ onto the Pt electrode because platinum is sensitive to the proton of the uncomplexed nitrogen of pbimH (shown in Fig. 3.21). Au and carbon electrodes, however, have a large over-potential for the proton reduction and so, presumably, there was no adsorption taking place in both cases on the electrode. Cyclic voltammetric data obtained from the reduction of $[(bpy)_2Ru(pbimH)](PF_6)_2$ with different working electrodes are summarized in Table 3.7.

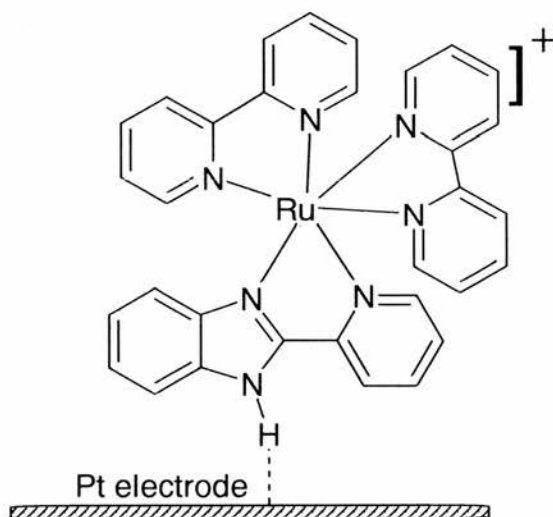
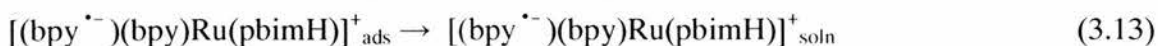


Fig. 3.21. The way the first reduced species $[(bpy^{\cdot-})(bpy)Ru(pbimC_2)]^+$ binds to the Pt electrode

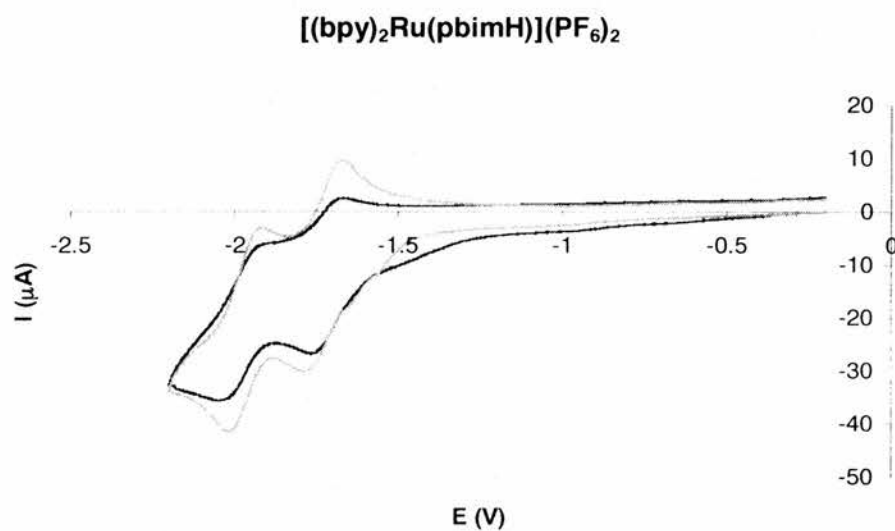


Fig. 3.22. Reduction of $[(bpy)_2Ru(pbimH)](PF_6)_2$ (1mM) in acetonitrile at Au (---) and carbon (—) electrodes. Scan rate was at 100 mVs^{-1} .

Table 3.7. Data obtained from the reduction of $[(bpy)_2Ru(pbimH)](PF_6)_2$ in acetonitrile at different electrodes. Scan rate was at 100 mVs^{-1} .

Electrode	Redox potential (V) vs. F_c / F_c^+		
	$E_p^{\text{red}} (E_p^{\text{ox}})$	$E_p^{\text{red}} (E_p^{\text{ox}})$	$E_p^{\text{red}} (E_p^{\text{ox}})$
	$E_{1/2}$	$E_{1/2}$	$E_{1/2}$
Pt	-1.635 (-)	-1.897 (-1.813)	-2.135 (-2.057)
		-1.855	-2.096
Au	-	-1.907 (-1.810)	-2.185 (-2.052)
		-1.858	-2.119
C	-	-1.925 (-1.813)	-2.161 (-2.061)
		-1.869	-2.111

3.5.5 Surface attachment chemistry

The nature of the chemical bond between a sensitizer and the semiconductor directly impacts on the excited-state and interfacial electron-transfer behaviour.² A chemical bond serves to anchor the sensitizer in place, control interfacial electron coupling and tuning the redox potentials of the sensitizer and the semiconductor. The carboxylic acid or ester functional group are necessary for the achieving high concentration of surface, apart from the porosity of the nanocrystalline semiconductor that was used for the electrode. The analogous sensitizers that do not possess such groups display surface coverage that are at least an order of magnitude lower.³⁴ Goodenough further suggested that a dehydrative coupling reaction between the sensitizer, 4,4'-dicarboxyl-2,2'-bipyridine for example, and the surface hydroxyl groups on rutile TiO₂ would yield an ester linkage on the surface with enhanced electronic coupling between the π^* orbital of the bipyridine ring and the Ti 3d orbital manifold of the semiconductor.³⁵ And a comparison of the photocurrent action and solution absorption spectra revealed a significant red shift upon surface attachment which is consistent with surface stabilization of the MLCT excited state.^{3,36}

1) IR spectroscopy

The infrared spectra of TiO₂ semiconductor and [(bpy)₂Ru(pbimC₂)](PF₆)₂ absorbed onto the TiO₂ semiconductor are shown in Fig. 3.23. The asymmetric stretching

$\nu(\text{CO}_2^-)$ at 1605 cm^{-1} indicated the formation of the ester bond between the carboxylic and the TiO_2 hydroxyl groups.

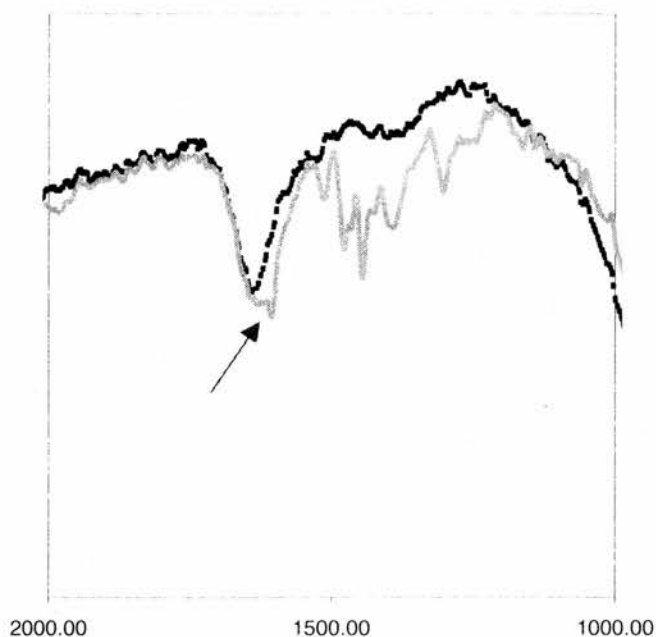


Fig. 3.23 Infrared spectra of TiO_2 coated on ITO glass (---) and $[(\text{bpy})_2\text{Ru}(\text{pbimC}_2)](\text{PF}_6)_2$ absorbed on the TiO_2 semiconductor electrode (—).

2) UV-Vis spectroscopy

On comparing closely the visible absorption spectrum of the surface-attached dye with the carboxylate form measured in acetonitrile solution, we found no obvious difference, as shown in Fig. 3.24. There is no evidence of the MLCT stabilization by the TiO_2 surface. Meyer³⁴ suggested that Brønsted acid-base chemistry dominates the

spectral shifts observed in the visible region upon the surface binding. Presumably, we do not see such shift because the binding group is not directly bonded to the chromophore bpy group.

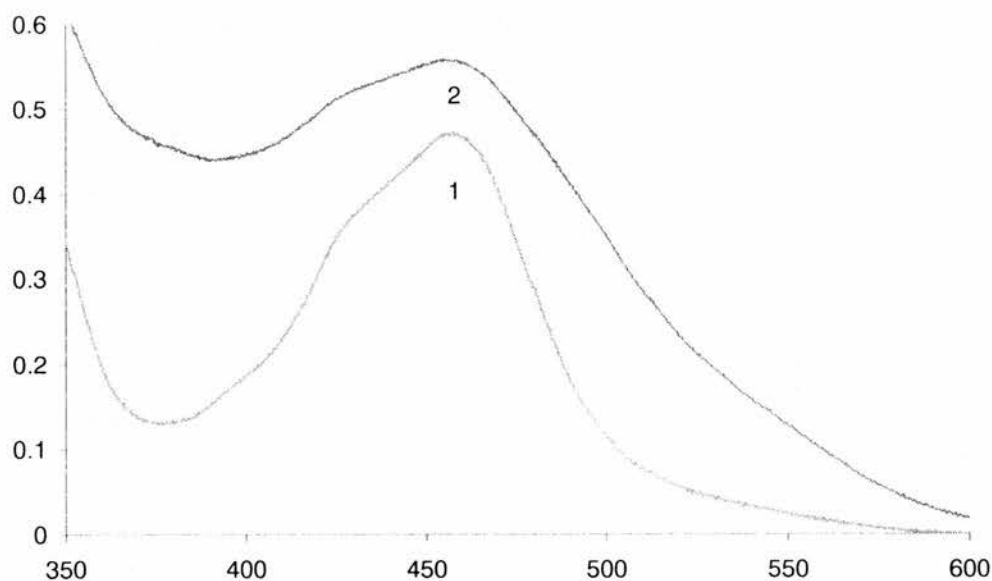


Fig. 3.24 UV-Vis absorption spectra of $[(bpy)_2Ru(pbimC_2)](PF_6)_2$ (1) free solution ($5 \times 10^{-5} M$) and (2) onto TiO_2 semiconductor electrode in MeCN.

3) Cyclic Voltammetry

Cyclic voltammograms of the oxidation of $[(bpy)_2Ru(pbimC_2)](PF_6)_2$ on a TiO_2 semiconductor electrode are shown in Fig. 3.25. Voltammetric data obtained from the oxidation processes of the complex in dichloromethane are summarized in Table 3.8.

Table 3.8. Voltammetric data obtained for the oxidation of $[(bpy)_2Ru(pbimC_2)](PF_6)_2$ absorbed onto a TiO_2 semiconductor electrode in CH_2Cl_2 . (ν = scanning rate, E_p = peak potential, $\Delta E_p = E_p^{ox} - E_p^{red}$, $E_{1/2} = E_p^{ox} + E_p^{red}$). Coverage $\Gamma_c = 2.11 \times 10^{-6} \text{ mol cm}^{-2}$, $\Gamma_v = 5.73 \times 10^{-5} \text{ mol cm}^{-2}$.

ν / mVs^{-1}	E_p^{ox} / mV	E_p^{red} / mV	$\Delta E_p / \text{mV}$	$E_{1/2} / \text{mV}$
20	785	649	136	717
40	783	645	138	714
80	791	633	158	712
100	801	615	186	708
200	827	599	228	713

As we can see, the complex $[(bpy)_2Ru(pbimC_2)](PF_6)_2$ displays a reversible Ru(III/II) redox process by cyclic voltammetry both in fluid solution and when anchored to the nanocrystalline TiO_2 film (Fig. 3.14 and Fig. 3.25). The peak-to-peak separation for the surface-bound sensitizer is almost twice that in the free solution, for example 186 mV (Table 3.8) for anchored dye and 80 mV (table 3.3) in solution at 100 mVs^{-1} . The redox process is therefore quasi-reversible. The area under the peak gives the surface coverage of electroactive complex (Γ_c , 3.14).

$$\Gamma_c = \frac{Q}{nFS} \quad (3.14)$$

$$\Gamma_v = \frac{A}{\epsilon} \quad (3.15)$$

where Q is charge, n is the number of the electrons transferred, F is the Faraday constant, S is the area of the electrode; A is absorbance at the peak maximum, ϵ is extinction coefficient. Comparing with that calculated from the UV-Vis photo-process (Γ_v , 3.15), more than 90% of ruthenium centers are inactive. This probably rules out lateral redox hopping between complexes on the surface of the TiO_2 . However, a recent paper has found much higher electroactivity in amine dye coatings, indicating lateral charge transfer.³⁷ The redox potential, however, was reduced from 808 to 708 mV, 100 mV in difference. This means that, once anchored to the semiconductor, the dye-sensitizer became more easily oxidized.

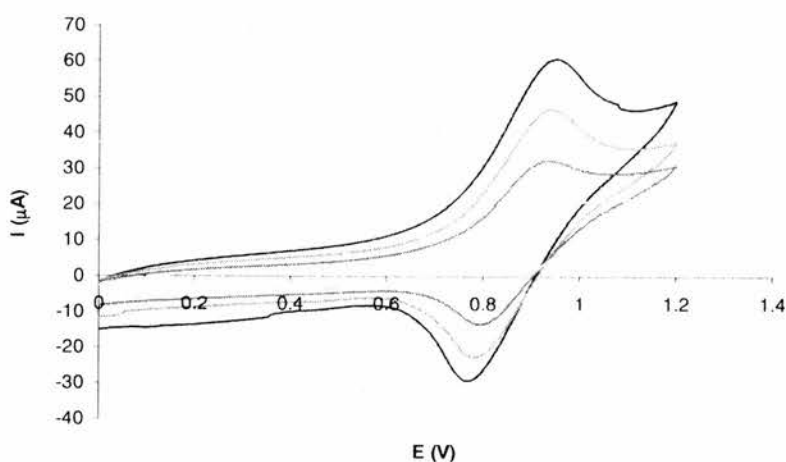


Fig. 3.25 Cyclic Voltammograms of $[(\text{bpy})_2\text{Ru}(\text{pbimC}_2)](\text{PF}_6)_2$ absorbed onto TiO_2 semiconductor electrode in $0.1 \text{ M } ^t\text{Bu}_4\text{NPF}_6 \text{ CH}_2\text{Cl}_2$ solution. The data were recorded at 20, 40, 80 and 100 mVs^{-1}

3.5.6 Time-resolved photoluminescence Spectroscopy

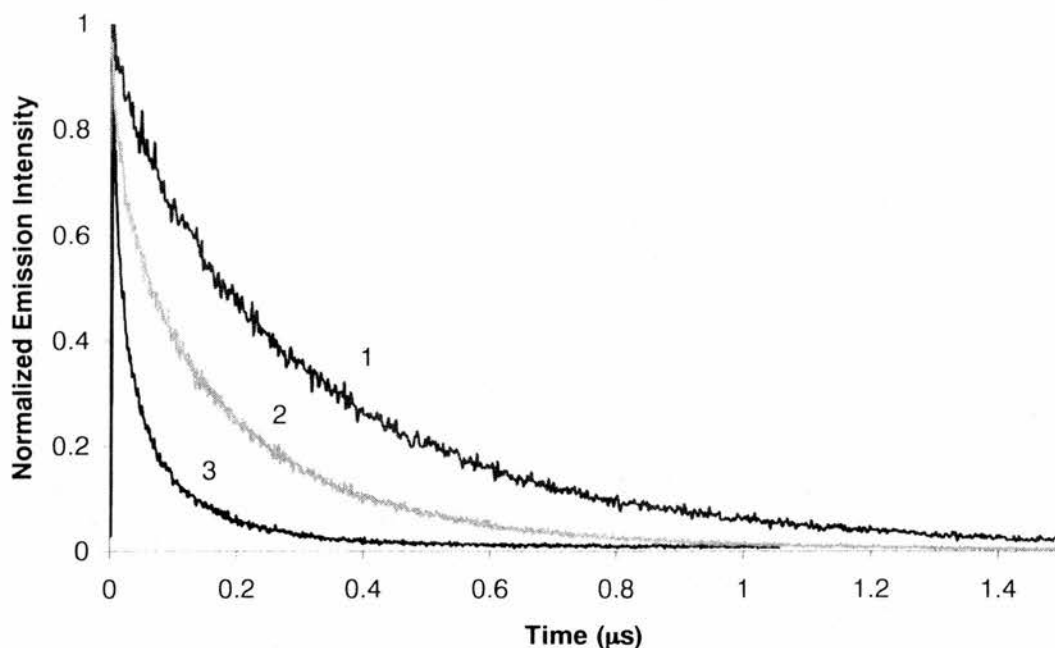


Fig. 3.26 Normalized time-resolved photoluminescence spectra recorded at 650 nm after pulsed at 400 nm excitation of $[Ru(bpy)_2(pbimC_2)](PF_6)_2$ on (1) ZrO_2 (2) in free solution and (3) on TiO_2 films of acetonitrile solution

Normalized photoluminescence quenching decays of the dye-sensitizer $[Ru(bpy)_2(pbimC_2)](PF_6)_2$ both in free solution and on ZrO_2 and TiO_2 films are shown in Fig. 3.26. Data from experiments on the other dye-sensitizer are collected in Table 3.9. The lifetimes were obtained from the second-order exponential decay fit of the spectra. Clearly, as shown Fig. 3.26, electron injection from the dye-sensitizer to the TiO_2 semiconductor electrode and the lifetime of the dye is short-lived. However, on ZrO_2 films, there was no electron transfer occurs because the energy level of the conduction

band is higher than that of the excited state of the dye-sensitizer. The same phenomena were observed for pbimC₃ and pbimC₄ complexes. Comparing our results with those of [Ru(bpy)₂(4,4'-(PO₃H₂)₂bpy)](PF₆)₂ tested on TiO₂ film (27 ns) and on ZrO₂ film (960 ns),³⁸ [Ru(bpy)₂(pbimC₂)](PF₆)₂ has relatively a longer lifetime possibly because of the chain-length effect. The same effect has been observed in our experiments, even it is not obvious, that the dye-sensitizers of shorter chain-lengths have shorter lifetimes (Table 3.9), while pbimC₂ and pbimC₃ complexes have almost identical lifetimes.

Table 3.9 Lifetimes (ns) of the dye-sensitizers obtained from both free solution and onto TiO₂ films ($\Gamma_v \approx 6.0 \times 10^{-5} \text{ mol cm}^{-2}$).

	MeCN solution			ZrO ₂ films			TiO ₂ films		
	τ_1	τ_2	τ_{ave}	τ_1	τ_2	τ_{ave}	τ_1	τ_2	τ_{ave}
[Ru(bpy) ₂ (pbimC ₂)](PF ₆) ₂	224	27.6	159	467	173	309	88.6	11.5	50
[Ru(bpy) ₂ (pbimC ₃)](PF ₆) ₂	206	18.2	148	388	102	320	138	16.3	51
[Ru(bpy) ₂ (pbimC ₄)](PF ₆) ₂	297	180	237	386	147	300	109	11.1	74

The shorter lifetimes detected on TiO₂ indicate that probably the complexes have efficient charge injection but it is not easy to be quantitative due to one or more of the following reasons:

- Multiple sites
- Impurities
- Charge injection from molecules away from the surface

We conclude therefore that charge injection is not a problem in our complexes, and the subsequent behaviour should resemble that of other pendent chain complexes such as $[(\text{bmp})_2\text{RuL}]^{2+}$ (bmp = 4,4'-dimethyl-2,2'-bipyridyl, L = 4-(3-carboxypropyl)-2,2'-bipyridyl).³⁹ In particular, these complexes have similar redox potentials and so the driving force for the back reaction and the reaction with iodide should be comparable.

3.5.7 Solar cell performance

The general procedure for constructing the cell was similar to previously reported methods.³ It is important to correct the IPCE for the light harvesting efficiency (see below), and then to correct for the absorption of the ITO and the electrolyte.

The efficiency of the solar cell is often measured by the incident photon to current conversion efficiency (IPCE), the ratio of the number of electrons flowing through the external circuit to the number of incident photons. For a given area of cell the IPCE can then be expressed as follows:

$$\text{IPCE} = 1250 i_{\text{corrected}} (\mu\text{A}) / [\lambda (\text{nm}) P(\mu\text{W})] \quad (3.16)$$

Where I_{corr} is the dark-current corrected maximum (short-circuit) photocurrent and P is the incident light intensity. Clearly, the IPCE is wavelength dependent and can be related to the light harvesting efficiency (LHE), which in turn is closely related to the absorption characteristics of the dye.

$$\text{IPCE}(\lambda) = \text{LHE}(\lambda) (\phi_{\text{inj}}) (\eta_{\text{ef}}) \quad (3.17)$$

$$\text{LHE}(\lambda) = 1 - 10^{-A} \quad (3.18)$$

Where $A = 1000(\text{cm}^3 \text{ L}^{-1}) \epsilon(\lambda) (\text{mol}^{-1} \text{ L cm}^{-1}) \times \Gamma (\text{mol cm}^{-2})$, ϕ_{inj} is the charge injection yield that depends on the lifetime (τ^{-1}) and the injection rate (k_2) which depends on the excited state redox potential relative to the TiO_2 band edge and the coupling of the dye energy levels to the TiO_2 levels. $\phi_{\text{inj}} = k_2 / (k_{-1} + k_2)$. η_{eff} is the charge collection efficiency that depends on the structure and morphology of semiconductor layer. LHE measurements show that these cells have much larger values than previous cells due to the greater coverage of dye, thanks in the main to the much greater surface area of the TiO_2 present.

The maximum in the IPCE is measured at the λ_{max} of the IPCE curve. When the IPCE is integrated over the AM 1.5 solar spectrum is related to the maximum power output of the cell $(IV)_{\text{max}}$ which due to resistance effects will be smaller than product of

I_{\max} (= I_{SC} , the short-circuit current) and V_{\max} (= V_{OC} , the open-circuit voltage) by a factor known as the fill-factor, f .^{40, 41} Solar cells constructed using the N3 dye have efficiencies of 10.4 % with $I_{\text{SC}} = 18 \text{ mA cm}^{-2}$, $V_{\text{OC}} = 0.72 \text{ V}$ and $f = 0.73$. The cell can operate for $>10^7$ redox cycles, compared to 10^4 for organic dyes.

The IPCE values that we observed for the pbim complexes are very small. Low IPCE values has also been observed for sensitizers with pendent linkage groups, for example, inserting a phenyl group between the bpy and the carboxylic acid group was found to decrease the IPCE from over 80% to only 8%, while a single CH_2 group led to only about a 50% reduction.⁴⁰ Reductions in IPCE to 2% or less were also observed using proline-type anchors of length 14-16 Å instead of the usual carboxylated bpy ligands.³⁷ In contrast, for a series of merocyanine dye sensitizers the efficiency increased as the chain length increased to 18-20 carbon atoms. It was proposed that the back electron transfer reaction was much more dominant in this case.⁴² A fascinating study was carried out on $[\text{ReCl}(\text{CO})_3(\text{bpy}-(\text{CH}_2)_2\text{COOH})]$ sensitizers.⁴³ It was shown that inserting the first CH_2 group led to a 200-fold drop — much greater than predicted from Marcus theory of electron-transfer distance dependence, similar to that observed for Fe sensitizers.⁴⁴ Thereafter, however, increasing the chain length decreased the rate in line with theory. A further, perhaps more serious problem with the pbim complexes is that the π^* energy level of the pbim ligand is much higher than that of the other bpy ligands. Evidence for this lies in the assignment of the first two reduction potentials as being bpy based. This means that in the excited state the electron resides on the bpy ligand, rather than the pbim. As a consequence the electron is very far from the anchoring point to the surface of the TiO_2 .

It has been shown that this is deleterious to the IPCE. For example, in terpy/biquinoline mixed ligand sensitizers the IPCE falls from 75.6 % to 1.74 %.⁴⁵

In our case, the observed lifetimes of the complexes on TiO₂ showed that the electron injection from the dye to the semiconductor electrode was quite efficient and independent of the chain-length. Instead, we believe that the instability of the oxidized or the excited states of the pbim complexes could be the main reason that leads to the low efficiency of the solar cells. Laemmel⁴⁶ suggested that photo-instability of the ruthenium complexes is not apparent in the dye-sensitized solar cells since it was found that the absorbance spectrum of the cell showed no change while exposed to light for ca. 6 hours. However, Meyer et al³⁴ suggested that low IPCE values of complexes [Ru(bpy)₂(ina)₂](PF₆)₂ (ina = isonicotinic acid) and [Ru(py)₂(deeb)₂](PF₆)₂ (deeb = 4,4'-(COOEt)₂-2,2'-bipyridyl) were due to instability or side reactions of Ru³⁺ or Ru^{2+*}. Further measurements on the dependence of the charge recombination rate on the chain-length and the state of the excited state for our sensitizers are necessary.

The open-circuit voltage (V_{oc}) and short-circuit current (I_{sc}) tested under direct sunlight (AM 1.5) of the solar cells based on the dye-sensitizer pbim derivative complexes are shown in Table 3.9. The voltage of the pbim derivative ruthenium complexes detected has the trend: [(bpy)₂Ru(pbimC₂)](PF₆)₂ > [(bpy)₂Ru(pbimC₃)](PF₆)₂ > [(bpy)₂Ru(pbimC₄)](PF₆)₂, which follows the expected order as the chain-length increases. The longer chain-length is, detrimental to the electron injection efficiency from the dye to the semiconductor electrode. The low IPCEs expected, however, are probably

not within the detection limits of our current apparatus. Hence we are currently awaiting testing using a more sensitive apparatus at Imperial College, London.

Table 3.10. Data from the solar cell of the pbim derivatives of ruthenium complex tested under direct sunlight ($\Gamma_v \approx 6.0 \times 10^{-5} \text{ mol cm}^{-2}$).

Compound	V_{oc} (mV)	I_{sc} (μA)
$[\text{Ru}(\text{bpy})_2(\text{pbimC}_2)](\text{PF}_6)_2$	273	96
$[\text{Ru}(\text{bpy})_2(\text{pbimC}_3)](\text{PF}_6)_2$	177	60
$[\text{Ru}(\text{bpy})_2(\text{pbimC}_4)](\text{PF}_6)_2$	135	47

3.6 CONCLUSIONS

In this chapter, pbim derivatives of different chain-lengths (pbimC₂, pbimC₃, pbimC₄) and their ruthenium complexes have been synthesized and characterized by NMR, UV, IR. The electrochemistry, electronic absorbance behaviour, time-resolved fluorescence and surface chemistry onto TiO₂ nanocrystalline semiconductor electrode have been studied. We found that the UV-Vis absorbance of pbimH complex is pH dependent. The IPCE values of the solar cells based on the ruthenium pbim derivative complexes were too small to be measured precisely possibly because of the chain-length effect. Originally, this was thought to be due to a low rate of electron injection, however, this was disapproved by the observation of efficient luminescence quenching in TiO₂ compared to ZrO₂. The low IPCE is therefore probably due to the instability or side

reactions of the oxidized or excited states of the pbim complexes. The V_{oc} and I_{sc} values show a noticeable dependence on the chain-length which deserves further investigation.

3.7 REFERENCES

1. B. O'Regan and M. Grätzel, *Nature*, 1991, **353**, 737.
2. A. Hagfeldt and M. Grätzel, *Chem. Rev.*, 1995, **95**, 49.
3. Md. K. Nazeeruddin, A. Kay, I. Rodicio, R. Humphry-Baker, E. Muller, P. Liska, N. Vlachopoulos and M. Grätzel, *J. Am. Chem. Soc.*, 1993, **115**, 6382.
4. K. Chrysson, V. J. Catalano, R. Kartaran and P. Falaras, *Inorg. Chim. Acta.*, 2002, **328**, 204.
5. A. C. Lees, C. J. Kleverlaan, C. A. Bignozzi and J. G. Vos, *Inorg. Chem.*, 2001, **40**, 5343.
6. A. Islam, H. Sugihara, K. Hara, L. P. Singh, R. Katoh, M. Yanagida, Y. Takahashi and S. Murata, *Inorg. Chem.*, 2001, **40**, 5371.
7. C. Bauer, G. Boschloo, E. Mukhtar and A. Hagfeldt, *J. Phys. Chem., B*, 2001, **105**, 5585.
8. M. K. Nazeeruddin, S. M. Zakeeruddin, R. Humphry-Baker, S. I. Gorelsky, A. B. P. Lever and M. Grätzel, *Coord. Chem. Rev.*, 2000, **208**, 213.
9. G. Wolfbauer, A. M. Bond, G. B. Deacon, J. Howitt, D. MacFarlane and L. Spiccia, *J. Electrochem. Soc.*, 2001, **148**, E97-104.
10. C. R. Rice, M. D. Ward, M. K. Nazeeruddin, M. Grätzel
New J. Chem., 2000, **24**, 651.
11. Md. K. Nazeeruddin, S. M. Zakeeruddin, R. Humphry-Baker, T. A. Kaden and M. Grätzel, *Inorg. Chem.*, 2000, **39**, 4542.

12. S. M. Zakeeruddin, M. K. Nazeeruddin, P. Péchy, F. P. Rotzinger, R. Humphry-Baker, K. Kalyanasundaram, M. Grätzel, V. Shklover and T. Haibach, *Inorg. Chem.*, 1997, **36**, 5937.
13. A. Zaban, S. Ferrere and B. A. Gregg, *J. Phys. Chem. B.*, 1998, **102**, 452.
14. A. Juris, V. Balzani, F. Barigelletti, S. Campagna, P. Belser and A. V. Zelewsky, *Coor. Chem. Rev.*, 1988, **84**, 85.
15. K. A. Opperman, S. L. Mecklenburg and T. J. Meyer, *Inorg. Chem.*, 1994, **33**, 5295.
16. K. Kalyanasundaram, M. Grätzel and M. K. Nazeeruddin, *J. Chem. Soc., Dalton Trans.*, 1991, 343.
17. S. Campagna, G. Denti, L. Sabatino, S. Serroni, M. Ciano and V. Balzani, *J. Chem. Soc, Chem. Commun*, 1989, 1500.
18. M. K. Nazeeruddin, E. Müller, R. Humphry-Baker, N. Vlachopoulos and M. Grätzel, *J. Chem. Soc., Dalton Trans.*, 1997, 4571.
19. K. Kalyanasundaram, and M. K. Nazeeruddin, *Chem. Phys. Lett.*, 1992, **193**, 292.
20. P. A. Andreson, G. F. Strouse, J. A. Treadway, F. R. Keene and T. J. Meyer, *Inorg. Chem.*, 1994, **33**, 3863.
21. F. Bargelletti, L. Flamigni, V. Balzani, J. P. Collin, J. P. Sauvage, A. Sour, E. C. Constable and A. M. W. Cargill Thompson, *J. Chem. Soc, Chem. Commun*, 1993, 942.
22. G. Sprintschink, H. W. Sprintschink, P. P. Kirsch and D. G. Whitten, *J. Am. Chem. Soc.*, 1977, **99**, 4947.
23. T. Ohno, K. Nozaki and M. Haga, *Inorg. Chem.*, 1992, **31**, 548.

24. D. Gust, T. A. Moore, P. A. Liddell, G. A. Nemeth, L. R. Makings, A. L. Moore, D. Barrett, P. J. Pessiki, R. V. Bensasson, M. Rougee, C. Chachaty, F. C. de Schryver, M. V. der Auweraer, A. R. Holzwarth and J. S. Connolly, *J. Am. Chem. Soc.*, 1987, **109**, 846.
25. P. Seta, E. Bienvenue, A. L. Moore, P. Mathis, R. V. Bensasson, P. A. Liddell, P. J. Pessiki, A. Joy, T. A. Moore and D. Gust, *Nature (London)*, 1985, **316**, 653.
26. R. Argazzi, C. A. Bigozzi, T. A. Heimer, F. N. Castellano and G. J. Meyer, *J. Am. Chem. Soc.*, 1995, **117**, 11815.
27. J. M. Stipkala, F. N. Castellano, T. A. Heimer, C. A. Kelly, K. J. T. Livi and G. J. Meyer, *Chem. Mater*, 1997, **9**, 2341.
28. G. J. Meyer, *J. Chem. Edu.*, 1997, **74**, 652.
29. M. A. Haga, *Inorg. Chim. Acta.*, 1983, **75**, 29.
30. B. Durham, S. R. Wilson, D. J. Hodgson and T. J. Meyer, *J. Am. Chem. Soc.*, 1980, **102**, 600.
31. X. M. Xiao, M. A. Haga, T. Matsumurainoue, Y. Ru, A. W. Addison and K. Kano, *J. Chem. Soc. Dalton Trans.*, 1993, 2477.
32. M. A. Haga and A. Tsunemitsu, *Inorg. Chim. Acta.*, 1989, **164**, 137.
33. G. Wolfbauer, A. M. Bond, G. B. Deacon, D. MacFarlane and L. Spiccia, *J. Am. Chem. Soc.*, 2000, **122**, 130.
34. P. Qu, D. W. Thompson and G. J. Meyer, *Langmuir*, 2000, **16**, 4662.
35. S. Anderson, E. C. Constable, M. P. Dare-Edwards, J. B. Goodenough, A. Hamnett, K. R. Seddon and R. D. Wright, *Nature*, 1979, **280**, 571.
36. D. A. Gulino and H. G. Drickamer, *J. Phys. Chem.*, 1984, **70**, 285.

37. P. Bonhote, E. Gogniat, S. Tingry, C. Barbe, N. Vlachopoulos, F. Lenzmann, P. Comte, M. Grätzel, *J. Phys. Chem. B.*, 1998, **102**, 1498.
38. S. A. Trammell, J. A. Moss, J. C. Yang, B. M. Nakhle, C. A. Slate, F. Odobel, M. Sykora, B. W. Erickson, and T. J. Meyer, *Inorg. Chem.*, 1999, **38**, 3665.
39. T. A. Heimer, S. T. Darcangelis, F. Farzad, J. M. Stipkal and G. J. Meyer, *Inorg. Chem.*, 1996, **35**, 5319.
40. M. X. Tan, P. E. Laibinis, S. T. Nguyen, J. M. Kesselman, C. E. Stanton and N. S. Lewis, in *Prog. in Inorg. Chem.*, 1994. **141**, 21-144.
41. Z. S. Wang, F. Y. Li, C. H. Huang, L. Wang, M. Wei, L. P. Jin and N. Q. Li, *J. Phys. Chem. B*, 2000, **104**, 9676.
42. K. Sayama, S. Tsukagoshi, K. Hara, Y. Ohga, A. Shinpou, Y. Abe, S. Suga, and H. Arakawa, *J. Phys. Chem. B*, 2002, **106**, 1363.
43. J. B. Asbury, E. C. Hao, Y. Q. Wang and T. Q. Lian, *J. Phys. Chem. B*, 2000, **104**, 11957.
44. S. Ferrere, *Chem. Mat.*, 2000, **12**, 1083.
45. B. W. Jing, H. Zhang, M. H. Zhang, Z. H. Lu and T. Shen, *J. Mater. Chem.*, 1998, **8**, 2055.
46. A.C. Laemmel, J. P. Collin, J. P. Sauvage, *Eur. J. Inorg. Chem.*, 1999, **3**, 383.

CHAPTER FOUR

Derivatives of Tris(2-pyridylmethyl)amine – A New Ligand and its Ruthenium Complexes

4.1 INTRODUCTION

Tripodal and tetradentate ligands are facially coordinating, tri- or tetra-dentate chelate ligands which have received considerable attention in both coordination and organometallic chemistry.¹⁻¹¹ The ligands allow studies of metal complexes having uncommon coordination geometries, for example Hg(II) complexes which are tetrahedral instead of hexahedral.^{12,13} Complexes of these ligands with metal ions favouring tetrahedral coordination, in particular Zn(II), have been shown to serve as useful models for the action of carbonic anhydrase.¹⁴ Complexes with hard metal centres such as early transition metals may act as versatile Lewis-acid catalysts.¹⁵ Molybdenum and tungsten complexes were shown to be strong Lewis acids, catalysing Diels-Alder cyclisations, addition of silyl enol ethers to aldehydes, and hydrocyanations. Transition metal complexes of tris(pyridylmethyl)amine (tmpa) ligands and their derivatives have been much studied recently as models for the active sites of various metalloproteins.¹⁶⁻¹⁹ For example, high-valent iron-oxo intermediates have been proposed in the dioxygen activation cycles of many heme and nonheme iron enzymes.^{16, 17} Binuclear and polynuclear complexes of manganese tmpa complexes are involved in a wide variety of biological oxidative processes.¹⁸

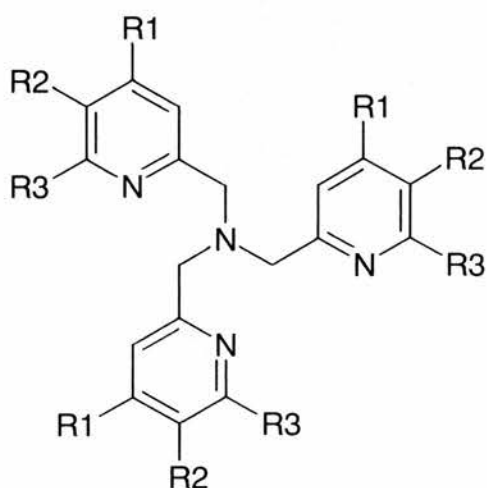
Tris(2-pyridylmethyl)amine (tpma) and its derivatives are of great interest in the understanding of metalloenzymes through their structural and functional modelling for dinuclear and mononuclear active sites which contain Fe, Cu sites as dioxygen activation centres.²⁴⁻²⁸ The tpa ligands include three π -acceptors (pyridyl group) and one σ -donor (tertiary amino group) and also provide thermodynamic stability through tetradentate chelation. Wei²⁹ et al reported that such ligands are able to stabilize reduced copper(I) ion complexes, without the often encountered problem of disproportionation to Cu(0) and Cu(II).

There has been considerable interest in the ruthenium^{20, 21} and rhenium^{22, 23} complexes of polypyridyl ligands such as 2,2'-bipyridyl and 1,10-phenanthroline, primarily because of their potential as photosensitizers in significant process such as water or carbon dioxide reduction. Complexes of tripod ligands stabilize, for example, the Co(I) (d^8) state, in the same manner as 2,2'-bipyridine and its congeners where such stabilisation had generally been attributed to the π -acceptor properties of the bidentate ligands.¹⁹ The synthetic versatility of the tripod and tetradentate ligands commends their use in the study of a number of aspects relating to the bonding in complexes of polypyridyl ligands, including not only structural features but also the physical properties of such complexes.

In order to improve the sensitization efficiency of the dyes and the overall conversion efficiency of the solar cells, much work has been carried out including the study of the mechanism of energy migration and electron transfer between the sensitizer

and the nanocrystalline porous film electrode. Many researchers have studied extensively methods of preparation of electrodes, the bonding method of the dye to the surface of the electrode and the design and synthesis of new ligands. Clearly, the ligand is one of the main factor which affects the properties of the dye, in particular, the light sensitivity, redox potential, the lifetime of the excited state of the dye.

It has been a central issue in the discussion of Ru sensitizers to elucidate the degree of π -back-bonding from the Ru centre to the pyridine derivatives, since such interactions play indispensable roles in the excited-state behaviour involving photo-redox reactions, luminescence, photo-substitution, and photo-induced electron transfer. However, very few papers have reported on [Ru(tpma)] complexes and their derivatives.^{28, 30} In order to explore molecular structures and chemical properties of Ru complexes with tightly bound tetradentate pyridylamine ligands and the possibility of using the complexes as the dye-sensitizer for the solar cells, we attempted to synthesize a series of tpma derivatives including tris[2-(6-carboxypyridyl)methyl]amine (**I**), tris[2-(5-carboxypyridyl)methyl]amine (**II**) and tris[2-(4-carboxypyridyl)methyl]amine (**III**) and their ruthenium complexes. The carboxylic group here not only will serve as the linkage to the semiconductor electrode, but also tune the ligand to be a better π -acceptor because of its electron-withdrawing nature.



- I: $R_1 = R_2 = H$, $R_3 = COOH$ (tmpa262)
II: $R_1 = R_3 = H$, $R_2 = COOH$ (tmpa252)
III: $R_2 = R_3 = H$, $R_1 = COOH$ (tmpa 242)

Fig. 4.1 Derivatives of tris(2-pyridylmethyl)amine

4.2 EXPERIMENTAL

All the chemicals were used as received without further purification, THF (Fluka) was dried over potassium / benzophenone and ethanol (Fluka) was absolute. NMR spectra were recorded on a Varian VNMR 300 MHz spectrometer. Elemental analysis were carried out by the Microanalytical Service, School of Chemistry, University of St Andrews.

All the other experiments like the electrochemistry, UV-Vis and solar cells performance were carried out under the same conditions as described in Chapter 3.

4.2.1 Synthesis of the ligands

Tris(2-methylpyridyl)amine *Method A* A solution of 2-picoly chloride hydrochloride (Aldrich, 5.0 g, 30 mmol) in 10 ml of distilled water was cooled to 0 °C. The solution was treated with 5.3 M aqueous NaOH (5.7 ml, 30 mmol). A solution of 2-(amimomethyl)pyridine (1.6 ml, 15 mmol) in 20 ml dichloromethane was added rapidly dropwise with vigorous magnetic stirring to ensure mixing of the two phases. The mixture was allowed to warm to room temperature, and an additional portion of 5.3 M aqueous NaOH (5.7 ml, 30 mmol) was added dropwise over 24 h. The organic phase was separated from the mixture and washed with 2.5 M aqueous NaOH (15 ml) and the inorganic phase was extracted with CH₂Cl₂ (2 × 50 ml). The organic phase was combined and dried over MgSO₄. After the removal of the solvent, the red-brown solid was extracted with diethyl ether. Removal of the solvent afforded the product which was recrystallized from hexane. ¹H NMR (*d*₆-DMSO) δ 8.46 (d, 1 H), 7.73 (t, 1 H), 7.54 (d, 1 H), 7.22 (t, 1 H), 3.80 (s, 2 H).

Method B 2-picoly chloride hydrochloride (Aldrich, 5.0 g, 30 mmol) was treated with 5.0 M aqueous NaOH (6 ml, 30 mmol) and then combined with 2-(amimomethyl)pyridine (Aldrich, 1.6 ml, 15 mmol) while being stirred. An additional portion of 5.0 M aqueous NaOH (6 ml, 30 mmol) was added dropwise for a period over 1

h. The resulting brown solution was stirred at ambient temperature over 24 h and then neutralized with excess concentrated HClO₄, generating a tan precipitate of crude [H₃tmpa](ClO₄)₃. Recrystallization and purification were accomplished in one step by preparing a solution of 0.1 M both in [H₃tmpa](ClO₄)₃ and [Cr(H₂O)₆](ClO₄)₃ (to complex with the impurities and the desired product), adjusting the pH value of the solution to 2.0 with HClO₄, and boiling for about 15 min. The snow-white crystals that formed upon cooling was washed with cold water and then air-dried. ¹H NMR (*d*₆-DMSO) δ 8.90 (d, 1 H), 8.42 (t, 1 H), 8.00 (d, 1 H), 7.80 (t, 1 H), 4.27 (s, 2 H). Anal. Calcd for C₁₈H₂₁N₄Cl₃O₁₂: C, 36.58; H, 3.58; N, 9.47. Found: C, 37.06; H, 3.17; N, 9.62. (**Caution!** Perchlorate salts of metal complexes with organic ligands are potentially explosive. They should be handled in small quantity and with caution.)

6-(bromomethyl)-2-(hydroxymethyl)pyridine 2,6-di(hydroxymethyl)pyridine (Aldrich, 8 g, 58mmol) was dissolved in 48% HBr (80 ml). The solution was heated to reflux for 1 h under N₂ while it was stirring. After reaction, mixture was cooled to 0 °C in an ice bath and 40% of NaOH aqueous solution was added dropwise to neutralize the solution while it was still stirring. To this solution, 300 ml (3 × 100 ml) dichloromethane was added to extract the products which include 6-(bromomethyl)-2-(hydroxymethyl)-pyridine (**1**) and 2,6-di(bromomethyl)pyridine (**3**). They were separated and purified by chromatography by using first dichloromethane as eluent to give 3.5 g of **3** (25% yield) and then wet diethyl ether 4.6 g of **1** (42% yield). White crystals, m.p. 70-71 °C ¹H NMR (**1**) (CDCl₃) δ 7.75 (t, 1 H), 7.38 (d, 1 H), 7.20 (d, 1 H), 4.75 (s, 2 H), 4.50 (s, 2 H), 4.25

(broad, 1 H); Anal. Calcd for C_7H_8NBrO : C, 41.79; H, 3.98; N, 6.79. Found: C, 41.66; H, 3.63; N, 6.82.

2,6-di(bromomethyl)pyridine white powder, m.p. 79-80 °C. 1H NMR (**1**) ($CDCl_3$) δ 7.69 (t, 1 H), 7.28 (d, 2 H), 4.48 (s, 2 H), Anal. Calcd for $C_7H_8NBr_2$: C, 31.94; H, 2.66; N, 5.32. Found: C, 32.00; H, 2.34; N, 5.17.

Tris[6-(hydroxymethyl)-2-pyridylmethyl]amine 6-(bromomethyl)-2-(hydroxymethyl)pyridine (4.20 g, 21 mmol) was dissolved in 40 ml acetonitrile. To this solution ammonium acetate (Aldrich, 0.54 g, 7 mmol) and sodium carbonate (1.5 g, 14 mmol) were added. The mixture was stirred at room temperature for 2 days under N_2 and then another portion of sodium carbonate (0.75 g, 7 mmol) was added. The reaction was monitored by thin layer chromatography (TLC). After reaction, the solid was filtered off and washed well with CH_3CN . The solvent was evaporated and a 1:1 ratio of CH_2Cl_2 / acetone was introduced to the residue. The precipitate was filtered and washed well with diethyl ether to give 2.9 g (70% yield) of the product. 1H NMR (**1**) (d_6 -DMSO) δ 7.75 (t, 1 H), 7.42 (d, 1 H), 7.25 (d, 1 H), 5.42 (t, 1 H), 4.50 (d, 2 H), 3.73 (s, 2 H).

Ethyl pyridine-2,5-dicarboxylate Pyridine-2,5-dicarboxylic acid (12.0 g, 72 mmol) was dissolved in 150 ml of ethanol and to this solution concentrated H_2SO_4 (2.5 ml) was added. The solution was refluxed under N_2 for 10 h. After the reaction, the solvent was evaporated and CH_2Cl_2 (200 ml) was added, washed with 200 ml of $NaHCO_3$ saturated solution and then water and dried in $MgSO_4$. CH_2Cl_2 was removed to afford

ethyl pyridine-2,5-dicarboxylate (15.0 g, 94% yield) and the crude product was recrystallized from n-hexane to afford a white solid. $^1\text{H NMR}$ (d_6 -acetone) δ 9.20 (s, 1 H), 8.46 (dd, 1 H), 8.20 (d, 1 H), 4.40 (q, 4 H), 1.40 (t, 6 H). Anal. Calcd for $\text{C}_{11}\text{H}_{13}\text{NO}_4$: C, 59.3; H, 5.83; N, 6.28. Found: C, 59.65; H, 5.69; N, 6.23.

Ethyl 2-methoxypyridine-5-carboxylate *Method A* Ethyl pyridine-2,5-dicarboxylate (5 g, 22.4 mmol) and sodium borohydride NaBH_4 (0.55 g, 14.6 mmol) were dissolved in 25 ml of ethanol. The mixture was heated to reflux and stirred for 1h. After reaction, 20 ml of hydrochloride (2ml, 12 M) acidified water was added dropwise and stirred for another 30 min. Ethanol was evaporated and the residue was neutralized with Na_2CO_3 solution. Dichloromethane (2 \times 100 ml) was added to extract the product, dried in MgSO_4 and purified by recrystallization from diethyl ether (3.0 g, 72 % yield). Yellowish crystals, m. p. 74 ~75 $^\circ\text{C}$. $^1\text{H NMR}$ (CDCl_3) δ 9.10 (s, 6 H), 8.25 (d, 4 H), 7.30 (d, 3 H), 4.75 (s, CH_2OH), 4.40 (q, CH_2CH_3), 3.60 (broad, CH_2OH), 1.38 (t, CH_2CH_3). m.p. 74-75 $^\circ\text{C}$. $^{13}\text{C NMR}$ (MeOD) δ 167.5 (COO), 166.7 (2 C), 150.9 (6 C), 139.8 (4 C), 126.8 (5 C), 121.9 (3 C), 65.8 (CH_2OH), 63.0 (CH_2CH_3), 14.9 (CH_2CH_3). Anal. Calcd for $\text{C}_9\text{H}_{11}\text{NO}_3$: C, 59.67; H, 6.08; N, 7.73. Found: C, 59.76; H, 5.99; N, 7.78.

Method B Ethyl 2,5-pyridyldicarboxylate (10 g, 45 mmol) and sodium borohydride NaBH_4 (1.0 g, 26 mmol) was dissolved in 50 ml of ethanol. The solution was treated dropwise at -10 to -5 $^\circ\text{C}$ with CaCl_2 (1.5 g, 13 mmol) in ethanol, stirred for 2.5 h at room temperature. After the reaction, 20 ml of water with HCl (8 ml, 6 M) was added to the solution, stirred for another 1 h and ethanol was evaporated after the

reaction. CH_2Cl_2 (100 ml) was added to the remaining water to extract the product. The aqueous phase was neutralized with sodium carbonate and extracted with CH_2Cl_2 (100 ml). The organic phase was combined and washed with Na_2CO_3 solution, and then dried over MgSO_4 . Evaporation of the solvent gave the crude product which was recrystallized from diethyl ether (6.5 g, 82% yield).

Method C This followed the same procedure as method B, except that LiCl was used. Yield 55%.

5-ethoxycarbonylpyridine-2-carboldoxime Ethyl pyridine-2,5-dicarboxylate (10g, 45 mmol) was dissolved in 250 ml of tetrahydrofuran, cooled under argon to $-60\text{ }^\circ\text{C}$, and reduced with LiAlH_4 (Aldrich, 3.5 g, 92 mmol) in 20 min. The reaction temperature was then held constant for another hour. The reaction was terminated by adding a mixture of tetrahydrofuran (45 ml), water (18 ml) and acetic acid (27 ml). The reaction mixture was evaporated to dryness under vacuum, and the residue was extracted with diethyl ether (3×100 ml). The extract was evaporated and the residue was mixed with a solution of hydroxylamine hydrochloride (5.0 g, 71 mmol) in 30 ml water neutralized with NaCO_3 . The mixture was allowed to stand in a refrigerator to give 2.0 g (30 % yield) of the product, which was recrystallized from 50 % aqueous ethanol. ^1H NMR (d_6 -acetone) δ 11.0 (s, 1 H), 9.0 (s, 1 H), 8.20 (dd, 1 H), 8.06 (d, 1 H), 7.80 (d, 1 H), 4.24 (q, 2 H), 1.26 (t, 3 H).

Ethyl 6-methylnicotinate 6-methylnicotinic acid (Aldrich, 1.0 g, 7.3 mmol) was dissolved in 50 ml of ethanol. To this solution a catalytic amount of Conc. H₂SO₄ was added and then the solution was refluxed for 8 h under N₂. After the reaction, ethanol was evaporated and CH₂Cl₂ (100 ml) was added to extract the residue. The solution was washed with 100 ml saturated NaHCO₃ aqueous solution and then dried over MgSO₄ anhydrous. The solvent was removed to give 1.2 g yellowish oil, 99 % yield. ¹H NMR (CDCl₃) δ 9.15 (s, 1 H), 8.20 (d, 1 H), 7.20 (d, 1 H), 4.30 (q, 2 H), 2.65 (s, 3 H), 1.70 (t, 3 H).

Ethyl 2-bromomethylpyridine-5-carboxylate *Method A* To a 100 ml of CCl₄ solution of ethyl 6-methylnicotinate (1.2 g, 8.5 mmol) was added NBS (1.4 g, 8.5 mmol) and a catalytic amount of AIBN under an atmosphere of nitrogen. The resulting mixture was refluxed for 2 h. After cooling, the solution was washed with a 5 % sodium dicarbonate solution and then dried over MgSO₄. Evaporation of the solvent gave a mixture of monobromide, dibromide and unreacted starting materials which was purified by chromatography. ¹H NMR (CDCl₃) δ 9.19 (s, 1 H), 8.30 (d, 1 H), 7.60 (d, 1 H), 7.20 (s, 1 H), 4.60 (s, 2 H), 4.40 (q, 2 H), 1.42 (t, 3 H).

Method B Ethyl 2-methoxypyridine-5-carboxylate (3 g, 16.6 mmol) in CH₂Cl₂ (150 ml) was treated successively at 0 °C with methanesulfonyl chloride (5 ml, 64 mmol) and triethylamine (12 ml, 86.7 mmol). After addition, the solution was allowed to warm to room temperature and stirred for 30 min. The mixture was washed with saturated aqueous ammonium chloride solution (2 ×150 ml). The organic phase was dried over

MgSO₄ and the solvent was evaporated. To the crude mesylate (brown oil) in THF (150 ml) anhydrous lithium bromide (8 g, 93.6 mmol) was added under stirring and the mixture was heated to 40 °C for 1 h. After evaporation, the crude product was portioned between CH₂Cl₂ and saturated aqueous ammonium chloride solution (1:1, 200 ml). The aqueous layer was separated and extracted with CH₂Cl₂ (100 ml). The organic layer was combined and dried over MgSO₄. Evaporation gave the crude product, purified by column chromatography with CH₂Cl₂ as eluent. Reddish liquid, 2.9 g, 72 % yield. ¹H NMR (CDCl₃) δ 9.10 (s, 1 H), 8.20 (d, 1 H), 7.40 (d, 1 H), 4.50 (s, 2 H), 4.28 (q, 2 H), 1.30 (t, 3 H).

Tris[2-(5-ethoxycarbonylpyridyl)methyl]amine This method followed the same procedure as for the preparation of tris[6-(hydroxymethyl)-2-pyridylmethyl]amine except that ethyl 2-bromomethyl-5-pyridylcarboxylate was used as the starting material, the crude product was recrystallized from hexane, 49% yield. ¹H NMR (*d*₆-DMSO) δ 9.05 (s, 1 H), 8.30 (d, 1 H), 7.78 (d, 1 H), 4.40 (q, 2 H), 3.98 (s, 2 H), 1.38 (t, 3 H). Calcd for C₂₇H₃₀N₄O₆: C, 64.03; H, 5.93; N, 11.07. Found: C, 64.50; H, 6.45; N, 10.41.

Tris[2-(5-carboxypyridyl)methyl]amine Tris[2-(5-ethoxycarbonylpyridyl)methyl]amine (1.0 g, 1.97 mmol) was dissolved in 25 ml 75 % aqueous ethanol solution. To the solution NaOH (1.5 g, 37.5 mmol) was added and the mixture was warmed at low steam for 40 min. After the reaction, the mixture was cooled down and 50 ml cold water was added and the pH value of the solution was adjusted to 2. The precipitate was filtered and washed with water, acetone and diethyl ether (0.80 g, 96

%). ^1H NMR (d_6 -DMSO) δ 9.05 (s, 1 H), 8.30 (d, 1 H), 7.78 (d, 1 H), 4.00 (s, 2 H). Calcd for $\text{C}_{21}\text{H}_{18}\text{N}_4\text{O}_6 \cdot \text{H}_2\text{O}$: C, 57.27; H, 4.54; N, 12.72. Found: C, 57.41; H, 3.99; N, 12.76.

Pyridine-2,4-carboxylic acid

KMnO_4 (128.6 g, 814 mmol) was dissolved in 2 liters of water and was heated to 60 - 70 $^\circ\text{C}$. To this solution 2,4-lutidine (Fluka, 22 g, 210 mmol) was added separately by portion. After addition, the solution was heated to boiling for 3 h. The solution was allowed to stand still overnight after reaction, filtered twice and washed with water. The filtrate was concentrated to 350 ml and acidified with concentrated HCl to pH = 2 and then put into refrigerator overnight. After the solution was warmed to room temperature, washed with water and then acetone. It was air-dried to afford 2,4-dicarboxylic pyridine (23g, 68 % yield) (A trace amount of 4-methyl-2-carboxylic pyridine was detected). ^1H NMR ($\text{D}_2\text{O}/\text{NaOH}$) δ 8.60 (d, 1 H), 8.18 (s, 1 H), 7.78 (d, 1 H). Anal. Calcd for $\text{C}_7\text{H}_5\text{NO}_4 \cdot \text{H}_2\text{O}$: C, 45.41; H, 3.78; N, 7.57. Found: C, 45.50; H, 3.27; N, 7.45.

Ethyl pyridine-2,4-dicarboxylate

This method followed the same procedure as that for the preparation of ethyl pyridine-2,5-dicarboxylate, colorless liquid, 95% yield. ^1H NMR (CDCl_3) δ 8.87 (d, 6 H), 8.52 (s, 3 H), 7.96 (d, 5 H), 4.38 (q, CH_2CH_3), 1.36 (t, CH_2CH_3). ^{13}C NMR (CDCl_3) δ 165.0 (C_2 -COO), 164.7.0 (C_4 -COO), 151.0 (6 C), 149.6 (2 C), 139.4 (4 C), 126.4 (5 C), 124.7 (3 C), 62.7, 62.6 (2 CH_2CH_3), 14.7, 14.6 (2 CH_2CH_3).

Ethyl 4-methoxypyridine-2-carboxylate This method followed the same procedure as *method A* for the preparation of ethyl 2-methoxypyridine-5-carboxylate except that ethyl pyridine-2,4-dicarboxylate was used for the starting material. The product was recrystallized in diethyl ether / hexane to give white crystals, 67% yield. ^1H NMR (CDCl_3) δ 8.70 (d, 6 H), 7.76 (s, 3 H), 7.74 (d, 5 H), 4.77 (s, CH_2OH), 4.44 (q, CH_2CH_3), 3.13 (broad, CH_2OH), 1.30 (t, CH_2CH_3). ^{13}C NMR (CDCl_3) δ 165.6 (COO), 152.1 (2 C), 150.2 (6 C), 148.5 (4 C), 124.5 (5 C), 122.9 (3 C), 63.5 (CH_2OH), 62.4 (CH_2CH_3), 14.7 (CH_2CH_3). Anal. Calcd for $\text{C}_9\text{H}_{11}\text{NO}_3$: C, 59.67; H, 6.08; N, 7.73. Found: C, 59.54; H, 6.11; N, 7.70.

Ethyl 2-methoxypyridine-4-carboxylate This method followed the same procedure as *method B* for the preparation of ethyl 2-methoxypyridine-5-carboxylate except that ethyl pyridine-2,4-dicarboxylate was used for the starting material. The product was recrystallized in diethyl ether / acetone, white crystals, 65% yield. ^1H NMR (CDCl_3) δ 8.70 (d, 6 H), 8.03 (s, 3 H), 7.47 (d, 5 H), 4.77 (s, CH_2OH), 4.45 (q, CH_2CH_3), 2.89 (broad, CH_2OH), 1.32 (t, CH_2CH_3). ^{13}C NMR (CDCl_3) δ 165.4 (COO), 160.8 (2 C), 150.0 (6 C), 138.9 (4 C), 122.0 (5 C), 120.3 (3 C), 64.6 (CH_2OH), 62.3 (CH_2CH_3), 14.6 (CH_2CH_3). Anal. Calcd for $\text{C}_9\text{H}_{11}\text{NO}_3$: C, 59.67; H, 6.08; N, 7.73. Found: C, 60.12; H, 6.14; N, 7.65.

Ethyl 2-bromomethylpyridine-4-carboxylate This method followed the same procedure as that for the preparation of ethyl 2-bromomethylpyridine-5-carboxylate except that ethyl 2-methoxypyridine-4-carboxylate was used for the starting material.⁷²

% yield. $^1\text{H NMR}$ (CDCl_3) δ 8.68 (d, 1 H), 7.90 (s, 1 H), 7.70 (d, 1 H), 4.50 (s, 2 H), 4.40 (q, 2 H), 1.30 (t, 3 H).

Tris[2-(4-ethoxycarbonylpyridyl)methyl]amine This method followed the same procedure as the for the preparation of tris[6-(hydroxymethyl)-2-pyridylmethyl]amine except that ethyl 2-bromomethyl-4-pyridylcarboxylate was used as the starting material. The crude product was recrystallized from hexane, 47% yield. $^1\text{H NMR}$ ($d_6\text{-DMSO}$) δ 8.73 (d, 1 H), 8.00 (s, 1 H), 7.70 (d, 1 H), 4.38 (q, 2 H), 4.05 (s, 2 H), 1.38 (t, 3 H).

Tris[2-(4-carboxypyridyl)methyl]amine This method followed the same procedure as that for the preparation of tris[2-(5-carboxypyridyl)methyl]amine except that tris[2-(4-ethoxycarbonylpyridyl)methyl]amine was use as the starting material, 95% yield. $^1\text{H NMR}$ ($d_6\text{-DMSO}$) δ 8.73 (d, 1 H), 8.00 (s, 1 H), 7.70 (d, 1 H), 4.02 (s, 2 H). Calcd for $\text{C}_{21}\text{H}_{18}\text{N}_4\text{O}_6 \cdot \text{NaCl}$: C, 52.44; H, 3.75; N, 11.65. Found: C, 52.06; H, 3.39; N, 11.39.

Ethyl pyridine-2,6-dicarboxylate This method followed the same procedure as that for the preparation of ethyl pyridine-2,5-dicarboxylate except that pyridine-2,6-dicarboxylic acid was used as the starting material. The crude product was purified by recrystallization from hexane. $^1\text{H NMR}$ (CDCl_3) δ 8.30 (d, 3, 5 H), 7.88 (t, 4 H), 4.46 (q, 2 CH_2CH_3), 1.42 (t, 2 CH_2CH_3). Anal. Calcd for $\text{C}_{11}\text{H}_{13}\text{NO}_4$: C, 59.2; H, 5.83; N, 6.28. Found: C, 59.11; H, 5.73; N, 6.20.

Ethyl 2-methoxypyridine-6-carboxylate *Method A* This method followed the same procedure as *method B* for the preparation of ethyl 2-methoxypyridine-5-carboxylate, except that reaction time was 30 min. The product was recrystallized from diethyl ether / acetone, colorless crystals, 60% yield. $^1\text{H NMR}$ (CDCl_3) δ 8.00 (d, 5 H), 7.76 (t, 4 H), 7.42 (d, 3 H), 4.78 (s, CH_2OH), 4.46 (q, CH_2CH_3), 3.00 (broad, CH_2OH), 1.35 (t, CH_2CH_3). $^{13}\text{C NMR}$ (MeOD) δ 166.7 (COO), 163.8 (2 C), 148.6 (6 C), 140.0 (4 C), 125.7 (5 C), 124.9 (3 C), 65.7 (CH_2OH), 63.4 (CH_2CH_3), 14.9 (CH_2CH_3). Calcd for $\text{C}_9\text{H}_{11}\text{NO}_3$: C, 59.67; H, 6.07; N, 7.73. Found: C, 59.55; H, 6.20; N, 7.59.

Method B This method followed the same procedure as *method C* for the preparation of ethyl 2-methoxypyridine-5-carboxylate, 83% yield.

Ethyl 2-bromomethylpyridine-6-carboxylate This method followed the same procedure as that for the preparation of ethyl 2-bromomethylpyridine-5-carboxylate except that ethyl 2-methoxypyridine-6-carboxylate was used for the starting material. 70% yield. $^1\text{H NMR}$ (CDCl_3) δ 7.96 (d, 1 H), 7.80 (t, 1 H), 7.44 (d, 1 H), 4.42 (s, 2 H), 4.28 (q, 2 H), 1.27 (t, 3 H).

Tris[2-(6-ethoxycarbonylpyridyl)methyl]amine This method followed the same procedure as the for the preparation of tris[6-(hydroxymethyl)-2-pyridylmethyl]amine except that ethyl 2-bromomethylpyridine-6-carboxylate was used as the starting material. $^1\text{H NMR}$ ($\text{Acetone-}d_6$) δ 7.97 (d, 1 H), 7.82 (t, 1 H), 7.68 (d, 1 H), 4.57 (q, 2 H), 3.98 (s, 2 H), 1.38 (t, 3 H).

Tris[2-(6-carboxypyridyl)methyl]amine This method followed the same procedure as that for the preparation of tris[2-(5-carboxypyridyl)methyl]amine except that tris[2-(6-ethoxycarbonylpyridyl)methyl]amine was used as the starting material, 95% yield. Calcd for $C_{21}H_{18}N_4O_6 \cdot 5/2H_2O$: C, 53.96; H, 4.92; N, 11.99. Found: C, 54.21; H, 4.67; N, 12.01.

4.2.2. Synthesis of the complexes

[RuCl₂(tmpa)](ClO₄) To a refluxing solution of RuCl₃•3H₂O (Aldrich, 0.52 g, 2 mmol) in ethanol (100 ml) was added a mixture including TPA•3HClO₄ (1.18 g, 2 mmol) and NaOH (0.184 g, 4.6 mmol) in ethanol (150 ml). The mixture was refluxed for 24 h and an orange precipitate emerged. The precipitate was washed with diethyl ether and air dried, 1.0 g, 82 % yield. Calcd for RuC₁₈H₁₈N₄Cl₃O₄: C, 38.53; H, 3.21; N, 9.99. Found: C, 38.95; H, 2.95; N, 7.55.

[RuCl(CO)(tmpa242)]Cl•C₂H₅OH RuCl₃•3H₂O (Aldrich, 0.26 g, 1 mmol) and tris[2-(4-carboxypyridyl)methyl]amine (tmpa242) (0.42 g, 1 mmol) were dissolved in 15 ml DMF and refluxed under N₂ for 8 h. The mixture was cooled down and 30 ml ethanol was added to the solution which was then put in the refrigerator overnight. The precipitate was collected by filtration and air-dried. 0.32 g, 51 % yield. IR, 1970 cm⁻¹ (νCO), 1719, 1618 cm⁻¹ (νCO₂⁻). Calcd for RuC₂₄H₃₀N₆Cl₂O₆: C, 41.03; H, 4.30; N, 11.96. Found: C, 40.67; H, 4.39; N, 11.25.

$[\text{RuCl}(\text{tmpa242})(\text{DMSO})]\text{ClO}_4$ $[\text{RuCl}(\text{tmpa242})(\text{DMSO})]\text{ClO}_4$ was prepared by following the same method as that used for the preparation of $[\text{RuCl}_2(\text{tpma242})]\text{Cl}$ except that $\text{Ru}(\text{DMSO})_4\text{Cl}_2$ was used as the starting material. ^1H NMR ($\text{D}_2\text{O} / \text{NaOD}$) δ 9.65 (d, 1 H), 8.82 (d, 2 H), 7.84 (s, 2 H), 7.66 (t, 2 H), 7.48 (s, 1 H), 5.38 (d, 1 H). IR, 1719, 1611 cm^{-1} (νCO_2^-), 1071 cm^{-1} ($\nu\text{S}=\text{O}$). Calcd for $\text{RuC}_{23}\text{H}_{24}\text{N}_4\text{Cl}_2\text{O}_{11}\text{S}\cdot\text{H}_2\text{O}$: C, 36.60; H, 3.45; N, 7.43. Found: C, 36.58; H, 3.58; N, 7.68.

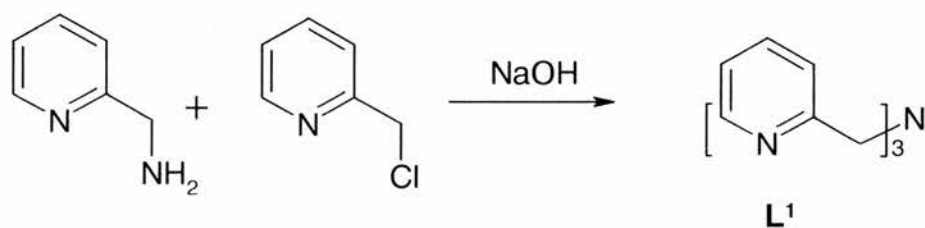
$[\text{Ru}(\text{N})\text{Cl}(\text{tmpa252})]_2\text{Cl}_2$ $[\text{RuCl}_2(\text{tmpa252})]\text{Cl}$ was prepared by following the same method as that for the preparation of $[\text{RuCl}(\text{CO})(\text{tmpa242})]\text{Cl}_2$ except that tris[2-(5-carboxypyridyl)methyl]amine (tmpa252) was used as the starting material. IR, 1970 cm^{-1} (νCO), 1719, 1618 cm^{-1} (νCO_2^-). Calcd for $\text{Ru}_2\text{C}_{44}\text{H}_{36}\text{N}_{10}\text{Cl}_4\text{O}_{14}$: C, 41.52; H, 2.85; N, 11.01. Found: C, 41.46; H, 2.98; N, 11.51.

4.3 RESULTS AND DISCUSSIONS

4.3.1 Synthesis of the ligands and the complexes

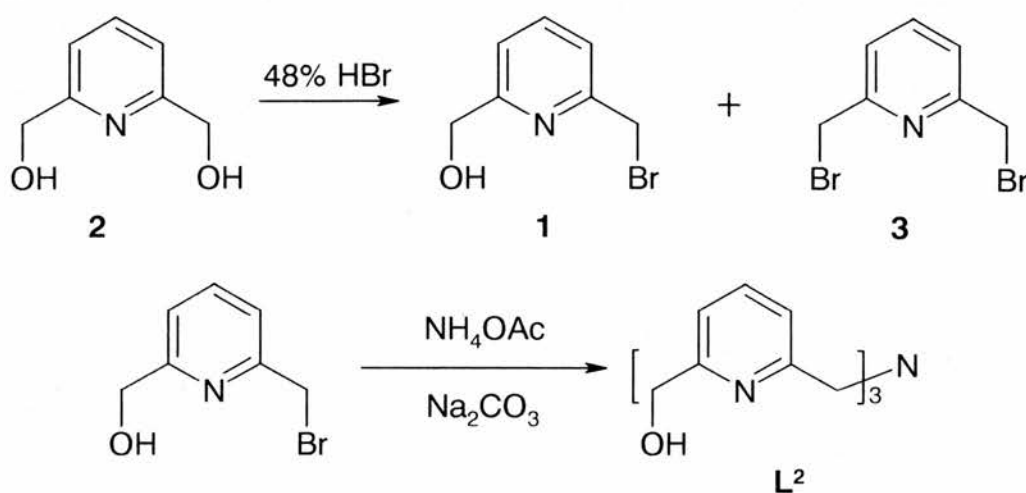
Tris(2-pyridylmethyl)amine (tmpa, L^1) was synthesized with 2-picolyl chloride hydrochloride and 2-(aminomethyl)pyridine as the starting materials.^{11, 31} First, 2-picolyl chloride hydrochloride was neutralized with NaOH aqueous solution, and then 0.5 moles of 2-(aminomethyl)pyridine was added to the mixture, with the further addition of NaOH to remove HCl, which would otherwise protonate the aminomethyl group and slow down

the reaction. (*Scheme 1*) The purification of the product was reported by Gafford and Holwerda, and involves the addition of perchloric acid to precipitate the product as the ammonium salt.³² Recrystallisation and purification *via* the Cr complex were accomplished in one step by mixing solutions of $[H_3tmpa](ClO_4)_3$ and $[Cr(H_2O)_6](ClO_4)_3$.



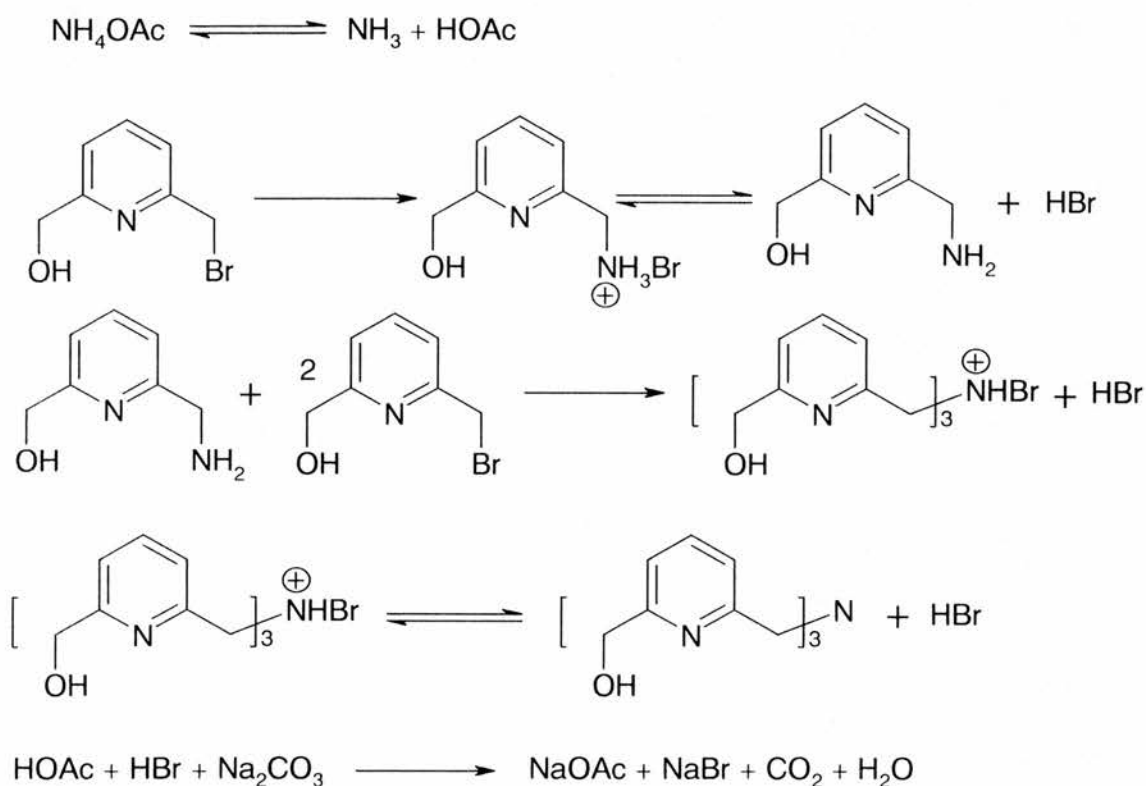
Scheme 1. Preparation of tris(2-pyridylmethyl)amine (tmpa)

Tris[6-(hydroxymethyl)-2-pyridylmethyl]amine (**L²**) was prepared from 6-(bromomethyl)-2-(hydroxymethyl)-pyridine (**1**), which was obtained by reacting 2,6-*bis*(hydroxymethyl)pyridine (**2**) in 48% HBr solution.¹⁰ This reaction also gives 2,6-*bis*(bromomethyl)pyridine (**3**) as a by-product. Reaction of ammonium acetate and 6-(bromomethyl)-2-(hydroxymethyl)-pyridine with sodium carbonate as the base gives the product in a reasonable yield. (*Scheme 2*)



Scheme 2. Preparation of Tris[6-(hydroxymethyl)-2-pyridylmethyl]amine

The ligand tmpa (L^1) may be synthesized in one step from 2-(aminomethyl)pyridine and 2-picolyl chloride hydrochloride (60-80% yield) in a concentrated solution of sodium hydroxide. The preferential formation of the tertiary amine without quaternary ammonium formation appears to be at least in part due to templating by the sodium ion, which the ligand is known to bind.³³ Few synthetic derivatives of tmpa ligands have been prepared, possibly partly because of the restrictive reaction conditions used to prepare the parent compound. Indeed, our first attempts of synthesis of tmpa came to a very low yield because the timing of the addition of sodium hydroxide to the solution mixture and the pH value of the solution is of great importance. The addition of perchlorate acid to the solution after reaction is helpful for the purification of the final product, which was further crystallized and purified by using $[\text{Cr}(\text{H}_2\text{O})_6](\text{ClO}_4)_3$ as the complex host and the crystalline ligand product at the pH = 2.

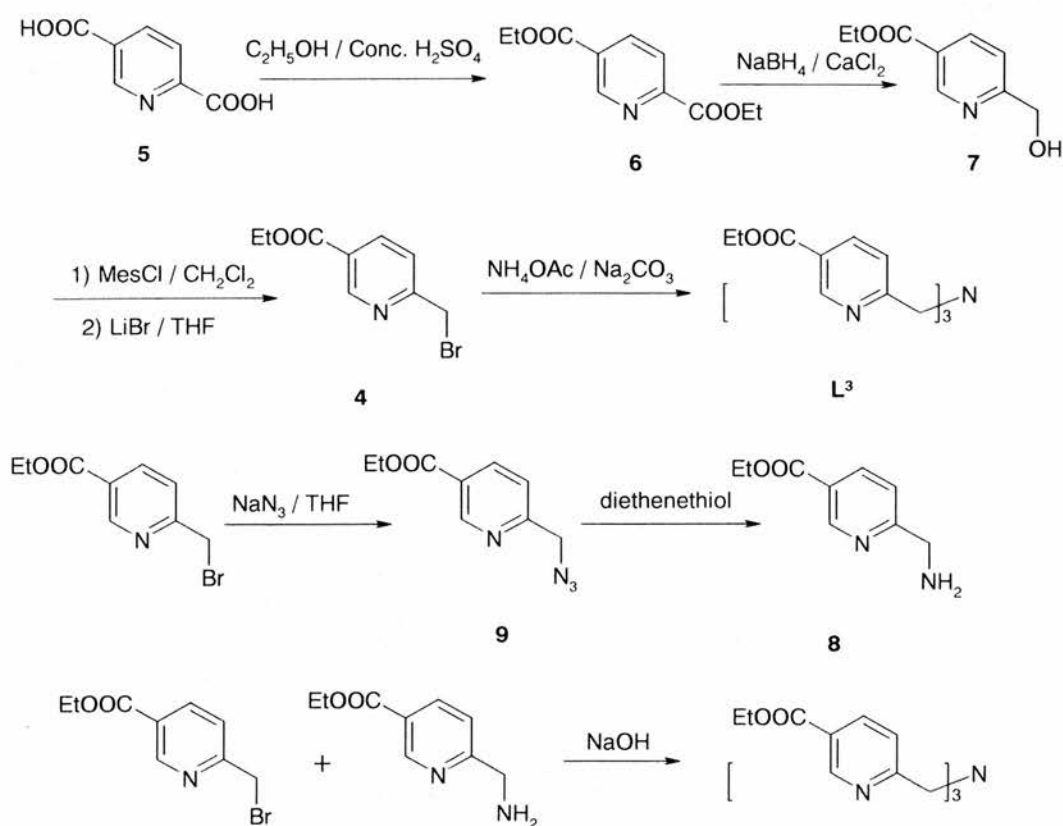


Scheme 3. The possible mechanism of the reactions of compound **1** reacting with ammonium acetate.

The process of preparing tris[6-(hydroxymethyl)-2-pyridylmethyl]amine (L²) serves as an example of how restrictive the reaction conditions are for the preparation of tmpa compounds. Following the procedure described above for L¹, the synthesis was unsuccessful. The reaction was finally accomplished by reacting 6-(bromomethyl)-2-(hydroxymethyl)-pyridine (**1**) and ammonium acetate in presence of sodium carbonate that neutralizes the protons generated by the reaction. (**Scheme 3**) Completion of the reaction was monitored by thin layer chromatography and the typical reaction time takes about 2 to 3 days. Furthermore, this reaction is quite sensitive to the light. The reaction hardly

proceeded at all while it was kept in the dark conditions, the reason for that is, however, still unknown to us. We used 2,6-bis(hydroxymethyl)pyridine (**2**) as the starting material, which reacts in 48% HBr to give both monobromo- and a dibromo- products. The reaction takes about 1 hour by refluxing, longer times yielding higher ratio of the dibromo- product. The monobromo- and dibromo mixture was separated by chromatography.

By implementing the same method used in the synthesis of tris[6-(hydroxymethyl)-2-pyridylmethyl]amine, tris[2-(5-carboxypyridyl)methyl]amine (**L⁴**) can be prepared from ethyl 2-bromomethylpyridine-5-carboxylate (**4**), which was obtained from by a routine synthesis,^{34, 35} starting from pyridine-2,5-dicarboxylic acid (**5**). Esterification of **5** in ethanol with conc. H₂SO₄ as catalyst gives ethyl pyridine-2,5-dicarboxylate (**6**), which was reduced by NaBH₄ to afford ethyl 6-hydroxymethyl-nicotinate (**7**). Compound **7** then was reacted with MsCl and then LiBr to afford **4**, which further reacted with ammonium acetate to give tris[2-(5-ethoxycarbonylpyridyl)methyl]amine (**L³**). Hydrolysis of **L³** affords the final product tris[2-(5-carbonylpyridyl)methyl]amine (**L⁴**). Or rather theoretically, the synthesis could be achieved by reacting ethyl-2-bromomethylpyridine-5-carboxylate with ethyl 2-aminomethylpyridine-5-carboxylate (**8**) in the presence of sodium carbonate, which is similar to the method that was used for the synthesis of tmpa (**L¹**), with the same starting material **5**. Compound **4** was converted to 5-(ethoxycarbonyl)-2-pyridylmethylazide (**9**) by reacting with sodium azide, then further reduced to **8** by using diethenethiol as the reducing agent. (*Scheme 4*)

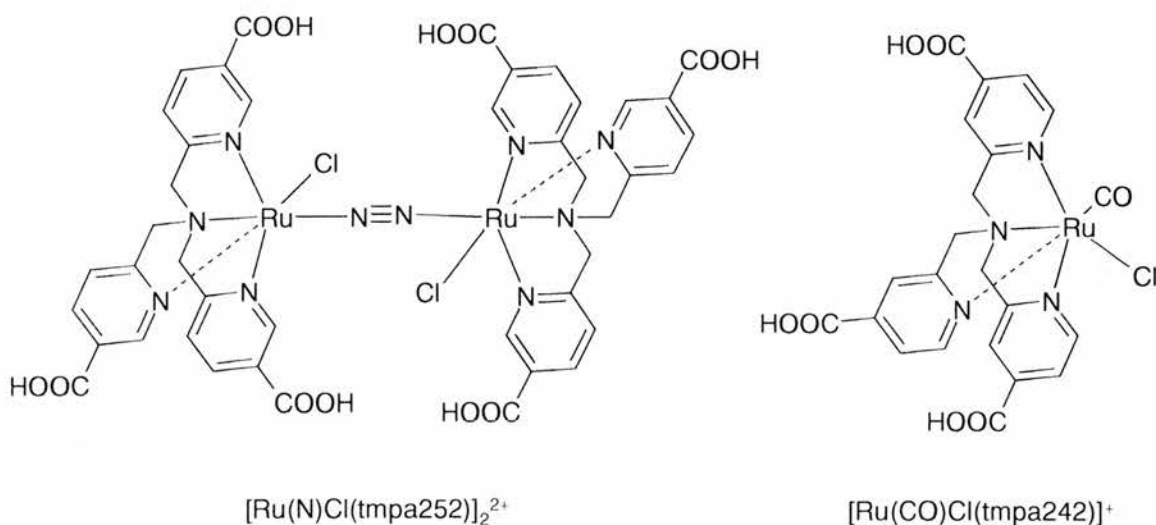


Scheme 4 Preparation of tris[5-(ethoxycarbonyl)-2-pyridylmethyl]amine (L^3)

Following the same procedure, the ligand *tris*[2-(4-carboxypyridyl)methyl]amine (L^5) can also be made with the starting material 2,4-lutidine, which was oxidized by potassium permanganate to give pyridine-2,4-dicarboxylic acid.

Unlike the bipyridyl ligands, tmpa has been shown to form Ru(III) complexes when reacting with $\text{RuCl}_3 \cdot 3\text{H}_2\text{O}$ in DMF.³⁶ $[\text{RuCl}_2(\text{tmpa})]\text{Cl}$ was obtained in high yield and the reaction was very clean. The preparation of $[\text{RuCl}(\text{CO})(\text{tmpa}242)]\text{Cl}$ and

[Ru(N)Cl(tpa252)]₂Cl₂ proved to give a lower yield and the reaction gave Ru(II) complexes instead of Ru(III) as one would expect. To synthesize the Ru(II) complex, *cis*-[RuCl₂(DMSO)₄] was used as the starting material. This compound has been used to obtain many Ru(II) complexes including phosphorus-containing compounds.³⁷ Further attempts to synthesize the thiocyanate substituted *tris*[4-carboxyl-2-pyridylmethyl]amine (tpa242) complex failed because of decomposition when trying to isolate and purify the compound. In the IR spectrum (KBr pellet) of compound [RuCl(tpa242)DMSO]Cl, an absorption observed at 1071 cm⁻¹ was assigned to ν(S-O). This assignment was made by comparing the IR spectrum of [RuCl(tpa)DMSO]ClO₄³⁶ and [RuCl(CO)(tpa242)]Cl and reported values of [RuCl(tpa)DMSO]ClO₄ (1072 cm⁻¹), which was almost the same in the light of resolution (4 cm⁻¹). The absorption bands at 1719 and 1611 cm⁻¹ were the assignment of the ν(C=O) of the pyridine carboxylic groups.

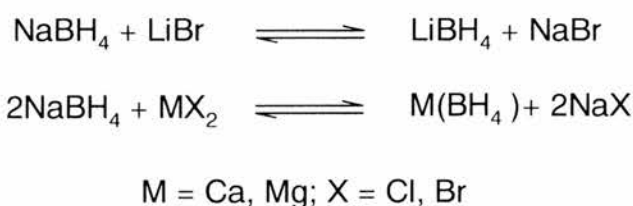


When the reactions were carried out in DMF, CO tended to coordinate with the metal centre as a good π -acceptor to stabilize the Ru(II). Interestingly, the reaction of tmpa252 with $\text{RuCl}_3 \cdot 3\text{H}_2\text{O}$ in DMF gave the product as a dimer with N_2 as the bridging ligand, while tmpa242 gave its monomeric complex. The same phenomenon was observed by Abbenhuis et al³⁸ in the synthesis of $[(\mu\text{N}_2)(\text{mer,trans-RuCl}_2(\text{L}))_2]$ complex ($\text{L} = 2,6\text{-[Bis(dimethylamino)methyl]pyridine}$). He discovered that complex of such structure turned to green upon exposure to air. Our complex, however, is stable in the air possibly due to the electron-drawing effect of the carboxylic acid group on the pyridyl rings. According to elemental analysis, C/H and C/N ratios were consistent with a product with molecular formula $[(\text{N}_2)(\text{RuCl}(\text{tmpa252}))_2]\text{Cl}_2$. It is worthwhile to point out that further experiment could be carried out under argon atmosphere to test this assignment.

When reacted under the same condition with $\text{RuCl}_3 \cdot 3\text{H}_2\text{O}$, tmap242 and tmpa252 gave different products. The mechanism of such reactions is not fully understood as different isomers could give different products under the same reaction condition. A possible reason is that tmap242 is a better π -acceptor than tmpa252 as the carboxylic group is in the opposite position to the nitrogen which is coordinated to the metal centre. A molecule of N_2 was then introduced in the dimer to stabilize the complex.

4.3.2 Regioselective reduction of the pyridyl diesters

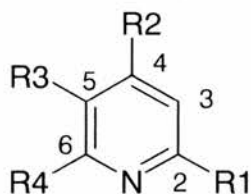
For the selective reduction of aldehyde and ketone groups, sodium borohydride is a very useful and widely used reagent.³⁹ The reduction of the ester and similar functional groups is relatively difficult. However, ester reduction has been facilitated by changing the solvent or by changing the cation.⁴⁰ The reduction of esters by sodium borohydride was achieved in the presence of metal salts such as LiI,⁴¹ LiBr, CaCl₂,⁴² MgX₂ (X= Cl, Br), ZnCl₂⁴³ or AlCl₃.⁴⁴ The reducing agent in these cases could be the metal borohydride formed *in situ* according to *Scheme 1*. It has been reported that the rate of the reduction of the aliphatic and aromatic esters is dependent on the solvent and the different reducing agents that were used. Later on, the selective reduction of pyridyl diester was reported by Matsumoto by using sodium borohydride and CaCl₂, in which only the 2-substituted position was reduced.⁴⁵



Scheme 5 Cation exchange of the metal borohydrate reducing agent.

We have studied the selective reduction of pyridyl diesters (Fig. 4.2) by using NaBH₄ as the reducing agent at the reflux temperature in ethanol and also CaCl₂, LiCl as the metal salts while it was carried out at low temperature. Nicotinic acid and its

derivatives have been of great interest in the studies of metal complexes⁴⁶⁻⁴⁸ and biochemical metabolism,⁴⁹ but the systematic study of the reduction of the pyridyl diesters has not hitherto been reported.



- a** $R_1 = R_2 = \text{COOEt}$, $R_3 = R_4 = \text{H}$
b $R_1 = R_3 = \text{COOEt}$, $R_2 = R_4 = \text{H}$
c $R_1 = R_4 = \text{COOEt}$, $R_2 = R_3 = \text{H}$
d $R_1 = \text{CH}_2\text{OH}$, $R_2 = \text{COOEt}$, $R_3 = R_4 = \text{H}$
e $R_1 = \text{COOEt}$, $R_2 = \text{CH}_2\text{OH}$, $R_3 = R_4 = \text{H}$
f $R_1 = \text{CH}_2\text{OH}$, $R_3 = \text{COOEt}$, $R_2 = R_4 = \text{H}$
g $R_1 = \text{CH}_2\text{OH}$, $R_4 = \text{COOEt}$, $R_2 = R_3 = \text{H}$

Fig. 4.2. Pyridyl diesters and its derivatives

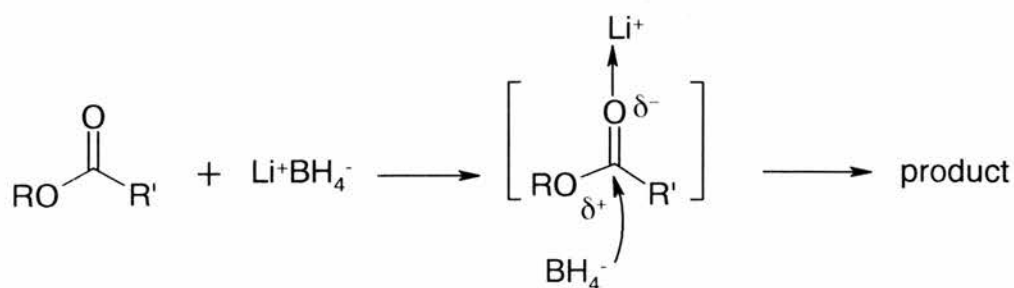
1) Reduction of the pyridyl diesters with NaBH_4 as the reducing agent

No reduction of the ester using NaBH_4 below $0\text{ }^\circ\text{C}$ ⁵⁰ was observed and only poor yields at room temperature were observed even after several hours.⁵¹ This reflects the known poor reactivity of NaBH_4 in ethanol for ester reduction.⁴⁰ It is possible, however, to enhance the reactivity at refluxing temperature. As shown in **Table 4.1**, reactions with ethyl pyridine-2,4-dicarboxylate (**a**) and ethyl pyridine-2,5-dicarboxylate (**b**) in the presence of NaBH_4 in refluxing ethanol were successful. Isomers ethyl 2-methoxypyridine-4-carboxylate (**d**), ethyl 4-methoxypyridine-2-carboxylate (**e**) and ethyl

2-methoxypyridine-5-carboxylate (*f*) were isolated respectively. Clearly, carbonyl substituents at the 2-position of the pyridine ring will have enhanced reactivity with nucleophilic than the other substituted positions, due to the π -electron withdrawing nature of the pyridine ring. For compound *b*, the ester group in the 5-position is far more electron rich than in the 2-position and is thus less likely to be reduced even after the coordination of the metal cation with the oxygen atom of the carbonyl group. In compound *a*, however, the electron density difference (~10%) between the 2- and 4-substituted positions is only marginally in favour of the 2-position being reduced. Rather surprisingly, the product (*e*) of reduced 4-position alcohol was the main reducing product at the reflux temperature. It should be pointed out that higher temperatures would reduce the selectivity. Diols were detected if the reflux was extended.

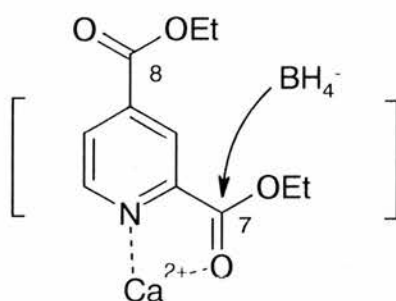
2) Reduction of the pyridyl diesters with NaBH₄ as the reducing agent and CaCl₂ as the metal salt

By following the method reported by Masumoto,⁴⁵ we carried out the reduction of *b* with sodium borohydride as the reducing agent and CaCl₂ as the metal salt at the temperature -10 to -5 °C. As expected, the 2-position of the diester was selectively reduced to alcohol *f*. According to Brown,⁴⁴ the S_N2 mechanism of this reaction is shown in *Scheme 6*.



Scheme 6 the mechanism of the reduction of ester
with LiBH_4 as the reducing agent

In the presence of metal cation, the reaction might undergo the mechanism as shown in **Scheme 7**. The carbonyl group at the 2-position is already more electron deficient because of the electron withdrawing nature of the pyridine ring. It becomes even more likely to be reduced due to the coordination of the calcium ion with the nitrogen and the oxygen from the ester group. In the presence of CaCl_2 , diester **a** gave exclusively **d**, while both isomers **d** and **e** were products when it was at the reflux temperature in the absence of CaCl_2 .



Scheme 7 Effect of Ca^{2+} complexation on the reduction of **a** by $\text{NaBH}_4 / \text{CaCl}_2$

Table 4.1 Effect of added metal cations on the reduction of pyridyl diesters with NaBH₄ as the reducing agent in ethanol

Reducing agent	diesters	product	Reacting time (h)	Yield (%)
NaBH ₄ ¹	a	d, e (1:2)	1.0	62
	b	f	1.0	72
	c	-	-	-
NaBH ₄ + CaCl ₂ ² (1:0.5)	a	d	2.5	67
	b	e	2.5	82
	c	g	0.5	60
NaBH ₄ + LiCl ² (1:1)	a	d, e (2:1)	2.5	70
	b	f	2.5	55
	c	g	1.5	83

¹Reactions carried out at reflux temperature. ²Reactions were carried out at -10 to -5 °C. Mole ratio of NaBH₄ to metal is 1:0.5 (Ca) and 1:1 (Li).

In order to test this theory, we recorded the ¹³C NMR spectra of ethyl 2,4-pyridyldicarboxylate (**a**) in MeOD in the absence and in the presence of LiCl or CaCl₂. (Fig. 4.3) Clearly, the carbon signal C₇ shifts upfield when the metal ion was present in the solution, and this carbon thus more likely to be reduced. The lack of an upfield shift for C₈ suggests that little complexation of this group occurs.

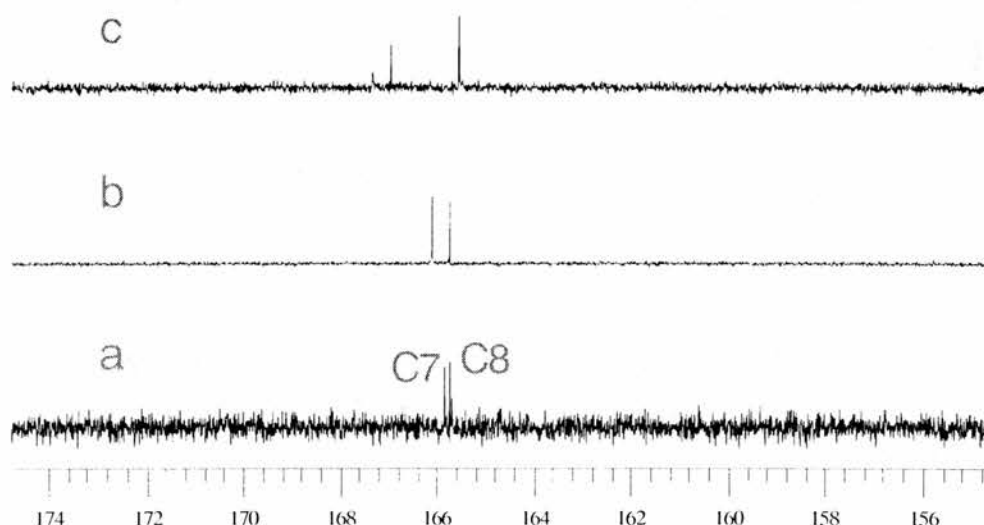


Fig. 4.3. ^{13}C NMR PENDANT spectra (carbonyl region) of **1** in MeOD (a) in the absence of metal cations; (b) in the presence of LiCl; (c) in the presence of CaCl_2

3) Reduction of the diesters with NaBH_4 as the reducing agent and LiCl as the metal salt

When lithium chloride was used for the reduction of **a**, it gave **d** and **e** in a mole ratio of about 2:1. As seen from the NMR evidence, it is possible that Li^+ ion is less strongly coordinated, leading to the competitive reduction of the esters in both 2- and 4-positions.

As we can see from Table 4.1, for the reduction of ethyl pyridine-2,6-dicarboxylate (**c**), LiCl is the preferred choice over CaCl_2 from the point of view of both yield and selectivity in the reduction of only one ester group to give ethyl 2-methoxypyridine-6-carboxylate (**g**). Perhaps when CaCl_2 was used, it tended to reduce

the ester group at both positions, lowering the yield of **g**. However in the presence of LiCl, it gave 2-position alcohol only, and with a higher yield. As for the reduction of **b**, however, CaCl₂ seems to be a more effective additive better than LiCl.

4.3.3 Electrochemistry

1) Oxidation

Voltammetric data obtained for the oxidation of the [RuCl₂(tmpa)]ClO₄ complex in acetonitrile at a platinum electrode with Bu₄NPF₆ (0.1 M) as the supporting electrolyte are summarized in Table 4.2. A reversible oxidation process of the metal center has been observed near +1.384 V, corresponding to the oxidation of Ru³⁺ to Ru⁴⁺. The electrochemical reversibility is confirmed by the invariance of the redox potential with the scan rate and a ΔE_p similar to that of the one-electron couple ferrocene in the same solvent, although, ideally, ΔE_p = 59/n mV. The larger ΔE_p is due to slow electron transfer and/or electrolyte resistance. The *i*_p^a increases as the square root of the scan rate. However, the cathodic peak is not fully realized indicating that the oxidized form undergoes a slow follow-up chemical reaction (EC reaction). The cyclic voltammetry of the electrochemical oxidation of the complex is shown in Fig. 4.4. The redox potential was calibrated with ferrocene.

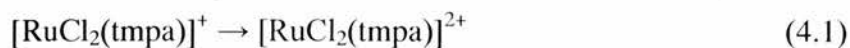


Table 4.2. Voltammetric data obtained for the $\text{Ru}^{3+/2+}$ oxidation of $[\text{RuCl}_2(\text{tmpa})]\text{ClO}_4$ (1 mM) complex in acetonitrile at a platinum electrode. (ν = scan rate, E_p = peak potential, $\Delta E_p = E_p^{\text{ox}} - E_p^{\text{red}}$, $E_{1/2} = E_p^{\text{ox}} + E_p^{\text{red}}$).

ν / mVs^{-1}	$E_p^{\text{ox}} / \text{V}$	$E_p^{\text{red}} / \text{V}$	$\Delta E_p / \text{mV}$	$E_{1/2} / \text{V}$
10	1.438	1.336	102	1.387
20	1.426	1.342	84	1.384
40	1.424	1.346	78	1.385
60	1.426	1.346	80	1.386
80	1.426	1.342	84	1.384
100	1.426	1.342	84	1.384
200	1.434	1.338	96	1.386
400	1.450	1.322	132	1.386

The data we obtained agree with that of Kojima³⁶, who further pointed out that the observation of this redox wave is due to the two electron-donating chloride anions on the Ru(III) center lowering the redox potential of the oxidation process. The redox wave from Ru^{3+} to Ru^{4+} was not observed, however, when the experiment was carried out in DMF solution, possibly due to solvent oxidation. Only one reversible reduction of the Ru^{3+} to Ru^{2+} process took place as we will mention later on.

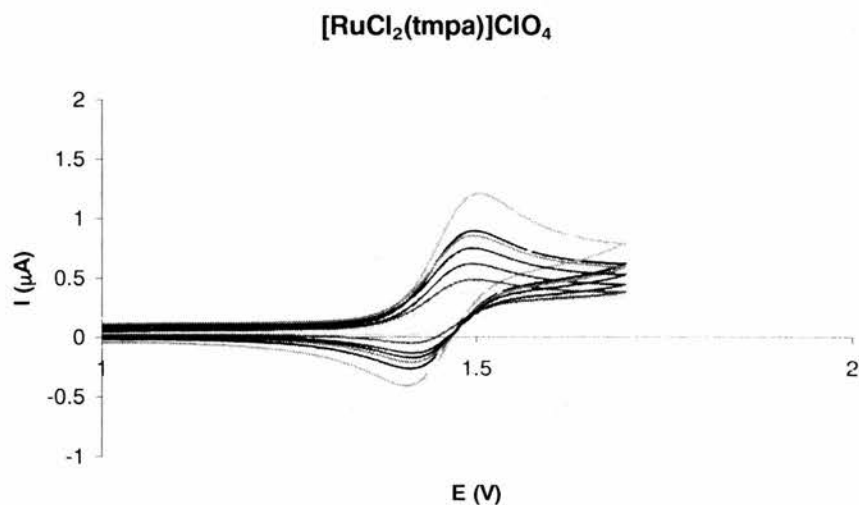


Fig. 4.4 Oxidation of $[\text{RuCl}_2(\text{tmpa})]\text{ClO}_4$ (1 mM) at the platinum electrode in acetonitrile with scan rates from 10 to 400 mVs^{-1} .

2) Reduction

Cyclic voltammetric reduction of $[\text{RuCl}_2(\text{tmpa})]\text{ClO}_4$ in acetonitrile took place at -0.27 V vs. Fc / Fc^+ , corresponding to the Ru^{3+} to Ru^{2+} process (eq. 4.2). The CVs of this reduction process at different scan rates from 10 to 400 mVs^{-1} are shown in Fig. 4.5. Voltammetric data obtained from the reduction of the $[\text{RuCl}_2(\text{tmpa})]\text{ClO}_4$ in acetonitrile at a platinum electrode are summarized in Table 4.3.

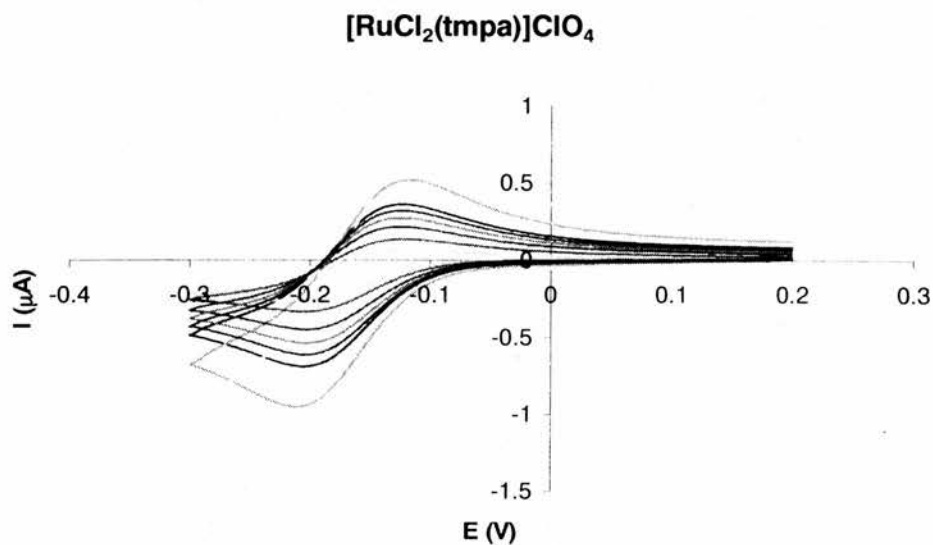


Fig. 4.5 Reduction of [RuCl₂(tmpa)]ClO₄ (1 mM) at the platinum electrode in Acetonitrile with scan rates from 10 to 400 mVs⁻¹

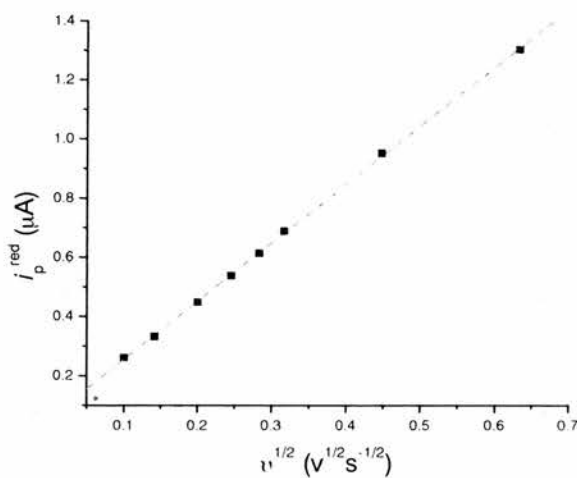


Fig. 4.6 Plot of i_p^{red} versus $v^{1/2}$ from cyclic voltammograms (i_p^{red} = reduction peak current, v = scan rate) over the scan rate range of 10 to 900 mVs⁻¹

As we expected, the $E_{1/2}$ is independent of the scan rate. A plot of i_p^{red} versus $\nu^{1/2}$ from cyclic voltammograms (i_p^{red} = reduction peak current, ν = scan rate) is linear over the scan rate range of 10 to 900 mVs^{-1} as shown in Fig. 4.6. The same electrochemical behaviour for the reduction was observed for $[\text{RuCl}_2(\text{tmpa})]\text{ClO}_4$ in DMF. An irreversible process corresponding to the reduction of tmpa (eq. 4.3) occurred when the potential was scanned more negatively (Fig. 4.7).

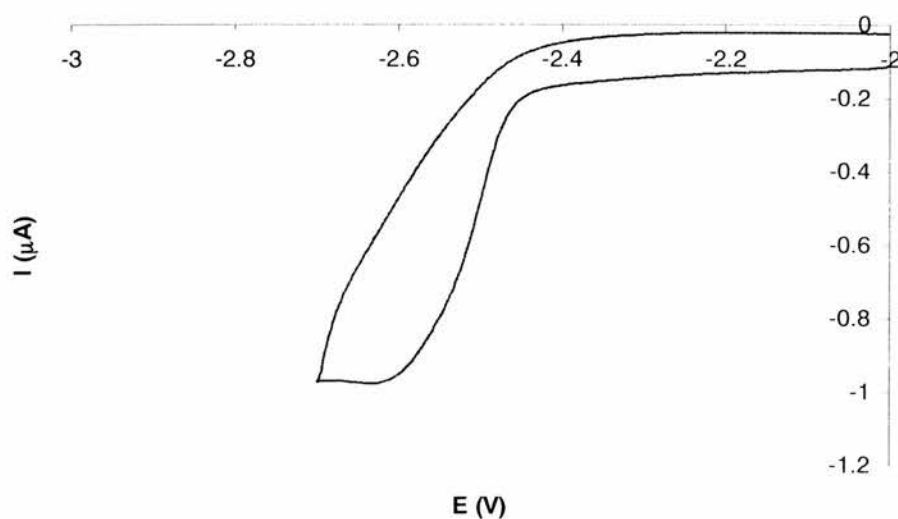
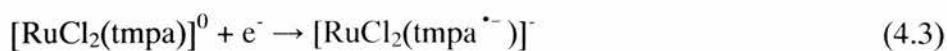
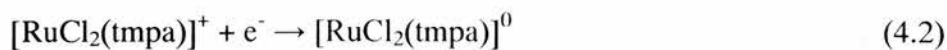


Fig. 4.7 Reduction of $[\text{RuCl}_2(\text{tmpa})]\text{ClO}_4$ (1 mM) at the platinum electrode in DMF with the scan rate 100 mVs^{-1} .

Table 4.3. Voltammetric data obtained for the reduction of $[\text{RuCl}_2(\text{tmpa})]\text{ClO}_4$ (1 mM) complex in acetonitrile at a platinum electrode. (ν = scan rate, E_p = peak potential, $\Delta E_p = E_p^{\text{ox}} - E_p^{\text{red}}$, $E_{1/2} = E_p^{\text{ox}} + E_p^{\text{red}}$).

ν / mVs^{-1}	$E_p^{\text{ox}} / \text{V}$	$E_p^{\text{red}} / \text{V}$	$\Delta E_p / \text{mV}$	$E_{1/2} / \text{mV}$
10	-0.284	-0.186	98	-0.235
20	-0.274	-0.192	82	-0.233
40	-0.270	-0.196	74	-0.233
60	-0.272	-0.196	76	-0.234
80	-0.272	-0.196	76	-0.234
100	-0.274	-0.195	79	-0.235
200	-0.280	-0.188	92	-0.234
400	-0.296	-0.178	118	-0.237

The voltammetric data obtained from the reduction of $[\text{RuCl}_2(\text{tmpa})]\text{ClO}_4$ in acetonitrile and DMF at a platinum electrode are shown in Table 4.4 as a comparison. A tentative explanation is that the DMF solvent stabilizes the cationic, oxidized half of the redox couple better than acetonitrile.

Table 4.4. Voltammetric data obtained for the reduction of $[\text{RuCl}_2(\text{tmpa})]\text{ClO}_4$ (1 mM) complex in acetonitrile and DMF at a platinum electrode, scan rate was 100 mVs^{-1} . (E_p = peak potential, $\Delta E_p = E_p^{\text{ox}} - E_p^{\text{red}}$, $E_{1/2} = E_p^{\text{ox}} + E_p^{\text{red}}$).

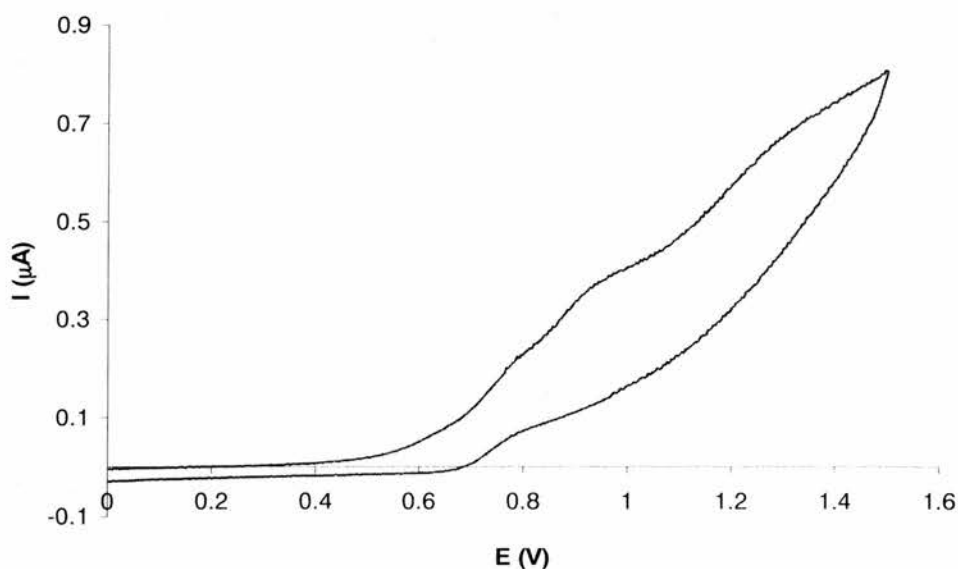
Solvent	Redox potential (V) vs. F_c / F_c^+		
	E_p^{red}	E_p^{ox}	$E_{1/2}$
Acetonitrile	-0.274	-0.195	-0.235
DMF	-0.341	-0.261	-0.301

Electrochemical oxidation and reduction of the other tmpa complexes are quite different from that of $[\text{RuCl}_2(\text{tmpa})]\text{ClO}_4$. Table 4.5 shows data for the reduction potentials of the tmpa complexes. The dimer $[(\mu\text{N}_2)(\text{RuCl}(\text{tmpa252}))_2]\text{Cl}_2$ has low redox potential comparing with that of the monomer $[\text{RuCl}(\text{CO})(\text{tmpa242})]\text{Cl}$. It is possible that chloride bonded the Ru(II) is a good electron donor to enrich the electron density of the metal centre thus it became easier to be reduced than the monomer. Compared with that of $[\text{RuCl}(\text{tmpa})(\text{DMSO})]\text{Cl}$ (0.61 V), the redox potential of $[\text{RuCl}(\text{tmpa242})(\text{DMSO})]\text{ClO}_4$ is quite similar (0.596 V). It indicates that on the one hand the carboxylic acid group of the ligand stabilizes the π^* level of the pyridine ring, and on the other hand it stabilizes the metal centre too because of its electron withdrawing effect. So the redox potential of the complex does not change much as it might have expected.

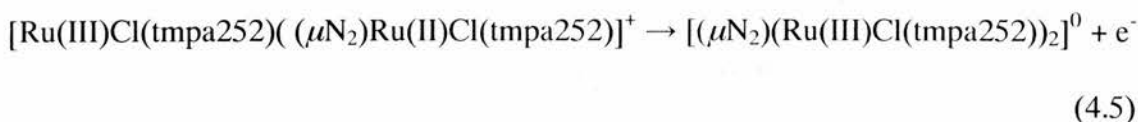
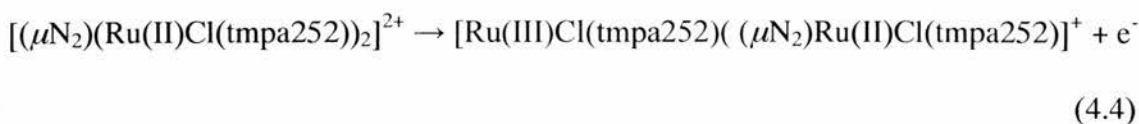
Table 4.5. Voltammetric data obtained for the reduction of Ruthenium tmpa complexes (1 mM) complex in DMF at a platinum electrode, scanning rate was 100 mVs⁻¹.

	Oxidation state	Redox potential (V) vs. F _c ⁺ /F _c	
		Ru ³⁺ / Ru ²⁺	Ru ⁴⁺ / Ru ³⁺
[RuCl ₂ (tmpa)]ClO ₄	Ru ³⁺	-0.235	1.384
[(μN ₂)(RuCl(tmpa252)) ₂]Cl ₂ ^a	Ru ²⁺	0.320	-
[RuCl(tmpa242)(DMSO)]ClO ₄	Ru ²⁺	0.596	-
[RuCl(CO)(tmpa242)]Cl	Ru ²⁺	0.712	-

a) irreversible peaks

Fig. 4.8 Oxidation of [(μN₂)(RuCl(tmpa252))₂]Cl₂ (1 mM) at the platinum electrode in DMF with the scan rate 100 mVs⁻¹.

The cyclic voltammetry of the electrochemical oxidation of the complex $[(\mu\text{N}_2)(\text{RuCl}(\text{tmpa252}))_2]^{2+}$ at platinum electrode in DMF is shown in Fig. 4.8. Slightly but not obviously, there were three oxidation process taking place at the electrode. The first two possibly indicate that the oxidation of the dimer (4.4, 4.5) and the third process possibly due to the free chloride oxidation.



4.3.4 UV-Vis Absorption

Fig. 4.9 shows electronic spectra of the complexes $[\text{RuCl}_2(\text{tmpa})]\text{ClO}_4$, $[\text{RuCl}(\text{tmpa242})(\text{DMSO})]\text{Cl}$ and $[\text{RuCl}_2(\text{tmpa242})]\text{Cl}$ in the visible light region. The absorption bands can be assigned to the MLCT due to $\text{Ru}(d\pi) \rightarrow \text{py}(p\pi^*)$ transitions.²⁸ As we can see, when the tmpa was replaced by tmpa242 in the Ru(III) complex, the absorption maximum band moved from 440 nm to 466 nm. When the carboxylic groups were introduced to the tmpa pyridine rings, the pyridines are stabilized and thus bring down the energy level of the π^* . And because of this, less energy is required for the MLCT transition so the absorption band is red-shifted. The maximum absorption band of the Ru(II) tmpa complex is even further red-shifted to 498 nm. The absorption bands are quite similar as that of the standard dye $[\text{Ru}(\text{dcpv})_2(\text{SCN})_2]$ even the pyridines are not

conjugated in the tris(2-pyridylmethyl)amine derivative complexes. Possible reasons are the contribution from both the stabilized pyridine rings and the electron pair of the amine group. In another words, the modification of the tmpa ligand by attaching the carboxylic group to the pyridine ring makes the absorption band of the ruthenium complexes red-shifted in the visible light region as we expected. Data from the absorption spectra are summarized in Table 4.6.

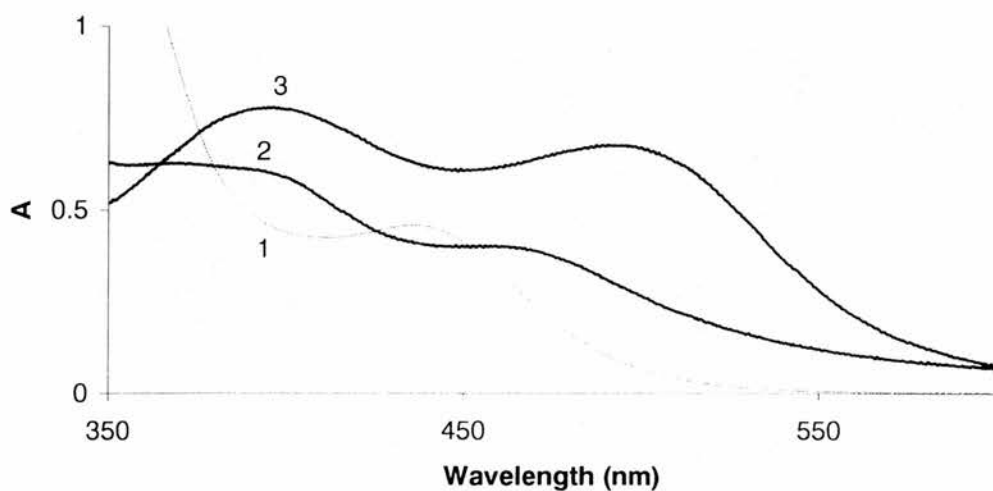


Fig 4.9 UV-Vis absorption in the visible light region of (1) $[\text{RuCl}_2(\text{tmpa})]\text{ClO}_4$ and (2) $[\text{RuCl}(\text{CO})(\text{tmpa242})]\text{Cl}$ (0.5 mM) measured in DMF and (3) $[\text{RuCl}(\text{tmpa242})(\text{DMSO})]\text{ClO}_4$ (0.2 mM) in ethanol.

Table 4.6 Electronic spectral data of ruthenium complexes of tmpa and its derivatives at room temperature.

Complex	λ_{\max} , nm (ϵ , $\text{dm}^3 \text{mol}^{-1} \text{cm}^{-1}$)
$[\text{RuCl}_2(\text{tmpa})]\text{ClO}_4^{\text{a}}$	440 (900), 352 (sh), 316 (4300)
$[\text{RuCl}_2(\text{tmpa242})]\text{Cl}^{\text{a}}$	466 (800), 375 (sh), 332 (1440)
$[\text{RuCl}(\text{DMSO})(\text{tmpa242})]\text{ClO}_4^{\text{b}}$	498 (3500), 397 (3850)
$[(\mu\text{N}_2)(\text{RuCl}(\text{tmpa252}))_2]\text{Cl}_2^{\text{b}}$	622 (580), 356 (3000)

^a) measured in DMF, ^b) in ethanol

4.3.5 IR spectroscopy

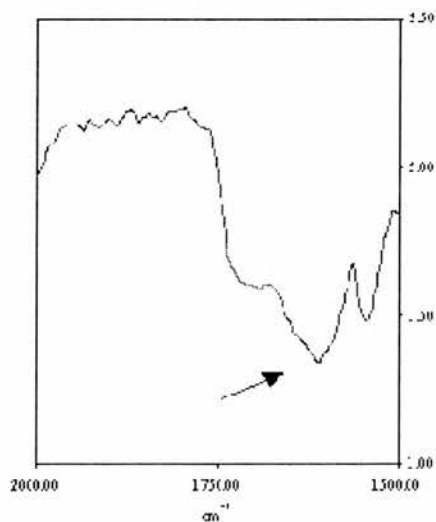


Fig. 4.10 Infrared spectrum of $[\text{Ru}(\text{tpma242})(\text{DMSO})\text{Cl}]\text{ClO}_4$ on TiO_2 semiconductor electrode

When the dye was adsorbed on the TiO₂ surface, the binding group and the surface form an ester bond which indicated by the infrared resonance spectroscopy at 1618 cm⁻¹ and 1710 cm⁻¹ (ν CO₂), as shown in Fig 4.10. It shows that there is an ester bonding when the semiconductor was dipped into the dye solution (0.5 mM). Due to those strong covalent bond, the complex did not leech from the surface upon washing.

4.4 CONCLUSIONS

In this chapter, we have been mainly concentrated on the modification and synthesis of *tris*(2-pyridylmethyl)amine (tmpa) ligands. We have successfully prepared some new tmpa carboxylic acid derivatives and their ruthenium complexes. Alternative methods for the preparations were described and compared. A study of the cation effect on the selective reduction of the pyridyl diesters to their mono-reduced alcohol species has been made. The compounds were mainly characterised by UV-Vis spectroscopy and electrochemistry. Due to the low solubility of the complexes, attempts to use them in the solar cells have run into difficulties. Their ester derivatives are thus strongly advised for further testing due to their better solubility and therefore more practical application in solar cells.

4.5 REFERENCES

1. G. C. Kulasingam and W. R. Mcwhinnie, *J. Chem. Soc. A*, 1967, 1253.
2. G. C. Kulasingam and W. R. Mcwhinnie, *J. Chem. Soc. A*, 1968, 254.
3. E. S. Kucharski, W. R. Mcwhinnie and A. H. White, *Aust. J. Chem.*, 1978, **31**, 2647.
4. D. L. White and J. W. Faller, *Inorg. Chem.*, 1982, **21**, 3119.
5. K. D. Karlin, J. C. Hayes, J. P. Hutchinson, J. R. Hyde and J. Zubieta, *Inorg. Chim. Acta.*, 1982, **64**, 1219.
6. F. R. Keene, M. R. Snow, P. J. Stephenson, and E. R. T. Tiekink, *Inorg. Chem.*, **1988**, **27**, 2040.
7. D. J. Szalda and F. R. Keene, *Inorg. Chem.*, 1986, **25**, 2795.
8. F. R. Keene and P. J. Stephenson, *Inorg. Chim. Acta*, 1991, **187**, 217.
9. L. F. Szczepura, L. M. Witham and K. J. Takeuchi, *Coord.Chem. Rev.*, 1998, **174**, 5.
10. Z. C. He, P. J. Chaimungkalanont, D. C. Craig and S. B. Colbran, *J. Chem. Soc., Dalton Trans.*, 2000, 1419.
11. M. Schatz, M. Becker, F. Thaler, F. Hampel, S. Schindler, R. R. Jacobson, Z. Tyeklar, N. N. Murthy, P. Ghosh, Q. Chen, J. Zubieta and K. D. Karlin, *Inorg. Chem.* 2001, **40**, 2312.
12. A. J. Canty, N. Chaichit, B. M. Gatehouse, E. E. George and G. Hayhurst, *Inorg. Chem.*, 1981, **20**, 2414.
13. A. J. Canty, J. M. Patrick and A. H. White, *Inorg. Chem.*, 1984, **23**, 3827
14. R. S. Brown and J. Huguet, *Can. J. Chem.*, 1980, **58**, 889.

15. J. W. Faller and Y. Ma, *J. Am. Chem. Soc.*, 1991, **113**, 1579. J. W. Faller and L. L. Gundersen, *Tetrahedron Lett.* 1993, **34**, 2275.
16. L. Que, Jr. and Y. Dong, *Acc. Chem. Res.*, 1996, **29**, 190.
17. H. F. Hsu, Y. Dong, L. Shu, V. G. Young, Jr. and L. Que, Jr., *J. Am. Chem. Soc.*, 1999, **121**, 5230.
18. P. A. Goodson, A. R. Oki, J. Glerup and D. J. Hodgson, *J. Am. Chem. Soc.*, 1990, **112**, 6254.
19. F. R. Keene, D. J. Szalda and T. A. Wilson, *Inorg. Chem.*, 1987, **26**, 2211.
20. N. Sutin and C. Creutz, *Pure Appl. Chem.*, 1980, **52**, 2717.
21. K. Kalyanasundram, *Coord. Chem. Rev.*, 1982, **46**, 159.
22. B. P. Sullivan, and T. J. Meyer, *Organometallics*, 1986, **5**, 1500.
23. J. Hawecker, J. –M. Lehn, R. Zeissel, *Helv. Chim. Acta.*, 1986, **69**, 1990.
24. Y. Zang, T. E. Elgren, Y. Dong and L. Que, *J. Am. Chem. Soc.*, 1993, **115**, 811.
25. Y. M. Chiou and L. Que, *J. Am. Chem. Soc.*, 1995, **117**, 3999.
26. Z. Tyeklar, R. R. Jacobson, N. Wei, N. N. Murthy. J. Zubieta and K. D. Karlin, *J. Am. Chem. Soc.*, 1993, **115**, 2677.
27. H. Nagao, N. Komeda, M. Mukaida, M. Suzuki and K. Tanaka, *Inorg. Chem.*, 1996, **35**, 7082.
28. T. Kojima, T. Amano, Y. Ishii, M. Ohba, Y. Okaue and Y. Matsuda, *Inorg. Chem.*, 1998, **37**, 4076.
29. N. Wei, N. N. Murthy and K. D. Karlin, *Inorg. Chem.*, 1994, **33**, 6093.
30. T. Kojima, *Chem. Lett.*, 1996, 121.
31. G. Anderegg and F. Wenk, *Helv. Chim. Acta.*, 1967, **50**, 2330

32. B. G. Gafford and R. A. Holwerda, *Inorg. Chem.*, 1989, **28**, 60.
33. H. Toftlund and S. Ishiguro, *Inorg. Chem.*, 1989, **28**, 2236.
34. M. Harata, K. Jitsukawa, H. Masuda and H. Einaga, *J. Coord. Chem.*, 1998, **44**, 311.
35. J. Bielavsky, J. Kassa, I. Elsnerova and L. Dejmek, *Collect. Czech. Commu.*, 1998, **63**, 199.
36. T. Kojima, T. Amano, Y. Ishii, M. Ohba, Y. Okaue and Y. Matsuda, *Inorg. Chem.*, 1998, **37**, 4076.
37. I. P. Evans, A. Spencer, G. Wilkinson, *J. Chem. Soc., Dalton Trans.*, 1973, 204.
38. R. A. T. M. Abbenhuis, I. del Río, M. M. Bergshoef, J. Boersma, N. Veldman, A. L. Spek and G. van Koten, *Inorg. Chem.*, 1998, **37**, 1749.
39. S. W. Chaikin and W. G. Brwon, *J. Am. Chem. Soc.*, 1949, **71**, 122.
40. H. C. Brown, S. Narasimhan and Y. M. Choi, *J. Org. Chem.*, 1982, **47**, 4702.
41. J. Kollonitsch, O. Fuchs and V. Gabor, *Nature (London)*, 1954, **173**, 125.
42. J. Kollonitsch, O. Fuchs and V. Gabor, *Nature (London)*, 1955, **175**, 346.
43. M. Periasamy and M. Thirumalaikumar, *J. Organomet. Chem.*, 2000, **609**, 137.
44. H. C. Brown and Subba Rao, B. C., *J. Am. Chem. Soc.*, 1956, **78**, 2582.
45. I. Matsumoto, *Chem. Abs.*, 1973, **79**, 31912j.
46. L. E. Gerdom and H. M. Goff, *Inorg. Chem.*, 1982, **21**, 3847.
47. J. C. Chang, L. E. Gerdom, N. C. Baenziger and H. M. Goff, *Inorg. Chem.*, 1983, **22**, 1739.
48. C. A. Green, R. J. Bianchini, and J. I. Legg, *Inorg. Chem.*, 1984, **23**, 2713.
49. P. Bisel, J. P. Gies, G. Schlewer, and C. G. Wermuth, *Bioorg. Med. Chem. Lett.*, 1996, **6**, 3025.

50. P. Scrimin, P. Tecilla and U. Tonellato, *Org. Prep. Proced. Int.*, 1991, **21**, 204.

51. K. Inoue, T. Sugaya, T. Ogasa and S. Tomioka, *Synthesis*, 1997, 113.

CHAPTER FIVE

Some other Metal polypyridyl complexes and Future Work

5.1 SOME OTHER METAL COMPLEXES

Apart from the ruthenium polypyridyl complexes that we have mentioned in the last two chapters, we have tried to synthesize some other metal complexes like tungsten and cupric complexes as an attempt of interest.

1) $[W(dcbpy)(DMF)(CO)_3]^+$ $W(CO)_6$ (176 mg, 0.5 mmol) and 2,4-dicarboxylic acid (112 mg, 0.5 mmol) were dissolved in 30 ml xylene / DMF (5:1). The mixture was refluxed for 5 h under N_2 . The precipitate was collected upon cooling by filtration and the product was dried on vacuum line, dark purple crystals. The complex is both air and photo-sensitive. UV-Vis, 390 nm ($\epsilon = 4200 M^{-1} cm^{-1}$), 550 nm ($\epsilon = 5800 M^{-1} cm^{-1}$). 1H NMR (300 MHz, $DMSO-d_6$), 9.28 (d, 6H), 9.02 (s, 3H), 8.02 (d, 5H), 7.92 (s, \underline{HCO}).

As we can see, tungsten mono-dcbpy complex has very similar absorption behaviour as the standard N3 dye (Fig. 5.1). Two MLCT bands, $W(d_\pi) \rightarrow dcbpy(\pi^*)$ in the visible region.^{2,3} The problem is that the complex is air-sensitive and leads to photo-decomposition in solution.

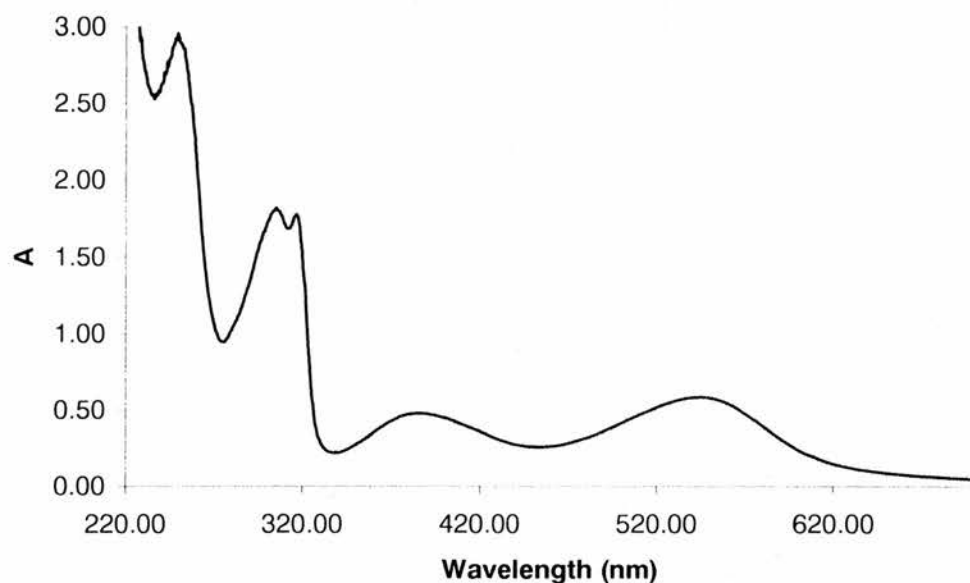


Fig. 5.1 UV-Vis absorption of $W(bpy)(DMF)(CO)_3$ (10^{-4} M) measured in ethanol

2) $[CuCl(tmpaOH)]Cl^+$ $CuCl_2$ (30mg, 0.22 mmol) and tris[(6-hydroxyl)-2-pyridylmethyl]amine (80 mg, 0.2 mmol) were dissolved in 10 ml methanol. The solution was covered with 5 ml diethyl ether and placed still for three days. The crystals was collected by filtration and washed with diethyl ether and dried in air. UV-Vis, 430 nm ($\epsilon = 2400 M^{-1} cm^{-1}$), 640 nm ($\epsilon = 1700 M^{-1} cm^{-1}$). (Fig. 5.2). $E_{1/2} Cu^{3+}/Cu^{2+}$ (+0.252 V), $E_{1/2} Cu^{2+}/Cu^+$ (-0.275 V) vs. F_c / F_c^+ .

The starting materials, comparing with that used for the standard dye N3, are cheap and easily available. If those two complexes can be further tuned to make it more stable for tungsten complex and if a linkage can be achieved for cupric tmpa complex, it would be a good alternative choice for the solar cells, providing those complexes have

long enough lifetimes to survive for the electron junction from the excited dye to the semiconductor electrode.

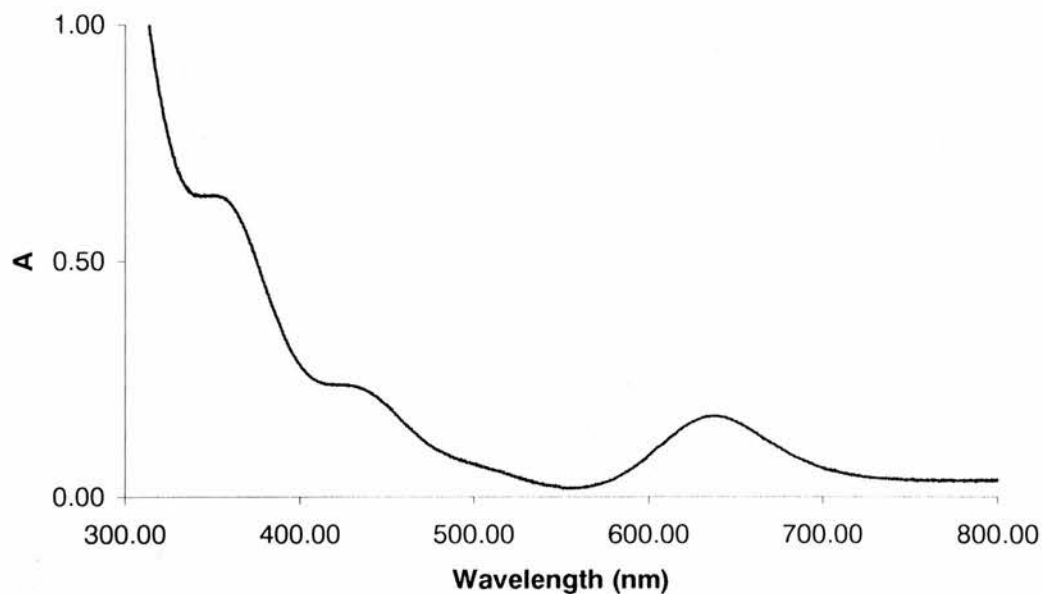


Fig. 5.2 UV-Vis absorption of $[\text{CuCl}(\text{tmpaOH})]\text{Cl}$ (10^{-4} M) measured in ethanol

5.2 FUTURE WORK

From the work we have done, we had the conclusion that bipyridine derivatives are good ligands for ruthenium centered complexes because they have delocalized π electrons thus have lower π^* energy level than most of the polypyridyl ligands such as tmpa and pbim. So it would be sensible if the future work could be concentrating on the bpy ligands. We suggest that the following ligands (**L¹** and **L²**, Fig. 5.3) would be good choices for the modification of the bpy ligand.

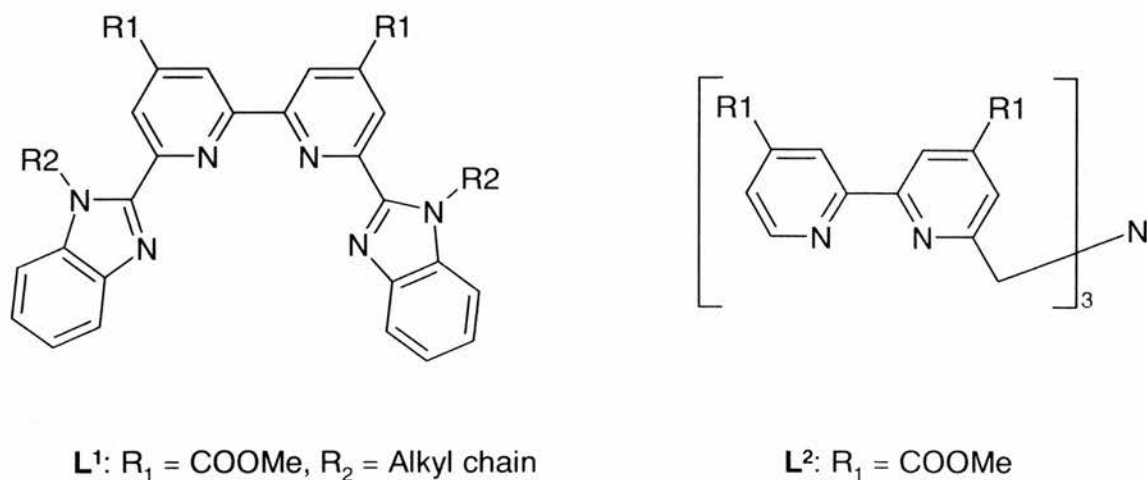


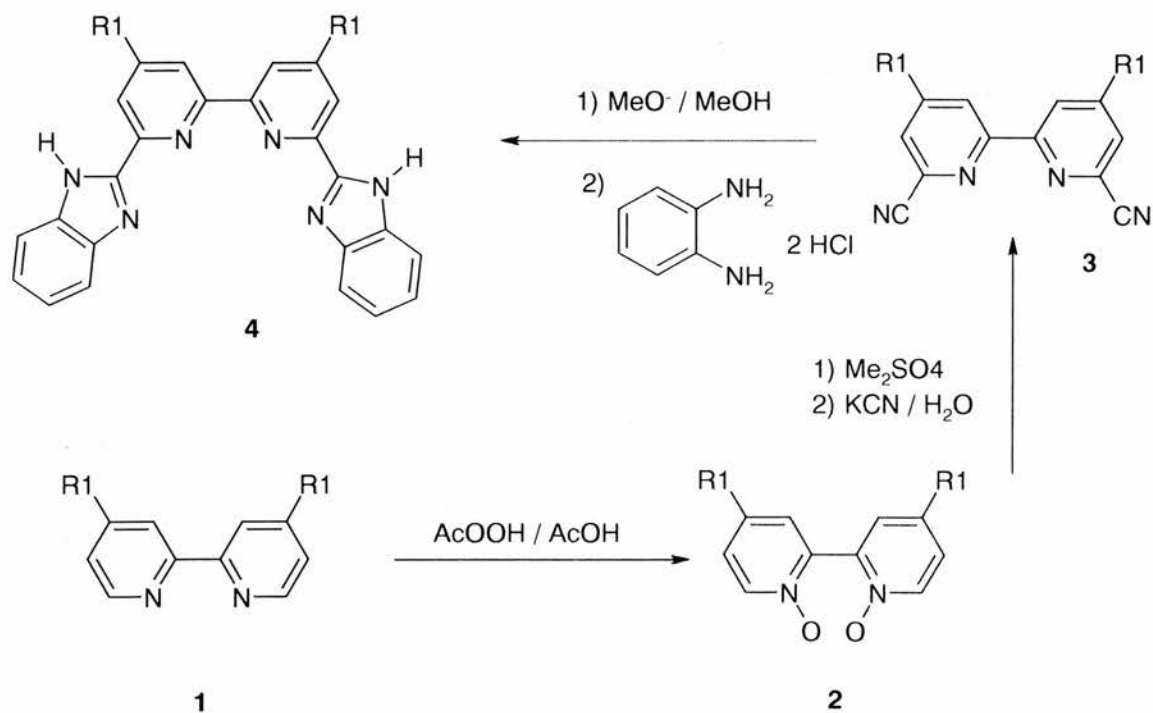
Fig. 5.3 Derivatives of bipyridine: **L¹**, 6,6'-(*N*-alkyl)bezenimidazole-4,4'-dimethoxyl carbonyl-2,2'-bipyridine, **L²**, Tris[2-(4,4'-dimethoxyl carbonyl)-2,2'-bipyridyl)methyl]amine

R₁ group, in both ligands, will serve as the linkage to the semiconductor electrode. The alkyl long chain, R₂, however, will not only enrich the electron density of **L¹** but also make the ligand more soluble in most of the solvents. The ligand **L²**, has seven nitrogens including that of amine, will offer a great opportunity for the coordination chemistry of dinuclear complexes or complexes with different metal centers, which will improve the light harvesting efficiency in the visible light region.

Synthesis proposal: **L¹** can be prepared from **4**, deprotonation of which and then further reaction with alkyl bromide to afford the target product. **4** was achieved from the

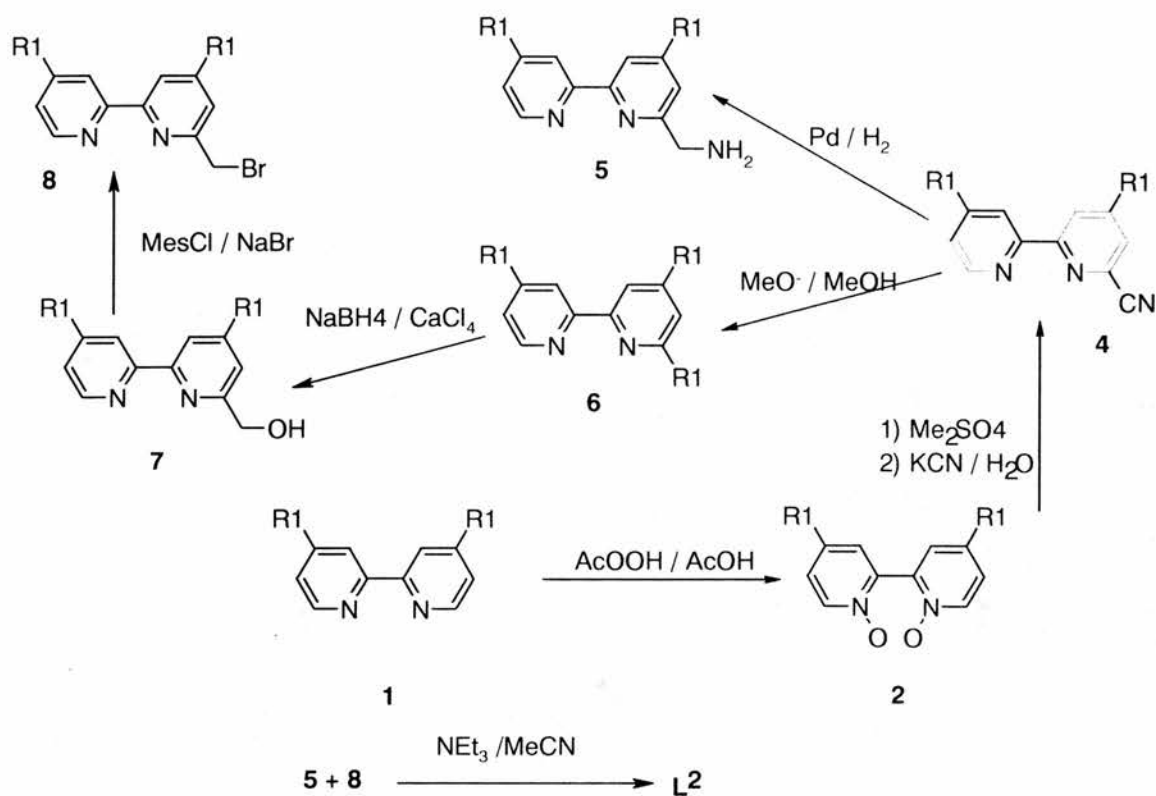
pyridyl diester **1**, following a series of reaction of N-oxidation, nucleophilic substitution by cyanide ions and finally copulation with 1,2-diaminobenzene.⁵ (Scheme 1)

Scheme 1



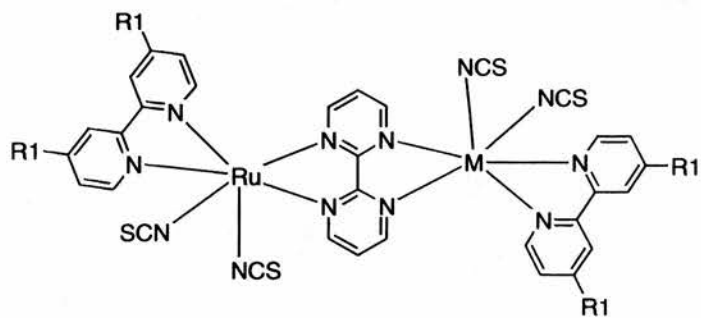
L² can be synthesized from **5** and **8**, which were prepared by following the same method as that of **L**¹. With the same starting material, single nucleophilic substitution by cyanide ion of **2** give **3** and reduction of **3** affords **5**. Methoxylation of **3** gives **6**, which can be selectively reduced by NaBH₄ in the presence of CaCl₂ to give **7**. Bromification of **7** yields **8**, which reacts with **5** in MeCN in the presence of NEt₃ to give **L**². (Scheme 2)

Scheme 2

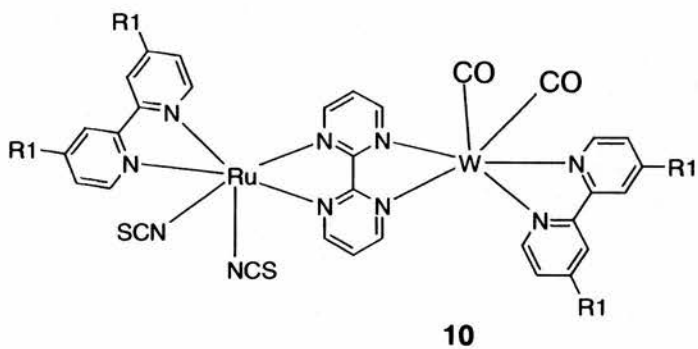


Further experiment can carry out by applying a bridging ligand to the multiple ruthenium centers complex *i.e.*, complex **9**, where R_1 is the binding group of the dye to the semiconductor electrode. Complex with such structure will be more conjugated and will lead to a red-shifted absorption in the visible light region. It could also be of interest if one of the ruthenium atoms to be replaced by some other metal such as Fe, Os or W (Scheme 3).

Scheme 3



9: M = Ru, Fe, Os



5.3 REFERENCES

1. E. W. Abel, M. A. Bennett and G. Wilkinson, *J. Chem. Soc.*, 1959, 2323.
2. A. J. Lees, *Coord. Chem. Rev.*, 1998, **177**, 3.
3. J. A. Connor and C. Overton, *J. Chem. Soc., Dalton Trans.*, 1982, 2397.
4. Z. C. He, P. J. Chaimungkalanont, D. C. Craig and S. B. Colbran, *J. Chem. Soc., Dalton Trans.*, 2002, 1419.
5. T. Renouard and M. Grätzel, *Tetrahedron*, 2001, **57**, 8145.